

An Improved Scheme to Suppress Spurious  
Orographic Resonance in Semi-Lagrangian Models

A thesis submitted for the degree of  
Doctor of Philosophy

Christian P. Lerrahn  
Diplom-Physiker

January 2012

School of Mathematical Sciences  
Monash University



# Contents

<b>Acknowledgements</b>	<b>11</b>
<b>1 Introduction</b>	<b>13</b>
1.1 Motivation . . . . .	13
1.2 Outline . . . . .	18
1.2.1 The Status Quo . . . . .	18
1.2.2 Testing the Various Off-Centring Schemes . . . . .	19
1.2.3 Applying the Findings to a GCM . . . . .	20
<b>2 Modelling the Atmosphere with SISL schemes</b>	<b>21</b>
2.1 The Equations . . . . .	22
2.1.1 The Primitive Equations . . . . .	22
2.1.2 The Shallow Water Equations . . . . .	24
2.2 Numerical Approaches . . . . .	27

2.3	The SISL method and its Limitations . . . . .	31
2.3.1	The Semi-Lagrangian, Semi-Implicit Approach . . . . .	31
2.3.2	SISL solution of the Shallow Water Equations . . . . .	34
2.3.3	Orographic Forcing in the Shallow Water Equations . . . . .	37
2.4	The Mountain Wave Resonance . . . . .	40
2.5	Mountain Waves in Nature . . . . .	43
2.5.1	The Discovery of Mountain Waves . . . . .	43
2.6	The Numerical Resonance . . . . .	45
2.7	Off-Centring . . . . .	48
2.7.1	The General Approach to Off-Centring . . . . .	48
2.7.2	The Adverse Effects of Off-Centring . . . . .	51
2.8	Off-Centring only the Height Equation . . . . .	52
2.9	Summary . . . . .	54
<b>3</b>	<b>SWiM – a Shallow Water Model</b>	<b>55</b>
3.1	Introduction . . . . .	55
3.2	The Shallow Water Equations in SWiM . . . . .	57
3.3	Solution Procedure . . . . .	58
3.3.1	Key Features . . . . .	58

<i>CONTENTS</i>	5
3.3.2 Bi-periodic Domain and $f$ -Plane . . . . .	59
3.3.3 Time Step . . . . .	61
3.3.4 Departure Points . . . . .	62
3.3.5 SOR Solver . . . . .	63
3.4 Off-Centring . . . . .	65
3.5 Variable Off-Centring Parameters . . . . .	67
3.6 Standard Tests applied to SWiM . . . . .	68
3.6.1 Advection Tests . . . . .	69
3.6.2 Tests for the SOR Solver . . . . .	78
3.6.3 Summary of Test Results . . . . .	81
<b>4 Shallow Water Experiments</b>	<b>83</b>
4.1 Reference Simulation . . . . .	85
4.2 No Off-Centring . . . . .	89
4.2.1 Simulations with Large Courant Numbers . . . . .	89
4.2.2 The Resonance in Detail . . . . .	101
4.2.3 The Spurious Resonance and Wave Interference . . . . .	106
4.3 Global Off-Centring . . . . .	108
4.3.1 Full Off-Centring Scheme (FOX) . . . . .	109
4.3.2 Off-Centring only the Height Equation (ROCKS) . . . . .	119
4.3.3 Off-Centring only the Momentum Equations . . . . .	128

<b>5</b>	<b>Variable Off-Centring in SWiM</b>	<b>133</b>
5.1	Designing a Variable Off-Centring Scheme . . . . .	134
5.2	Off-Centring All Equations (vFOX) . . . . .	139
5.3	Off-Centring only the Height Equation . . . . .	148
5.4	Conclusions . . . . .	158
<b>6</b>	<b>Off-Centring in a full GCM</b>	<b>161</b>
6.1	An Introduction to C-CAM . . . . .	161
6.1.1	C-CAM's Main Features . . . . .	162
6.1.2	The Equations in C-CAM . . . . .	164
6.1.3	Discretisation and Off-Centring . . . . .	166
6.2	The Spurious Orographic Resonance in C-CAM . . . . .	170
6.2.1	The Resonance in the Centred Equations . . . . .	171
6.2.2	Performance with Full Off-Centring . . . . .	173
6.2.3	Performance with Reduced Off-Centring . . . . .	175
6.2.4	Comparison between Full and Reduced Off-Centring . . . . .	177
6.2.5	Performance of the Existing Variable Off-Centring in C-CAM . . . . .	179
6.3	A New Variable Off-Centring Scheme in C-CAM . . . . .	180

<i>CONTENTS</i>	7
6.3.1 The implementation of the scheme in C-CAM . . . . .	180
6.3.2 Evaluation Methods and Selection of Key Regions . . .	185
6.3.3 Evaluation in Regions with Significant Orography . . .	194
6.3.4 Evaluation in Regions without Orography . . . . .	197
6.3.5 Evaluation in Regions of Intermediate Character . . .	201
6.3.6 Overall Performance of the Scheme in the Tropics . . .	207
6.4 Further Sensitivity Studies . . . . .	210
6.4.1 Sensitivity to Capping the Off-Centring Parameter . . .	210
6.4.2 Sensitivity to Scaling of the Off-Centring Parameter . .	216
6.5 Discussion . . . . .	226
<b>7 Conclusions</b>	<b>229</b>
<b>Bibliography</b>	<b>235</b>
<b>A SWiM Manual</b>	<b>243</b>
A.1 Prerequisites and Build Process . . . . .	243
A.2 Code structure . . . . .	244
A.3 Configuration options for SWiM . . . . .	245
A.4 Command line options . . . . .	249

A.5	Off-centring	251
A.6	Initialisation and Restart	251
A.6.1	Initialisation	251
A.7	Initialisation routine	252
A.8	Tests	254
A.9	Output format	254
A.10	Plotting Scripts	255
A.10.1	epsilon-plot.py	256
A.10.2	oroplot.py	256
A.10.3	oroplot-slice.py	256
A.10.4	swimplot.py	258
A.10.5	swimplot-slice.py	259
A.10.6	swimplot-vorticity.py	260
A.10.7	swimplot-energy.py	260

# Abstract

Semi-Lagrangian schemes, as are widely used in numerical weather prediction, exhibit a spurious resonance for time steps that result in Courant numbers  $C \gtrsim 1$ . The spurious resonance is caused by orographic forcing and can be removed by off-centring the discretised equations in time. This approach leads to increased numerical damping everywhere in the domain and may adversely affect accuracy even in regions of little orography. In this thesis, the off-centring approach is revisited and the traditional off-centring scheme validated. In an attempt to reduce the additional numerical damping while maintaining stability, the traditional scheme is then modified by limiting the off-centring to a subset of equations. After extensive numerical tests in a shallow water model, the schemes are then further modified to vary the additional damping across the computational domain as a function of the orography. Based on the findings in the shallow water model, a new scheme is implemented in a global climate model (GCM) and the impact of the new scheme assessed in detail.

Under the Copyright Act 1968, this thesis must be used only under the normal conditions of scholarly fair dealing. In particular no results or conclusions should be extracted from it, nor should it be copied or closely paraphrased in whole or in part without the written consent of the author. Proper written acknowledgement should be made for any assistance obtained from this thesis.

I certify that I have made all reasonable efforts to secure copyright permissions for third-party content included in this thesis and have not knowingly added copyright content to my work without the owner's permission.

I hereby declare that this submission is my own work and that, to the best of my knowledge and belief, it contains no material previously published or written by another person nor material which to a substantial extent has been accepted for the award of any other degree or diploma of the university or other institute of higher learning, except where due acknowledgment has been made in the text.

# Acknowledgements

I am very grateful to my supervisors Christian Jakob and John McGregor who have provided outstanding supervision for this PhD project. I want to thank John McGregor in particular for a lot of invaluable thoughts on how to best develop the project and great support in my learning process when working with the C-CAM model. I owe thanks to Christian Jakob for keeping a close eye on the progress of the project and for asking a number of critical questions of a non-numerical and non-technical nature which added relevance to the project. Most of all, however, he has made a great effort in proof-reading and editing this thesis, improving the readability and logical flow by a great deal. He has also assisted me numerous times in bureaucratic challenges that came with the candidature.

I also want to thank Andrew Staniforth who has answered several questions, to do with past research of his, in great detail and provided very helpful insights on more than one occasion.

I also am greatly indebted to a number of people in the administrative section of the School of Mathematical Sciences at Monash University. There are too many names to mention all of them here but a very special thanks goes to the Director of Postgraduate Studies John Lattanzio, the School

Manager Gertrude Nayak and the Head of School Kate Smith-Miles who have been of great help in overcoming a number of bureaucratic hurdles over the course of my candidature.

Beyond my professional environment, I want to thank my family who, even from a far distance, provided much needed support, encouragement and prayers in all the challenges of the past few years. A big thanks also goes to all the friends I have been able to make in the years I spent in Australia. A very special thank you I extend to the members of St Jude's Community Church Carlton and, in particular, its former minister Richard Shumack.

I dedicate this thesis to a group of people that has become very precious to me over the years of my PhD candidature, the Melbourne Somali community. Many members of this community have contributed a great deal to making my time in Australia a great experience. Their friendship, hospitality and generosity have also played a crucial part in the positive experience my time in Melbourne has been.

Last but not least, I thank Jesus Christ, my God and Saviour who has sustained me for many years in professional challenges just as in the many other challenges of life.

# Chapter 1

## Introduction

### 1.1 Motivation

The field of atmospheric science can be traced back for several millenia. Three thousand years ago, the Babylonians already recorded weather observations, described atmospheric phenomena and tried to predict the most prominent features of the weather like wind and rain. Formally, the field of meteorology was established by Aristotle with his publication *Meteorologica* which was published around 350BC and gave the field its name.

Just as Aristotle had defined the field, for almost two millenia it was studied as a part of natural philosophy. Until the 17th century systematic meteorological records were uncommon even though they did exist in different places for short periods at a time. As early as the 14th century, William Merle at Merton College recorded the weather at Oxford daily from 1337 to 1344 and in 16th century the Danish astronomer Tycho Brahe kept daily

weather records for the years 1582 to 1598. Such records were usually descriptive and qualitative and remained so until the 17th century when the thermometer and barometer were invented.

The invention of thermometer and barometer enabled the meteorologists to quantify a number of their observations and systematic records became increasingly popular. However, the ability to quantify aspects of the weather also led to a large number of new questions. In this climate of great change, René Descartes stimulated new thinking with his publication *Les météors*, an appendix to his *Discours de la méthode* (1637). It was this appendix, that was the first step in a process that gave meteorology the scientific character it has today. Over the course of the 17th century, the whole field transitioned from purely qualitative description to a quantitative observational science. Theories were formulated on the basis of such observations, such as Edmond Halley's theory of the trade winds in 1686. Nevertheless, the scientific treatment did not widely imply a mathematical approach for about another 200 years. Only then, did dynamical meteorology emerge as the mathematical theory of fluid motion on a rotating earth.

A challenge for meteorology ever since its inception was to predict the weather. Early forecasts were purely based on interpretations of synoptic weather maps, i.e. to a large degree subjectively predicting the weather based on weather maps and charts of recent observations. These synoptic forecasts attracted a lot of controversy and failed to evolve into a reliable and objectively validated prediction theory. The lack of reliability led to some weather services keeping their forecasts very broad or not issuing any public forecasts at all.

Only around the start of the 20th century, was the idea born to derive systems of differential equations from the laws of physics and to use these for predicting the weather. While he was not the only one to suggest a description of the atmosphere using a set of equations, the Norwegian physicist Vilhelm Bjerknes is usually considered the father of dynamic weather prediction. He called the set of equations he suggested the *primitive equations* (cf. Section 2.1.1). However, being aware that the equations could unlikely be solved analytically, Bjerknes (1914) suggested a graphical solution<sup>1</sup> process. Bjerknes became the strongest advocate of physical weather prediction and spread the idea in the scientific community. He was aware that the lengthy solution process made it impossible to use this forecasting technique operationally, but he believed that whenever physically accurate modeling was established, the timely forecasts would follow naturally.

Bjerknes most likely never considered solving the primitive equations numerically. It would take until the year 1922 when Lewis Fry Richardson published his book *Weather Prediction by Numerical Process* (Richardson, 1922) for this approach to see the light of day. Richardson's calculations were not very accurate and he had to invest 6 weeks to produce a 6h forecast. Nevertheless, he exhibited the concept that this was another possible approach to weather prediction, known ever since as numerical weather prediction (NWP).

Richardson actually dreamt of what sounds almost like a description of a parallel supercomputer, yet, it was a human cluster instead of one of computer processors. In his books he writes about his dream:

---

<sup>1</sup>Different graphical solution processes were employed in this era. Bjerknes suggested a map-based method which became known as *graphical calculus*.

*After so much hard reasoning, may one play with a fantasy? Imagine a large hall like a theatre, except that the circles and galleries go right round through the space usually occupied by the stage. The walls of this chamber are painted to form a map of the globe. The ceiling represents the north polar regions, England is in the gallery, the tropics in the upper circle, Australia on the dress circle and the antarctic in the pit. A myriad computers are at work upon the weather of the part of the map where each sits, but each computer attends only to one equation or part of an equation. The work of each region is coordinated by an official of higher rank. Numerous little "night signs" display the instantaneous values so that neighbouring computers can read them. Each number is thus displayed in three adjacent zones so as to maintain communication to the North and South on the map. From the floor of the pit a tall pillar rises to half the height of the hall. It carries a large pulpit on its top. In this sits the man in charge of the whole theatre; he is surrounded by several assistants and messengers. One of his duties is to maintain a uniform speed of progress in all parts of the globe. In this respect he is like the conductor of an orchestra in which the instruments are slide-rules and calculating machines. But instead of waving a baton he turns a beam of rosy light upon any region that is running ahead of the rest, and a beam of blue light upon those who are behindhand. (Richardson, 1922, p. 219)*

Richardson's publication enjoyed a lot of attention from the scientific community. But the challenges he had encountered in terms of computational cost and accuracy led other scientists to the conclusion that numerical

weather prediction was not feasible. Even Richardson himself considered numerical weather prediction for timely forecasts a dream and never returned to his studies. Not many years later he turned his back on meteorology altogether and dedicated himself to psychology and later peace research. The numerical approach to physical weather prediction would lie dormant for 35 years.

With John von Neumann it was a mathematician, without any links to meteorology, who reintroduced the idea of numerical weather prediction. Von Neumann had already experimented with the then new punched-card computers solving hydrodynamical problems. For unknown reasons, he later turned to meteorology as his prime field of interest for solving differential equations with the help of a computer. Most likely he was convinced that weather forecasts provided the most challenging unsolved scientific problem fit to be solved with the help of a computer. He therefore established the Meteorology Project at Princeton University's Institute for Advanced Study which became the starting point of modern numerical weather prediction.

When the Meteorology Project was born, the controversy over the feasibility of a general global circulation theory had not been resolved yet. There were very strong opinions on both ends of the spectrum with some arguing that a consistent general theory was out of reach while others believed its emergence was imminent (cf. [Richardson, 1922](#)). In the mid-1950s, the rapid development of the field silenced the sceptics. Particularly, the contributions of [Phillips \(1954, 1956\)](#) and [Lorenz \(1963\)](#) were major breakthroughs. While [Phillips'](#) experiment with a general circulation model strongly influenced the development of the Meteorology Project, [Lorenz'](#) work on predictability was a milestone in paving the way to modern numerical models which solve the primitive equations.

But even once numerical weather prediction had reached an operational stage, the two issues [Richardson](#) had already faced, computational cost and accuracy, remained the limiting factors to its practical applications and have posed a challenge ever since. In a constant effort of reducing the computational cost, while maintaining or even improving the accuracy of the numerical solutions, new schemes and approaches have constantly been developed. One of the more recent schemes which has found its way into many operational models is the semi-implicit semi-Lagrangian scheme. It combines the strengths of Eulerian finite difference methods with those of fully Lagrangian schemes. Despite its many advantages, there remain several issues when applying this scheme, among them a spurious resonance which can render the system unstable. The spurious resonance has no physical counterpart and is a direct result of the discretisation of the equations. It is triggered for high Courant numbers  $C = |U|\Delta t/\Delta x > 1$  (with velocity  $U$ , and time and spatial increments  $\Delta t$  and  $\Delta x$ ), when orographic forcing is present. This stability problem can be overcome by modified schemes which deliberately introduce additional numerical damping. The numerical damping in current schemes is indiscriminately applied to the entire computational domain. This thesis presents a comprehensive study of the spurious resonance and develops a scheme which allows the application of numerical damping only as needed locally.

## 1.2 Outline

### 1.2.1 The Status Quo

The previous section already provided a rough outline of the environment the current research is conducted in. [Chapter 2](#) provides an overview of two

sets of equations commonly used to describe the atmosphere – the primitive equations and the shallow water equations. The same chapter also discusses the semi-implicit semi-Lagrangian (SISL) approach to numerically solving the shallow water equations. It then moves on to describe how and why this numerical scheme exhibits a spurious resonance in the presence of orography. As the method of off-centring solves this problem of a spurious resonance, it is explained both conceptually and by way of mathematical proof of its effectiveness. This sets the scene to present a newly developed modification of the off-centring concept, which again is explained in detail, whereafter a mathematical proof of its value, analogous to that for the existing off-centring scheme, is attempted.

### 1.2.2 Testing the Various Off-Centring Schemes

As a means of experimentally verifying the analytical findings and determining the still unknown parameters necessary to ensure that the solution stays bounded, the numerical semi-implicit semi-Lagrangian shallow water model SWiM is introduced in Chapter 3. The custom developed model SWiM is described in detail and validation tests are shown.

Chapter 4 then uses SWiM to perform a number of experiments, which validate the existing off-centring scheme as devised by Rivest et al. (1994). These experiments are then followed by another group of experiments which implements and tests the new off-centring scheme described at the end of Chapter 2. This scheme reduces the amount of numerical damping introduced through off-centring, by only applying off-centring to a subset of the equations solved. In the experiments, the benefits and shortcomings of such a scheme are assessed.

Chapter 5 uses the findings of Chapter 4 to build on and further modify both schemes numerically tested in Chapter 4. It introduces an off-centring scheme which varies the so called off-centring parameter, which was constant in the off-centring schemes described earlier, in an attempt to reduce the numerical damping even further without risking stability or accuracy.

### 1.2.3 Applying the Findings to a GCM

The findings of Chapter 5 are used to devise a variable off-centring scheme for a global climate model (GCM). For this purpose, Chapter 6 provides an overview over the main features of the semi-implicit semi-Lagrangian GCM C-CAM and how it applies the off-centring concept. The modification that has been made to C-CAM to implement a variable off-centring scheme is described and validated by way of proof-of-concept experiments. This is then followed by a number of experiments that determine the qualitative and (to some degree) quantitative changes in the model's solutions owed to the newly introduced off-centring scheme.

Chapter 6 concludes with further modifications to the variable off-centring scheme, meant to improve the accuracy of the numerical results. These altered solutions are again evaluated both qualitatively and quantitatively.

A summary of the work described in this project closes the thesis, accompanied by the insights that were gained, conclusions that can be drawn and suggestions regarding future work.

## Chapter 2

# Modelling the Atmosphere with SISL schemes

The previous chapter introduced the concept of numerical weather prediction and, in particular, numerical weather prediction with semi-Lagrangian semi-implicit schemes. This chapter builds on that outline and introduces the reader to some aspects of modelling the atmosphere. It introduces two sets of equations which are commonly used in this context. It then broadly describes possible numerical approaches and the SISL scheme in particular. Additional terms that arise due to orographic forcing in the shallow water equations are introduced. It is then shown that, under certain circumstances, the orographic forcing can lead to a spurious resonance in the numerical solution. The common approach to overcoming this problem of a spurious resonance is described with mathematical proof of its effectiveness. This is followed by the introduction of a new, modified scheme and an attempt to prove effectiveness.

## 2.1 The Equations

### 2.1.1 The Primitive Equations

The primitive equations, which were first published as a set of equations to describe the atmosphere in 1901 by Cleveland Abbe and in 1904 by Wilhelm Bjerknes (cf. [Saltzman, 1967](#)), are still the basis of modern numerical weather prediction. They consist of the Navier-Stokes equations (i.e. momentum equations), the thermodynamic energy equation and an equation for mass conservation (continuity equation). The thermodynamic energy equation describes the thermodynamics of the system expressing the local temperature tendency in time as a function of temperature advection and heat sources and sinks.

In a coordinate system rotating around its  $z$ -axis which is aligned with the rotation axis of the Earth, one can define

$$\alpha = \frac{1}{\rho}, \quad (2.1)$$

$$\mathbf{g} = \mathbf{g}_a - \boldsymbol{\Omega} \times (\boldsymbol{\Omega} \times \mathbf{r}), \quad (2.2)$$

where  $\rho$  is the density,  $\mathbf{g}_a$  is the gravitational force,  $\boldsymbol{\Omega}$  the angular velocity of the earth and  $\mathbf{r}$  the position vector

$$\mathbf{r} = \begin{pmatrix} x \\ y \\ z \end{pmatrix}.$$

The primitive equations can then be written as

$$\frac{d\mathbf{V}}{dt} = -\frac{1}{\rho}\nabla p - 2\boldsymbol{\Omega} \times \mathbf{V} + \mathbf{g} + \mathbf{F}, \quad (2.3)$$

$$\frac{1}{\alpha} \frac{d\alpha}{dt} = \nabla \cdot \mathbf{V}, \quad (2.4)$$

$$p\alpha = RT, \quad (2.5)$$

$$Q = c_v \frac{dT}{dt} + p \frac{d\alpha}{dt}, \quad (2.6)$$

where  $\mathbf{V}$  is the fluid velocity in the rotating system,  $\mathbf{F}$  is the frictional force,  $p$  the pressure,  $R$  the gas constant for dry air,  $T$  the temperature,  $Q$  the rate of heat energy addition and  $c_v$  the specific heat at constant volume. The total derivative in Eqn. (2.3) contains curvature terms (containing the angular velocity) as a result of the rotation of the system.

Usually, at least one more equation for moisture will be added to describe the atmosphere. It can be written as

$$\frac{dq_s}{dt} = \frac{q_s T}{p} \left( \frac{LR - c_p R_v T}{c_p R_v T + q_s L^2} \right) \omega \equiv F\omega, \quad (2.7)$$

$$\frac{dq}{dt} = -\mathbf{V} \cdot \nabla q - \omega \frac{\partial q}{\partial p} - \delta F\omega + \frac{S_j}{\rho}, \quad (2.8)$$

where  $q_s$  is the saturation humidity,  $L$  the latent heat,  $c_p$  the specific heat at constant pressure,  $\omega = dp/dt$ ,  $R_v$  the water vapour gas constant,  $q$  the moisture and  $S_j$  the sources and sinks of water vapour.  $F$  is defined by the identity in Eqn. (2.7) and the Kronecker  $\delta$  is (cf. [Haltiner and Williams, 1980](#))

$$\delta = 1 \quad \text{for } \omega < 0 \text{ and } q \geq q_s, \quad (2.9)$$

$$\delta = 0 \quad \text{for } \omega \geq 0 \text{ or } q < q_s. \quad (2.10)$$

Modern numerical models may include more determining factors and variables, which will then lead to extended equation sets. Furthermore, with a finite discretisation rendering it impossible to fully resolve all physical processes, parametrisations are employed to represent processes that occur at length scales smaller than those resolved at a particular grid resolution.

### 2.1.2 The Shallow Water Equations

The primitive equations can be simplified further, if a few more, generally reasonable, assumptions are added (cf. [Haltiner and Williams, 1980](#)). Firstly, many processes can be described well as dry processes. This reduces the set of equations to equations (2.3) to (2.6).

As the atmosphere's characteristic depth  $D$  is much smaller than the length scale of horizontal motion  $L$  in the fluid, i.e.

$$\frac{D}{L} \ll 1, \quad (2.11)$$

it can be described as a thin layer of fluid with a rigid surface  $h_b$  at the bottom (the Earth's surface) and a free surface  $h$  at the top.

The assumption of incompressibility simplifies the continuity equation

$$\frac{\partial u}{\partial x} + \frac{\partial v}{\partial y} + \frac{\partial w}{\partial z} = 0 \quad (2.12)$$

which replaces Eqn. (2.4), the equation of mass conservation.

If, furthermore, the pressure is in hydrostatic equilibrium, pressure can be related to density and height as

$$\frac{\partial p}{\partial z} = -g\rho. \quad (2.13)$$

Using a boundary condition of

$$p(x, y, h) = p_0 \quad (2.14)$$

leads to a pressure function of the form

$$p = \rho g(h - z) + p_0. \quad (2.15)$$

Hence, Eqn. (2.13) yields horizontal pressure gradients that are independent of  $z$ . These can then be written as

$$\frac{\partial p}{\partial x} = \rho g \frac{\partial h}{\partial x}, \quad (2.16)$$

$$\frac{\partial p}{\partial y} = \rho g \frac{\partial h}{\partial y}. \quad (2.17)$$

This means that the horizontal accelerations are independent of  $z$  and one can make the reasonable assumption – i.e. assuming that the Taylor-Proudman theorem applies (cf. Pedlosky, 1992), that the velocities will also be independent of  $z$  if that is true initially.

The new momentum equations are

$$\frac{\partial u}{\partial t} + u \frac{\partial u}{\partial x} + v \frac{\partial u}{\partial y} + g \frac{\partial h}{\partial x} - fv = 0, \quad (2.18)$$

$$\frac{\partial v}{\partial t} + u \frac{\partial v}{\partial x} + v \frac{\partial v}{\partial y} + g \frac{\partial h}{\partial y} + fu = 0, \quad (2.19)$$

replacing Eqn. (2.3). Friction and curvature terms and the vertical components of the Coriolis force are neglected and the Coriolis parameter  $f$  is defined as  $f = 2\Omega \sin \vartheta$ , where  $\vartheta$  is the latitude and  $\Omega$  the Earth's angular velocity.

Knowing that  $u$  and  $v$  are independent of  $z$ , the incompressibility condition (2.12) can be integrated over height. Integrating over height and defining

$$H = h - h_b, \quad (2.20)$$

then making use of the definition of  $w$  and  $w(h_b) = 0$  yields

$$\frac{\partial H}{\partial t} + u \frac{\partial H}{\partial x} + v \frac{\partial H}{\partial y} + H \left( \frac{\partial u}{\partial x} + \frac{\partial v}{\partial y} \right) = 0. \quad (2.21)$$

Assuming that the perturbations in velocities and heights will be small, the physical variables can be expressed as sums of average values in space and time and perturbations.

$$u = U + u'(\mathbf{r}, t), \quad (2.22)$$

$$v = V + v'(\mathbf{r}, t), \quad (2.23)$$

$$\varphi = \bar{\varphi} + \varphi'(\mathbf{r}, t), \quad (2.24)$$

with the definition of the gravitational height  $\varphi = gH$ , the average velocities  $U$  and  $V$ , the average gravitational height  $\bar{\varphi}$ , the perturbation terms  $u'$ ,  $v'$  and  $\varphi'$  and the position vector  $\mathbf{r} = \begin{pmatrix} x \\ y \\ z \end{pmatrix}$ .

Assuming a flat bottom surface (i.e. no orographic forcing), the equations (2.18) to (2.21) can be simplified by linearising and neglecting products of perturbation terms. They then read

$$\frac{\partial u}{\partial t} + U \frac{\partial u}{\partial x} + V \frac{\partial u}{\partial y} + \frac{\partial \varphi}{\partial x} - fv = 0, \quad (2.25)$$

$$\frac{\partial v}{\partial t} + U \frac{\partial v}{\partial x} + V \frac{\partial v}{\partial y} + \frac{\partial \varphi}{\partial y} + fu = 0, \quad (2.26)$$

$$\frac{\partial \varphi}{\partial t} + U \frac{\partial \varphi}{\partial x} + V \frac{\partial \varphi}{\partial y} + \bar{\varphi} \left( \frac{\partial U}{\partial x} + \frac{\partial V}{\partial y} \right) = 0. \quad (2.27)$$

Again, curvature and friction terms have been neglected. For further details refer to [Pedlosky \(1992\)](#).

Eqns. (2.25) to (2.27) are called the *shallow water equations*. These equations share many mathematical features with the primitive equations, and are therefore a very useful simplification for modelling purposes and for testing numerical methods.

## 2.2 Numerical Approaches

The numerical solution strategies for differential equations are commonly categorised as finite difference and Galerkin methods. In the finite difference method, the atmosphere is discretised into a set of grid points in space

and time. The derivatives in the differential equations are approximated by differences calculated over intervals of time and space, rendering the differential equation into a difference equation. The finite difference equations are equivalent to Taylor series approximations of the partial differential equations.

A Galerkin method, on the other hand, approximates a function as a sum of basis functions. The coefficients of these basis functions are typically time dependent. This results in partial differential equations being transformed into a set of ordinary differential equations for the coefficients. The most prominent Galerkin methods in atmospheric science are spectral and finite element methods.

Yet another way of categorising numerical solution methods, one that might be more intuitive, is to divide methods into grid-based and particle-based methods. For grid-based methods, the atmosphere (or any other modelled fluid) can be imagined as discretised into a regular grid. Hence, the equations are solved at fixed points in space. This could also be imagined as an observer watching the fluid motion from a fixed position.

In particle-based methods, the discrete physical elements are thought of as fluid parcels. Each parcel is tracked in time and the equations describe the properties of the fluid parcel as it is moving through time and space. To employ the image of the observer again, the observer would now be “travelling with” the particle and observe the changes in the state of the fluid as a change of his otherwise static environment. So, while the grid-based method can be likened to an spectator watching a race and the contestants passing the spectator, the particle-based method is more like the contestant’s view of the same race.

Historically, finite difference or Eulerian methods were first used to model the atmosphere. While the regular grid meant equally distributed discrete solutions in space, its use also entailed the Courant-Friedrich-Lewy (CFL) criterion as a limiting factor to the maximum time step allowed to ensure numerical stability. According to the CFL criterion, for the numerical solution to remain bounded, the time step can never be longer than the quotient of grid spacing over local velocity. In other words, a fluid parcel can never cross more than one grid cell per time step. This criterion is usually expressed in terms of the so called Courant number  $C = |U|\Delta t/\Delta x$  which must not be greater than unity for Eulerian schemes. Hence, while long time steps are desirable for efficient solutions, stability concerns will only allow for longer time steps with decreased resolution, which comes at the cost of reduced accuracy.

Particle-based or Lagrangian methods, on the other hand, are not subjected to the CFL criterion in the same manner. The length of the time step only determines the accuracy but does not affect stability. Therefore, much larger time steps can be achieved without risking stability. Unfortunately, this comes at the cost of an uneven distribution of known discrete solutions in space. In principle, regular grid solutions could be interpolated from the known solutions. However, if the discrete fluid parcels that describe the flow converge or diverge, thus depleting most of the space of known solutions, such interpolated solutions would become very inaccurate. With atmospheric science being a field where local solutions are of utmost importance, this is a major flaw which cannot easily be mitigated.

Obviously, efficient solutions are rather crucial when it comes to climate and weather forecast models. It is of no practical value to have the forecast for tomorrow by the day after tomorrow. Also, as the climate reacts to forcing

only very slowly, it needs to be modelled for a significant amount of time in order to be able to make statistically justifiable assertions about the presence of a climate change signal. These aspects imply a significant computational constraint on the use of traditional Eulerian methods in weather and climate prediction.

Switching to a fully Lagrangian approach is also unpractical. Numerical weather prediction can only be of practical use, if forecasts can be produced for defined regions. This is impossible if the locations of the fluid parcels do not allow a description of the fluid attributes with sufficient detail over an area of interest.

As a result of the problems described above, [Robert \(1981\)](#) suggested a semi-implicit semi-Lagrangian (SISL) algorithm for use in weather forecast models. Semi-implicit, semi-Lagrangian schemes implicitly solve the terms that would lead to gravitational oscillations in an explicit scheme. They therefore already allow for a longer time step than in an explicit scheme at no cost in accuracy for applications where gravity waves do not carry an important part of the energy of the flow (cf. [Robert, 1969](#); [Robert et al., 1972](#)). However, in the quest for higher efficiency, one would still like to increase the time step even further. This is what the semi-Lagrangian scheme achieves. The basic idea of a semi-Lagrangian scheme is to keep the discrete solutions on a grid while still solving the advective terms in the governing equations in their Lagrangian form. In this way the strengths of Eulerian grids (i.e. equal distribution of point solutions) can be combined with the strengths of Lagrangian particle methods (i.e. large time steps). As it forms the foundation of this thesis, the following section describes the semi-implicit semi-Lagrangian method in some more detail. For a full description of the method, the reader is referred to [Staniforth and Côté \(1991\)](#).

## 2.3 The Semi-Lagrangian Semi-Implicit Method and Its Limitations

### 2.3.1 The Semi-Lagrangian, Semi-Implicit Approach

The semi-Lagrangian approach to solving the governing equations, as its name already suggests, combines elements of the Eulerian and Lagrangian approaches to differential equations. In terms of advection, while one keeps solving the equations on a stationary grid, thus Eulerian because the fluid moves with respect to the observer's frame of reference, it is assumed for every single time step that this grid is the result of an ensemble of fluid parcels moving over the past time step  $\Delta t$  to arrive at just the grid points defined beforehand. To that end, a theoretical back trajectory for every grid point is calculated and the starting point of that trajectory is taken as the fluid parcel's departure point at the preceding time step.

The idea of semi-Lagrangian algorithms evolved over a period of more than 20 years. The pioneering work can be found in [Fjørtoft \(1952, 1955\)](#), [Wiin-Nielsen \(1959\)](#), [Krishnamurti \(1962\)](#), [Sawyer \(1963\)](#), [Leith \(1965\)](#), [Mathur \(1970\)](#) and [Purnell \(1976\)](#). It needs to be mentioned that the early algorithms were only designed to work at Courant numbers of  $C < 1$  and thus did not address the Eulerian schemes' most significant limitation.

To explain how a semi-Lagrangian scheme works, the following presents the algorithm step by step using the example of a 1D advection equation as found in [Staniforth and Côté \(1991\)](#). The advection equation solved is

$$\frac{dF}{dt} = \frac{\partial F}{\partial t} + U(x, t) \frac{\partial F}{\partial x} = 0, \quad (2.28)$$

where

$$U(x, t) = \frac{dx}{dt}. \quad (2.29)$$

The variable  $F$  is therefore constant along a trajectory that the fluid parcel travels on.

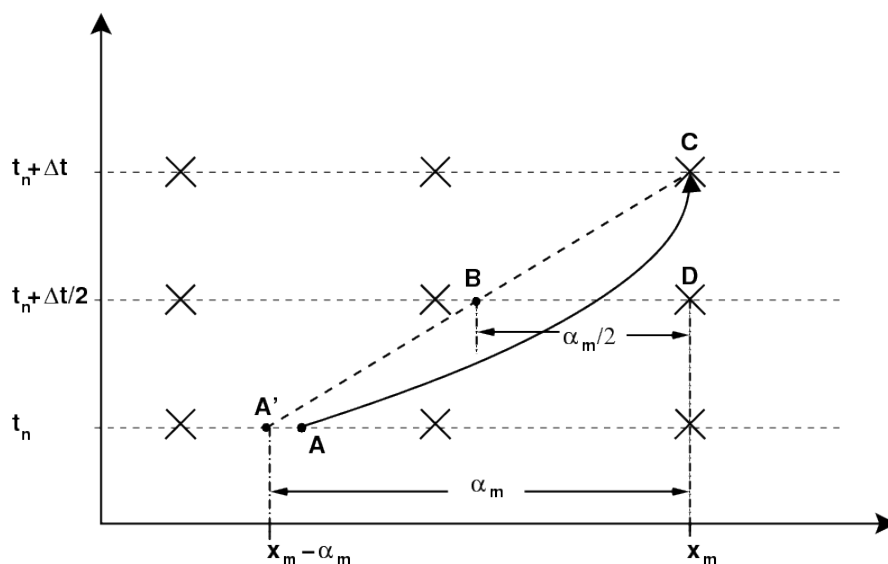


Figure 2.1: Sketch of semi-Lagrangian advection in 1D.

Fig. 2.1 shows a graphical sketch of a two time level scheme for semi-Lagrangian advection. This sketch was copied from Staniforth and Côté (1991). The solid curve  $AC$  in Fig. 2.1 represents the real trajectory of the fluid parcel between time  $t_n$  and time  $t_n + \Delta t$ . Once the departure point of the fluid parcel arriving at point  $C$  at time  $t_n + \Delta t$  has been estimated, the trajectory can be approximated by the dashed line  $A'C$ . The semi-Lagrangian algorithm integrates Eqn. (2.28) along this approximate

trajectory as

$$\frac{F(x_m, t_n + \Delta t) - F(x_m - \delta_{xm}, t_n)}{\Delta t} = 0, \quad (2.30)$$

where  $\delta_{xm}$  now represents the distance approximately travelled in time  $\Delta t$ . The value of  $\delta_{xm}$  needs to be determined. This follows from the definition of the Lagrangian time derivative as

$$\frac{dA}{dt} = \frac{A^{\text{arr}} - A^{\text{dep}}}{\Delta t}. \quad (2.31)$$

The algorithm to determine the departure points and the values of physical variables at these points can be described in three steps.

1. **Determine  $\delta_{xm}$ .** The displacement  $\delta_{xm}$  in a two time level scheme is usually determined iteratively. One possible way<sup>1</sup> of determining it, is as

$$\delta_{x(m+1)} = \Delta t V^*(x - \delta_{xm}/2, t + \Delta t/2) \quad (2.32)$$

$$V^*(x, t + \Delta/2) = \frac{3}{2}V(x, t) - \frac{1}{2}V(x, t - \Delta t) + O(\Delta t^2) \quad (2.33)$$

As the point at  $x - \delta_{xm}/2$  is likely not a grid point, extrapolation has to be used to find the velocity  $V$  at that point at the times in the past used to find  $\delta_{xm}$ . This is usually done using linear extrapolation. The iterative process is typically started with  $\delta_0$  set to the value obtained at the same grid point in the last time step. In the first time step the iteration is started with  $\delta_0 = 0$ .

---

<sup>1</sup>This approach is described in [Staniforth and Côté \(1991\)](#). An alternative algorithm is described in [McGregor \(1996\)](#) and in Section 3.3.4.

2. **Interpolate value of  $F$  at point  $A'$  and time  $t_n$ .** Again, the required value of  $F(x_m - \delta_{x_m}, t_n)$  is unlikely to be a grid point value. At this point, typically cubic interpolation is used.
3. **Update point  $x_m$  for the current time step  $t + \Delta t$  as the value found in the preceding step.** In this example there is nothing happening but mere advection. Therefore, no further terms need to be evaluated. In a more complex equation, it might be required to solve more spatial derivatives or source terms for the new time step (cf. Staniforth and Côté, 1991).

In the case of a coupled set of differential equations, one variable (e.g. the height in the shallow water equations) is typically solved implicitly to ensure stability (cf. Section 2.2). The system is combined into an elliptic equation which can be solved with standard solvers. The remaining variables (e.g. velocities in the shallow water equations) are then resubstituted explicitly. Hence, such an algorithm is referred to as *semi-implicit*.

Historically, there are two and three time level schemes. While a three time level algorithm solves the equations for time  $t + \Delta t$  based on two previous time steps  $t$  and  $t - \Delta t$ , a two time level algorithm uses the time levels  $t$  and  $t + \frac{\Delta t}{2}$ . However, three time level algorithms are less commonly used today. They mainly owed their existence to stability concerns which have meanwhile been satisfactorily resolved.

### 2.3.2 The SISL Approach Applied to the Shallow Water Equations

To illustrate the semi-Lagrangian approach in more detail and also show the semi-implicit component of the process, it is helpful to use the linearised

shallow water equations as an example. The shallow water equations are the simplest set of equations that show a number of key phenomena of the atmosphere's (or the ocean's) dynamics.

The one-dimensional shallow water equations without orographic forcing in their Eulerian form are as shown earlier in Eqns. (2.25-2.27).

In terms of the total derivative  $\frac{\partial a}{\partial t} + U \frac{\partial a}{\partial x} + V \frac{\partial a}{\partial y}$ , they can be written as

$$\frac{du}{dt} + \frac{\partial \varphi}{\partial x} - fv = 0, \quad (2.34)$$

$$\frac{dv}{dt} + \frac{\partial \varphi}{\partial y} + fu = 0, \quad (2.35)$$

$$\frac{d\varphi}{dt} + \bar{\varphi} \left( \frac{\partial u}{\partial x} + \frac{\partial v}{\partial y} \right) = 0. \quad (2.36)$$

From these equations, using Eqn. (2.31), the discretised form is now derived as

$$u^+ = \Delta t \left( -\frac{\varphi_x^+ + \varphi_x^0}{2} + \frac{1}{2} ((fv)^+ + (fv)^0) \right) + u^0, \quad (2.37)$$

$$v^+ = \Delta t \left( -\frac{\varphi_y^+ + \varphi_y^0}{2} - \frac{1}{2} ((fu)^+ + (fu)^0) \right) + v^0, \quad (2.38)$$

$$\varphi^+ = -\Delta t \left( \frac{\bar{\varphi}}{2} [(u_x + v_y)^+ + (u_x + v_y)^0] \right) + \varphi^0, \quad (2.39)$$

where + marks an arrival point at time  $t + \Delta t$  and 0 marks a departure point and implies the time  $t$ . The notation  $A_x$  refers to the partial derivative  $\partial A / \partial x$ .

As is obvious from Eqns. (2.37) - (2.39),  $\varphi^+$  can only be calculated if the new values of  $u$  and  $v$  (and therefore their derivatives) are already known. All that is known about these new values, however, are equations (2.37) and (2.38), which can be combined to yield

$$\begin{aligned} u^+ &= -\frac{\Delta t}{2} (a\varphi_x^+ + b\varphi_y^+) \\ &\quad -\frac{\Delta t}{2} (a(\varphi_x^0 - 2fv^0) + b(\varphi_y^0 + fu^0)) + au^0, \end{aligned} \quad (2.40)$$

$$\begin{aligned} v^+ &= -\frac{\Delta t}{2} (a\varphi_y^+ - b\varphi_x^+) \\ &\quad -\frac{\Delta t}{2} (a(\varphi_y^0 + 2fu^0) - b(\varphi_x^0 - fv^0)) + av^0, \end{aligned} \quad (2.41)$$

where  $a = [1 + (f\Delta t/2)^2]^{-1}$  and  $b = (f\Delta t/2)a$  and  $f_x = f_y = f_t = 0$  and the notation  $W_x^0$  refers to the derivative of  $W$  in  $x$  at the departure point (and analogously for  $y$  and the arrival point) and  $W$  is any of the three physical variables  $\varphi$ ,  $u$  and  $v$ . In these equations, and from here onwards, it is assumed that we are dealing only with cases where  $f$  is constant.

Substituting these two equations into Eqn. (2.39) leads to an an elliptic or Helmholtz equation for  $\varphi$  which reads

$$\begin{aligned} a(\varphi_x^+)_x + b(\varphi_x^+)_y - b(\varphi_y^+)_x \\ + a(\varphi_y^+)_y - \frac{4\varphi^+}{(\Delta t)^2\bar{\varphi}} &= -a((\varphi_x^0)_x + (\varphi_y^0)_y + 2f(u_y^0 - v_x^0)) \\ &\quad -b((\varphi_y^0)_x - (\varphi_x^0)_y + f(u_x^0 + v_y^0)) \\ &\quad + \frac{2}{\Delta t} ((u_x^0 + v_y^0)(1 + a)) - \frac{4}{(\Delta t)^2\bar{\varphi}}\varphi^0. \end{aligned} \quad (2.42)$$

For continuous  $\varphi$  the cross-derivative terms on both sides of the equation cancel.

The Helmholtz equation can be solved with the help of a number of different standard solvers. The simplest of these solves the equation by successive over-relaxation, an accelerated Gauß<sup>2</sup>-Seidel method (cf. Section 3.3.5).

### 2.3.3 Orographic Forcing in the Shallow Water Equations

One of Earth's main features is the fact that its surface is not entirely flat but features a number of significant mountain ranges. Such obstacles in the computational domain pose an additional challenge to numerical models because the resulting forced deflection of the flow can be difficult to describe. The shallow water equations provide a good test bed for the study of the effects of orography because, despite their simplicity, they still exhibit many important features of the atmosphere (cf. Pedlosky, 1992).

Starting with primitive equations without orographic forcing, orography can be added to the equations as a rigid bottom of the fluid layer. This then results in a height equation like in Section 2.1.2,

$$\frac{\partial \varphi}{\partial t} + U \frac{\partial \varphi}{\partial x} + V \frac{\partial \varphi}{\partial y} + U \frac{\partial \varphi_s}{\partial x} + V \frac{\partial \varphi_s}{\partial y} + \bar{\varphi} \left( \frac{\partial u}{\partial x} + \frac{\partial v}{\partial y} \right) = 0, \quad (2.43)$$

where  $\varphi_s$  is the product of the orographic height and the gravitational acceleration and  $\varphi$  the geopotential fluid depth. The sum  $\varphi_s + \varphi$  is then the full

<sup>2</sup>named after Carl Friedrich Gauß whose name is often spelled the latinised way *Gauss*

geopotential layer height which, in the earlier derivations of the shallow water equations without orographic forcing, was equivalent to the geopotential fluid depth.

Writing the time derivative as a substantial derivative, this takes the more compact form

$$\frac{d(\varphi + \varphi_s)}{dt} + \bar{\varphi} \left( \frac{\partial u}{\partial x} + \frac{\partial v}{\partial y} \right) = 0. \quad (2.44)$$

Discretising these equations and combining them as in Section 2.1.2 leads to the set of equations

$$\begin{aligned} u^+ &= -\frac{\Delta t}{2} (a(\varphi_x^+) + b(\varphi_y^+)) \\ &\quad -\frac{\Delta t}{2} (a(\varphi_x^0 - 2fv^0) + b(\varphi_y^0 + fu^0)) \\ &\quad + au^0, \end{aligned} \quad (2.45)$$

$$\begin{aligned} v^+ &= -\frac{\Delta t}{2} (a(\varphi_y^+) - b(\varphi_x^+)) \\ &\quad -\frac{\Delta t}{2} (a(\varphi_y^0 + 2fu^0) - b(\varphi_x^0 - fv^0)) \\ &\quad + av^0, \end{aligned} \quad (2.46)$$

$$\begin{aligned} a(\varphi_x^+)_x + b(\varphi_x^+)_y - b(\varphi_y^+)_x \\ + a(\varphi_y^+)_y - \frac{4\varphi^+}{(\Delta t)^2 \bar{\varphi}} &= -a((\varphi_x^0)_x + (\varphi_y^0)_y + 2f(u_y^0 - v_x^0)) \\ &\quad -b((\varphi_y^0)_x - (\varphi_x^0)_y + f(u_x^0 + v_y^0)) \\ &\quad + \frac{2}{\Delta t} ((u_x^0 + v_y^0)(1 + a)) \\ &\quad - \frac{4}{(\Delta t)^2 \bar{\varphi}} (\varphi_0 + \varphi_s^+ - \varphi_s^0). \end{aligned} \quad (2.47)$$

Alternatively, the orography can be introduced in the momentum equations as found in [Rivest et al. \(1994\)](#). The equations then read

$$\frac{\partial u}{\partial t} + U \frac{\partial u}{\partial x} + V \frac{\partial u}{\partial y} + \frac{\partial \varphi}{\partial x} - fv = -\frac{\partial \varphi_s}{\partial x}, \quad (2.48)$$

$$\frac{\partial v}{\partial t} + U \frac{\partial v}{\partial x} + V \frac{\partial v}{\partial y} + \frac{\partial \varphi}{\partial y} + fu = -\frac{\partial \varphi_s}{\partial y}, \quad (2.49)$$

$$\frac{\partial \varphi}{\partial t} + U \frac{\partial \varphi}{\partial x} + V \frac{\partial \varphi}{\partial y} + \bar{\varphi} \left( \frac{\partial u}{\partial x} + \frac{\partial v}{\partial y} \right) = 0. \quad (2.50)$$

Again, discretising and combining the equations as above, the discretised set of equations becomes

$$\begin{aligned} u^+ &= -\frac{\Delta t}{2} (a(\varphi_x^+ + \varphi_{s,x}^+) + b(\varphi_y^+ + \varphi_{s,y}^+)) \\ &\quad -\frac{\Delta t}{2} a (\varphi_x^0 - 2fv^0 + \varphi_{s,x}^0) \\ &\quad -\frac{\Delta t}{2} b (\varphi_y^0 + fu^0 + \varphi_{s,y}^0) \\ &\quad + au^0, \end{aligned} \quad (2.51)$$

$$\begin{aligned} v^+ &= -\frac{\Delta t}{2} (a(\varphi_y^+ + \varphi_{s,y}^+) - b(\varphi_x^+ + \varphi_{s,x}^+)) \\ &\quad -\frac{\Delta t}{2} a (\varphi_y^0 + 2fu^0 + \varphi_{s,y}^0) \\ &\quad +\frac{\Delta t}{2} b (\varphi_x^0 - fv^0 + \varphi_{s,x}^0) \\ &\quad + av^0, \end{aligned} \quad (2.52)$$

$$\begin{aligned}
& a(\varphi_x^+)_x + b(\varphi_x^+)_y - b(\varphi_y^+)_x \\
& + a(\varphi_y^+)_y - \frac{4\varphi^+}{(\Delta t)^2 \bar{\varphi}} = -a((\varphi_x^0)_x + (\varphi_y^0)_y + 2f(u_y^0 - v_x^0)) \\
& \quad - a((\varphi_{s,x})_x^0 + (\varphi_{s,y})_y^0) \\
& \quad - b((\varphi_y^0)_x - (\varphi_x^0)_y + f(u_x^0 + v_y^0)) \\
& \quad - b((\varphi_{s,x})_y^0 - (\varphi_{s,y})_x^0) \\
& \quad - a((\varphi_{s,x})_x^+ + (\varphi_{s,y})_y^+) \\
& \quad - b((\varphi_{s,x})_y^+ - (\varphi_{s,y})_x^+) \\
& \quad + \frac{2}{\Delta t} ((u_x^0 + v_y^0)(1 + a)) \\
& \quad - \frac{4}{(\Delta t)^2 \bar{\varphi}} \varphi_0. \tag{2.53}
\end{aligned}$$

While the results obtained from either set of equations should be very similar, it can be considered more consistent to introduce orographic forcing into the primitive equations before reducing them to two dimensions.

The equations as derived here are of great significance to the following analytical and numerical studies. They exhibit resonant features in both the exact and the numerical solutions. These resonances are the subject of the following sections.

## 2.4 The Mountain Wave Resonance

To model a one-dimensional domain with orography, orographic forcing as in Eqns. (2.48) to (2.50) is used and the equations are reduced to one dimension. One then obtains the following set of equations (cf. Rivest et al., 1994).

$$\frac{\partial u}{\partial t} + U \frac{\partial u}{\partial x} + \frac{\partial \varphi}{\partial x} - f v = -\frac{\partial \varphi_s}{\partial x}, \quad (2.54)$$

$$\frac{\partial v}{\partial t} + U \frac{\partial v}{\partial x} + f u = 0, \quad (2.55)$$

$$\frac{\partial \varphi}{\partial t} + U \frac{\partial \varphi}{\partial x} + \bar{\varphi} \frac{\partial u}{\partial x} = 0. \quad (2.56)$$

This set of equations possesses a resonant solution leading to a wave which is stationary in relation to the orography. To show this, this problem is solved by decomposing all variables into Fourier harmonics  $a \cdot e^{ik(x-ct)}$ , where  $a$  is any of  $\{v_0, u_0, \varphi_0\}$  (cf. Rivest et al., 1994). As only the resonant solution is of interest here, this solution has to be stationary with respect to the orographic forcing, i.e. it is a solution for the condition  $c = 0$ . The Fourier harmonics are

$$\begin{pmatrix} v \\ u \\ \varphi \end{pmatrix} = \begin{pmatrix} v_0 \\ u_0 \\ \varphi_0 \end{pmatrix} e^{ikx}. \quad (2.57)$$

Solving the system of equations (2.54) to (2.56) for these Fourier harmonics yields

$$ikUu_0 - fv_0 + ik\varphi_0 = -ik\varphi_s, \quad (2.58)$$

$$ikUv_0 + fu_0 = 0, \quad (2.59)$$

$$ikU\varphi_0 + ik\bar{\varphi}u_0 = 0, \quad (2.60)$$

or in matrix form equivalent

$$\mathbf{A} \begin{pmatrix} v_0 \\ u_0 \\ \varphi_0 \end{pmatrix} = \begin{pmatrix} 0 \\ -ik\varphi_s \\ 0 \end{pmatrix}, \quad (2.61)$$

where

$$\mathbf{A} = \begin{pmatrix} ikU & f & 0 \\ -f & ikU & ik \\ 0 & ik\bar{\varphi} & ikU \end{pmatrix}. \quad (2.62)$$

For the stationary solution,  $|A|$  vanishes, so that the resonance condition becomes

$$\begin{aligned} |\mathbf{A}| &= -ik^3U^3 + ik^3\bar{\varphi}U + ikf^2U \\ &= -k^2U^2 + k^2\bar{\varphi} + f^2 \\ \Rightarrow U &= \pm \sqrt{\bar{\varphi} + \left(\frac{f^2}{k^2}\right)}. \end{aligned} \quad (2.63)$$

Under this condition, the solution is singular and grows linearly with time (cf. [Rivest et al., 1994](#)) amplifying the amplitude of the stationary wave. This resonant wave is commonly referred to as mountain wave, mountain lee wave or just lee wave.

The resonance condition (2.63) can be met in nature but would require very high wind speeds in a shallow water model as described above. This resonance can play a role in the so-called mountain lee waves or just mountain

waves which can form over mountain ranges. These waves are very popular with glider pilots who can soar great distances on such waves.

## 2.5 Mountain Waves in Nature

This research project does not refer to mountain waves but only to a spurious resonance that is mathematically related to the physical mountain wave resonance. Nevertheless, mountain waves are a fascinating phenomenon and do occur in nature. The physical resonance condition can be met over high mountain ranges like the Himalayas or the Andes or even the Alps (cf. [Kuettner, 1938, 1939](#), and later publications of the same author).

### 2.5.1 The Discovery of Mountain Waves

The discovery of mountain waves is owed to the sport of gliding. In 1933, one of the most famous glider pilots of his time, Wolf Hirth, watched Hans Deutschmann, one of the instructors at his soaring school, ascend to a height that seemed impossible to reach in the day's weather conditions. Only a couple of years before, thermals had been understood and soaring pilots knew how to ascend in these. However, there seemed to be no thermal present and Deutschmann was also covering too large a distance to be in a thermal for the whole time he kept ascending.

Hirth decided to get into the cockpit himself and found that he could easily ascend to great heights in a way he had never experienced before. While they were soaring over a ridge which often allowed them to ascend in the winds rushing up the ridge, Hirth knew that this was not what was happening on

this occasion. He already suspected that the “long wave”, as he called it, had something to do with the nearby Riesengebirge mountain range.

It would take another four years until the secret of mountain waves was finally unlocked. In 1937, Joachim Kuettner, a doctoral candidate in meteorology visited Hirth’s gliding school. He had Hirth and his fellow gliders gather scientific data on their flights which he would then analyse to understand the reasons for the mysterious phenomenon Hirth and Deutschmann had discovered.

Kuettner had several possible theories about the nature of the phenomenon. All of them seemed promising but none could readily explain all the observed details. Kuettner already wondered if the phenomenon could be due to a stationary wave originating from the Riesengebirge mountains. He knew that stationary waves could be found in water moving over obstacles. Nevertheless, he did not yet rule out other explanations, either. For example, the effect could also have been caused by the local ridge or a vortex could create the lift.

Another phenomenon that was already known to coincide with the mysterious lift, was a stationary lenticular cloud (cf. Fig. 2.2 for a photo). In soaring jargon it had become known as the Moazagotl cloud. It was in an attempt to find out how high this cloud was that Kuettner established a new record soaring at 22,300ft. While the height record can be considered accidental, this flight is evidence for Kuettner’s determination and his enthusiasm for his research. He actually reached this incredible height in an open cockpit in utterly inadequate clothing and without an oxygen tank. Only when he felt the effects of the lack of oxygen in his bloodstream, did he finally abort his daredevil flight.

As a result of his soaring flights and the data gathered in his and other glider pilots' flights, Kuettner finally established the mountain wave theory as it is known today. He described the lift as the result of a stationary long wave caused by a mountain range.

Kuettner's mountain wave theory caused a lot of excitement in the scientific community, and after World War II he left Germany and continued his research in the United States. There he had the chance to lead the Sierra Wave Project, the first project to study the mountain wave phenomenon systematically.

In his meteorological career of seven decades, Kuettner published more than 40 papers concerned with mountain waves and soaring.

For a very detailed history of mountain wave research, the reader may refer to [Whelan \(2000\)](#) who offers an anecdotal account of the evolution of mountain wave research since the very discovery of the phenomenon.

## **2.6 The Numerical Resonance**

In addition to the well-understood mountain wave resonance, both the shallow water and the primitive equations have a second resonant solution when solved numerically in their discretised form. [Coiffier et al. \(1987\)](#) showed that, due to their large time steps, semi-Lagrangian methods can be affected by this additional resonance and suffer from a spurious stationary solution. As this resonant solution only exists for the discretised equations, it is referred to as the numerical or spurious resonance. It has a significant impact on the validity and possibly even the stability of numerical models and needs



Figure 2.2: A lenticular or Moazagotl cloud over the glacier Skaftafell (Iceland). Used under Creative Commons License. Source: [http://en.wikipedia.org/wiki/Lenticular\\_cloud](http://en.wikipedia.org/wiki/Lenticular_cloud) .

to be addressed. Otherwise, stationary short scale waves will be numerically amplified around a strongly varying topography, therefore locally altering the model's flow patterns (cf. [Ritchie and Tanguay, 1996](#)).

It can easily be shown that the discretisation of the shallow water equations, generically representing any set of hydrodynamical equations commonly used in atmospheric science, affects the resonance condition. Following [Rivest et al. \(1994\)](#), if Eqns. (2.54) to (2.56) are discretised as

$$\frac{Du}{Dt} + \overline{\frac{\partial \varphi}{\partial x} - fv}^t = -\overline{\frac{\partial \varphi_s}{\partial x}}^t, \quad (2.64)$$

$$\frac{Dv}{Dt} + \overline{fu}^t = 0, \quad (2.65)$$

$$\frac{D\varphi}{Dt} + \overline{\frac{\partial u}{\partial x}}^t = 0, \quad (2.66)$$

where

$$\frac{Dg}{Dt} = \frac{g(x, t) - g(x - U\Delta t, t - \Delta t)}{\Delta t}, \quad (2.67)$$

$$\bar{g}^t = \frac{g(x, t) + g(x - U\Delta t, t - \Delta t)}{2}, \quad (2.68)$$

averaging the forcing along the trajectory.

and then decomposed into Fourier harmonics and addition theorems used, one finds

$$\frac{Da}{Dt} = a_0 \frac{e^{ikx} - e^{i(kx-2\vartheta)}}{\Delta t} \quad (2.69)$$

$$= 2a_0 \frac{i \sin \vartheta e^{i(kx-\vartheta)}}{\Delta x} \quad (2.70)$$

$$\bar{a}^t = a_0 \frac{e^{ikx} + e^{i(kx-2\vartheta)}}{2} \quad (2.71)$$

with  $\vartheta = kU\Delta t/2$ ,  $a = \{u, v, \varphi\}$  and  $a_0 = \{u_0, v_0, \varphi_0\}$ .

Calculating  $|\mathbf{A}|$  again as in Section 2.4 with the above discretisation (cf. Rivest et al., 1994), the resonance condition becomes

$$\tan\left(\frac{kU\Delta t}{2}\right) = \pm \left(\frac{k\Delta t}{2}\right) \sqrt{\bar{\varphi} + \frac{f^2}{k^2}}. \quad (2.72)$$

In the limit  $\Delta t \rightarrow 0$  this resonance condition equals the resonance condition in Eqn. (2.63). However, for a finite  $\Delta t$ , spurious resonances are introduced. Rewriting the resonance condition (2.72) as a function of the Courant number  $C = U\Delta t/\Delta x$  and the non-dimensional wave number  $K = k\Delta x$  (cf. Rivest et al., 1994) leads to

$$\tan\left(\frac{KC}{2}\right) = \pm \left(\frac{C}{2U}\right) \sqrt{K^2\bar{\varphi} + f^2(\Delta x)^2}. \quad (2.73)$$

The non-dimensional wave number  $K$  is determined by the resolvable scales of the model with  $K = 0$  corresponding to the largest resolvable scale and  $K = \pi$  corresponding to the smallest resolvable scale. It is evident from Eqn. (2.73) that a spuriously resonant solution exists for Courant numbers  $C \gtrsim 1$  (cf. Rivest et al., 1994) (cf. Section 4.2.2 for more detail).

## 2.7 Off-Centring

### 2.7.1 The General Approach to Off-Centring

To overcome the problem as described in the previous section, Kaas (1987) suggested to spatially average the orographic forcing along the trajectory. However, Tanguay et al. (1992) showed that although this approach alleviates the problem it does not solve it. Rivest et al. (1994) then developed what has since been known as the off-centring scheme. In the Lagrangian form of the hydrodynamical equations, as they are solved in two time level semi-Lagrangian models, the forcing terms are usually centred over the trajectory of the fluid parcel, i.e.

$$\frac{\partial\varphi}{\partial x} \equiv \frac{1}{2} \left( \left( \frac{\partial\varphi}{\partial x} \right)^+ + \left( \frac{\partial\varphi}{\partial x} \right)^0 \right). \quad (2.74)$$

In this form the system of equations has a singular solution and therefore a spurious numerical resonance as described above. As can be shown, this spurious resonance can be removed by off-centring the forcing terms to read

$$\frac{\partial \varphi}{\partial x} \equiv \left( \alpha \left( \frac{\partial \varphi}{\partial x} \right)^+ + \beta \left( \frac{\partial \varphi}{\partial x} \right)^0 \right) \quad (2.75)$$

with  $\alpha + \beta = 1$  and generally  $\alpha > \beta$ . The parameter  $\alpha$ , or sometimes also expressed as  $\varepsilon = 2(\alpha - 1/2)$ , is referred to as the *off-centring parameter*.

The equations then read

$$\begin{aligned} u^+ &= \Delta t \left( -\alpha_1(\varphi_x^+ + \varphi_{s,x}^+) - \beta_1(\varphi_x^0 + \varphi_{s,x}^0) + (\alpha_2(fv)^+ + \beta_2(fv)^0) \right) \\ &\quad + u^0, \end{aligned} \quad (2.76)$$

$$\begin{aligned} v^+ &= \Delta t \left( -\alpha_1(\varphi_y^+ + \varphi_{s,y}^+) - \beta_1(\varphi_y^0 + \varphi_{s,y}^0) - (\alpha_2(fu)^+ + \beta_2(fu)^0) \right) \\ &\quad + v^0, \end{aligned} \quad (2.77)$$

$$\varphi^+ = -\Delta t \left( \bar{\varphi} \left[ \alpha_3(u_x + v_y)^+ + \beta_3(u_x + v_y)^0 \right] \right) + \varphi^0. \quad (2.78)$$

It can be shown that this scheme does not suffer from the spurious resonance. Following the same approach as in Section 2.6, Eqn. (2.68) can be changed to read

$$\bar{g}^t = \alpha g(x, t) + \beta g(x - U\Delta t, t - \Delta t), \quad (2.79)$$

and a new matrix (analogous to (2.62)) can be shown to be

$$\mathbf{B} = \begin{pmatrix} i \sin \vartheta e^{-i\vartheta} & \frac{f\Delta t}{2} (\alpha + \beta e^{-2i\vartheta}) & 0 \\ -\frac{f\Delta t}{2} (\alpha + \beta e^{-2i\vartheta}) & i \sin \vartheta e^{-i\vartheta} & \frac{ik\Delta t}{2} (\alpha + \beta e^{-2i\vartheta}) \\ 0 & \frac{ik\bar{\varphi}\Delta t}{2} (\alpha + \beta e^{-2i\vartheta}) & i \sin \vartheta e^{-i\vartheta} \end{pmatrix} \quad (2.80)$$

which then leads to the resonance condition (analogous to the one found in Rivest et al. (1994) for a second order scheme)

$$(1 - e^{-2i\vartheta})^2 + (\Delta t(k^2\bar{\varphi} + f^2))(\alpha + \beta e^{2i\vartheta}) = 0, \quad (2.81)$$

$$E^2(1 \pm i\alpha\Lambda) - E(1 \mp i\beta\Lambda) = 0, \quad (2.82)$$

with  $E = e^{2i\vartheta}$  and  $\Lambda^2 = (\Delta t)^2(k^2\bar{\varphi} + f^2)$  as shown in Rivest et al. (1994). As this equation's only solution is  $|E| = 1$  but this solution is excluded by the definition of the off-centring scheme (cf. Rivest et al., 1994), the singularity is removed from the problem.

Rivest et al. (1994) also showed that while the amplitude of the geopotential close to the former singularity is still overestimated, it is now very similar to the analytic value.

In a later study, Ritchie and Tanguay (1996), instead of off-centring strongly, treated the orography in a spatially averaged Eulerian way. This avoids the loss of accuracy that comes with the increased time truncation error (and resulting numerical damping) introduced by the off-centring scheme but also results in new resonances. It needs to be pointed out that while

the additional resonances are much milder and the gradients around the original resonances are much smaller as a result of this treatment, a weak first order off-centring is usually still required to keep the scheme stable. This, however, still means a large gain in accuracy at a relatively lower cost than the second order off-centring scheme that [Rivest et al. \(1994\)](#) suggested to maintain acceptable accuracy.

Following the suggestions by [Ritchie and Tanguay \(1996\)](#), [Li and Bates \(1996\)](#) and [Lindberg and Alexeev \(2000\)](#) studied this approach further, explaining why it performs well in the models despite the fact that the resonances are not completely removed from the problem. The scheme has been adopted by production models such as the ECMWF<sup>3</sup> model (cf. [Hortal, 1998](#)).

### 2.7.2 The Adverse Effects of Off-Centring

Off-centring should be understood as a pragmatic approach and not an ideal solution for the spurious mountain wave resonance. Its basic function is to smooth out a singularity by adding numerical damping. While this might be an acceptable solution close to the singularity, it introduces unnecessary damping away from the resonance. The preferable solution to the problem would be to remove the resonance altogether. If this is impossible, the numerical damping added to the equations should be minimised in any way possible. The obvious first condition would be to introduce no stronger off-centring than needed. In other words, one wants to off-centre only those equations and terms that contribute to the resonance. Where one does off-centre, the off-centring parameter  $\varepsilon$  should be kept as small as possible.

---

<sup>3</sup>European Centre for Medium-Range Weather Forecasts

The next section investigates if this treatment can be limited to only one equation.

## 2.8 Off-Centring only the Height Equation

In an attempt to reduce the amount of off-centring used, one can try off-centring only the height equation but not the momentum equations. In practice, such a scheme has proven stable in C-CAM, Australia's Commonwealth Scientific and Industrial Research Organisation's (CSIRO) semi-implicit semi-Lagrangian climate prediction and weather forecast model (cf. Chapter 6).

It is interesting to investigate how the off-centring of just one equation affects the stability analysis presented above for the fully off-centred equations. As a first step, the stability analysis as in Section 2.6 was modified with the modified equations reading

$$u^+ = \Delta t \left( -\frac{\varphi_x^+ + \varphi_{s,x}^+ - (\varphi_x^0 + \varphi_{s,x}^0)}{2} + \frac{1}{2} ((fv)^+ + (fv)^0) \right) + u^0, \quad (2.83)$$

$$v^+ = \Delta t \left( -\frac{\varphi_y^+ + \varphi_{s,y}^+ - (\varphi_y^0 + \varphi_{s,y}^0)}{2} - \frac{1}{2} ((fu)^+ + (fu)^0) \right) + v^0, \quad (2.84)$$

$$\varphi^+ = -\Delta t (\bar{\varphi} [\alpha(u_x + v_y)^+ + \beta(u_x + v_y)^0]) + \varphi^0. \quad (2.85)$$

Decomposing into Fourier harmonics again leads to the matrix

$$\mathbf{B}' = \begin{pmatrix} i \sin \vartheta & \frac{f\Delta t}{2} \cos \vartheta & 0 \\ -\frac{f\Delta t}{2} \cos \vartheta & i \sin \vartheta & \frac{ik\Delta t}{2} \cos \vartheta \\ 0 & \frac{ik\bar{\varphi}\Delta t}{2} (\alpha e^{i\vartheta} + \beta e^{-i\vartheta}) & i \sin \vartheta \end{pmatrix}, \quad (2.86)$$

analogous to Eqns. (2.62) and (2.80).

From this follows a resonance condition of the form

$$(i \sin \vartheta)^3 + \frac{f^2(\Delta t)^2}{4} i \cos^2 \vartheta \sin \vartheta + \frac{k^2(\Delta t)^2\bar{\varphi}}{4} i \sin \vartheta \cos \vartheta (\alpha e^{i\vartheta} + \beta e^{-i\vartheta} + \gamma e^{-2i\vartheta}) = 0 \quad (2.87)$$

which can be expressed as

$$\begin{aligned} \tan \vartheta &= \pm \left( \frac{k\Delta t}{2} \right) \\ &\times \left( \frac{f^2}{k^2} + \bar{\varphi} \left( \alpha(1 + i \tan \vartheta) + \beta(1 - i \tan \vartheta) + \gamma \frac{2}{e^{4i\vartheta} + e^{2i\vartheta}} \right) \right)^{1/2}. \end{aligned} \quad (2.88)$$

As the complex square root is

$$\sqrt{a + bi} = \sqrt{\frac{\sqrt{a^2 + b^2} + a}{2}} \pm i \sqrt{\frac{\sqrt{a^2 + b^2} - a}{2}}, \quad (2.89)$$

and

$$a = \frac{f^2}{k^2} + \bar{\varphi} \left( \alpha + \beta + \gamma \Re \left( \frac{2}{e^{4i\vartheta} + e^{2i\vartheta}} \right) \right) \quad (2.90)$$

$$b = \frac{f^2}{k^2} + \bar{\varphi} \left( \tan \vartheta - \tan \vartheta + \gamma \Im \left( \frac{2}{e^{4i\vartheta} + e^{2i\vartheta}} \right) \right) \quad (2.91)$$

there is no form corresponding to the condition (2.82). It is not clear whether the condition for resonance can be met or not. While the resonance might have been shifted, it has not been removed, as the real part of this equation can still have different values than the resonant analytical solution.

According to Payne (2008), for adiabatic fully-compressible equations having one off-centring parameter  $\alpha_n = 1/2$  (as introduced earlier) means that the solution will show a weak polynomial-in-time growth. As Payne notes, other authors refer to this solution as “semi-stable”. Assuming that his findings can be directly transferred to the shallow water equations, those should show this kind of behaviour when off-centring is only applied to the height equation. However, even then it would be hard to predict, if this behaviour offers sufficient stability in the context of a comprehensive numerical model solving the primitive equations.

## 2.9 Summary

Recapping the findings above, it is well known that a spurious resonance may develop in the semi-implicit semi-Lagrangian discretised shallow water equations, within the presence of orography. The stability analysis as carried out by Rivest et al. (1994) confirmed that the off-centring approach effectively removes the resonance and stabilises the solution. Applying the same kind of stability analysis to a scheme which limited the off-centring approach to the height equation in the shallow water equations, within the presence of orography, led to an inconclusive resonance condition. As practical experience with the C-CAM model and the analytical findings of Payne (2008) are in contradiction, further numerical studies are necessary to draw more reliable conclusions about the usefulness of such a scheme.

## Chapter 3

# SWiM – A Semi-Lagrangian, Semi-Implicit Shallow Water Model

### 3.1 Introduction

There are a number of semi-implicit semi-Lagrangian models in use in the weather and climate communities today. The scheme has proven reliable and is in wide use. It therefore seems easy in principle to find a model to study the orographic resonance described in detail in Chapter 1. However, all the available models have in common that they tend to be highly complex weather forecast and climate prediction models. Using such a model for simple numerical experiments concerned with an instability of the dynamical core in the presence of a particular type of forcing may be impractical. The results will most likely vary significantly from model to model because

the effect of the spuriously resonant solution will likely lead to secondary effects. Modern models are very sophisticated and feature strong interaction between their dynamical cores and the modules that handle the various physical effects and parametrisations. It is therefore advisable to study the resonance problem in a simpler framework first.

The first step in the simplification is to find the simplest set of equations that can be used to study the spurious resonance phenomenon. As shown in Chapter 1 and Rivest et al. (1994), the shallow water equations constitute the simplest set of equations describing the atmosphere that are suitable to study the problem of the spurious orographic resonance.

To avoid complicating factors not relevant to the mountain wave resonance problem, the numerical framework should use Cartesian coordinates and a mountain of a very simple shape (e.g. a bell shape). As such a simple model is not freely and readily available, a new model was constructed to satisfy these requirements. The purpose of building a simple model is to study the resonance in detail without having to question the general validity of most of its results. As this model will be made freely available, it will hopefully also be of value to others who are interested in the response of the shallow water equations to orographic forcing.

In an attempt to make the custom developed semi-implicit semi-Lagrangian model, from here on referred to as SWiM<sup>1</sup>, as useful as possible for many different applications, it is designed to be highly flexible. It solves the linearised shallow water equations with orographic forcing. This orographic forcing can be introduced in two different ways, forcing either the momentum equations or the height equation or both the height and momentum

---

<sup>1</sup>the name SWiM is derived from **S**hallow **W**ater **M**odel

equations as explained in Section 2.3.3. Furthermore, it offers the choice of an adaptive time step, where a maximum Courant number is enforced at all times, or a fixed time step. Simulations can be configured with a maximum integration time or the number of time steps can be limited according to the requirements of the project.

Overall, SWiM follows the design principle that any additional level of complexity should be optional and disabling it should not require code modification. Therefore, almost all options except for the initial state of winds, heights and orography can be set in the configuration file or via the command line.

This chapter describes the main features of SWiM and presents validation tests. The next two chapters then present a systematic study of the numerical resonance and off-centring schemes to remove the resonance carried out with SWiM.

## 3.2 The Shallow Water Equations in SWiM

As shown in Section 2.3.3, the shallow water equations can vary slightly in form. The equations with orographic forcing are

$$\frac{\partial u}{\partial t} + u \frac{\partial u}{\partial x} + v \frac{\partial u}{\partial y} + \frac{\partial \varphi}{\partial x} - fv = -\frac{\partial \varphi_s}{\partial x}, \quad (3.1)$$

$$\frac{\partial v}{\partial t} + u \frac{\partial v}{\partial x} + v \frac{\partial v}{\partial y} + \frac{\partial \varphi}{\partial y} + fu = -\frac{\partial \varphi_s}{\partial y}, \quad (3.2)$$

$$\frac{\partial \varphi}{\partial t} + u \frac{\partial \varphi}{\partial x} + v \frac{\partial \varphi}{\partial y} + \bar{\varphi} \left( \frac{\partial u}{\partial x} + \frac{\partial v}{\partial y} \right) = 0. \quad (3.3)$$

where  $\varphi = gH$ , the product of the fluid depth  $H$  and the gravitational acceleration  $g$ .

[Rivest et al. \(1994\)](#) used this form for their study of the resonance.

The alternative form introduces the orographic forcing via the height equation. As the work of [Rivest et al. \(1994\)](#) provides the main point of reference for the shallow water experiments, the alternative form was not used and hence the details are omitted here. The reader is referred to [Pedlosky \(1992\)](#) for more details.

### 3.3 Solution Procedure

#### 3.3.1 Key Features

SWiM uses a semi-implicit semi-Lagrangian scheme for the numerical solution process as described in detail in Section [2.3.1](#). It solves the shallow water equations on a bi-periodic staggered Cartesian grid. The grid is laid out in Arakawa C-grid configuration (cf. [Arakawa and Lamb, 1977](#)), i.e. the  $u$  and  $v$  velocity components are shifted relative to the heights by half a grid spacing in  $x$  and  $y$  respectively. This is illustrated in [Fig. 3.1](#). SWiM assumes a constant Coriolis parameter  $f$  which is defined as  $f = 2\Omega \sin \vartheta$  where  $\vartheta$  is the latitude and  $\Omega$  the Earth's angular velocity. Thus, the latitude is assumed constant across the computational domain. As mentioned above, the orographic forcing can be introduced either via the height equation or via the momentum equations.

The semi-implicit scheme combines the momentum and height equations into a Helmholtz equation as described in detail in Section [2.3.2](#). This

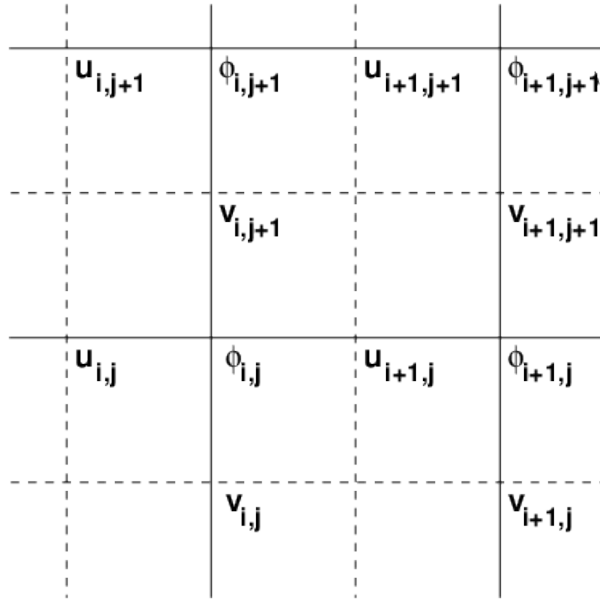


Figure 3.1: Staggering of grids in SWiM.

Helmholtz equation is solved implicitly as described in Section 3.3.5. With the new heights obtained from this first step the momentum equations can then be solved explicitly to complete the iteration according to Eqns. 2.76 and 2.77.

The solution procedure is very similar to many other shallow water models and very closely follows Staniforth and Côté (1991). It allows solving the shallow water equations using time steps equivalent to Courant numbers  $C > 1$ . At these large Courant numbers, it is then possible to trigger the numerical resonance which is the subject of this thesis.

### 3.3.2 Bi-periodic Domain and $f$ -Plane

Using a bi-periodic domain and an  $f$ -plane is unusual. Most shallow models are based on spherical domains as is the case for the models used by Rivest

et al. (1994) or Ritchie and Tanguay (1996) or more recently by Giraldo et al. (2003). Typically, these models also solve an equation for  $f$  as a function of the grid point's latitude.

The main incentive to choose spherical geometry is that there is a well established standard test suite for such models (Williamson et al., 1992). However, with a Cartesian grid, the derivatives are much simpler and linearity is preserved much more easily. The proof of the spurious resonant solution as shown in Section 2.6 also uses Cartesian derivatives, providing evidence that a Cartesian grid does not prevent the spuriously resonant solution. There is then no gain in a more sophisticated grid structure which only introduces additional complexity.

For the same reason, an  $f$ -plane is a good choice in the interest of simplicity. A Coriolis parameter  $f = f(\mathbf{r})$  which is a function of the position vector results in non-linear effects that make the problem unnecessarily complex. Usually, an  $f$ -plane implies that the length scale in latitude has to be small to ensure that the change of Coriolis parameter is negligible (cf. Wurtele, 1960). In the experiments needed for this project, even this argument is without importance. The numerical instability and spurious resonance may develop for any imaginary planet or arbitrary size and rotation speed. Again, the development of spurious resonance is independent of the value of the Coriolis parameter or its dependence on latitude and there is no gain in solving an additional equation.

Thus, choosing a bi-periodic Cartesian grid and assuming an  $f$ -plane is reasonable in the interest of keeping the model as simple as possible. This simplicity eliminates the possibility that additional numerical effects are in-

troduced and possibly mask the effects of the deliberately triggered spurious orographic resonance.

For wider use of SWiM, the choices made above could have more serious implications. A bi-periodic grid in three dimensions is a torus and cannot represent a sphere. The periodicity over the latitudinal boundary would be problematic, if the domain was considered a latitudinal band on the earth. Even with different boundary conditions, the Cartesian grid results in geometrical errors if the latitudinal band is too wide and the  $f$ -plane introduces an additional error. The model could still be used with a band narrow in latitude, if the latitudinal boundary condition was adjusted in a reasonable manner.

### 3.3.3 Time Step

As the Courant number is of central importance to studying the numerical resonance, the time step is defined according to a maximum Courant number. The time step is calculated from the grid spacing and the maximum velocity in the domain and defined as

$$\Delta t = C \times \max(\Delta x/u_{\max}, \Delta y/v_{\max}). \quad (3.4)$$

Over the course of the simulation, this time step can then be maintained constant or adapted according to this condition in every time step. For this study, an adaptive time step is the better choice because it facilitates determining the correlation between the resonance and the Courant number.

### 3.3.4 Departure Points

As a result of the staggered grid, departure points are determined separately for all physical values. The algorithm follows [McGregor \(2005, p. 15\)](#) where the departure points are determined in a three step process. All interpolations needed for the process outlined below are performed as bi-linear interpolations. As a consequence of the staggered grids, the values of the two other variables are always interpolated to the correct grid, again using bi-linear interpolation.

The first iteration for the departure point  $\mathbf{r}^0$  is

$$\mathbf{r}_1^0 = \mathbf{r}^+ - \mathbf{u}(\mathbf{r}^+)\Delta t, \quad (3.5)$$

where  $\mathbf{r}^+$  is the arrival point (i.e. the grid point) and

$$\mathbf{u} = u\hat{e}_x + v\hat{e}_y, \quad (3.6)$$

where  $\mathbf{u}$  is the velocity at the last time step with components  $u$  in  $x$  and  $v$  in  $y$ . The vectors  $\hat{e}_x$  and  $\hat{e}_y$  are the unit vectors in the  $x$  and  $y$  directions, respectively.

The second and third iteration are

$$\mathbf{r}_n^0 = \mathbf{r}^+ - (\mathbf{u}(\mathbf{r}^+) + \mathbf{u}(\mathbf{r}_{n-1}^0))\Delta t/2, \quad (3.7)$$

where  $n = \{2, 3\}$  and  $\mathbf{r}_3^0$  is then used as the final departure point.

Alternatively, SWiM offers an algorithm as described by [Staniforth and Côté \(1991\)](#) which was found to perform well. It is defined iteratively as

$$\delta_n = \Delta t \left( \frac{3}{2} \mathbf{u}(\delta_{n-1}/2, t) - \frac{1}{2} \mathbf{u}(\delta_{n-1}, t - \Delta t) \right), \quad (3.8)$$

$$\mathbf{r}_n^0 = \mathbf{r}^+ - \delta_n, \quad (3.9)$$

where  $\delta_n$  is the back trajectory for iteration  $n$  and  $\delta_0 = 0$  in the first time step of the simulation. In any later time step,  $\delta_0$  is the value  $\delta_m$  determined for  $t - \Delta t$  where  $m$  represents the last iteration for the preceding time step.

The [Staniforth and Côté](#) algorithm was found not to converge fully in experiments with SWiM and it is advisable to limit it to less than ten iterations. SWiM offers an implementation of this algorithm based on four iterations. It can be activated as an alternative to the default method described above.

### 3.3.5 SOR Solver

The semi-implicit semi-Lagrangian scheme used in SWiM determines the new heights implicitly from a Helmholtz equation as demonstrated in [Section 2.3.1](#). This process uses an accelerated Gauß-Seidel method known as successive over-relaxation (SOR).

The Helmholtz equation ([2.53](#)) can be discretised and expressed in the form

$$c_{i,j}\varphi_{i+1,j} + d_{i,j}\varphi_{i-1,j} + e_{i,j}\varphi_{i+1,j} + l_{i,j}\varphi_{i,j-1} + o_{i,j}\varphi_{i,j} = q_{i,j}, \quad (3.10)$$

where  $\varphi$  is the variable we want to determine and the coefficients are functions of  $i$  and  $j$ , the grid coordinates in  $x$  and  $y$ . All the grid spacings and time steps from the discretisation in time and space have been incorporated into the coefficients.

For the iterative solution process, we define the residual

$$\eta_{i,j} = c_{i,j}\zeta_{i+1,j} + d_{i,j}\zeta_{i-1,j} + e_{i,j+1}\zeta_{i+1,j} + l_{i,j}\zeta_{i,j-1} + o_{i,j}\zeta_{i,j} - q_{i,j}, \quad (3.11)$$

and then calculate a new  $\zeta_{i,j}$  as

$$\zeta_{i,j}^{n+1} = \zeta_{i,j}^n - \omega \frac{\eta_{i,j}}{q_{i,j}}, \quad (3.12)$$

where  $\omega$  is called the *relaxation parameter*. The relaxation parameter is  $\omega = 1$  for the Gauß-Seidel method and  $\omega > 1$  for successive over-relaxation. The optimal relaxation parameter depends on the problem and can typically not be calculated beforehand.

The iteration is repeated until a certain convergence criterion is reached. Typically, this convergence criterion is defined using the norm of the residual. A slow rate of change in the residual is then considered a sign of the algorithm having converged to the final solution.

In SWiM, the convergence criterion for the SOR solver is based on the maximum change of the residual across the computational domain dropping below a prescribed threshold. Once this condition is fulfilled, the solution is considered accurate and the solver passes on the results. The SOR solver also aborts the solution process after a certain number of iterations if the convergence criterion has not been met. This is a precaution for the case that the solution does not converge fast enough. SWiM's model output alerts the user to possibly corrupt results whenever this fallback is used.

The SOR solver in SWiM uses a red-black scheme (cf. [Press et al., 2007](#)) which determines the new values for odd and even numbered grid points separately for every iteration. This is possible because the mixed derivatives in Eqn. (2.53) vanish and odd and even grid points decouple into two independent grids for the SOR process.

### 3.4 Off-Centring

As the numerical resonance is at the centre of this study, the off-centring scheme in SWiM is designed to be very flexible. It offers a first order off-centring scheme which can optionally be disabled completely and very flexibly configured when enabled. A simulation without off-centring will solve the centred equations as shown in Eqns. (2.51) to (2.53). When running SWiM with off-centring, the off-centring parameters  $\alpha_n$  (and thus also the resulting  $\beta_n$ ) need to be defined with  $n \in \{1, 2, 3\}$ . By default, SWiM then

solves Eqns. (3.1) to (3.3) which in their time discretised form become

$$\begin{aligned} u^+ &= \Delta t (-\alpha_1(\varphi_x^+ + \varphi_{s,x}^+) - \beta_1(\varphi_x^0 + \varphi_{s,x}^0) + (\alpha_2(fv)^+ + \beta_2(fv)^0)) \\ &\quad + u^0, \end{aligned} \quad (3.13)$$

$$\begin{aligned} v^+ &= \Delta t (-\alpha_1(\varphi_y^+ + \varphi_{s,y}^+) - \beta_1(\varphi_y^0 + \varphi_{s,y}^0) - (\alpha_2(fu)^+ + \beta_2(fu)^0)) \\ &\quad + v^0, \end{aligned} \quad (3.14)$$

$$\varphi^+ = -\Delta t (\bar{\varphi} [\alpha_3(u_x + v_y)^+ + \beta_3(u_x + v_y)^0]) + \varphi^0. \quad (3.15)$$

Derivatives are denoted using a subscript ( $x$  or  $y$ ). All derivatives are evaluated at the point denoted by the superscript. The notation of all variables is as before.

The coefficients  $\alpha_n$  and  $\beta_n$  are defined as

$$\alpha_n + \beta_n = 1, \quad (3.16)$$

where the off-centring parameter  $\alpha_n \geq 1/2$ .

In the height equation (3.15) the unknown values of  $u^+$  and  $v^+$  are substituted using the corresponding momentum equations (3.13) and (3.14). This leads to the elliptic equation

$$\begin{aligned}
a(\varphi_x^+)_x &+ b(\varphi_x^+)_y - b(\varphi_y^+)_x + a(\varphi_y^+)_y - \frac{\varphi^+}{\alpha_1\alpha_3(\Delta t)^2\bar{\varphi}} \\
&= -\frac{a}{\alpha_1} (\beta_1 ((\varphi_x^0)_x + (\varphi_{x,s}^0)_x + (\varphi_y^0)_y + (\varphi_{y,s}^0)_y) + f(u_y^0 - v_x^0)) \\
&\quad -\frac{b}{\alpha_1} (\beta_1 ((\varphi_y^0)_x + (\varphi_{y,s}^0)_x - (\varphi_x^0)_y - (\varphi_{x,s}^0)_y) + \beta_2 f(u_x^0 + v_y^0)) \\
&\quad + \frac{1}{\alpha_1\Delta t} \left( (u_x^0 + v_y^0) \left( \frac{\beta_3}{\alpha_3} + a \right) \right) \\
&\quad - \frac{1}{\alpha_1\alpha_3(\Delta t)^2\bar{\varphi}} \varphi^0 + a ((\varphi_{x,s}^+)_x - (\varphi_{y,s}^+)_y) , \tag{3.17}
\end{aligned}$$

for the set of equations (3.13) to (3.15) where  $a = [1 + (\alpha_2 f \Delta t)^2]^{-1}$  and  $b = (\alpha_2 f \Delta t)a$  and  $f_x = f_y = f_t = 0$ .

By setting the values of  $\alpha_1$ ,  $\alpha_2$  and  $\alpha_3$  independently a large range of different off-centring schemes can be tested. Off-centring can be applied only to the momentum equations, only the height equation or to all the equations.

### 3.5 Variable Off-Centring Parameters

As discussed earlier, SWiM can apply off-centring in a variety of ways. In most models, off-centring parameters are chosen and applied over the entire computational domain and are held constant in space and time. SWiM can reproduce this behaviour and additionally it can vary the off-centring over the computational domain. The local  $\alpha_n$  for every grid point is then determined offline and maintained at constant value for the duration of the simulation.

To determine the local  $\alpha_n$ , SWiM searches the vicinity of every grid point for the largest gradient in orography. The radius of this search is preset as a

parameter in the SWiM model. Then, the local  $\varepsilon_n = 2\alpha_n - 1$  is determined as

$$(\varepsilon_n)_{\text{loc}} = (2\alpha_n - 1) \times \max \left( \left| \frac{(\Delta\varphi_s)_{\text{vic}}}{(\Delta\varphi_s)_{\text{max}}} \right| \right) \quad (3.18)$$

where  $(\Delta\varphi_s)_{\text{vic}}$  is any orography gradient within the search radius and  $(\Delta\varphi_s)_{\text{max}}$  the maximum orography gradient in the computational domain.

### 3.6 Standard Tests applied to SWiM

New atmospheric models have been developed for several decades now and with every new numerical scheme, and often also with a new generation of scientists, comes a new generation of climate models. These models need to be tested and validated before they can be used with confidence. As even across different numerical schemes, climate models generally share a lot of features, [Williamson et al. \(1992\)](#) designed a test suite suitable for testing the main dynamical features of global climate models.

The tests by [Williamson et al.](#) cannot be used for SWiM because of the rather different design. SWiM is not a global model and, as a result, does not share some of the main features of global models. While a global model would also show bi-periodicity in the sense that a feature can travel across the whole domain continuously, the  $f$ -plane is a major obstacle to using most of the standard test cases.

To still be able to test SWiM adequately, a suitable suite of test cases was developed, which is partly inspired by the [Williamson et al.](#) test suite. It

is comprised of simple advection tests and a test for the SOR solver which solves the Helmholtz equation. In all cases, an exact solution is known and the numerical solution can be compared with this exact solution.

### 3.6.1 Advection Tests

#### Simple Linear Advection

To test the semi-Lagrangian advection, a few simple advection tests were performed. For the test cases, the velocities are maintained at a constant value and a simple advection equation is solved for a scalar distribution that is advected. Any height profile should then be advected by the winds and thus just be translated to a new position.

The advection test was executed in three different configurations. In test case 1, advection only took place in the  $x$ -direction with the winds being set to  $u = 50 \text{ m/s}$  and  $v = 0$ . In test case 2, the advection was limited to the  $y$ -direction with the winds set to  $u = 0$  and  $v = 50 \text{ m/s}$ . Test case 3 then combined the former two test cases for diagonal advection at  $u = 50 \text{ m/s}$  and  $v = 50 \text{ m/s}$ .

All test cases were run on a  $256 \times 256$  grid with a Coriolis parameter  $f = 10^{-4} \text{ s}^{-1}$ , a mean height  $\bar{\varphi} = 5.5 \times 10^4 \text{ m}^2/\text{s}^2$  and a resolution of  $\Delta x = \Delta y = 50 \text{ km}$ .

The advected height profile was a circular Gaussian hill of the shape

$$\varphi_0 = 0.1\bar{\varphi} \times \exp\left(-5 \times 10^{-3} \times (x - x_{\text{ctr}})^2 - 5 \times 10^{-3} \times (y - y_{\text{ctr}})^2\right), \quad (3.19)$$

where  $x_{\text{ctr}}$  and  $y_{\text{ctr}}$  are the coordinates of the centre of the computational domain. The values for  $\varphi$  are then bounded as  $0 < \varphi \leq 5500 \text{ m}^2/\text{s}^2$ .

The exact solution for the advection test cases is

$$\begin{aligned} \varphi_{\text{exact}} = & 0.1\bar{\varphi} \times \exp \left( -5 \times 10^{-3} \times (x - x_{\text{ctr}} + ut)^2 \right. \\ & \left. -5 \times 10^{-3} \times (y - y_{\text{ctr}} + vt)^2 \right), \end{aligned} \quad (3.20)$$

where  $t$  is the total time since the start of the simulation.

The error of the numerical result is defined as the difference between numerical and analytic solution. All figures show the absolute error of the numerical solution for  $\varphi$ , i.e.  $e_\varphi = \varphi_{\text{numerical}} - \varphi_{\text{exact}}$ . For advection in  $x$  (Fig. 3.2) the time step is defined by a prescribed Courant number of  $C = 4.5$ , i.e.  $\Delta t = 4500 \text{ s}$ . For advection in  $y$  (Fig. 3.3), the Courant number is  $C = 4.3$  with a resulting  $\Delta t = 4300 \text{ s}$ . For simultaneous advection in  $x$  and  $y$  (Fig. 3.4), the Courant number is  $C = 3.7$  which results in a time step  $\Delta t = 3700 \text{ s}$ . The different Courant numbers ensure that the interpolation errors are not artificially kept constant across different test simulations. In all test cases the moving feature crosses the entire domain at least two to three times.

The absolute error in Figs. 3.2 and 3.3 is never larger than  $\sim 6 \text{ m}^2/\text{s}^2$ . The largest error is associated with the maximum of the Gaussian hill which results in a relative error of less than  $\sim 0.15\%$ . The errors are identical between the advection tests in  $x$  and  $y$  despite the Courant numbers being different. This indicates that the interpolations yield good results.

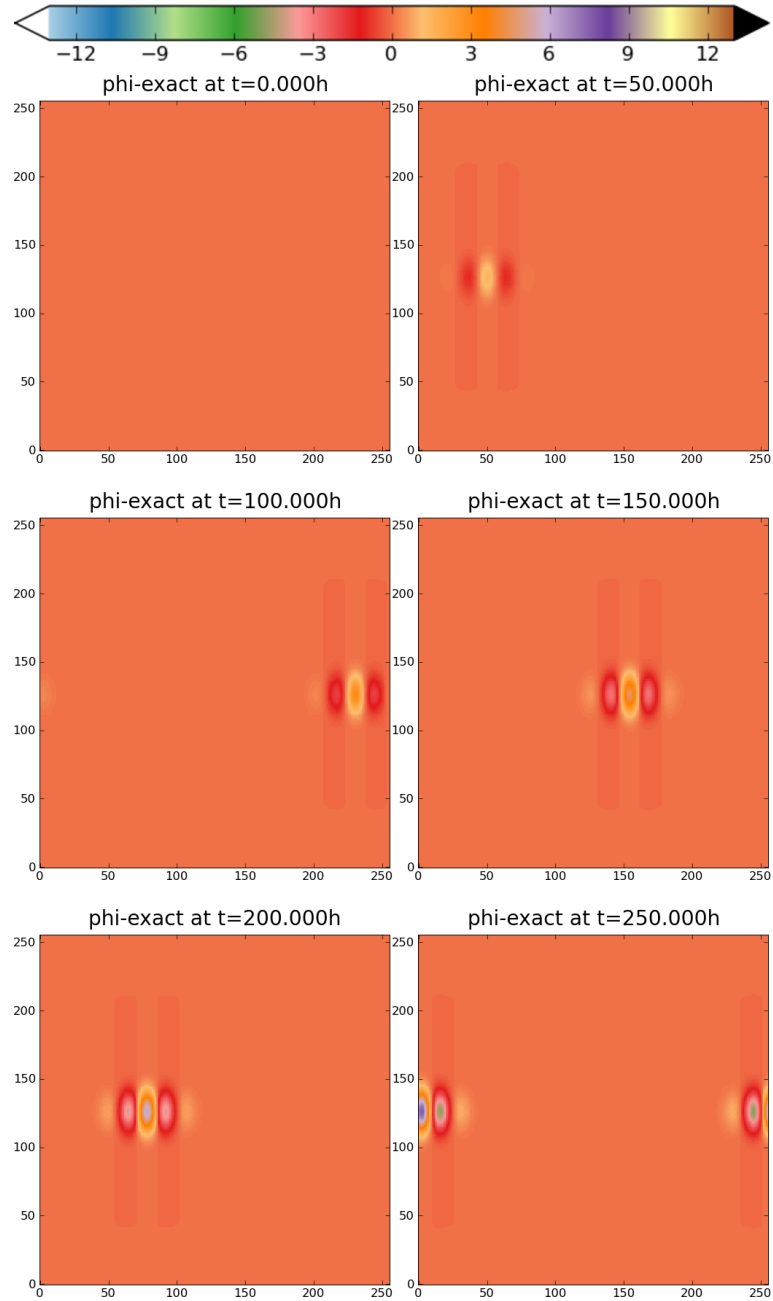


Figure 3.2: Absolute error for a circular Gaussian hill in  $\varphi$  (in  $m^2/s^2$ ) advected in  $x$  at Courant number  $C = 4.5$  and  $u = 50m/s$ . Shown are iterations  $\{0, 40, 80, 120, 160, 200\}$  (Test 1).

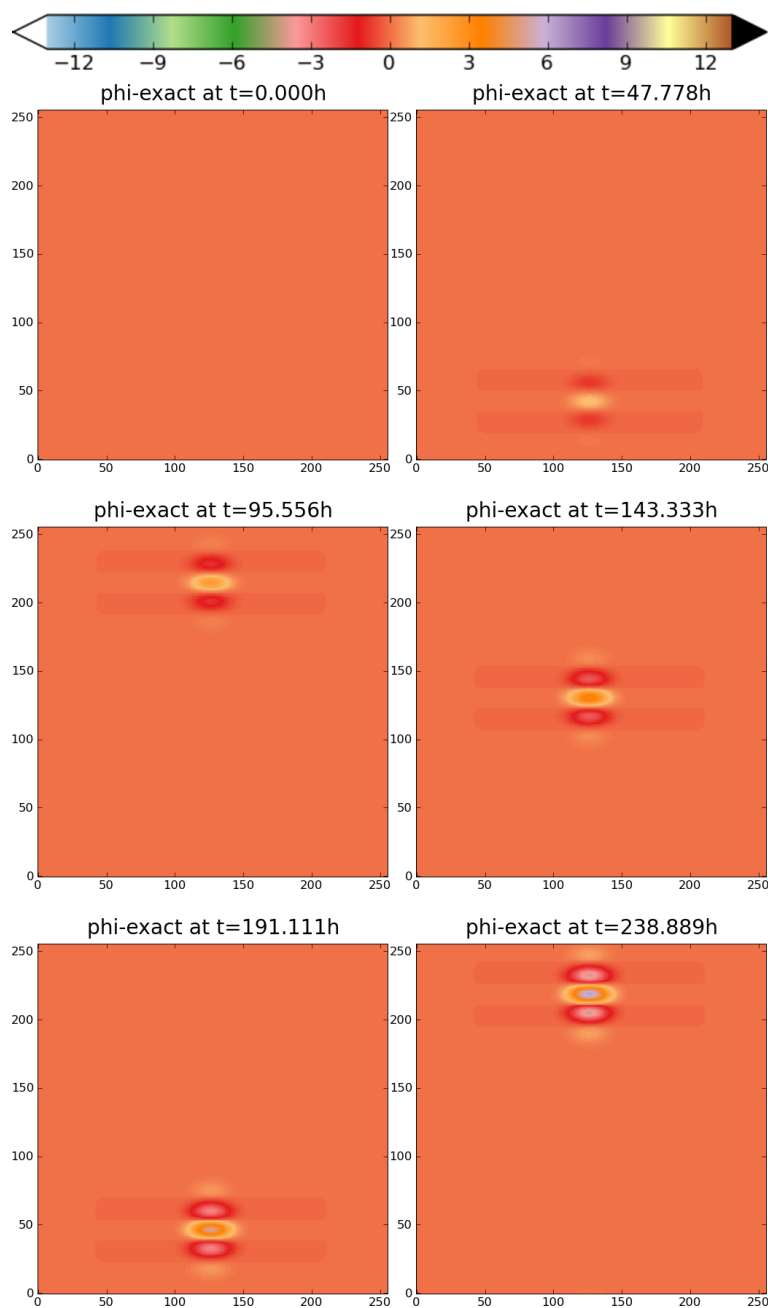


Figure 3.3: Absolute error for a circular Gaussian hill in  $\varphi$  (in  $m^s/s^2$ ) advected in  $y$  at Courant number  $C = 4.3$  and  $v = 50m/s$ . Shown are iterations  $\{0, 40, 80, 120, 160, 200\}$  (Test 2).

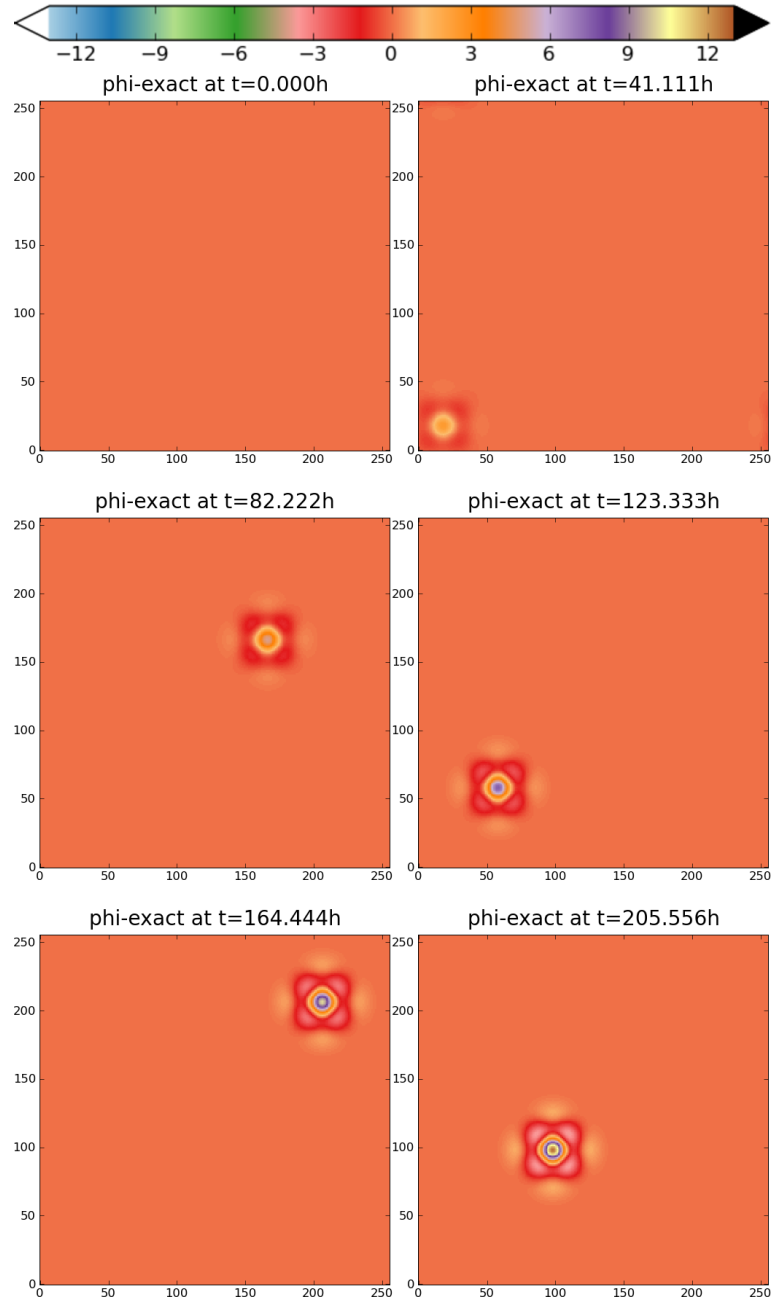


Figure 3.4: Absolute error for a circular Gaussian hill in  $\varphi$  (in  $m^s/s^2$ ) advected in  $x$  and  $y$  at Courant number  $C = 3.7$  and  $u = v = 50m/s$ . Shown are iterations  $\{0, 40, 80, 120, 160, 200\}$  (Test 3).

Fig. 3.4 shows about double the error of up to  $\sim 12 \text{ m}^2/\text{s}^2$  for advection in both dimensions  $x$  and  $y$ . This is to be expected as a result of the need to interpolate in both dimensions in this case. The relative error is still less than  $\sim 0.25\%$ .

The error's growth rate and the maximum observed relative error of  $\sim 0.2\%$  are acceptable and the numerical results have proven sufficiently accurate.

### Advection under Rotation

With the test cases for linear advection having yielded acceptable accuracy, the next step was testing advection under rotating winds. This served the purpose of further testing the interpolations that are carried out as part of the departure point identification and to determine the values of  $\varphi$  at the departure points. Test case 4 used the same height profile as test cases 1 to 3 and a velocity profile which results in a rigid rotation in the center of the domain and a differential rotation further away from the centre which vanishes on the edges of the computational domain. The velocity profile is defined as

$$\omega = \begin{cases} 1 & (r < 0.75) \\ \frac{1-r}{1-0.75} & (0.75 < r < 1) \\ 0 & (r > 1) \end{cases} , \quad (3.21)$$

where  $\omega$  is the angular velocity and  $r$  the distance from the centre of the computational domain. A transformation to Cartesian coordinates yields  $u$  and  $v$  for every grid point.

To make the rotation visible, this time a stretched Gaussian hill of the shape

$$\varphi_0 = 0.1\bar{\varphi} \times \exp\left(-5 \times 10^{-3} \times (x - x_{\text{ctr}})^2 - 5 \times 10^{-4} \times (y - y_{\text{ctr}})^2\right), \quad (3.22)$$

was used and the exact solution then being the original configuration (i.e. the Gaussian hill) rotated by the angle  $\omega(r)t$ .

Fig. 3.5 shows that under rotation the error now does not contain a preference for a certain dimension. However, the error in the centre, where the Gaussian hill follows a rigid rotation, is not proportional to the height values or the height gradients. This could be a result of the fixed-length time step. The trailing edges in the outer, differentially rotating, part of the domain ( $0.75 < r < 1$ ) mainly reflect the same trailing edges as can be seen in the exact solution.

The relative error in test case 4 is larger than in test cases 1 to 3 and reaches about  $\sim 0.7\%$ . This does not come unexpected because the velocity pattern is more complex now. This is likely to lead to larger errors in the calculation of the departure points.

Test case 5 (shown in figure 3.6) replaces the Gaussian hill used in test cases 1 to 4 with a step function of the form

$$\omega = \begin{cases} 0 & (x \leq x_0 - \epsilon) \\ 100 & (x_0 - \epsilon < x < x_0 + \epsilon) \\ 0 & (x \geq x_0 + \epsilon) \end{cases}, \quad (3.23)$$

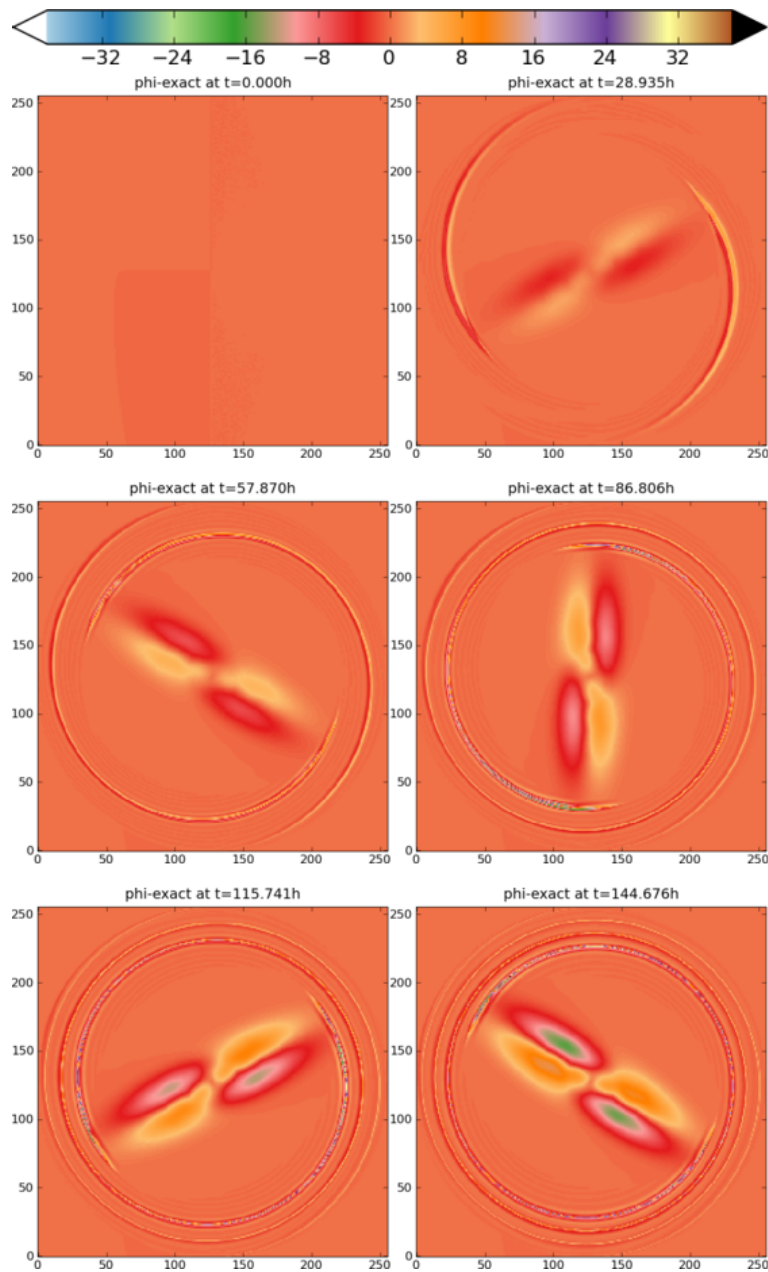


Figure 3.5: Absolute error for a stretched Gaussian hill in  $\varphi$  (in  $m^s/s^2$ ) under (partly differential) rotation at maximum Courant number  $C = 3$  (Test 4).

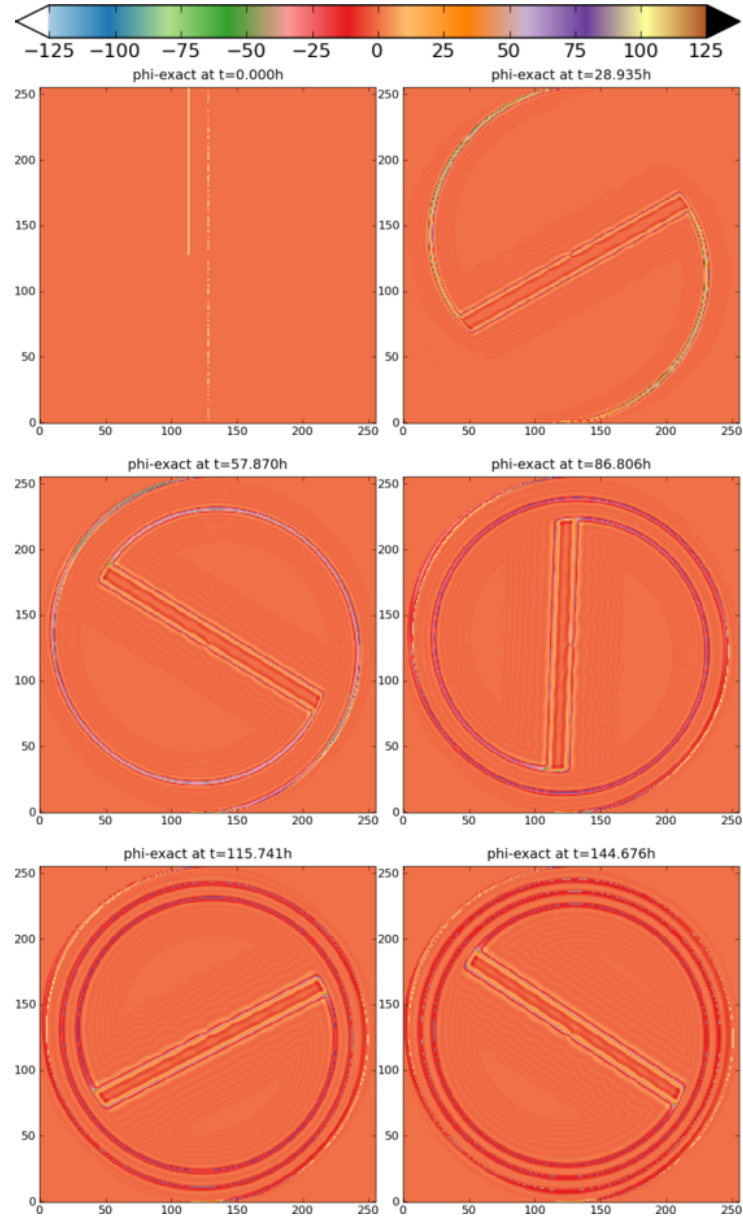


Figure 3.6: Absolute error for initial step function in  $\varphi$  (in  $m^s/s^2$ ) under (partly differential) rotation at maximum Courant number  $C = 5$  (Test 5).

where  $x_0$  is the center of the step and  $2\epsilon$  is the step width. The error is largest around the edges of the rotating feature.

As the errors in the numerical representation of the exact solution are already non-zero in small regions at time  $t = 0$ , there is clearly a contribution from errors in the “exact” solution. While the exact solution only solves a geometrical equation, this equation is still solved numerically. Using the compiler’s arcsin function to determine the rotated feature for the current time step introduces a truncation error into what is considered “exact” here. This error in the geometrical equation’s solution (which is used as the comparison) is negligible in comparison with the error in the numerical solution of the advection equation. Nevertheless, this error does still contribute to the total error found for the advection equation’s numerical solution.

With an integration time of the order of one to two weeks, the test simulations were on about the same time scales as most of the experiments conducted. This implies that the error for the experiment can also be expected to be below 1%. This is small enough to consider the numerical solution for simulations of a few weeks accurate.

### 3.6.2 Tests for the SOR Solver

Having shown that the advection properties of SWiM are accurate, the second component which requires testing is the SOR solver. For that purpose, the velocities were set to a known exact solution in each time step and only the height equation was solved numerically. The quality of the solution which the SOR solver yields can then be assessed from the ability and rate of convergence to the exact solution for the heights. For technical reasons,

this test is performed across several time steps. In every time step, the SOR solver performed 500 iterations. This approach of testing the solver across several time steps minimises the amount of code modification required to set up the test case and takes advantage of the stationary exact solution the numerical solution is converging to.

This test case design was based on the linearised geostrophic motion which has the exact solution

$$\varphi(x, y, t) = \varphi_0 \cos(kx + ly), \quad (3.24)$$

$$u(x, y, t) = -\frac{1}{f} \frac{\partial \varphi}{\partial y} = \varphi_0 \frac{l}{f} \sin(kx + ly), \quad (3.25)$$

$$v(x, y, t) = \frac{1}{f} \frac{\partial \varphi}{\partial x} = -\varphi_0 \frac{k}{f} \sin(kx + ly), \quad (3.26)$$

where the wave vector  $\mathbf{k} = \begin{pmatrix} k \\ l \end{pmatrix}$  with  $k$  the wave number in  $x$  and  $l$  the wave number in  $y$ .

In the test, the amplitude of height disturbance was set to  $\varphi_0 = 1.0 \times 10^{-3} \bar{\varphi}$  and  $\bar{\varphi} = 5.5 \times 10^4 \text{ m}^2/\text{s}^2$  and the Coriolis parameter was  $f = 10^{-4} \text{ s}^{-1}$ . The wave vector components were chosen as  $k = 2\pi x_{\text{dim}}$  and  $l = 2\pi y_{\text{dim}}$  where  $x_{\text{dim}}$  and  $y_{\text{dim}}$  are the size of the computational domain in  $x$  and  $y$  respectively. The variable for which the equation was solved numerically (height or one of the velocity components) was always initialised to zero everywhere.

Fig. 3.7 shows snapshots of iterations  $n \in \{0, 2000, 4000, 6000, 8000, 10000\}$ . This is equivalent to time steps  $n \in \{0, 40, 80, 120, 160, 200\}$  in the figure's

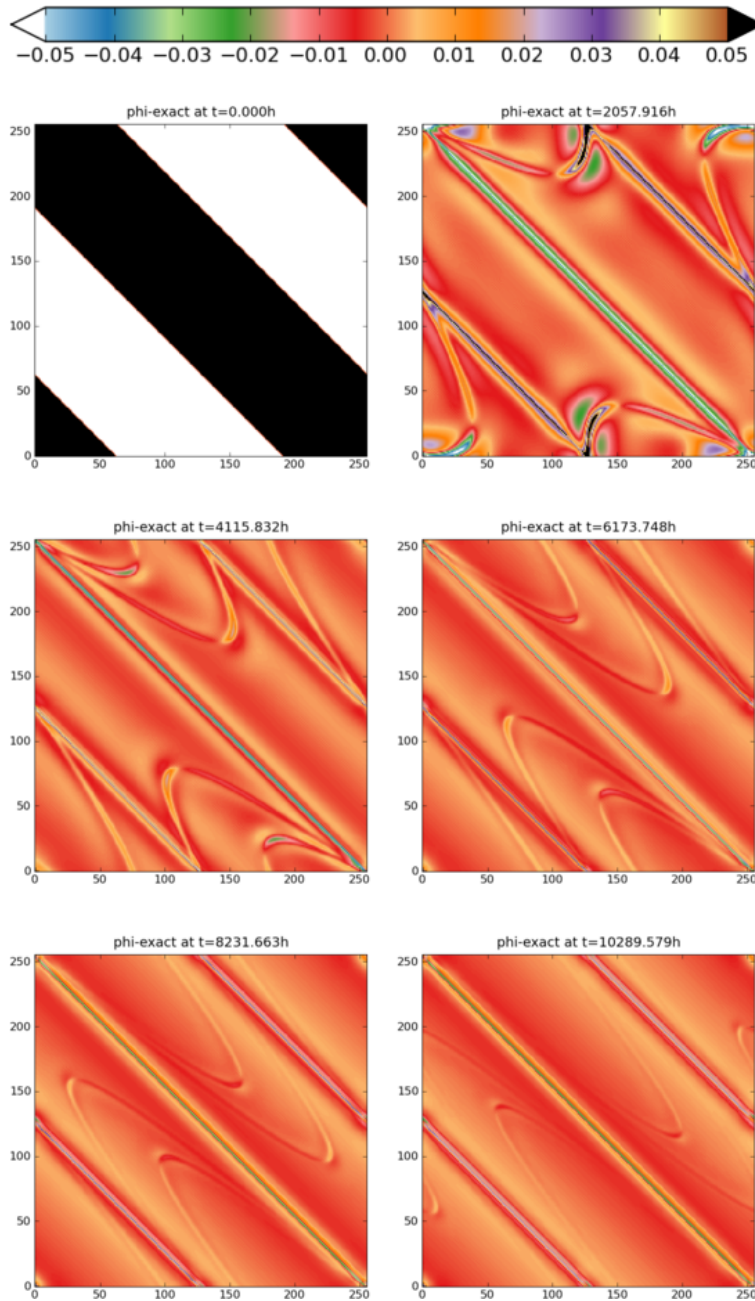


Figure 3.7: Error of numerical solution of  $\varphi$  converging to exact solution.  $u$  and  $v$  according to exact solution and  $C = 1$ . Shown are iterations  $\{0, 2000, 4000, 6000, 8000, 10000\}$ .

legend. The numerical solution has converged very well to the exact solution after 6000 to 8000 iterations. The remaining error after 10000 iterations for the heights is no more than  $\sim 0.1\%$  (with  $\varphi = [-55, 55]$ ).

In early iterations seen in Fig. 3.7 the largest error is found close to the periodic boundaries. This is most likely introduced by slight discontinuity at the boundaries resulting from round-off errors when initialising the domain with the exact solution for the velocities. At a later point, when the solver only converges very slowly, the largest error is clearly associated with the extrema of the stationary solution where the gradients are the smallest.

### 3.6.3 Summary of Test Results

Several simple tests were carried out with SWiM to test its key components, namely the advection behaviour and the SOR solver. All test results showed satisfactory accuracy. The advection on the time scale as used in most of the experiments in the following chapters is very accurate with an acceptable error. While the SOR solver converged rather slowly to the stationary exact solution, the resulting errors are small. The errors are also small enough to consider results from simulations of the order of several weeks valid.

That the SOR solver converges slowly implies that the relaxation parameter used ( $\omega = 1.4$ ) was not optimal for the problem. This could be different for the experiments but is solely an efficiency issue and of no importance to accuracy.



## Chapter 4

# Off-Centring Experiments in a Shallow Water Model

The preceding chapter introduced SWiM and its main features. It also presented tests that were designed to ensure that SWiM solves the shallow water equations sufficiently accurately to use it for the numerical experiments carried out in this thesis.

In this chapter, SWiM is applied to problems that include orographic forcing. To study the effects of the resonance, the experiments are comprised of a number of setups where both centred and off-centred equations are solved at different Courant numbers.

First, the findings by [Rivest et al. \(1994\)](#) concerning the numerical resonance are reproduced and verified. This involves the deliberate triggering of the numerical resonance by solving the centred equations with orographic forcing at large Courant numbers. The first order off-centring scheme, which [Rivest](#)

[et al.](#) propose, is then applied to verify that it is capable of removing the numerical resonance.

As the next step, the off-centring scheme is applied to only a subset of the equations. The results obtained from these modified schemes are compared to those of the full off-centring scheme and those of centred simulations at small Courant numbers. This prepares the ground for Chapter 5 which introduces a new variable off-centring scheme.

The basic setup of the simulations was designed to mimic the setup of [Rivest et al. \(1994\)](#) as closely as possible. The resolution was therefore set to  $\Delta x = 50 \text{ km}$  and  $\Delta y = 50 \text{ km}$  and a mean height  $\bar{\varphi} = 5.5 \times 10^4 \text{ m}^2/\text{s}^2$  with a Coriolis parameter  $f = 10^{-4} \text{ s}^{-1}$  if not indicated otherwise. Also in agreement with [Rivest et al.](#), the orographic forcing is introduced as detailed in earlier chapters. The wind fields are always initialised with  $u = 50 \text{ m/s}$  and  $v = 0$ .

As [Rivest et al.](#) used a global model and therefore employed a description of the Coriolis parameter  $f$  that depends on latitude, this point is different between their setup and the one used here. While this does obviously affect the results, it has no effect on the impact of the numerical resonance as explained earlier.

All simulations were carried out with a domain size of  $256 \times 256$  grid points. Due to [Rivest et al.](#) working on the sphere at the same spatial resolution ( $50 \text{ km}$  or  $\sim 1/2^\circ$ ) as the experiments in this chapter, their domain was much larger. However, this again has no qualitative impact on the observed features caused by the resonance (cf. Section 4.2.3).

## 4.1 Reference Simulation

As there is no known general analytical solution to the time-dependent shallow water equations, a numerical reference is needed for comparison with later results. This reference simulation has to be designed with the objective of solving the equations as precisely as is possible in the numerical context considered. This is achieved by using the simplest configuration and a relatively high resolution in time and space.

The reference simulation was performed at the same spatial resolution and domain size as all later simulations. However, to achieve small Courant numbers, a short time step was ensured by imposing a maximum Courant number of  $C = 1/2$ . This prevented the studied numerical resonance from being triggered accidentally. The use of an adaptive time step maintained this Courant number throughout the course of the simulation. All resonant solutions can be expected to differ significantly from this reference.

Fig. 4.1 shows snapshots of the height anomaly field (multiplied by standard gravity  $g$ ) of the reference simulation. The orography is (in good approximation) flat except for a small peak which has a Gaussian shape. The orography is defined as

$$\varphi_{\text{oro}}(x, y) = \frac{\bar{\varphi}}{2} \times \exp \left( -3.5 \times 10^{-2} (x - 3/4 \times x_{\text{dom}})^2 - 2.5 \times 10^{-2} (y - 1/2 \times y_{\text{dom}})^2 \right), \quad (4.1)$$

where  $x_{\text{dom}}$  and  $y_{\text{dom}}$  are the length and width of the computational domain. The fact that the shape is not symmetrical is of no significance to

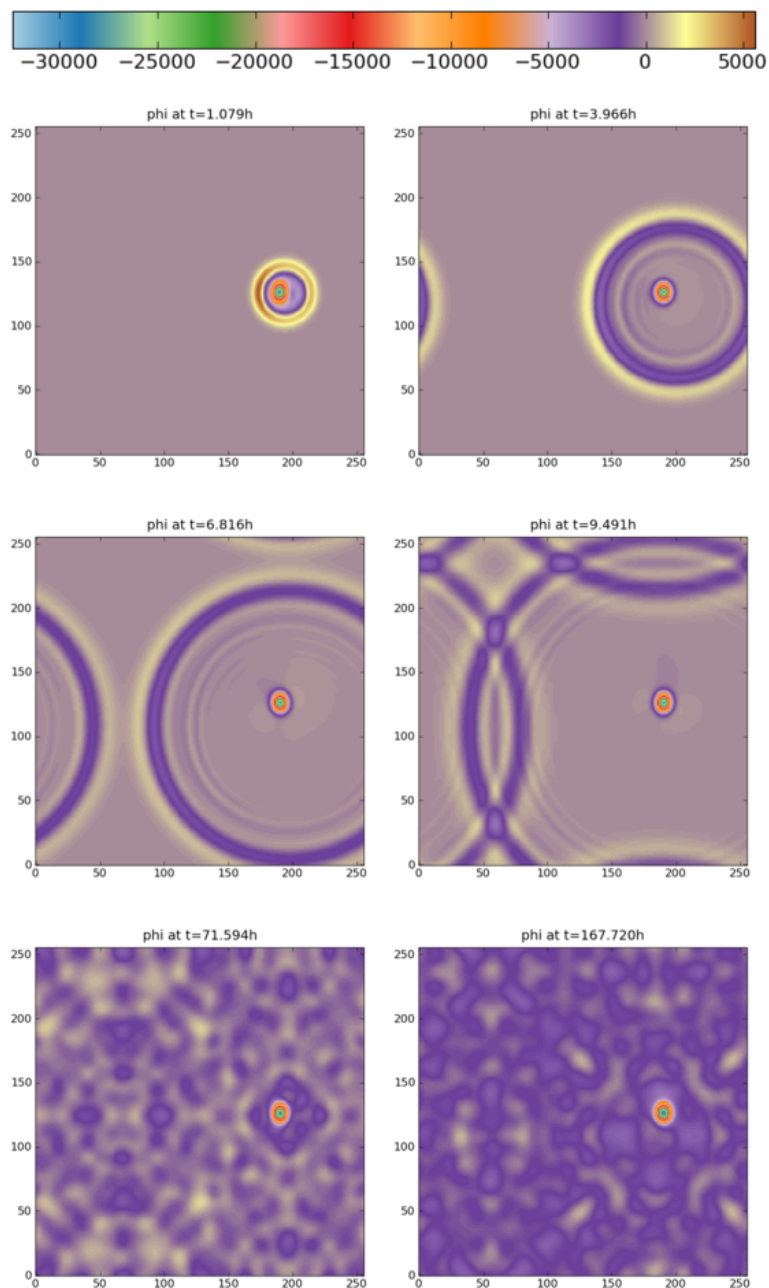


Figure 4.1: Height anomaly  $\varphi$  (in  $m^2/s^2$ ) for  $C = 1/2$ . Showing early time evolution and state at 7 days.

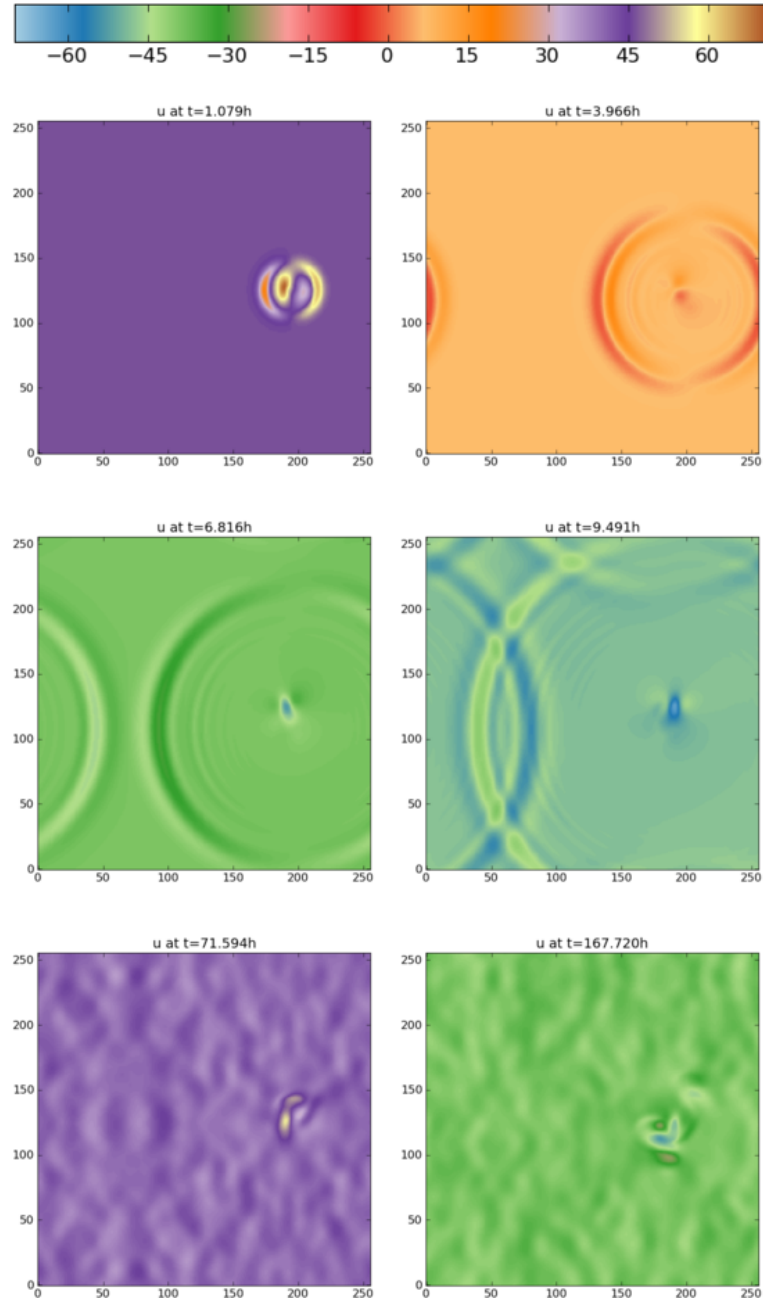


Figure 4.2: Velocity component  $u$  (in  $m/s$ ) for  $C = 1/2$ . Showing early time evolution and state at 7 days.

the problem. The equations used are centred, i.e. they have the form as in Eqns. (2.51) to (2.53).

At the start of the simulation, a wave is excited by the orography and then travels through the domain. Due to the periodicity of the domain, this wave interferes with itself and results in a complex but still regular pattern. Over time this pattern develops into background noise but still preserves a degree of regularity.

As the shallow water equations also provide solutions for the velocity components at every time step, these are shown for component  $u$  in Fig. 4.2. Component  $v$  shows a pattern that is equivalent to a rotation of component  $u$  and is not shown. The patterns in the two velocity components correspond well with those seen in the height anomalies in Fig. 4.1. The same travelling and self-interfering wave can be seen clearly and over time a noisy but not entirely irregular pattern emerges.

While these results are not an analytical solution and should not be considered equivalent, either, they can be validated by a plausibility argument. The scenario is very much like a tub of water which is suddenly dented from the bottom pushing up a column of water. The water, which was at rest before, reacts to the dent by flowing away from the obstacle to create a smooth surface again. The result is a wave moving concentrically away from the new obstacle in all directions. The reason why the shape is not circular around the obstacle in Figs. 4.1 and 4.2 is the Coriolis term in the shallow water equations and the fact that the obstacle in the domain is not circular in shape. If the tub from the example was basically mounted on a rotating body which results in a Coriolis force in the co-rotating system, then the wave propagation would not be concentric any more in this system.

## 4.2 No Off-Centring

The reference simulation used a semi-Lagrangian scheme based on centred equations. As explained in Chapter 2, in such a scheme the values of all physical variables or their derivatives for one iteration in the time integration are determined as averages of the value at the departure point and the arrival point at the corresponding times. For the small Courant number in the reference simulation, this scheme yields stable results with no indication of numerical resonance near the orography, just as Section 4.1 illustrated.

According to the stability considerations in Section 2.6, the scheme should become unstable or at least show spurious flow patterns if the Courant number is raised to  $C \gtrsim 1$ . The question arises then, how such a spuriously resonant solution is different from the solution obtained in the reference simulation. The following presents a suite of experiments which test how the flows differ in solutions for Courant numbers  $C \geq 1$ .

### 4.2.1 Simulations with Large Courant Numbers

Having established a reference, the logical next step is to increase the Courant number to  $C \geq 1$ . As shown in Section 2.4 (and originally by Rivest et al., 1994), the spurious numerical resonance is only triggered for Courant numbers of  $C \gtrsim 1$ .

The resonance is closely linked to the Courant number and thus the approach of using an adaptive time step to ensure a certain Courant number in the domain will again be applied. As the Courant number will vary across the domain, the adaptive time step is calculated using the maximum velocity

across the domain. If the velocity gradients are not too large across the domain, this gives a good estimate of the Courant numbers everywhere. Even if there is some significant velocity gradient, this method ensures that for no grid point the prescribed maximum Courant number is exceeded.

The goal of the large Courant number simulations is to trigger the numerical resonance. Later, several approaches to off-centring to remedy the resonance are evaluated against these simulations. Just as the reference simulation presented earlier allows comparison with a “correct” solution, these centred schemes at large Courant numbers are the reference for simulations that have become resonant.

It is not practical to show all resonant and non-resonant simulations on one colour scale. Therefore, the colour scale used from this point on is generally suitable for the reference simulation ( $C = 1/2$ ). Particularly for resonant simulations, this results in large regions of some plots being out of range and appearing white (below range minimum) or black (above range maximum).

### **Courant Number $C = 1$**

At Courant number  $C = 1$  it is not obvious a priori what scenario should emerge. While a simulation at that Courant number could become resonant, it is hard to predict if it actually will. Because of the use of the adaptive time step based on the maximum Courant number in the domain, most of the domain still has Courant numbers  $C < 1$ . Furthermore, there are very few wave numbers that lead to a resonant solution for Courant numbers  $C \approx 1$  as is evident from Eqn. (2.73).

To begin the evaluation of the results of a simulation at Courant number  $C = 1$ , Fig. 4.3 shows the simulated height anomaly equivalent to Fig. 4.1. It

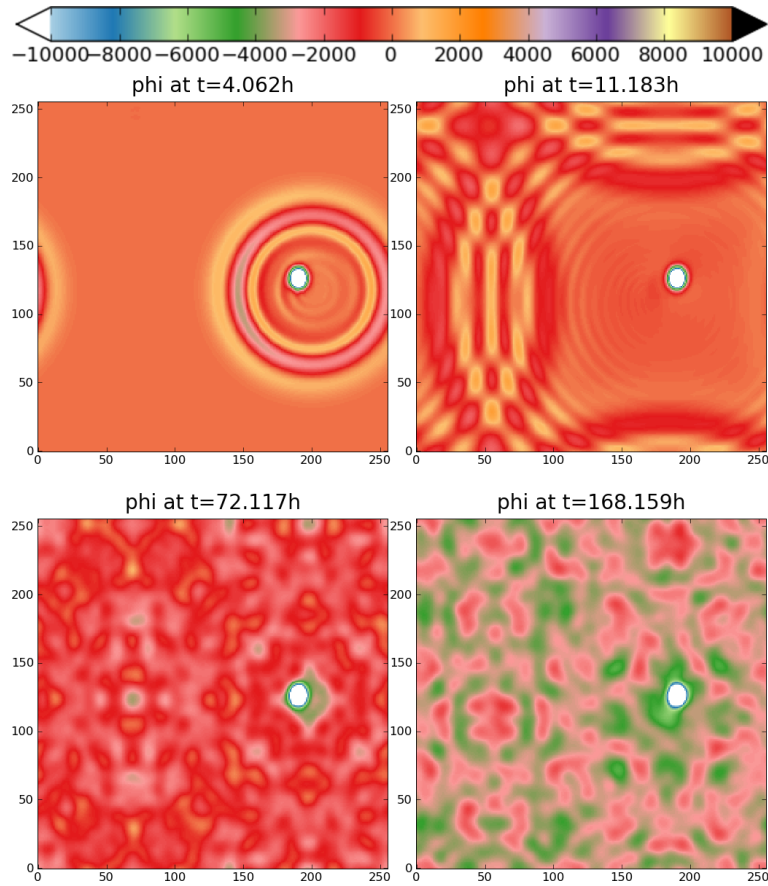


Figure 4.3: Height anomaly  $\varphi$  (in  $m^2/s^2$ ) for  $C = 1$ . Showing early time evolution and state at 7 days.

is evident that the features in the height anomaly distribution are still rather smooth. There is no obvious change in amplitude of the wave pattern and no conspicuous change in the dynamical structure. Nevertheless, comparison of height anomaly fields obtained in this simulation with the reference simulation's height anomaly fields, reveals some differences. Fig. 4.4 shows a comparison of this simulation (left panels) with the reference simulation (right panels) for two selected time steps ( $4h$  and  $7d$ ). The most obvious difference is that the height anomalies are overestimated by about a factor of two for the state after 7 days (bottom panels). There is also a slight

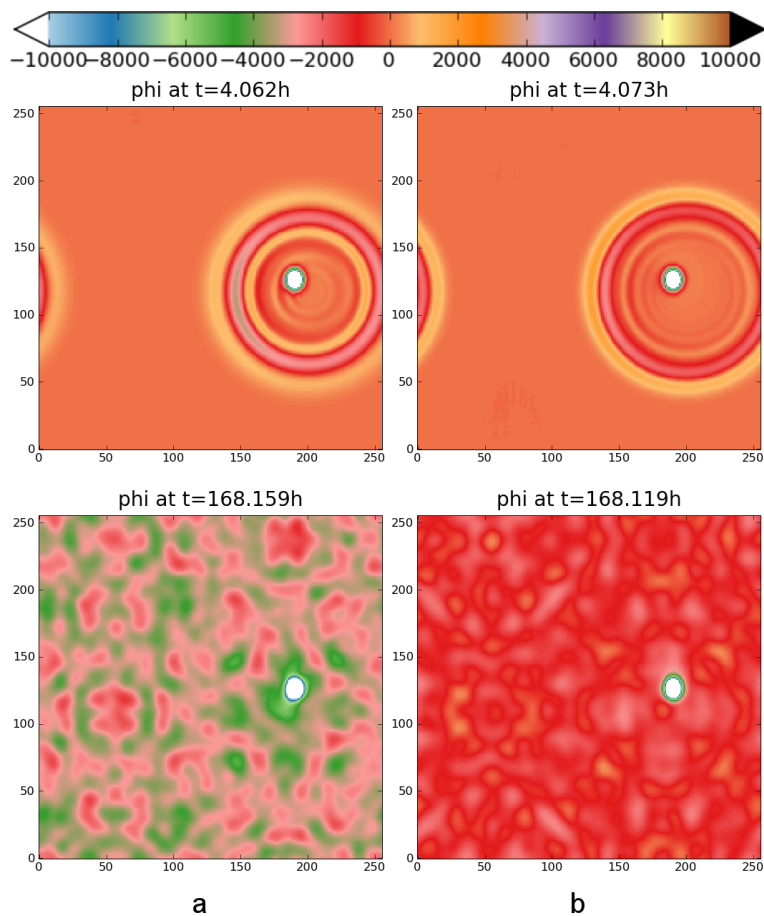


Figure 4.4: Height anomaly  $\varphi$  (in  $m^2/s^2$ ) for a)  $C = 1$  b)  $C = 1/2$ . Showing early time evolution and state at 7 days.

difference in the early wave propagation and amplitude which is due to the semi-implicit solution procedure (cf. Haltiner and Williams, 1980). As the phase error in implicit and semi-implicit schemes grows with the Courant number, comparing the propagation speed of waves across Courant numbers would be unwise when looking for signs of resonant behaviour. The following discussions of results will therefore not comment on wave propagation unless there is reason to expect that it was affected by the resonance beyond the error from the semi-implicit solution procedure.

If the observed differences in the simulation with Courant number  $C = 1$  are due to the resonance or just slightly different solutions is hard to say. The errors between simulations of different Courant number will never be exactly the same because of different departure points and a difference in the number of iterations needed to reach a certain point in time. Hence, this simulation is not different enough to classify as clearly resonant beyond reasonable doubt at this point. Section 4.3.1, which introduces the off-centring approach as originally suggested by Rivest et al. (1994), will therefore revisit this case to shed more light on the question if this case is resonant or not.

#### **Courant Number $C = 2$**

Raising the Courant number to  $C = 2$  results in the solutions shown in Fig. 4.5. There is now obvious change to the flow patterns when compared to the reference simulation. However, an amplitude change in the wave at early times can be observed. Also, the amplitudes after 7 days (168h) are now overestimated by a factor of about four to five and there is no sign of regularity as there is in the reference simulation. This is evidence that for this Courant number the resonance now has significant impact. The distribution of height anomaly has changed more than they could have as a result of changing error in the solution. Nevertheless, the amplitudes are still of a similar order of magnitude as in the reference simulation.

#### **Courant Number $C = 2.5$**

While some impact from the resonance was visible for a Courant number  $C = 2$ , it is at Courant number  $C = 2.5$  where its effect on the dynamics

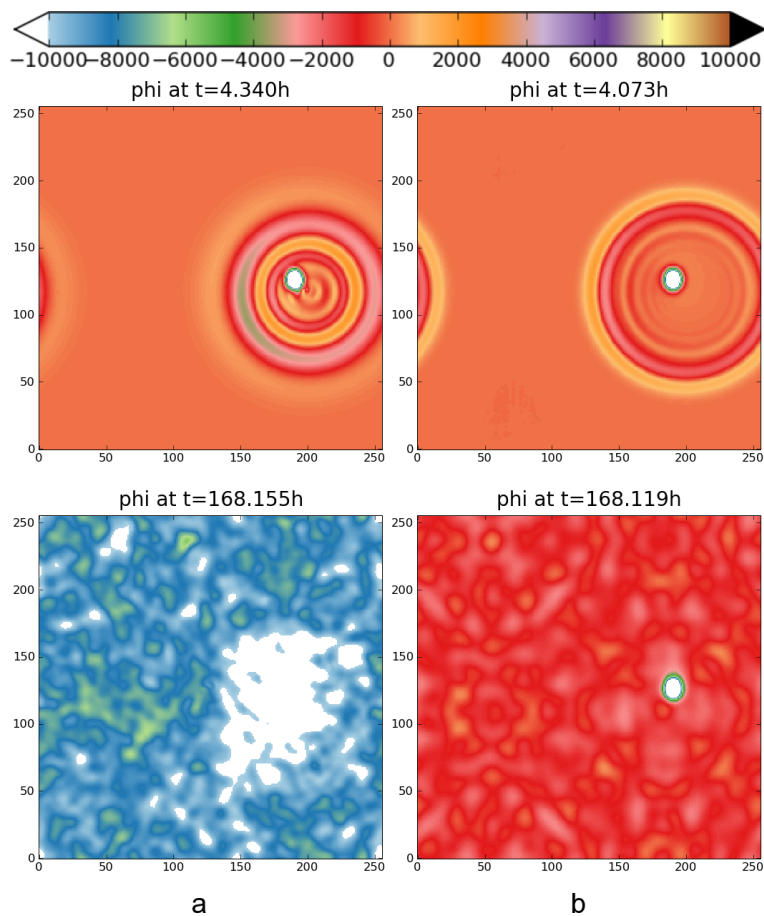


Figure 4.5: Height anomaly  $\varphi$  (in  $m^2/s^2$ ) for a)  $C = 2$  b)  $C = 1/2$ . Showing early time evolution and state at 7 days.

becomes dominant. The solution in Fig. 4.6 shows a state of the height anomaly field after 7 days which is almost entirely out of range on the used colour scale. In the first 11h, the dynamics are already driven by a very well-defined and distinct wave pattern unlike the ones seen in simulations of smaller Courant numbers. After 3 days, it is also impossible to define clear axes of symmetry for the simulation at large Courant number while this is easily possible for the reference simulation.

The comparison in Fig. 4.7 reveals that the two simulations bear virtually no

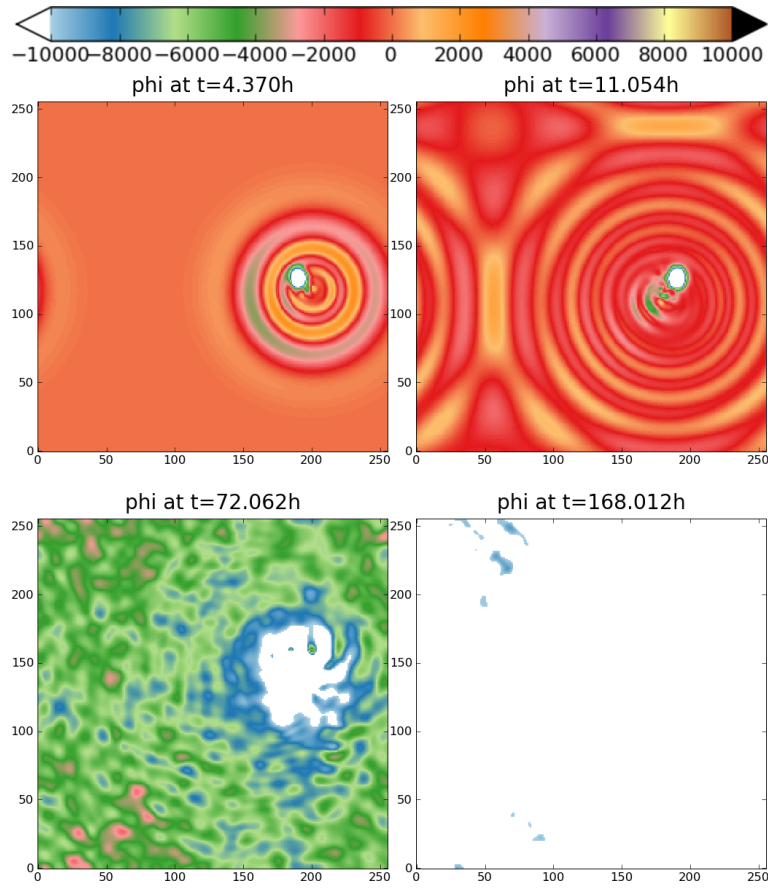


Figure 4.6: Height anomaly  $\varphi$  (in  $m^2/s^2$ ) for  $C = 2.5$ . Showing early time evolution and state at 7 days.

resemblance even for a time as early as  $4h$  into the simulation. The excited wave has larger amplitude than in the reference simulation. After  $4h$  the observed wave is very different in nature from the one in the reference simulation. The primary wave which has not crossed the domain and interfered with itself, yet, is much more distinct for the large Courant number. While the difference after  $4h$  might be attributed to a mere difference in phase velocity, this effect is not sufficient to explain the fundamental differences after 7 days.

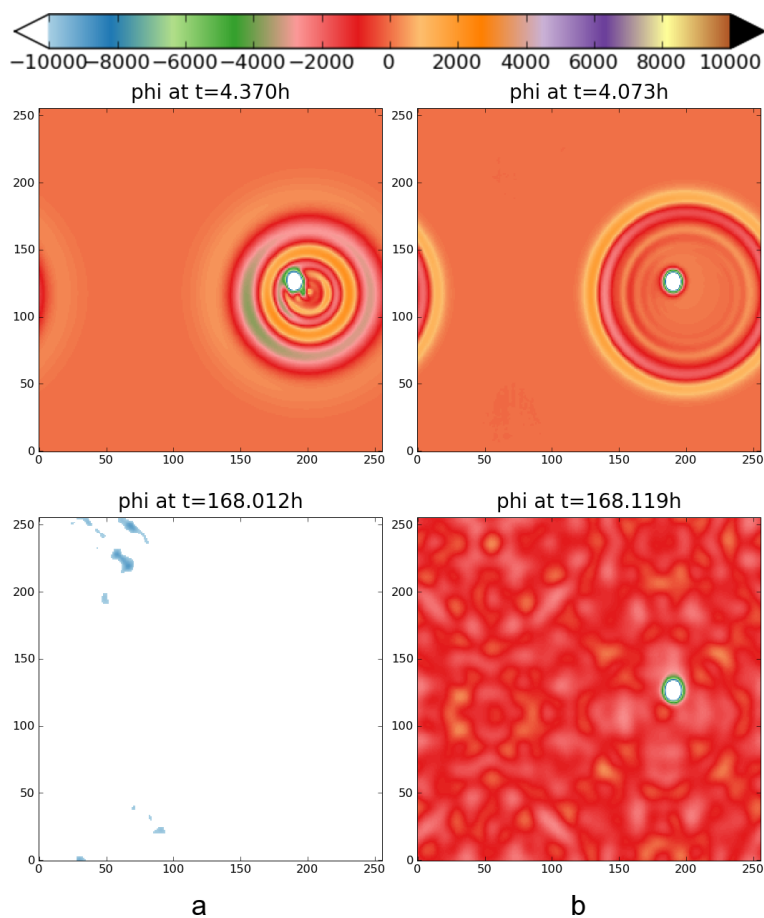


Figure 4.7: Height anomaly  $\varphi$  (in  $m^2/s^2$ ) for a)  $C = 2.5$  b)  $C = 1/2$ . Showing early time evolution and state at 7 days.

### Courant Number $C = 4$

Based on the findings for the Courant numbers used in the preceding sections, one would now expect that for a Courant number  $C > 2.5$  the effect becomes even more pronounced. Only to a very limited degree is that the case. Even raising the Courant number to  $C = 4$  does not result in the solution that one would extrapolate from the findings for Courant numbers  $1 \leq C \leq 2.5$ . In line with expectation, the amplitude of the height anomalies now grows faster than for  $C = 2.5$ . Comparing the results for Courant

number  $C = 4$  with those obtained at Courant number  $C = 2.5$ , however, Fig. 4.8 reveals that for  $C = 2.5$  a larger area is below the minimum value of the colour scale after 7 days than is for  $C = 4$ .

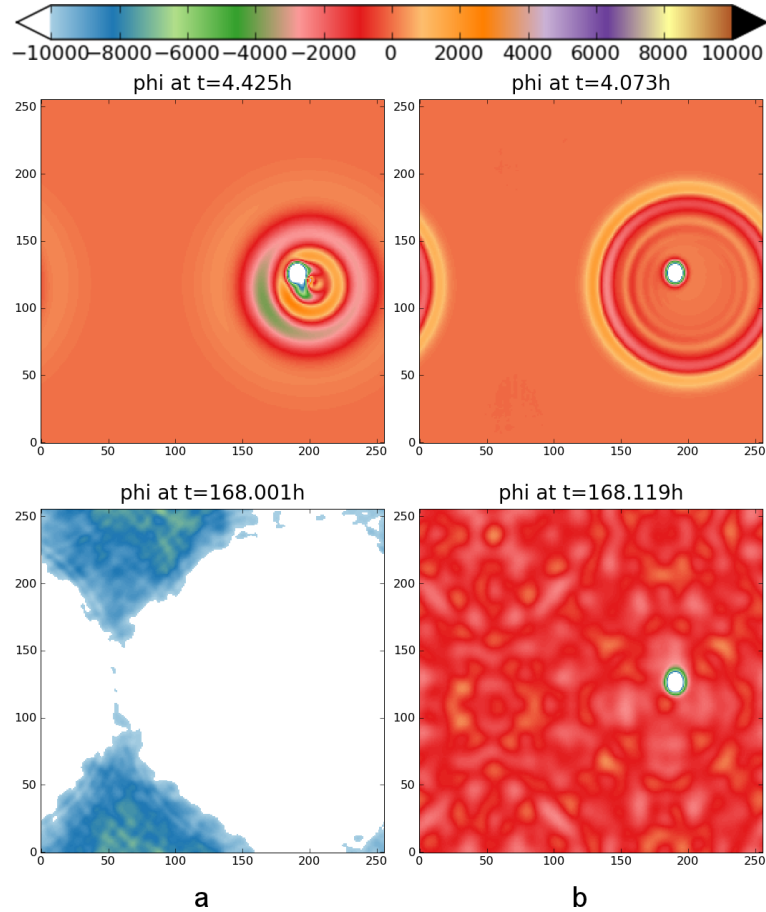


Figure 4.8: Height anomaly  $\varphi$  (in  $m^2/s^2$ ) for a)  $C = 4$  b)  $C = 1/2$ . Showing early time evolution and state at 7 days.

As one would expect, in Fig. 4.8 any resemblance between the reference simulation and the simulation with Courant number  $C = 4$  has disappeared. The dynamics of the domain are now dominated by a short wave-length wave originating from the orography. This wave appears to have a shorter wave length in the simulation with Courant number  $C = 4$  than it does in the

simulation with  $C = 2.5$ .

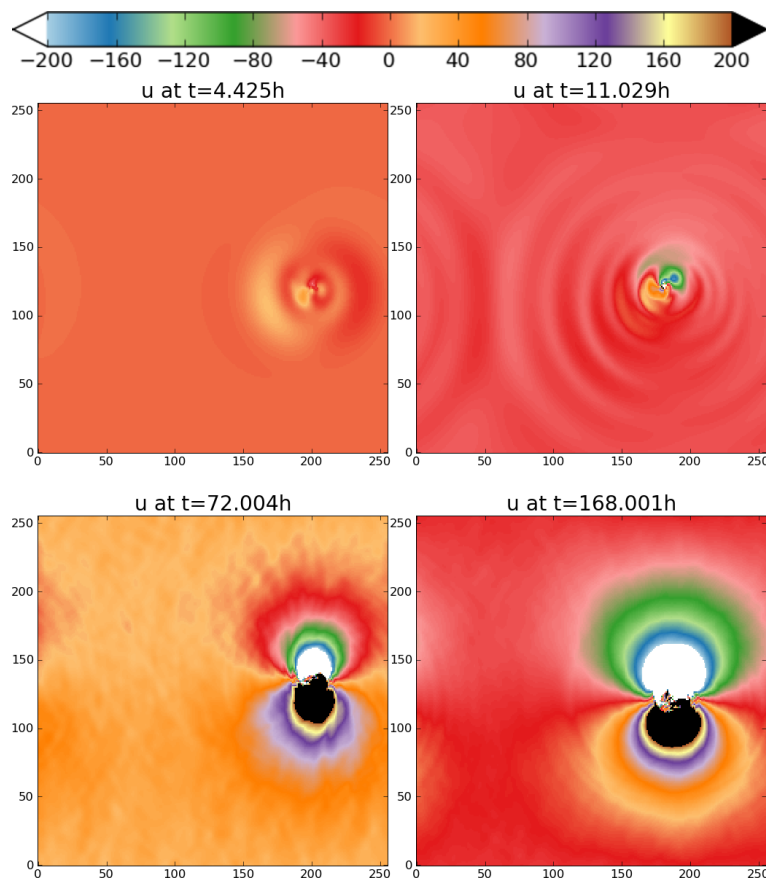


Figure 4.9: Velocity component  $u$  (in  $m/s$ ) for  $C = 4$ . Showing early time evolution and state at 7 days.

To further clarify the details around the development for Courant number  $C > 2.5$ , it is useful to investigate the development of the velocity for a clearly resonant simulation. Figs. 4.9 and 4.10 show the velocity components for the  $C=4$  simulation. From the oppositely growing velocities to two sides of the orography, it is evident that the anti-clockwise vorticity in the domain grows significantly over time. The growth of vorticity originates from the orographic forcing. The vortex pattern is always centred over the domain and grows steadily. The vortex pattern appears larger in  $u$  than in  $v$  due to

the fact that the orography is not symmetrical and the difference in velocity components  $u$  and  $v$ . Qualitatively, the vortex growth is the same in both velocity components.

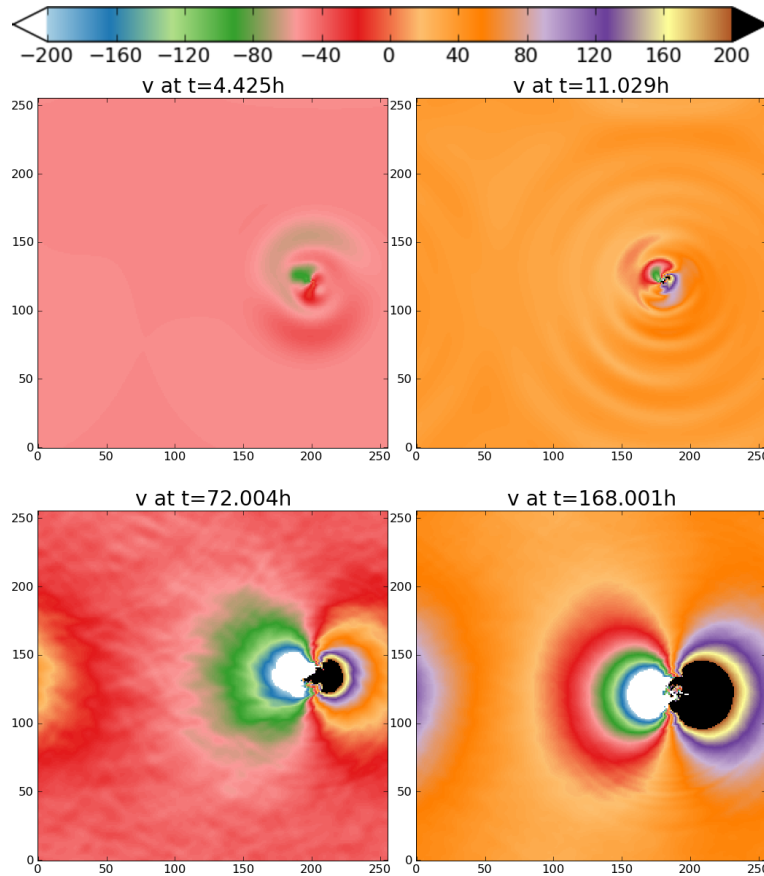


Figure 4.10: Velocity component  $v$  (in  $m/s$ ) for  $C = 4$ . Showing early time evolution and state at 7 days.

One could compare this growth in vorticity for different Courant numbers visually by plotting the velocities like in Figs. 4.9 and 4.10. It is more useful, however, to evaluate the differences between the simulations by defining the total kinetic energy per unit mass in the domain as an indicator for stability

which is

$$E_{\text{kin}} = \sum_{\text{domain}} \frac{1}{2} (u^2 + v^2) \quad (4.2)$$

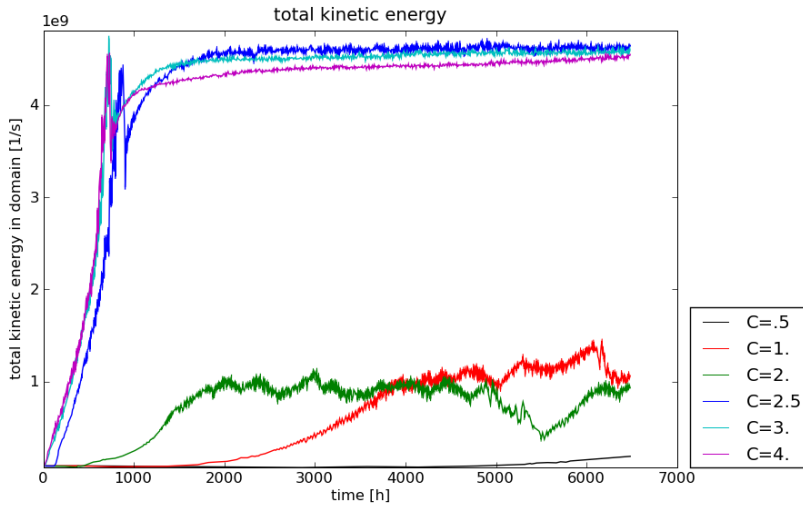


Figure 4.11: Time evolution of kinetic energy per unit mass in the domain for different Courant numbers.

The total kinetic energy per unit mass is shown as a function of time for Courant numbers  $C \in \{0.5, 1, 2, 2.5, 3, 4\}$  in Fig. 4.11. The evolution of the kinetic energy explains the height evolution described earlier. A clear difference can be seen for simulations at Courant numbers  $C \geq 2.5$  and those of smaller Courant number. Within a relatively short time frame, all simulations at Courant numbers  $C \geq 2.5$  exhibit very rapid increase in kinetic energy. The same rapid growth can be observed for Courant numbers  $1 \leq C \leq 2$  but with a certain delay and a lower extreme value attained within the simulation. This leaves only the simulation at Courant number  $C = 0.5$  with an evolution of kinetic energy which seems to indicate stability.

While no simulation of Courant number  $C \geq 1$  seems stable, it comes as a surprise that there is such a striking difference between simulations of Courant numbers  $1 \leq C \leq 2$  and  $C \geq 2.5$ . Section 4.2.2 discusses this phenomenon in more detail.

### 4.2.2 The Resonance in Detail

As seen in the results shown in Section 4.2.1, the resonance does not suppress the generation of the wave which is excited by the orography. It does, however, change the nature of this wave.

To study the resulting different wave pattern more closely, it is useful to zoom in on the orography and study the very early development of the flows. This gives an indication of when and how the patterns diverge from the pattern seen in the reference simulation.

The height anomalies after 1h and 3h for Courant numbers  $C \in \{0.5, 2.5, 4\}$  are shown in Fig. 4.12. This allows for a comparison between the reference simulation and two different resonant simulations. The comparison confirms that the excited wave is radically different between the reference simulation and simulations at larger Courant numbers. The larger the Courant number, the more slowly the wave propagates due to the phase error from the semi-implicit solver as mentioned earlier. At the same time, this slower wave has a larger amplitude and new wave fronts are being generated over time. There is no sign that the amplitude of new wave fronts is decreasing. The wave also appears to not be excited at the point of highest elevation but somewhere in the vicinity of that point (centre of white spot).

In the early stages of the simulation, the nature of the wave is still very similar for all Courant numbers. It is unclear at this stage, if it has a

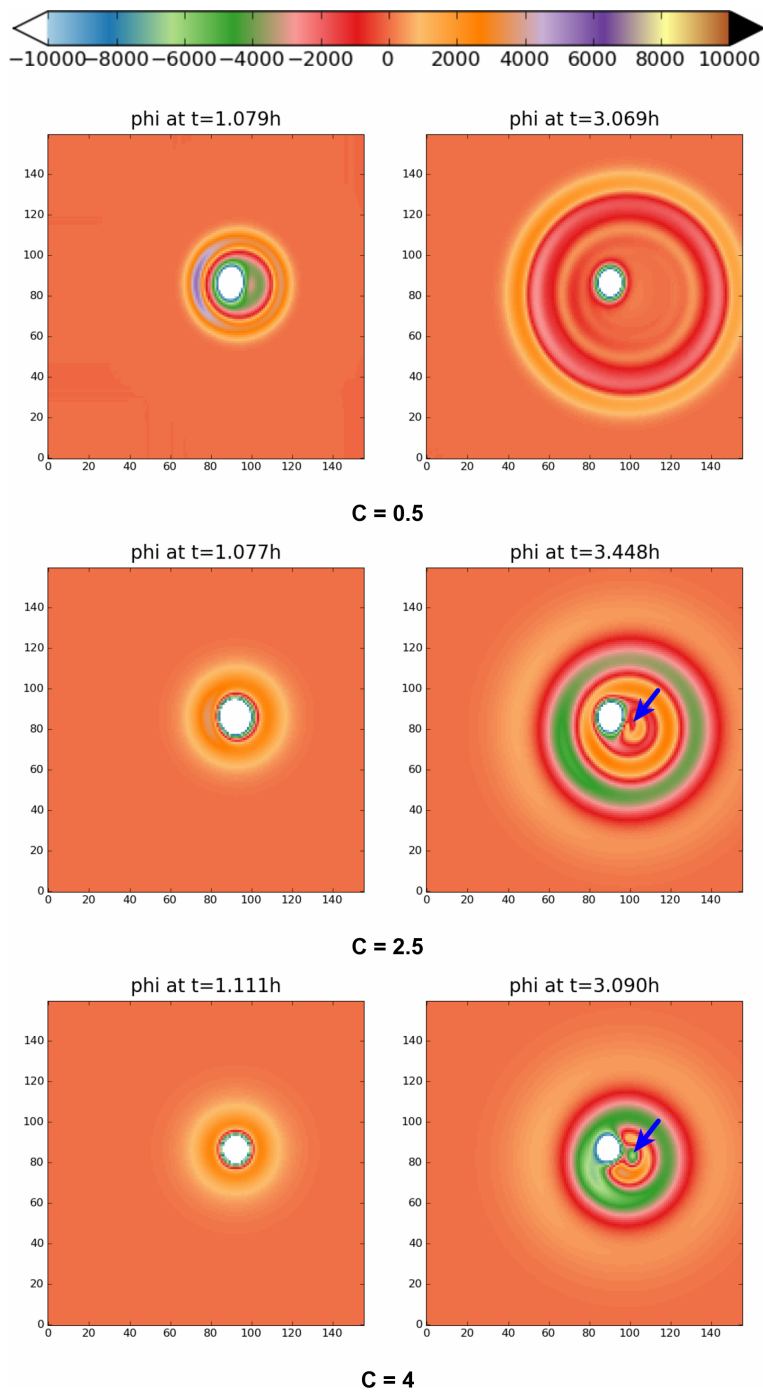


Figure 4.12: Height anomaly  $\varphi$  (in  $m^2/s^2$ ) at 1h and 3hrs for Courant numbers  $C \in \{0.5, 2.5, 4\}$ . No off-centring applied. Zoomed to  $\sim 2/3$  of computational domain.

$C$	.5	1	1.1	1.2	1.3
$\varphi_{\min}$	-32420	-35458	-35988	-34661	-35656
$\varphi_{\max}$	5595	4718	4763	4348	3978
$C$	1.4	1.5	1.7	2	2.1
$\varphi_{\min}$	-37925	-37346	-38059	-42147	-46902
$\varphi_{\max}$	4276	3954	3331	3433	3328
$C$	2.2	2.3	2.5	2.6	2.8
$\varphi_{\min}$	-172805	-634171	-702667	-879403	-868525
$\varphi_{\max}$	18301	8745	3625	23160	54374
$C$	3	3.5	4	4.5	
$\varphi_{\min}$	-872197	-1000432	-1096732	-1127177	
$\varphi_{\max}$	77232	62735	83298	163976	

Table 4.1: Extrema height anomalies for 7 day simulations at different Courant numbers

different amplitude or wave length. A striking feature, however, is the local minimum that appears to detach from the orography and appears to become the epicentre of the wave pattern. No equivalent can be seen in the reference simulation at any stage. This could be an indicator for resonant behaviour and would explain why much later the resonant simulations still show very distinct wave patterns and extremely overestimated amplitudes.

The resonance is also evident in the extrema of velocity and height. Table 4.1 shows the maxima and minima for the height in 7-day simulations at different Courant numbers. The velocities are omitted as they show very similar behaviour. While these extrema do not give any indication of how large a percentage of the computational domain is affected by these changes in amplitude between Courant numbers, they have proven to be a very good supportive tool for recognising the resonance. Note that the minimum and maximum do not necessarily occur at the same time in the simulation.

How the extrema of the heights correspond with resonant behaviour, becomes evident when plotting Table 4.1 as in Fig. 4.13. This figure shows the

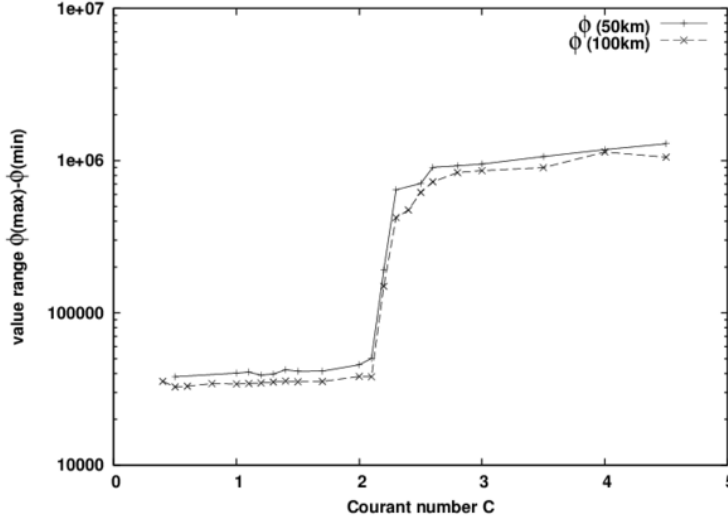


Figure 4.13: Difference between minimum and maximum of heights for different Courant numbers. Shown are height anomalies for  $\Delta x = \Delta y = 50 \text{ km}$  and  $\Delta x = \Delta y = 100 \text{ km}$  and an integration time of  $168h$ .

differences of maximum and minimum height for simulations at  $\Delta x = 100 \text{ km}$  and  $\Delta y = 100 \text{ km}$  as well as the default  $\Delta x = \Delta y = 50 \text{ km}$  at the same number of grid points. For either spatial resolution, it is impossible to identify resonant behaviour for Courant numbers  $C \lesssim 2$ . In fact, even in this plot with a logarithmic y-axis, a very steep growth is associated with the range of Courant numbers  $2.0 < C < 2.5$ , while the growth is moderate below and above these Courant numbers. This is very consistent with the very rapid growth of kinetic energy for  $C = 2.5$  observed before in Fig. 4.11. Just as the kinetic energy for short integration times, the value range grows only very mildly for all Courant numbers  $C \gtrsim 2.3$ .

The absence of any clearly resonant behaviour for  $C \lesssim 2.2$  and the steep rise in amplitude for  $C \approx 2.2$  is probably due to the setup chosen for the experiments where a number of parameters were always kept constant. Analogous to Fig. 1 in Rivest et al. (1994), Fig. 4.14 shows the resonances defined by

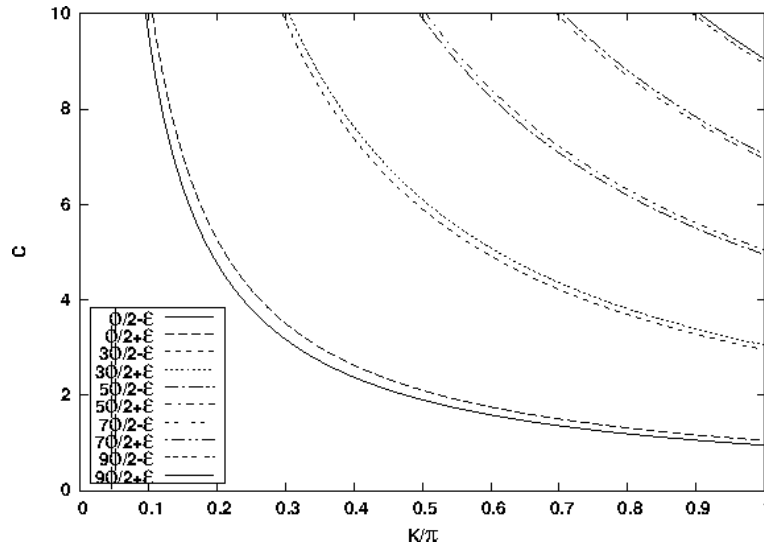


Figure 4.14: Resonances for 1D equations with  $u = 50\text{m/s}$ ,  $\Delta x = 50\text{km}$ ,  $f = 10^{-4}\text{s}^{-1}$ ,  $\bar{\varphi} = 5.5 \times 10^4\text{m}^2/\text{s}^2$  and  $\varepsilon = 0.05$  as follow from Eqn. (2.73).

Eqn. (2.73) as a function of the Courant number  $C$  and the non-dimensional wave number  $K$ . While the resonance can be triggered at  $C \approx 1$  this is only true for a very narrow range of  $K \approx [0.9\pi, \pi]$ . As, in the setup chosen here, the resonance only seems to be triggered at  $C \approx 2.2$ , the associated non-dimensional wave number would have to be  $K \approx 0.4\pi$ . This is equivalent to a wave length of  $\lambda \approx 5\Delta x$ . While it is hard to reliably identify this wave length from the plots presented, this is the order of magnitude of the observed wave length. Another fact that supports this hypothesis is that in Fig. 4.13, the setups of  $\Delta x = \Delta y = 50\text{ km}$  and  $\Delta x = \Delta y = 100\text{ km}$  yield almost identical results. As the resonance condition in Eqn. (2.72) is independent of  $\Delta x$ , this is exactly what one would expect.

### 4.2.3 The Spurious Resonance and Wave Interference

It could be argued that the bi-periodic setup is not optimal for studying the spurious numerical resonance. While global models, as were used by [Rivest et al. \(1994\)](#) or [Ritchie and Tanguay \(1996\)](#) to name just two, allow waves to travel throughout the whole domain and possibly interfere with themselves, this self-interference is certainly more likely and a dominant feature in the chosen setup using a bi-periodic domain.

However, the question that needs to be answered, is if the wave interference has any bearing on the development or dynamics of the spuriously resonant solution. The effect of the spurious numerical resonance observed in the studies here is very consistent with the description [Ritchie and Tanguay \(1996\)](#) give, i.e. short waves are amplified too much.

To show clearly that the interference does not affect the formation of the resonant solution which results from large Courant numbers, Fig. 4.15 shows a comparison of solutions obtained for different domain sizes and a Courant number  $C = 3$ . While for domain size  $256 \times 256$  (panel a) the wave has interfered several times at  $60h$  into the simulation, it has only interfered once for domain size  $1024 \times 1024$  (panel b) and not at all yet for domain size  $2048 \times 2408$  (panel c).

The effect of strongly amplified short waves which is caused by the spurious numerical resonance is clearly visible in all three simulations independent of domain size. While the wave interference clearly has an influence on the solution, this comparison proves that it is neither required nor does it affect the development of the spurious numerical resonance in any way.

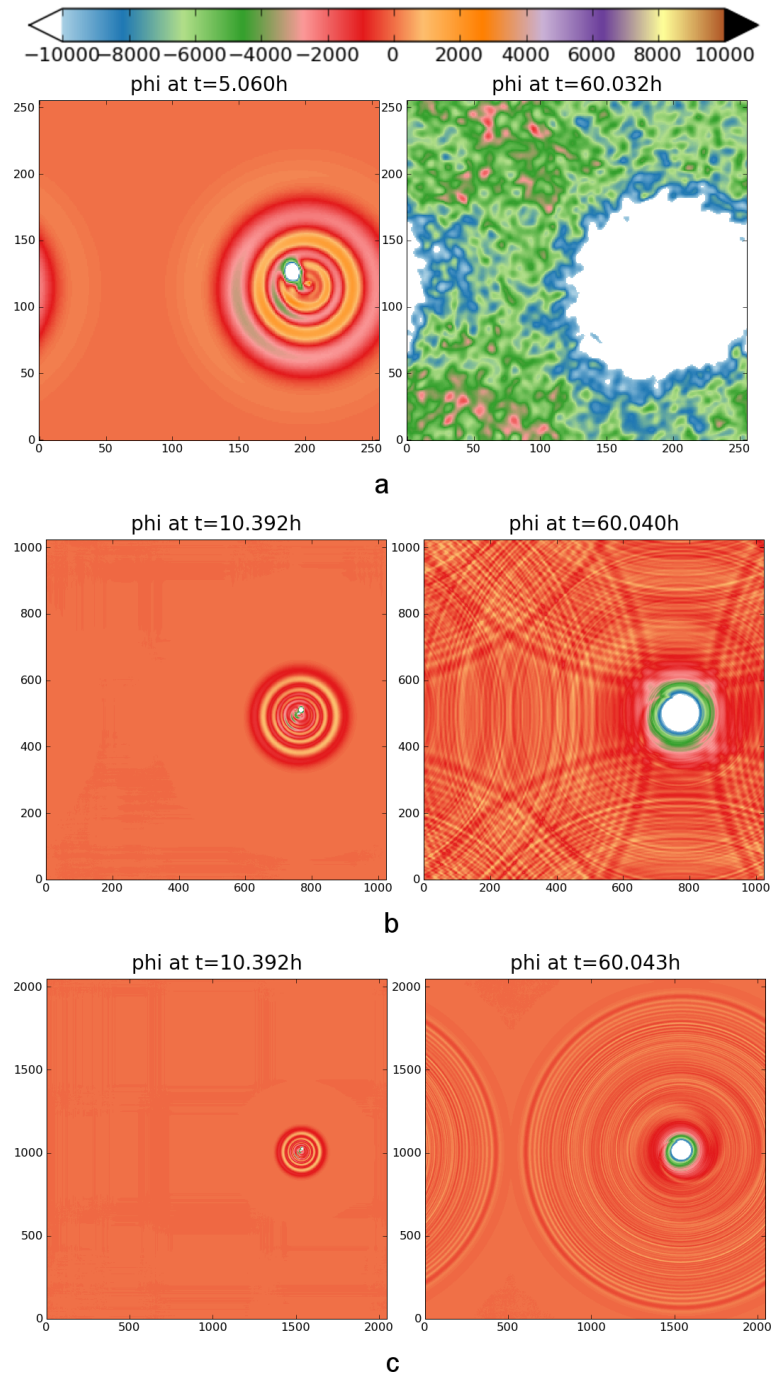


Figure 4.15: Height anomaly  $\varphi$  (in  $m^2/s^2$ ) for  $C = 3$  shown for domain sizes a)  $256 \times 256$  b)  $1024 \times 1024$  c)  $2048 \times 2048$  at grid spacing  $\Delta x = \Delta y = 50$  km.

### 4.3 Global Off-Centring

The previous sections showed that large Courant number simulations with SWiM were able to produce the numerical resonance that is the subject of this thesis. They established that the numerical resonance can affect the flow patterns strongly enough to lead to very different solutions over time. The focus of this section is on applying standard off-centring techniques to the equations to verify that an off-centred scheme can avoid the problem of the numerical resonance.

The first step in this testing process for the off-centring is naturally to use one constant off-centring parameter  $\alpha$  in all equations. This is the classical off-centring scheme as suggested and tested by Rivest et al. (1994). They show that this scheme is stable if the off-centring parameter is sufficiently large. All off-centring schemes described in the following are of first order (cf. Section 2.6 and Rivest et al., 1994).

After reproducing the classical off-centring scheme and showing that it is adequate, a new scheme is tested which reduces the introduced time truncation error and thus the resulting implicit numerical damping by combining centred momentum equations with an off-centred height equation as described in Section 2.8. Based on the stability analysis in Payne (2008) it is expected that this scheme does not fully remove the resonance. Instead, it will only reduce the rate at which amplitudes grow thus reducing the impact of the resonance on the flows. As a result, it cannot be determined generally if the resonance disturbs the flow pattern in a harmful manner. However, McGregor (personal comm.) has found it to be sufficiently stable in the C-CAM model.

The final section also tests a scheme which combines a centred height equation with off-centred momentum equations. Again, Payne’s findings suggest a similar outcome of solutions that are still mildly affected by the resonance.

### 4.3.1 Full Off-Centring Scheme (FOX)

The classical off-centring scheme described in Rivest et al. (1994) off-centres all equations with the same off-centring parameter  $\varepsilon = 2\alpha - 1$ . Using Eqns. (2.76) to (2.78), the off-centring parameters are set to be  $\alpha_1 = \alpha_2 = \alpha_3$  in all equations. To show the validity of this scheme, test its limits in the context of a shallow water model and use the obtained parameters for further experiments, a scheme using first order off-centring (cf. Rivest et al., 1994) and different values for  $\alpha$  was set up and run. To easily distinguish this scheme from later introduced ones, the scheme tested here which off-centres all equations equally, will be referred to as *FOX*<sup>1</sup>.

As, according to Rivest et al. (1994), for Courant numbers  $C \gtrsim 1$  sufficient stability should be achieved at  $\varepsilon = 0.4$  (or  $\alpha = 0.7$ ), the first experiment tests that off-centring parameter. For that purpose, the case of Courant number  $C = 1$  which yielded ambiguous results without off-centring is a good first candidate to assess the impact of off-centring and determine if the height anomalies show very different amplitudes in the off-centred case. As is evident from Fig. 4.16, the height anomalies with off-centring are within the same range as for the reference simulation. While the amplitudes might still be slightly overestimated in parts of the computational domain after 7 days (168h), they deviate very little overall from the ones seen in the reference simulation’s solutions. This indicates that not only the spurious resonance

---

<sup>1</sup>Full Off-Centring Scheme → FOCS → FOX

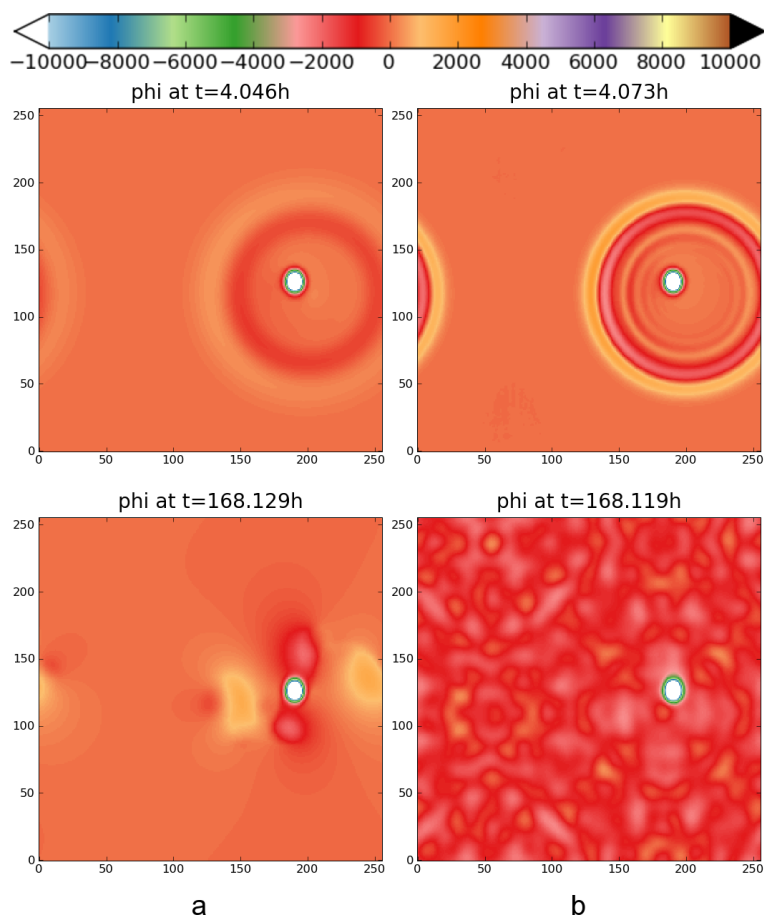


Figure 4.16: Height anomaly  $\varphi$  (in  $m^2/s^2$ ) for a)  $C = 1$  and  $\alpha_1 = \alpha_2 = \alpha_3 = 0.7$  and b) reference solution.

had an impact on the simulation with centred equations at Courant number  $C = 1$  but that the off-centring approach also mitigates the problem as expected.

Another effect that is obvious from Fig. 4.16 is that the solutions are strongly damped in comparison to the reference solutions. This damping is certainly not desirable and could possibly affect physical features like e.g. gravity waves as well. It is therefore useful to compare an off-centred version of the reference simulation to the off-centred simulation at larger Courant number.

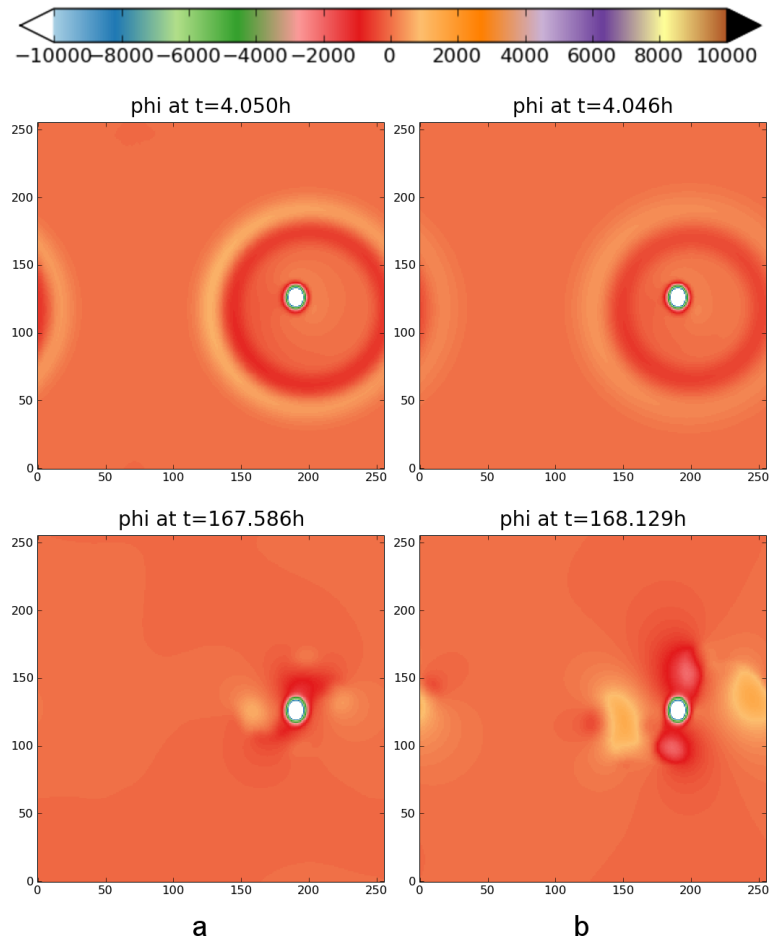


Figure 4.17: Height anomaly  $\varphi$  (in  $m^2/s^2$ ) for  $\alpha_1 = \alpha_2 = \alpha_3 = 0.7$  and a)  $C = 0.5$  b)  $C = 1$

That way it is possible to determine, how much of the damping effect originates from the larger Courant number and how much of it is caused by the off-centring.

As can be seen in Fig. 4.17, less damping can be observed in the case of the off-centred simulation at Courant number  $C = 0.5$ . However, the solution is already strongly damped in comparison with the reference simulation. It can thus be concluded that while some of the damping is a result of the larger Courant number, the off-centring accounts for most of it.

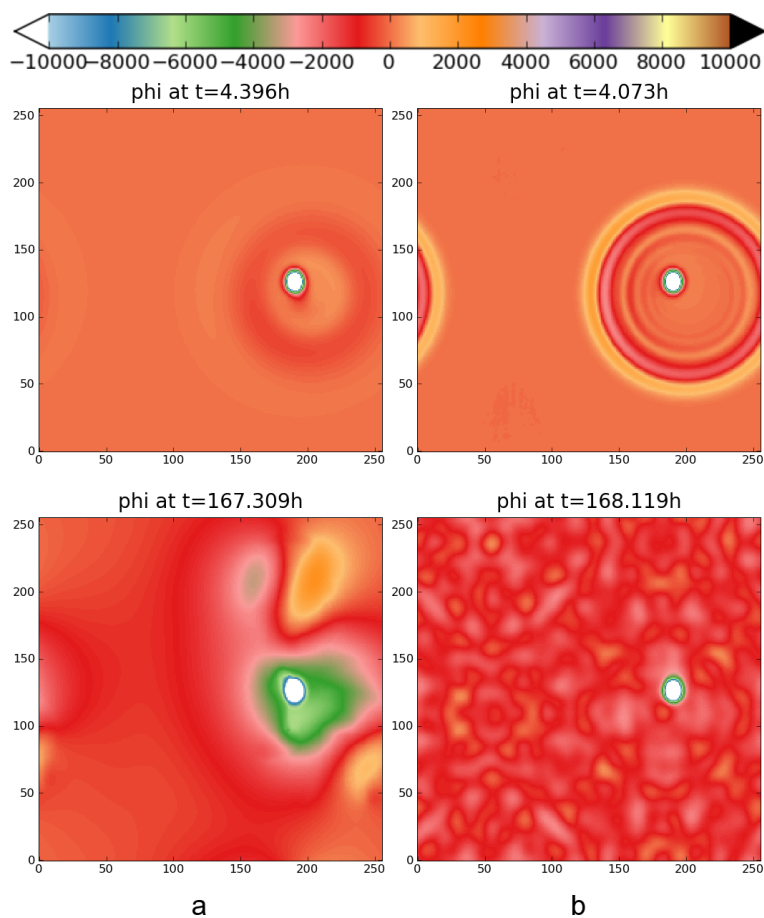


Figure 4.18: Height anomaly  $\varphi$  (in  $m^2/s^2$ ) for a)  $C = 3$  and  $\alpha_1 = \alpha_2 = \alpha_3 = 0.7$  b) reference solution.

To study the usefulness and limitations of off-centring, it is necessary to consider larger Courant numbers where the impact of the spurious resonance could be seen very clearly in the simulations without off-centring. Therefore, the results for a Courant number  $C = 3$  are shown in Fig. 4.18. In this setup, the primary wave is generally damped very strongly and therefore, over time, a situation emerges where hardly any dynamical structure is visible in the domain. While at  $4h$  some remnant of the wave pattern can still be seen, within  $24h$  the height anomaly is almost uniform across the domain and

close to the average of the height anomalies in the reference simulation.

After 7 days (168h), the situation has changed and a ring of strongly over-estimated height anomalies has formed around the orography. The height anomalies are about 3-4 times the height anomalies found in the reference simulation. Very close to the orography, the height anomalies have even grown to a value large enough to not be visualised on the used colour scale any more. This corresponds to a factor of about 5 or greater.

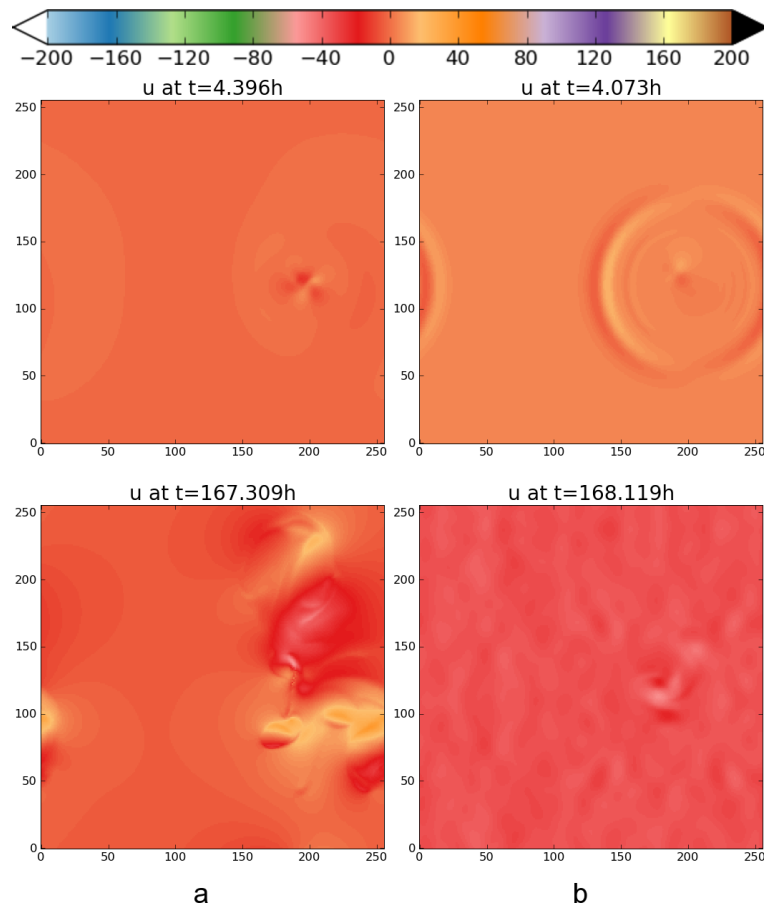


Figure 4.19: Velocity component  $u$  (in  $m/s$ ) for  $C = 3$  and a)  $\alpha_1 = \alpha_2 = \alpha_3 = 0.7$  b) reference run.

The velocity component  $u$  in Fig. 4.19 paints a similar picture but is not only

overestimated as was the case for the heights. Additionally, it shows much more turbulent features than can be observed in the reference simulation. The velocity component  $v$  is not shown here because it exhibits very similar features.

If the Courant number is raised further, the overestimation of the height anomaly as observed for  $C = 3$  gets even stronger. The heights are then similarly overestimated as in some of the earlier centred simulations at  $C > 1$ . The main difference between this off-centred simulation at  $C = 4$  and a centred simulation at  $C = 2$  is then that overall the height features are much smoother in the off-centred scheme.

Just as done earlier for the simulations without off-centring, it is again useful to compare the time evolution of the total kinetic energy per unit mass for the various FOX simulations. This time, the comparison does not involve different Courant numbers but instead it compares FOX simulations of different off-centring parameter at Courant number  $C = 3$ . Fig. 4.20 shows this comparison for the off-centring parameters  $\alpha_1 = \alpha_2 = \alpha_3 \in \{0.5, 0.6, 0.7, 0.8, 0.9\}$  for an integration time of 270 days. This comparison clearly shows that all off-centring parameters except  $\alpha = 0.6$  stabilise the scheme sufficiently keeping the kinetic energy bounded at a value similar to the one found for the reference simulation.

In the case of off-centring parameters  $\alpha < 0.7$ , the kinetic energy appears bounded at first but after about  $300 - 400h$  rises very suddenly to settle into a state very similar to the one found for a clearly resonant simulation.

The off-centring parameters  $\alpha \geq 0.7$  all show very similar long time scale behaviour. While the evolution of the total kinetic energy per unit mass

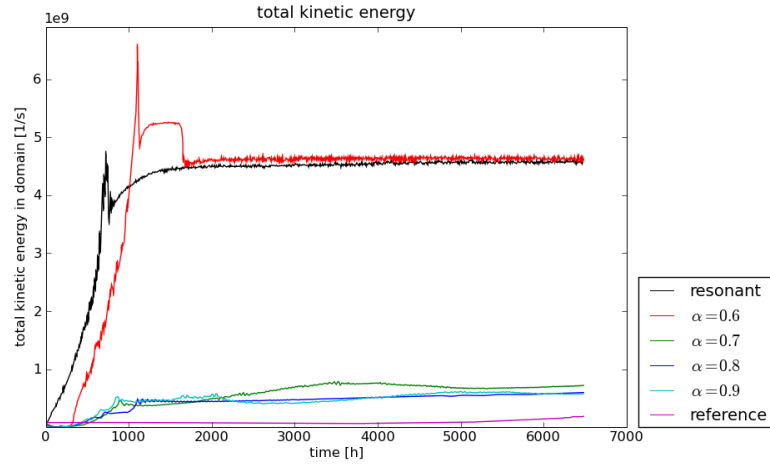


Figure 4.20: Time development of kinetic energy per unit mass in the domain for Courant number  $C = 3$  and fully off-centred simulations (FOX) at different  $\alpha_1 = \alpha_2 = \alpha_3$ .

saturates at a slightly higher value for  $\alpha = 0.7$ , the results for  $\alpha = 0.8$  and  $\alpha = 0.9$  only differ on short time scales but are virtually indistinguishable in the long time scale.

According to Fig. 4.20 raising the off-centring parameter to  $\alpha = 0.8$  might still benefit the quality of the solutions because the initial growth in kinetic energy is slower. In Figs. 4.21 the results of such a simulation with an off-centring parameter  $\alpha = 0.8$  at Courant number  $C = 3$  are shown. The early time evolution is very similar to the one seen before for  $\alpha = 0.7$ . As one would expect, the wave is damped even more. At 7 days ( $168h$ ), the geopotential heights are still overestimated by a factor of  $\sim 2$  close to the orography. But, except for the direct vicinity of the orography, the height profile is smooth and very close to the results of the reference simulation. Repeating the experiment with a Courant number  $C = 4$ , results in almost the same solution. Off-centring the equations with an off-centring parameter

of  $\alpha = 0.8$  thus resulted in sufficient stability for all Courant numbers used in the experiments.

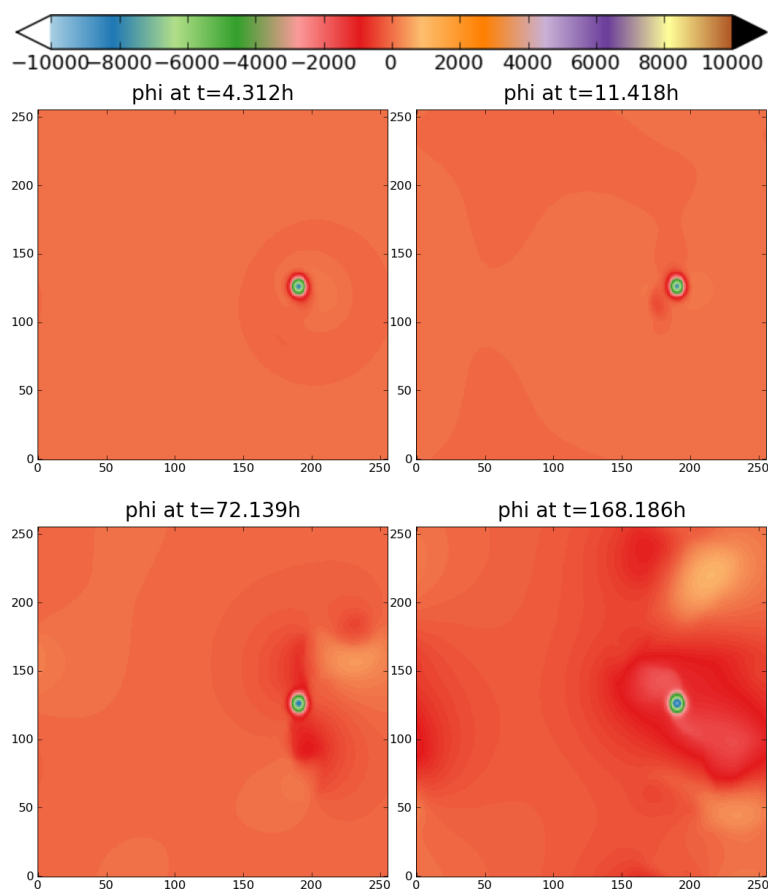


Figure 4.21: Height anomaly  $\varphi$  (in  $m^2/s^2$ ) for  $C = 3$  and  $\alpha_1 = \alpha_2 = \alpha_3 = 0.8$ .

Given the apparent improvement in short time scale stability that resulted from raising the off-centring parameter from  $\alpha = 0.7$  to  $\alpha = 0.8$ , it is a valid question to ask, what would happen if this was further increased to  $\alpha = 0.9$ . The results for the height anomaly field from such simulations in comparison with the simulations using  $\alpha = 0.8$  and a Courant number  $C = 4$  are shown in Fig. 4.22. After 7 days (168h), there is some visible difference. The heights are overestimated significantly less and the height

anomaly field is generally smoother for  $\alpha = 0.9$  than it is for  $\alpha = 0.8$ .

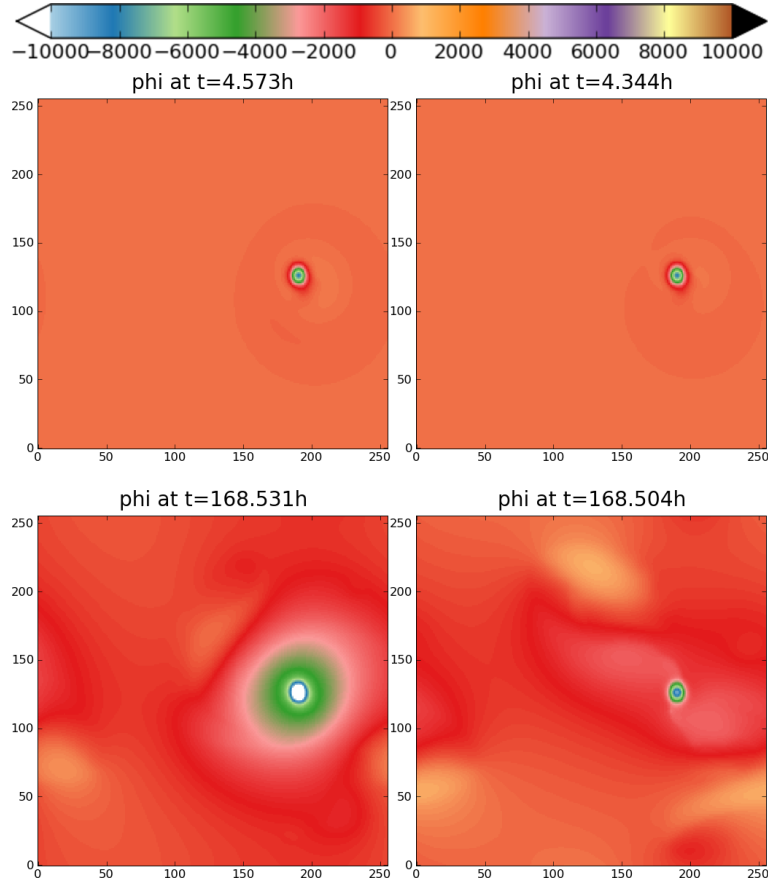


Figure 4.22: Height anomaly  $\varphi$  (in  $m^2/s^2$ ) for a)  $C = 4$  and a)  $\alpha_1 = \alpha_2 = \alpha_3 = 0.8$  b)  $\alpha_1 = \alpha_2 = \alpha_3 = 0.9$ .

In the light of the results detailed above,  $\alpha = 0.8$  is probably a sensible guess for a good off-centring scheme. While  $\alpha = 0.7$  might stabilise a simulation at Courant number  $C = 3$  sufficiently, there seems to be some risk that for larger Courant numbers the errors might be significantly larger. A scheme with  $\alpha = 0.9$  did show improvement over one with  $\alpha = 0.8$ , but the numerical damping is also very strong at this point. While  $\alpha = 0.7$  may not have shown enough stability, with overestimated heights in large parts of the domain,  $\alpha = 0.8$  confines the region where the heights are strongly overestimated

to the close vicinity of the orography. This off-centring parameter can then be considered sufficient, keeping the adverse effects of additional numerical damping to a minimum at the same time. In support of this decision, one can also plot the value range  $\varphi_{\max} - \varphi_{\min}$  again, as shown in Fig. 4.23, which also shows that the gain from the off-centring scheme saturates somewhere in the range  $0.7 < \alpha \leq 0.8$ . Fig. 4.23 is analogous to Fig. 4.13 but shows the value range as a function of the off-centring parameter  $\alpha$  instead of the Courant number  $C$ .

With an optimal off-centring parameter of  $\alpha = 0.8$ , the results here slightly deviate from those of Rivest et al.. They found that they could effectively remove the resonance by using  $\alpha = 0.7$ . This discrepancy is no reason for concern because it is rather small and has a subjective element to it. The subtle differences between computer models that are equivalent in principle can easily lead to such a difference. One example would be the interpolations that lead to some damping and could be of different order. Furthermore, judging solely by the time evolution of the kinetic energy, an off-centring parameter  $\alpha = 0.7$  would be sufficient in SWiM simulations as well.

All the results presented above lead to the conclusion that the resonance still influences the solution rather significantly even at large off-centring. While there is no more resonant behaviour and the solution is stable, the value of physical variables can still be overestimated close to where the resonance was triggered in the centred equations. However, with large off-centring the wave pattern is effectively smeared out to almost zero amplitude. As the resonance is manifested in a spurious wave pattern, this means that the numerical damping reduces the impact of the spurious resonance as desired but still at some significant cost to accuracy.

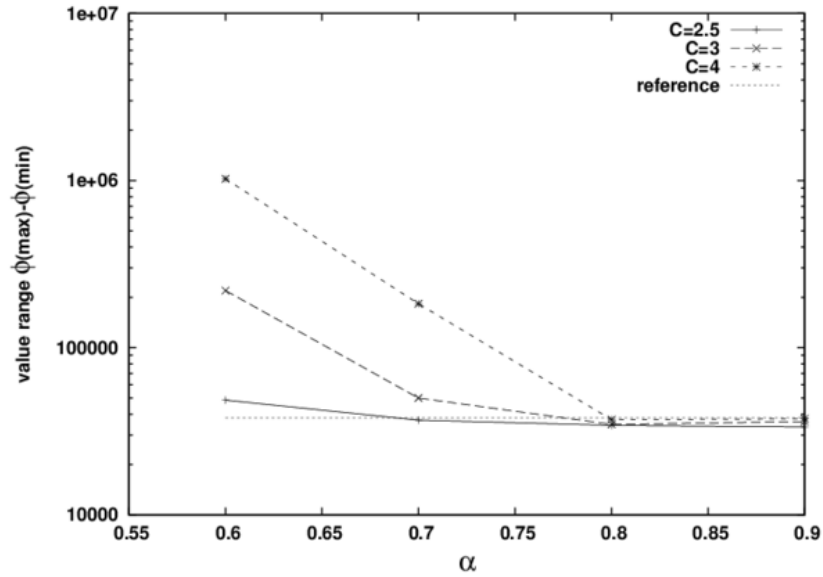


Figure 4.23: Difference between minimum and maximum of  $\varphi$  as a function of  $\alpha_1 = \alpha_2 = \alpha_3$  for a fully off-centred scheme.

#### 4.3.2 Off-Centring only the Height Equation (ROCKS)

As has been established in the previous section, off-centring does mitigate the impact of the resonance in the sense that it keeps the solution bounded. At the same time, it did also emerge that this comes at a cost to accuracy and the solution does significantly differ from the reference solution in some regions. This is not surprising because off-centring achieves stability by means of additional numerical damping. It can hence not be expected that the solution is still as accurate as it would have been in a centred scheme that does not become resonant due to small Courant numbers.

Currently, there is no ideal solution that would allow one to combine the stability of an off-centred scheme with the accuracy of a centred scheme of small Courant number while maintaining the benefit of large time steps. It has also become clear from earlier considerations that a reasonably large

off-centring parameter is required for stability purposes. Hence, it would be desirable to at least minimize the effect of off-centering. One obvious approach to doing so is to apply the off-centering to only a subset of the equations as described in Section 2.8. The following investigates such a scheme in practical application.

One possible approach, as detailed in Section 2.8, is to apply off-centring only to the height equation while the momentum equations are solved in their centred form. To express this mathematically, the off-centred shallow water equations

$$\begin{aligned} u^+ &= \Delta t (-\alpha_1(\varphi_x^+ + \varphi_{s,x}^+) - \beta_1(\varphi_x^0 + \varphi_{s,x}^0) + (\alpha_2(fv)^+ + \beta_2(fv)^0)) \\ &\quad + u^0 \end{aligned} \quad (4.3)$$

$$\begin{aligned} v^+ &= \Delta t (-\alpha_1(\varphi_y^+ + \varphi_{s,y}^+) - \beta_1(\varphi_y^0 + \varphi_{s,y}^0) - (\alpha_2(fu)^+ + \beta_2(fu)^0)) \\ &\quad + v^0 \end{aligned} \quad (4.4)$$

$$\varphi^+ = -\Delta t (\bar{\varphi}\alpha_3(u_x + v_y)^+ + \beta(u_x + v_y)^0) + \varphi^0 \quad (4.5)$$

are solved with the condition  $\alpha_1 = \alpha_2 = 1/2$  and  $\alpha_3 > 1/2$ .

In Section 2.8 it was already discussed that this approach should not yield a perfectly stable solution (Payne, 2008). The analytical considerations found in the same section could neither prove nor disprove this claim. As, even according to Payne, the spurious growth in the solution should be weak, it appears prudent to try this scheme in the shallow water experiments carried out here. The following describes the results of experiments where only the height equation has been off-centred but the momentum equations

remain centred. Again, in the interest of clarity the scheme is referred to as *ROCKS*<sup>2</sup>.

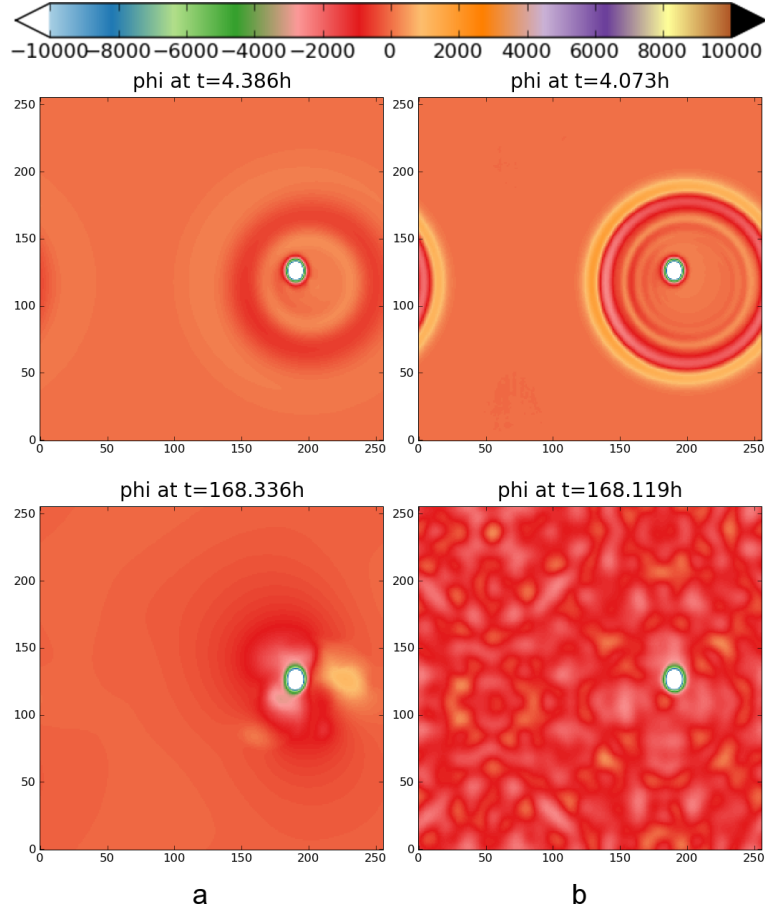


Figure 4.24: Height anomaly  $\varphi$  (in  $m^2/s^2$ ) for a)  $C = 2.5$  and  $\alpha_1 = \alpha_2 = 0.5$  and  $\alpha_3 = 0.8$  b) reference simulation.

Figs. 4.24 and 4.25 show comparisons of height anomaly fields for simulations with ROCKS and Courant numbers  $C \in \{2.5, 4\}$  with the reference solution. It is evident that for both Courant numbers, the wave that is excited by the orographic forcing early in the simulation is more distinct than in the FOX simulations. This can be understood as a result of the reduced damping in the momentum equations. Early on, the solution shows very similar

<sup>2</sup>Reduced Off-Centring Scheme  $\rightarrow$  ROCS  $\rightarrow$  ROCKS

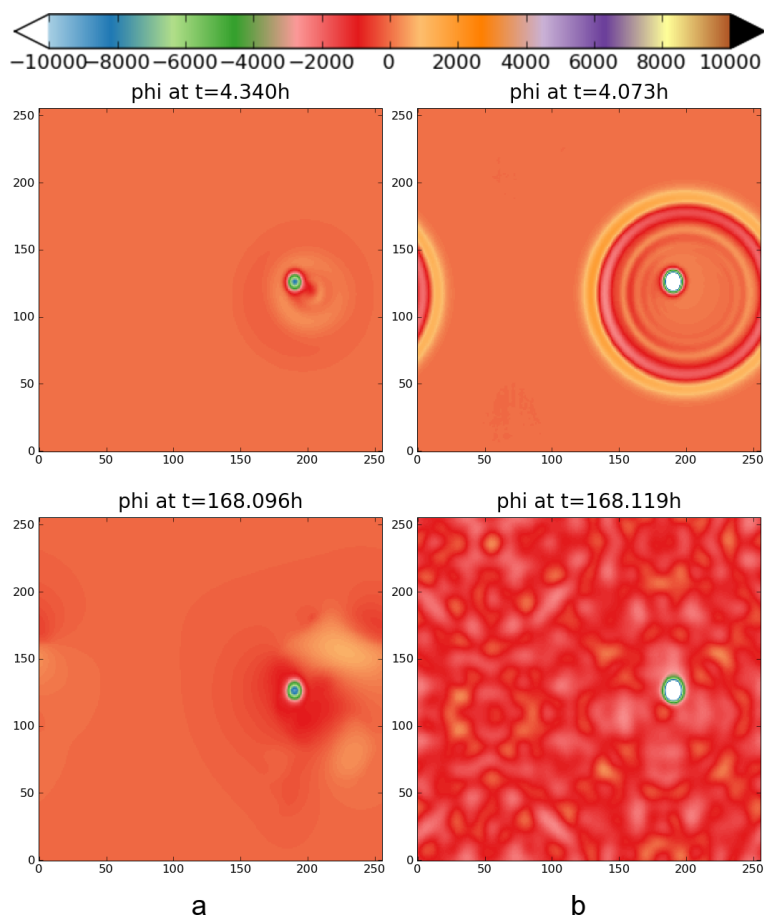


Figure 4.25: Height anomaly  $\varphi$  (in  $m^2/s^2$ ) for a)  $C = 4$  and  $\alpha_1 = \alpha_2 = 0.5$  and  $\alpha_3 = 0.8$  b) reference simulation.

features to the resonant simulations with a local height minimum forming close to the orography. The minimum is more distinct for a larger Courant number. Yet, this kind of resemblance with the resonant simulations does not exist any more in the long time scale evolution of the solution. While the resonant simulations show large height variations and sustained waves, the height anomalies already appear very smooth even at large Courant numbers for the solutions obtained with ROCKS presented here. After 7 days, the amplitudes are mildly overestimated just as was the case for the

fully off-centred solution.

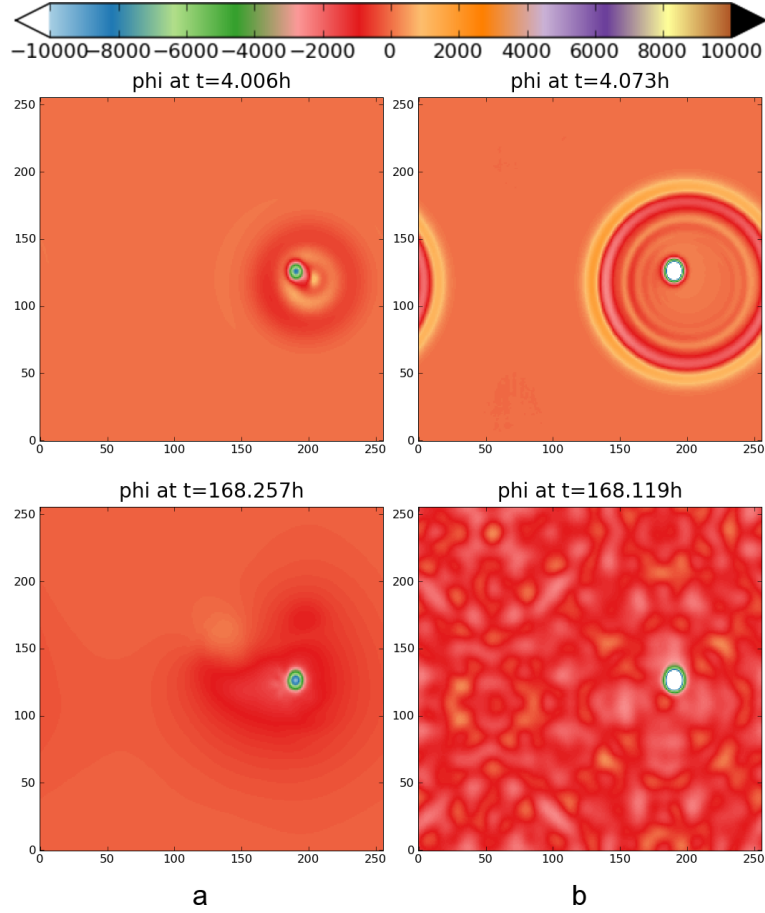


Figure 4.26: Height anomaly  $\varphi$  (in  $m^2/s^2$ ) for a)  $C = 4$  and  $\alpha_1 = \alpha_2 = 0.5$  and  $\alpha_3 = 0.6$  b) reference simulation.

With even a Courant number  $C = 4$  appearing to pose no challenge to ROCKS, it seems sensible to lower the off-centring parameter gradually. This can be done even to the point where it is  $\alpha_3 = 0.6$ , as is shown in Fig. 4.26. Even in this extreme case, the height anomalies stay smooth and are only mildly overestimated by a factor of  $\sim 3-4$  and only in the proximity of the orography.

Comparing the schemes of different off-centring parameter in terms of the

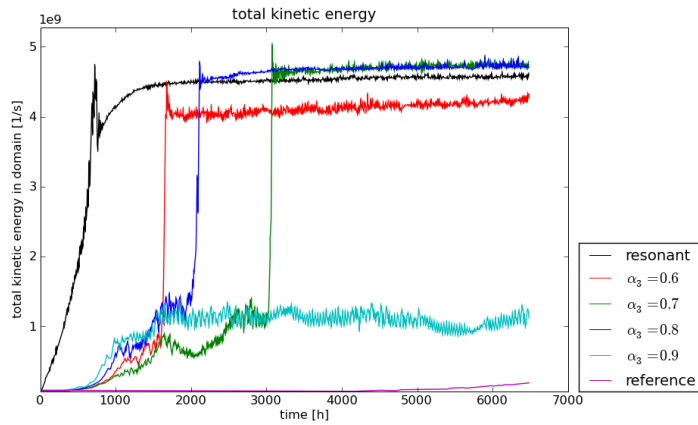


Figure 4.27: Long time scale development of kinetic energy per unit mass in the domain for Courant number  $C = 3$  and height off-centred simulations (ROCKS) at different  $\alpha_3$ .

evolution of the kinetic energy per unit mass, as shown in Fig. 4.27, reveals that the long time scale development is now very different from that seen in the case of the FOX scheme. Only a very large off-centring parameter of  $\alpha = 0.9$  seems to stabilise over time while simulations of lower off-centring parameters all seem to exhibit the resonance after a certain amount of integration time.

One interesting detail which can be observed in Fig. 4.27 is the fact that the short time scale performance expressed in kinetic energy is better, the lower the value of the off-centring parameter. Furthermore, the short time scale development of kinetic energy<sup>3</sup> for all off-centred simulations overlaps in a manner that it is even impossible to distinguish the curves in Fig. 4.28. This indicates that the ROCKS simulations behave very well on short time scale, this scheme certainly deserves a more extensive study.

<sup>3</sup>Note that the short time scale figures use a different axis scaling for the energy than the longer time scales as indicated by the factors above the  $y$ -axes.

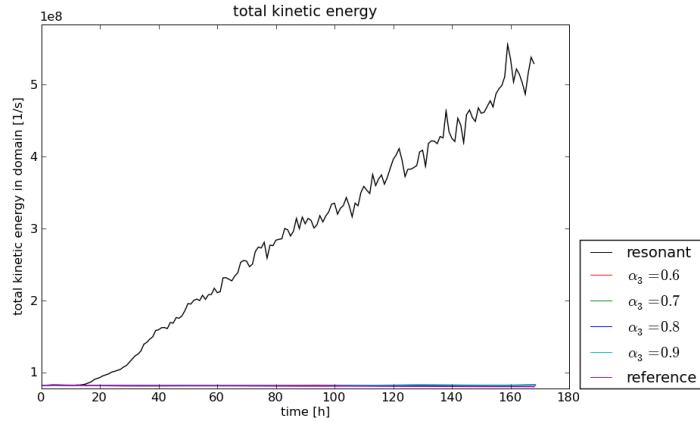


Figure 4.28: Short time scale development of kinetic energy per unit mass in the domain for Courant number  $C = 3$  and ROCKS simulations using different  $\alpha_3$ .

It comes as a surprise that only very little difference can be observed in short time scale simulation when varying the off-centring parameter in ROCKS. The kinetic energy per unit mass does not grow significantly even for an off-centring parameter as small as  $\alpha_3 = 0.6$  and the solution for the height anomaly field is reasonable even for off-centring parameter  $\alpha_3 = 0.6$  and Courant number  $C = 4$ . When comparing ROCKS simulations at Courant number  $C = 4$  and  $\alpha_3 \in \{0.6, 0.8\}$ , the solutions show only a small difference in amplitude near the orography in Fig. 4.29.

There is also a rather unexpected difference between the results obtained from the two different off-centring schemes FOX and ROCKS. Despite the ROCKS scheme introducing less implicit numerical damping, it yields smoother solutions after 7 days than FOX does. To explain this paradox, a comparison of short time scale development of the kinetic energy as shown for ROCKS in Fig. 4.28 to an equivalent representation of the short time scale development for FOX is very insightful. As is evident from Fig. 4.31,

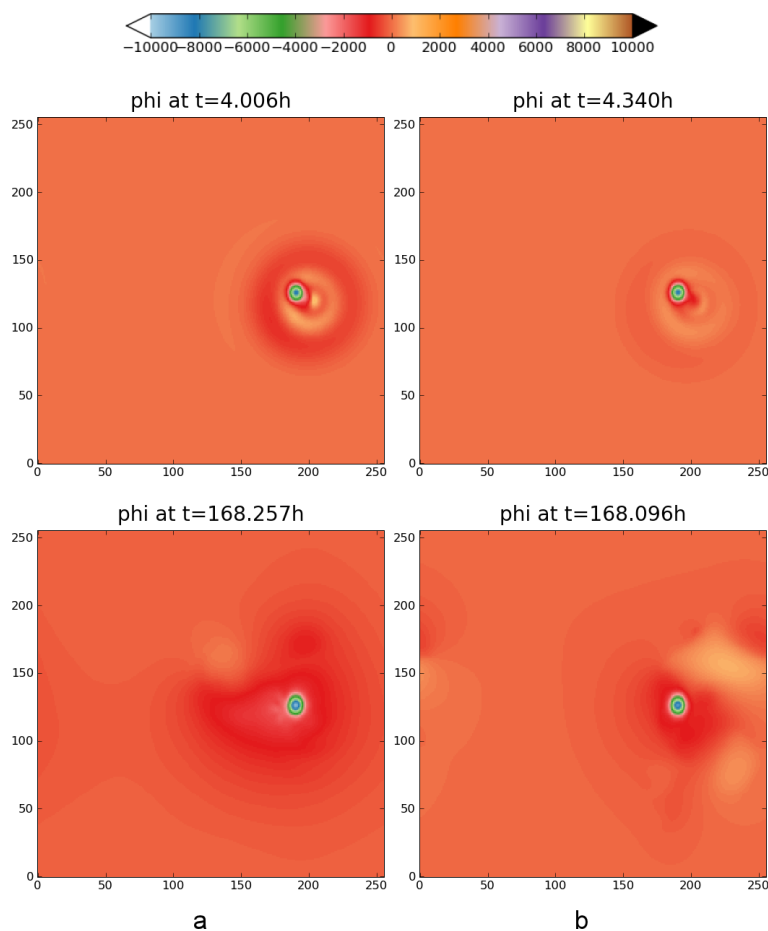


Figure 4.29: Height anomaly  $\varphi$  (in  $m^2/s^2$ ) for  $C = 4$  and  $\alpha_1 = \alpha_2 = 0.5$  and a)  $\alpha_3 = 0.6$  b)  $\alpha_3 = 0.8$ .

the kinetic energy with FOX is much less stable on short time scales than it is with ROCKS. While on the longer time scales, FOX may stabilise where ROCKS becomes resonant, short time scale ROCKS simulations exhibit a kinetic energy evolution very much like that of the reference simulation whereas the kinetic energy drops at first in FOX simulations. This certainly explains why ROCKS manages to keep the solutions smoother over the course of 7 days than FOX does. As a result, ROCKS is the better choice as long as the long time scale stability concerns can be addressed somehow

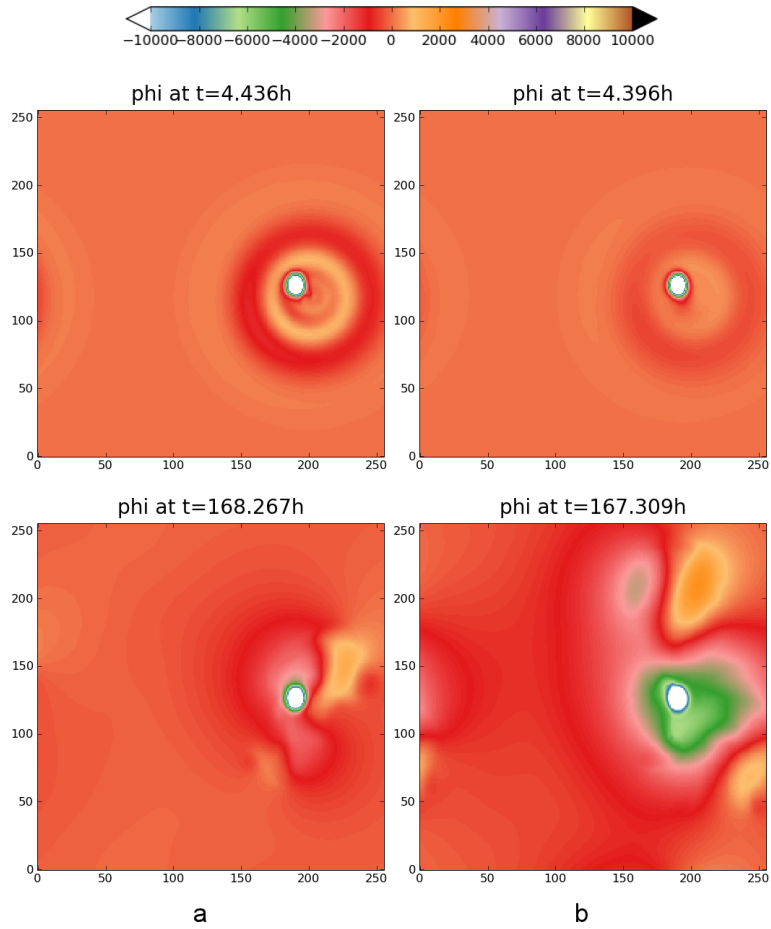


Figure 4.30: Height anomaly  $\varphi$  (in  $m^2/s^2$ ) for  $C = 3$  and a)  $\alpha_1 = \alpha_2 = 0.5$  and  $\alpha_3 = 0.7$  and b)  $\alpha_1 = \alpha_2 = \alpha_3 = 0.7$ .

in more complex a model.

As Payne (2008) predicts, the ROCKS simulations do not appear to be stable on long time scales. The effect which Payne calls “weak polynomial-in-time growth” might affect the reduced scheme and allow instability to develop if the integration time is long enough or some other nonlinear effect might lead to instability. As this thesis is only concerned with the general feasibility of such a scheme, to determine the exact cause of the observed

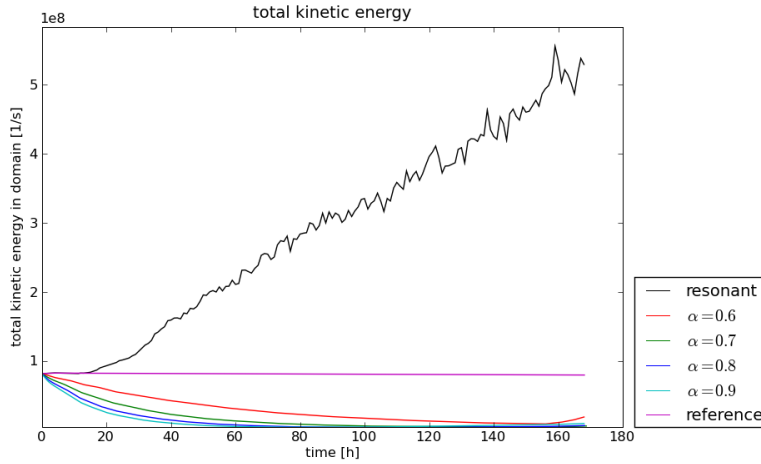


Figure 4.31: Short time scale development of kinetic energy per unit mass in the domain for Courant number  $C = 3$  and FOX simulations at different  $\alpha_1 = \alpha_2 = \alpha_3$ .

growth is beyond its scope. There was also no attempt made to mitigate this long term effect, e.g. by means of artificial horizontal diffusion.

Despite the instability observed in long time scale simulations, it can be established that there is obvious gain in employing a reduced scheme when looking at the short time scale development. Not only is there increased accuracy which results in some features resolving much better, but there is also reason to consider the solutions stable on short time scales and more accurate than when using a full off-centring scheme.

### 4.3.3 Off-Centring only the Momentum Equations

As off-centring only the height equation resulted in a scheme that was reasonably stable on the short time scales, one could also try off-centring only the momentum equations. The solutions for the heights obtained from such an approach for Courant number  $C = 3$  are shown in Fig. 4.32. While the

height equation is solved in its centred form (i.e.  $\alpha_3 = 0.5$ ), the momentum equations are now off-centred using  $\alpha_1 = \alpha_2 = 0.8$ .

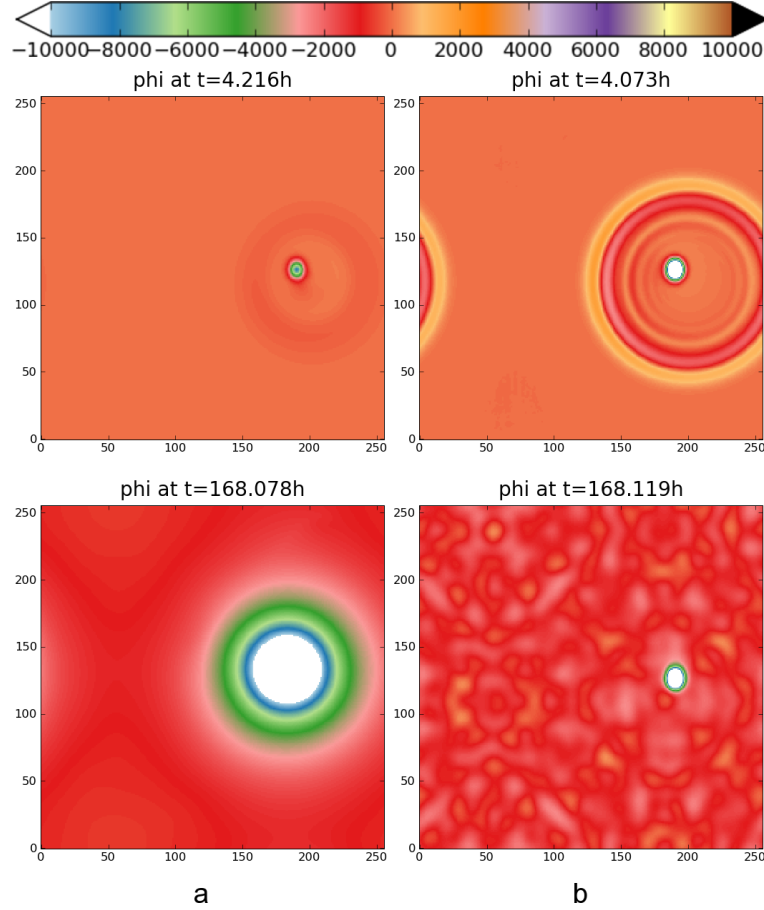


Figure 4.32: Height anomaly  $\varphi$  (in  $m^2/s^2$ ) for  $C = 3$  and a)  $\alpha_1 = \alpha_2 = 0.8$  and  $\alpha_3 = 0.5$  b) reference solution ( $\alpha_1 = \alpha_2 = \alpha_3 = 0.5$ ).

The comparison with the reference simulation leaves no doubt that there is very little gain in off-centring only the momentum equations. The amplitude growth is slowed down and the wave pattern is smoothed out almost completely. After 7 days, the amplitudes are still smaller for the off-centred case than they were for a centred scheme and similar Courant numbers but overestimated by a significant margin compared to the reference simulation

for a reasonably large part of the domain. While the additional damping can still be seen in the smoother features at this point, the off-centring of only the momentum equations has clearly failed to stabilise the solution sufficiently.

A look at the kinetic energy per unit mass in Fig. 4.33 does not confirm the finding from the comparison of height amplitudes. While small off-centring parameters of  $\alpha \leq 0.7$  settle into a resonant state, the kinetic energy development for off-centring parameters  $\alpha \geq 0.8$  makes these schemes appear stable.

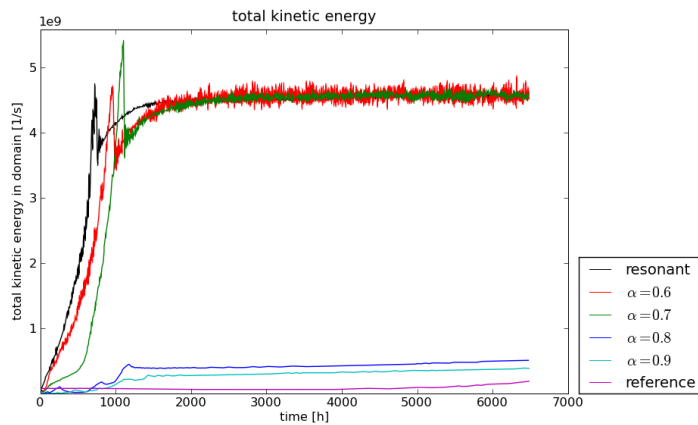


Figure 4.33: Time development of kinetic energy in the domain for Courant number  $C = 3$  and momentum off-centred simulations at different  $\alpha_3$ .

In the light of the findings above, it can still be concluded that off-centring only the momentum equations is not a viable option. While the kinetic energy seems to evolve well for large off-centring parameters, the height anomalies are clearly and significantly overestimated even for these large off-centring parameters. The solutions might thus be acceptable overall but the accuracy obtained in the vicinity of orography is clearly not satisfactory and this scheme can be ruled out.

Judging ROCKS only on the basis of the simple, purely dynamical model used in the experiments, it seems risky to advocate its use. However, at this point it might be of importance that not only does it exhibit stability on short time scales but it even yields better results in this time frame. Taking into account that a full-fledged GCM has many more factors contributing to its solutions than is the case for SWiM, there is clearly merit in further investigating this option in that context. Despite its instability in a purely dynamical model, the inclusion of further atmospheric parameters in a GCM may counter this instability to delay the rise of the resonance sufficiently long for the model to be stable in practical application.



## Chapter 5

# Variable Off-Centring in SWiM

Chapter 4 applied several approaches to off-centring to the shallow water model SWiM. It also explored the idea of reducing the off-centring in comparison with the classical scheme by applying it only to a subset of the full set of equations. Yet, it did not address the issue that off-centring in all operational methods used to date is applied as a global solution to a local problem and comes at a significant cost. While off-centring has been a reliable workaround for more than 15 years now, it may be unnecessarily expensive. A spurious resonance in the equations at certain locations (near orography) is removed by introducing numerical damping, but this affects the accuracy of the model. That might well mean that particularly physical processes in weather forecasts and climate prediction are adversely affected.

As the numerical resonance is a local problem, off-centring is only really needed where the orographic forcing is strong enough to introduce the spuriously resonant solution. Some distance from significant orography, the

orographic forcing is negligible and therefore the solution behaves like the solution of the free equations. This, at least in principle, makes off-centring unnecessary in regions of the computational domain that are far away from significant orography, such as the vast ocean areas of the Earth.

The goal of this thesis is to develop algorithms that are able to restrict off-centring to the regions where it is needed and generally maintain it at the lowest value possible and to evaluate the consequences of such an approach in a full GCM. Before doing so, variable off-centring approaches will be developed and tested in the simplified SWiM framework. As there is a myriad of algorithmic variants that could be developed to achieve the overall goal of reducing the influence of off-centring on the model solutions, it requires some principles to find the best way of expressing the off-centring parameter as a function of orography. Here, first and foremost, it is the simplicity principle that is applied and the algorithms developed and tested in the following are kept as simple as possible. In practice that means that they move from the simplest approach towards slightly more complexity according to the requirements of the problem as they emerge from the experiments.

## 5.1 Designing a Variable Off-Centring Scheme

The simplest approach to a variable off-centring scheme is to consider the difference in orographic height between the grid point and its immediate neighbours, apply large off-centring where this difference is large and apply a linear function to decrease the off-centring parameter as one moves away from orography. The resulting algorithm could then be described as follows.

1. Sweep over all grid points, calculating the orographic height differences to find the maximum difference  $\Delta\varphi_{\max}$  between any pair of adjacent grid points in the domain.
2. For each grid point
  - find set  $D$  of orographic height differences with four nearest neighbours.
  - find maximum  $\Delta\varphi_{\text{local}}$  of the four differences in  $D$ .
  - find scaling factor  $F = \Delta\varphi_{\text{local}}/\Delta\varphi_{\max}$
  - multiply the base off-centring parameter  $\alpha_{\text{base}}$  (set as input parameter) by the factor  $F$  found in the previous step.

This algorithmic approach leads to off-centring only being applied where the orographic height differences between neighbouring grid points do not vanish. Even just two grid points away from orography, the off-centring parameter could theoretically already vanish. As in this approach the off-centring parameter only depends on the orography, this method has the advantage that the field of off-centring parameters only needs to be calculated once for each model resolution and can be kept as an external set of parameters.

As shown in Section 2.4, the numerical resonance condition can only be met for Courant numbers  $C \gtrsim 1$ . The algorithm described above can only ever consider orography along a trajectory which spans at most two neighbouring grid points. Trajectories for velocities that result in  $C > 1$ , however, span across more than just neighbouring grid points. Hence, there is a possibility that grid points that are further away from significant orographic height differences still contribute to the resonance. This is a consequence of the sphere

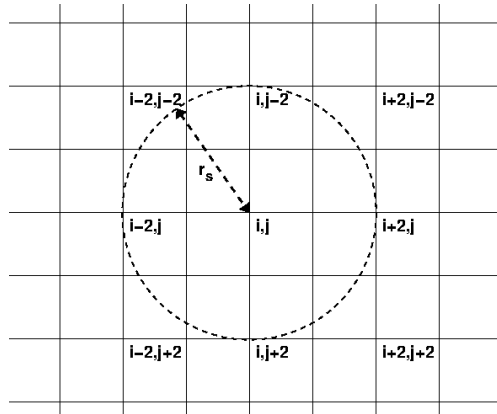


Figure 5.1: Finding neighbours  $D$  in variable off-centring scheme with search radius  $r_s = 2$ .

of influence of the difference equation which, when solved at a Courant number  $C > 1$ , is larger than one grid spacing (Courant et al., 1928). As the trajectory spans across several grid points, the whole space covered by the trajectory contributes to the solution of the differential equation. Following the line of reasoning in Courant et al. (1928), the sphere of influence of the difference equation should generally match that of the differential equation as closely as possible. As a consequence, all points that lie on the assumed trajectory should be seen as possibly contributing to the solution.

Following the considerations on trajectories, the algorithm above can then be modified to read as follows.

1. Sweep over all grid points, calculating the orographic height differences to find the maximum difference  $\Delta\varphi_{\max}$  between any pair of adjacent grid points in the domain.
2. For each grid point

- find set  $N$  of all neighbours that lie within a radius  $r_s$  and compile set  $D$  of orographic height differences between each point in  $N$  and its four nearest neighbours (cf. Fig. 5.1).
- find maximum  $\Delta\varphi_{\text{local}}$  of all differences in  $D$ .
- find scaling factor  $F = \Delta\varphi_{\text{local}}/\Delta\varphi_{\text{max}}$
- multiply the base off-centring parameter  $\alpha_{\text{base}}$  (set as input parameter) by the factor  $F$  found in the previous step.

The parameter  $r_s$  is referred to as the *search radius* from here on. The requirement for this parameter is that it be large enough to cover the local trajectories. As it is a function of trajectories, it is naturally a function of time and space. For every time step, the search radius could be calculated for every grid point based on the trajectories obtained from the semi-Lagrangian scheme. However, this would be computationally expensive and could also result in problems with continuity in the off-centring parameter field if the velocity gradients are large and search radii of adjacent grid points are very different. To avoid these potential problems, the field of off-centring parameters can instead be calculated off-line before the start of the simulation and the search radius assumed constant across the computational domain. As the grid spacing and the orography are static, the only remaining unknown quantity are the velocities. These need to be estimated in a manner that ensures that all trajectories occurring over the course of the simulation lie within the search radius around the grid points.

The required estimate of the search radius is the weak point of the algorithm developed above. In any context where the maximum Courant number is not constant in time, it is not easy to predict maximum velocities and derive

the value of the search radius  $r_s$  at the start of the simulation. One could just pick a rather large radius, but this would diminish the gain from the variable off-centring scheme because it would result in relatively large off-centring parameters in a big part of the domain. If, on the other hand, the radius is too small, the sphere of influence may not be covered adequately and the resonance not removed from the solution.

In SWiM, a justifiable value for the radius is

$$r_s(i, j) = C \times \max(\Delta x, \Delta y) \quad (5.1)$$

where  $C$  is the preset (or maximum expected) Courant number and  $\Delta x$  and  $\Delta y$  are the grid spacings in  $x$  and  $y$ .

In all experiments performed with SWiM and presented here, the grid spacings are the same in either dimension of the computational domain, i.e.  $\Delta x = \Delta y$  and a search radius  $r_s = (a + 1)\Delta x = (a + 1)\Delta y$  where  $a$  is a constant. In the following, the  $\Delta x$  and  $\Delta y$  are omitted and the search radii written without dimensions. This means that an increment by 1 and grid spacings as units for the search radius are implied.

Given the uncertainty in choosing an optimal  $r_s$ , it is also worthwhile experimenting with different search radii and comparing the outcomes with the goal of determining a best guess empirically. Hence, the following presents simulations of search radii  $0 \leq r_s \leq 16$  where  $r_s = 0$  means only local gradients are considered and  $r_s = 16$  is roughly equivalent to  $r_s \approx 4C$  for the largest Courant numbers used in the experiments.

The following sections follow the same pattern as the previous chapter did. They first present simulations where all equations are off-centred and then ones where only the height equation is off-centred. As only off-centring the momentum equations was ruled out earlier, this case is omitted. The approaches that are presented are individually tested with different search radii and Courant numbers similar to the experiments in the previous chapter.

## 5.2 Off-Centring All Equations (vFOX)

As classical off-centring applies to all equations equally, it comes naturally to first apply the proposed variable off-centring scheme to all equations as well. For this purpose, the above algorithm is combined with off-centring in all equations (FOX). As the best off-centring parameter found for FOX in Section 4.3.1 was  $\alpha = 0.8$ , all the simulations presented here use that value as their base value. The scaling of the off-centring parameter by the variable off-centring scheme is applied to all off-centring parameters in any of the equations solved. As a result, the point where the largest difference in orographic height is found is off-centred using  $\alpha = 0.8$ . The off-centring then decays to  $\alpha = 0.5$  (i.e.  $\varepsilon = 0$ ) far enough from the orography in the computational domain where the orographic height differences between neighbouring grid points vanish. Following the same naming scheme as in Chapter 4, this scheme is referred to as *vFOX*.

The experiments performed are comprised of simulations with search radii  $0 \leq r_s \leq 16$  and use the same kind of orography profile as in Chapter 4 (cf. Eqn. 4.1). Fig. 5.2 shows the off-centring profile for  $\varepsilon = 2(\alpha - 1/2)$  based on a maximum off-centring of  $\alpha = 0.8$  for the minimum ( $r_s = 0$ )

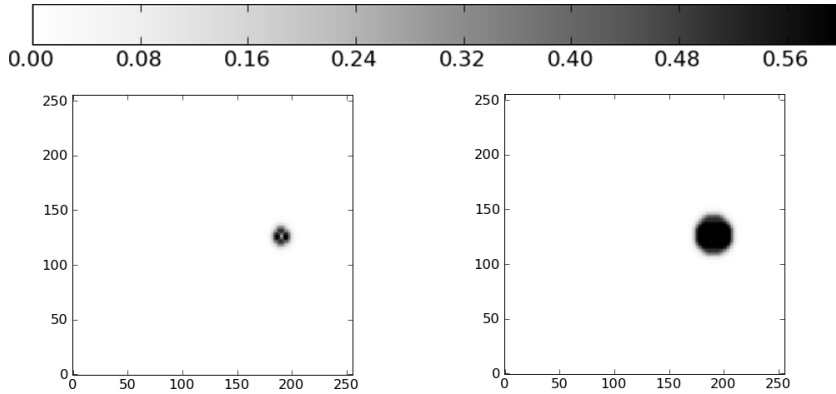


Figure 5.2:  $\varepsilon$  profile for base value  $\alpha = 2(\varepsilon - 0.5) = 0.8$  and search radius a)  $r_s = 0$  b)  $r_s = 16$ .

and maximum ( $r_s = 16$ ) search radii used in this study. A search radius of  $r_s = 0$  is synonymous with using only the orographic height differences between the grid point and its 4 nearest neighbours as the basis of the local off-centring parameter. As  $\alpha_1 = \alpha_2 = \alpha_3$  this profile is identical for all three off-centring parameters.

Applying the variable off-centring scheme with the two search radii proposed above and repeating the same simulations as in Chapter 4, results in solutions for the height anomaly field as shown in Figs. 5.3 and 5.4 for a Courant number  $C = 2.5$ . The setups of the two simulations are identical except for the search radius. The two search radii are chosen to maximise their difference and thus the associated effect. As Courant number  $C = 2.5$  proved strongly affected by the spurious resonance in Chapter 4, it is the best Courant number for a first investigation of the importance of the search radius.

There are three main aspects of interest when investigating the variable off-centring schemes. The first question is, how the solutions compare with the reference solution. Secondly, it is important to determine how they

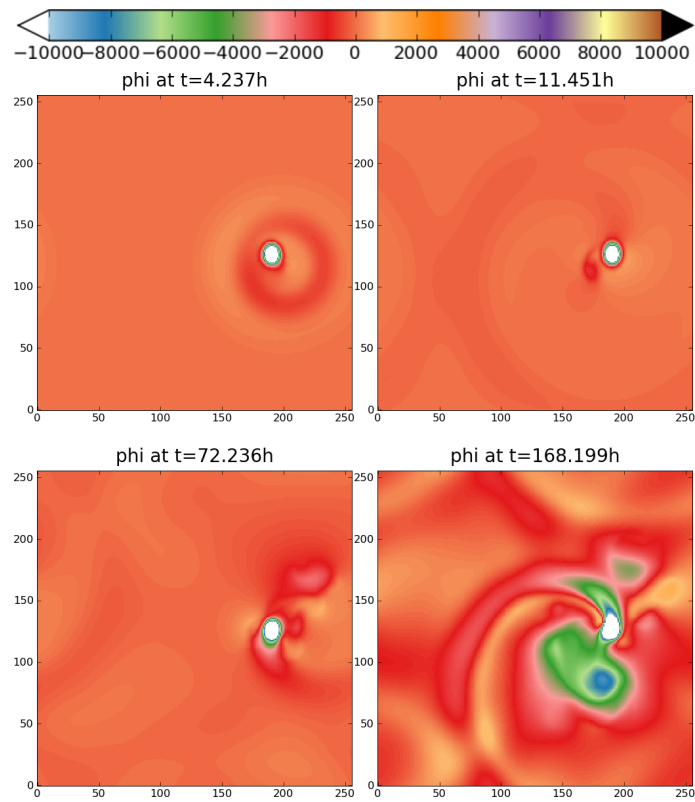


Figure 5.3: Height anomaly  $\varphi$  (in  $m^2/s^2$ ) for  $C = 2.5$  and variable off-centring with base  $\alpha_1 = \alpha_2 = \alpha_3 = 0.8$  and search radius  $r_s = 0$  (only local gradients considered).

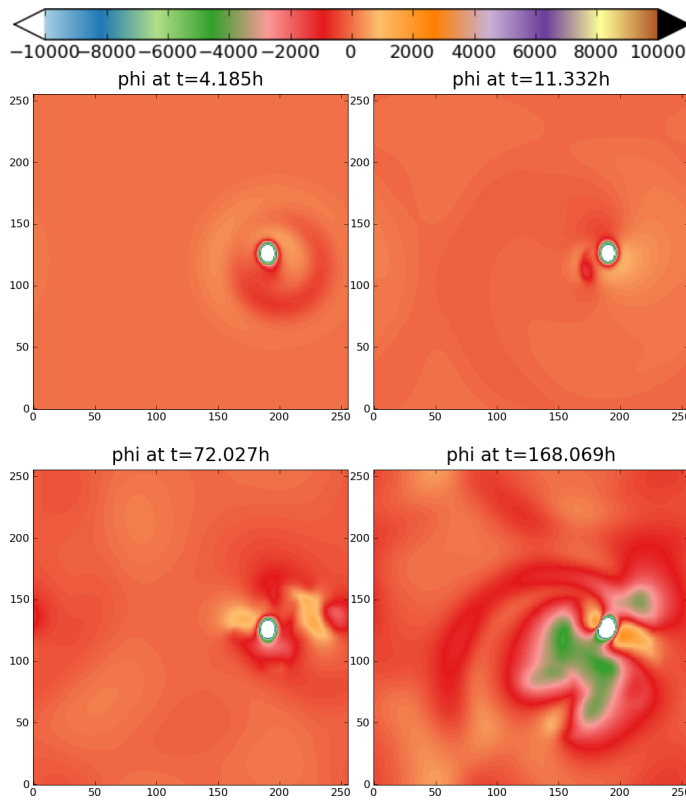


Figure 5.4: Height anomaly  $\varphi$  (in  $m^2/s^2$ ) for  $C = 2.5$  and variable off-centring with base  $\alpha_1 = \alpha_2 = \alpha_3 = 0.8$  and search radius 16.

compare with the corresponding constant off-centring schemes and, thirdly, the impact of the choice of search radius on the solution. The following will investigate these questions in that order.

Comparing both search radii introduced above with the reference simulation reveals very little similarity. Both with a search radius of  $r_s = 0$  as used for Fig. 5.5 and a search radius of  $r_s = 16$  as used for Fig. 5.6, the state after  $4h$  still looks very much like the results obtained with the FOX simulations. The wave speed is underestimated due to the large Courant number and the wave is smoothed out by the numerical damping, but there are no spurious features visible. This picture changes significantly over the first 7 days. At 7

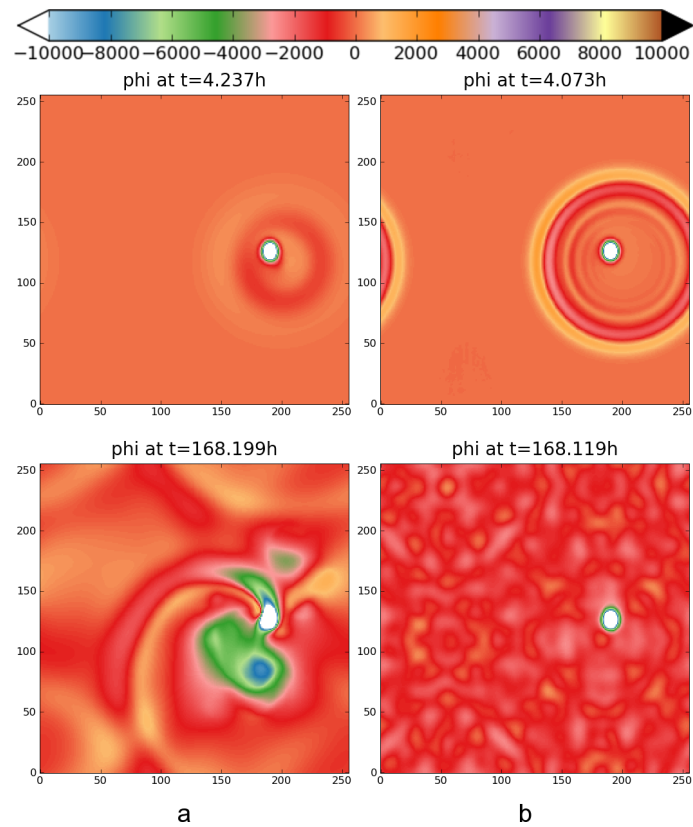


Figure 5.5: Height anomaly  $\varphi$  (in  $m^2/s^2$ ) for a)  $C = 2.5$  and variable off-centring with base  $\alpha_1 = \alpha_2 = \alpha_3 = 0.8$  and search radius  $r_s = 0$  b) reference simulation.

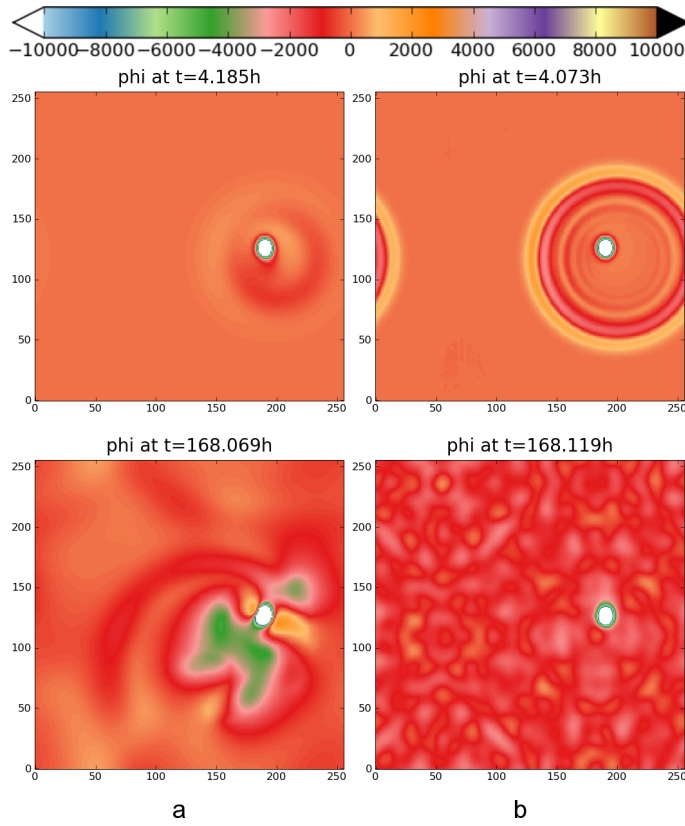


Figure 5.6: Height anomaly  $\varphi$  (in  $m^2/s^2$ ) for a)  $C = 2.5$  and variable off-centring with base  $\alpha_1 = \alpha_2 = \alpha_3 = 0.8$  and search radius 16 b) reference simulation.

days ( $168h$ ), both vFOX simulations appear rather turbulent. Furthermore, the wave amplitudes are overestimated by a factor of  $\sim 4$  for the small search radius  $r_s = 0$  and a factor of  $\sim 2$  for the large search radius  $r_s = 16$ . While a factor of  $\sim 2$  might be acceptable, the area of maximum error is rather large amounting to  $\sim 20 - 25\%$  of the computational domain in both simulations. On the other hand, without applying any off-centring to the equations the height anomalies are overestimated by more than a factor of  $\sim 5$  in the full domain (cf. Fig. 4.7).

While it would be desirable for the solution obtained using vFOX to com-

pare well with the reference solution, the possibly more important question is how it compares with the results of the FOX scheme. If vFOX was to yield results of the same quality as FOX, it would still come with the benefit of reduced numerical damping away from orography. Fig. 5.7 shows such a comparison for a maximum Courant number  $C = 2.5$  and  $\alpha_n = 0.8$  (where  $n \in \{1, 2, 3\}$ ). The search radius in the variably off-centred simulation is  $r_s = 0$ , i.e. only orographic height differences with nearest neighbours are considered. In other words, at the point of maximum orographic height difference, the variable off-centring scheme has the same off-centring parameter as the constant scheme and a lower parameter everywhere else.

Four hours into the simulation, the difference in numerical damping is clearly visible in the sharper wave front in the variably off-centred simulation. The wave front seems slightly offset between the two schemes. However, as the damping makes the wave features appear rather indistinct in the constantly off-centred case, it is impossible to tell how much difference there is. In any case, this difference is certainly very small and, in itself, no reason for concern. Much more importantly, after 7 days (168h) the height anomalies appear to carry very different dynamics in vFOX than they do in FOX.

A look at one of the velocity components in Fig 5.8 confirms that there is a fundamental difference in dynamics. While there is no clear indication of a vortex in the variably off-centred case, the dynamics are clearly more concentric around the orography. This pattern is obviously less desirable than the one in the FOX scheme's case because it reproduces the orography features much more closely. This is likely to be a result of the spurious orographic resonance not being eliminated sufficiently.

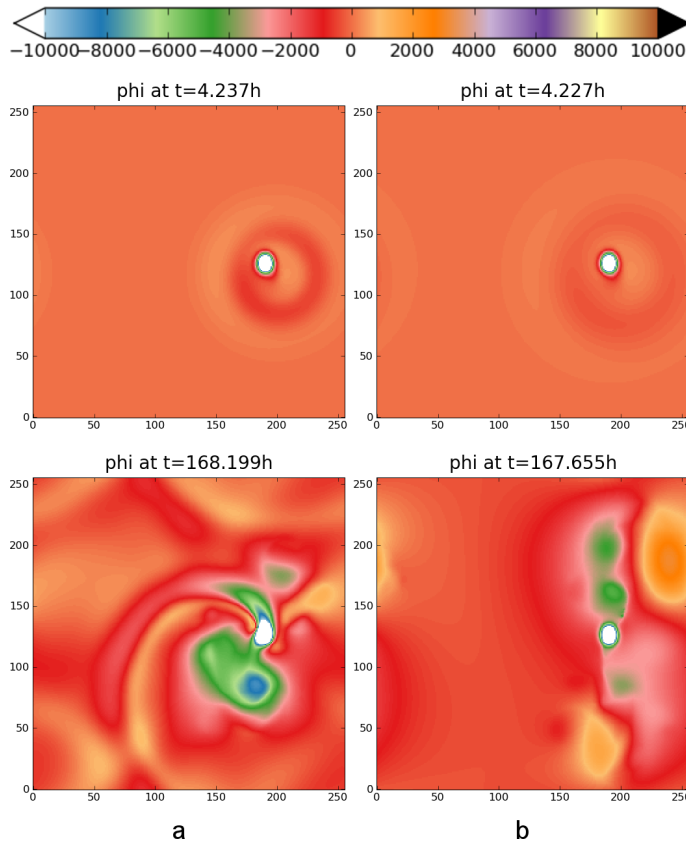


Figure 5.7: Height anomaly  $\varphi$  (in  $m^2/s^2$ ) for a)  $C = 2.5$  and vFOX with base  $\alpha_1 = \alpha_2 = \alpha_3 = 0.8$  and search radius  $r_s = 0$  b)  $C = 2.5$  and FOX with constant  $\alpha_1 = \alpha_2 = \alpha_3 = 0.8$ .

As the kinetic energy per unit mass has served well as an indicator of stability for the FOX simulations, it is shown again, this time for Courant number  $C = 3$  in Fig. 5.9. The evolution of the kinetic energy provides unambiguous confirmation that the vFOX scheme can not be considered stable. The kinetic energy grows even faster than for a centred simulation which is clearly resonant and tends to saturate at an even higher value than is the case in the absence of off-centring or does not saturate at all. Consequently, with no evidence for stability or accurate solutions, this scheme should not be considered further.

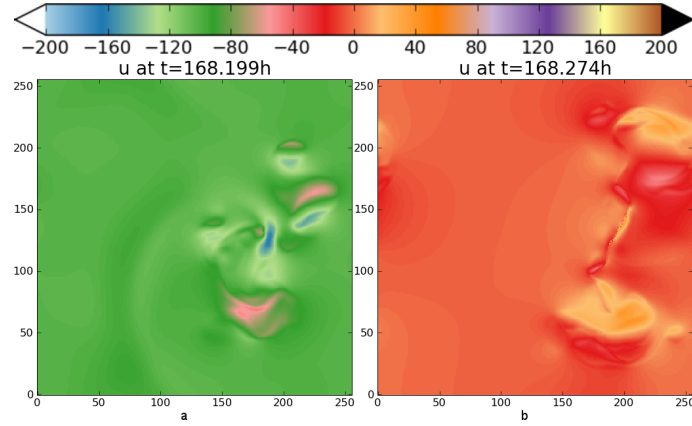


Figure 5.8: Velocity component  $u$  for a)  $C = 2.5$  and vFOX with base  $\alpha_1 = \alpha_2 = \alpha_3 = 0.8$  and search radius  $r_s = 0$  b)  $C = 2.5$  and FOX with constant  $\alpha_1 = \alpha_2 = \alpha_3 = 0.8$ .

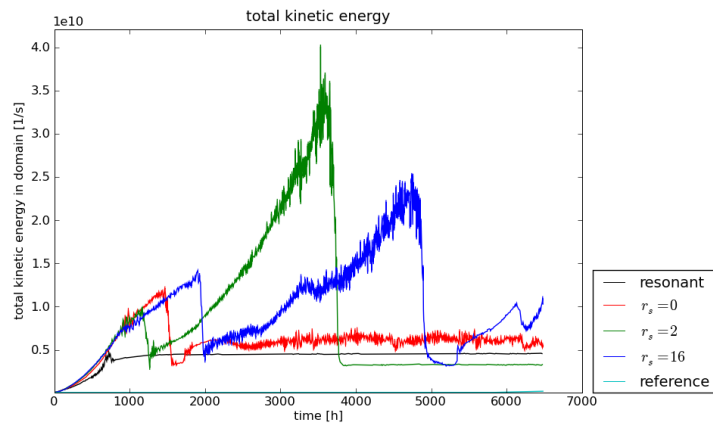


Figure 5.9: Time development of kinetic energy per unit mass in the domain for Courant number  $C = 3$  and fully off-centred simulations at different  $\alpha_1 = \alpha_2 = \alpha_3 = 0.8$  and different search radii  $r$ . Comparison with reference and simulation of constant off-centring.

### 5.3 Off-Centring only the Height Equation

The previous section indicated that varying the off-centring parameter in FOX to transform it to vFOX is not a viable or, at best, a risky option. On the other hand, as Section 4.3.2 showed, off-centring only the height equation (ROCKS) appears sufficiently stable in practice for a constant off-centring parameter even though a stringent proof of why this would be the case can not easily be given and the simulation might destabilise in long time scale simulations. Therefore, the following applies the variable off-centring scheme (vFOX) tested in the previous section for a setup where only the height equation is off-centred. The base value in these experiments was still  $\alpha_3 = 0.8$  but with  $\alpha_1 = \alpha_2 = 1/2$  everywhere. In other words the off-centring parameter fields shown in Fig. 5.2 are still used but only applied to  $\alpha_3 = \frac{1+\varepsilon_3}{2}$ .

Just as for the scheme in Section 5.2, experiments with different search radii were conducted. Analogous to the previous section, Figs. 5.10 and 5.11 show the results for search radii  $r_s = 0$  and  $r_s = 16$ , respectively. This corresponds to Figs. 5.3 and 5.4 in vFOX. The scheme introduced here is referred to as *vROCKS*.

As in the comparison between FOX and vFOX, the wave in vROCKS is now more distinct at  $4h$  than it was at the same time when using ROCKS. While the results for different search radii are virtually indistinguishable after  $4h$ , the search radius has some impact after  $11h$  where the wave front is slightly more distinct for the small search radius  $r_s = 0$ . After 7 days ( $168h$ ), the height anomalies are then different by a factor of  $\sim 2$  in the vicinity of the orography.

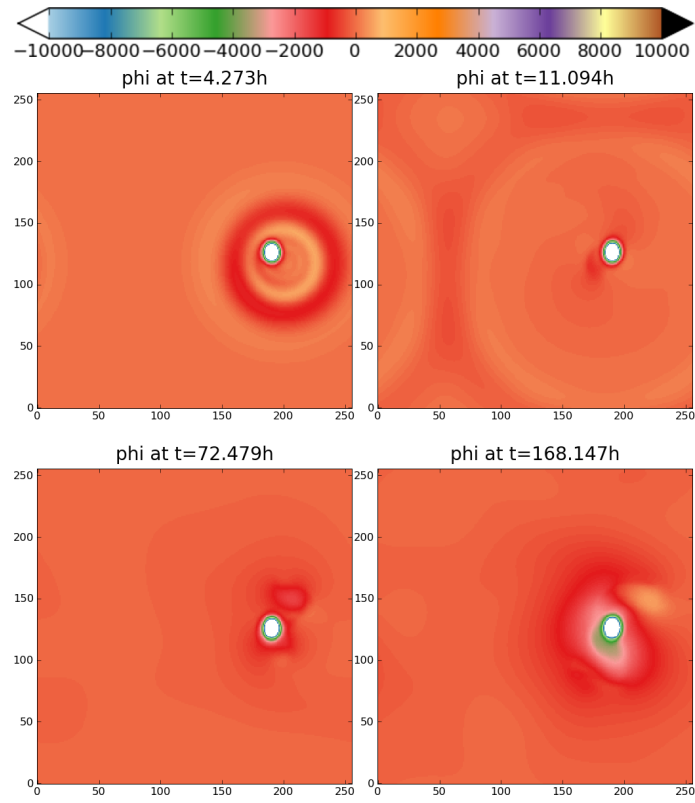


Figure 5.10: Height anomaly  $\varphi$  (in  $m^2/s^2$ ) for  $C = 2.5$  and variable off-centring with base  $\alpha_1 = \alpha_2 = 1/2$  and  $\alpha_3 = 0.8$  and search radius  $r_s = 0$  (only local gradients considered).

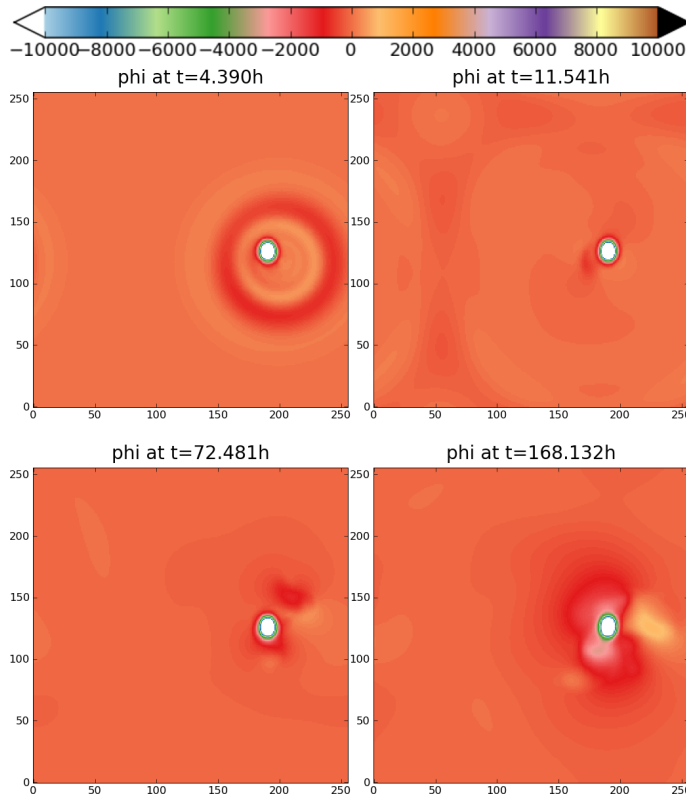


Figure 5.11: Height anomaly  $\varphi$  (in  $m^2/s^2$ ) for  $C = 2.5$  and variable off-centring with base  $\alpha_1 = \alpha_2 = 1/2$  and  $\alpha_3 = 0.8$  and search radius  $r_s = 16$ .

As Figs. 5.12 and 5.13 show, the solutions obtained with either search radius also compare well with the reference solution. While at this time in the integration the detailed dynamical features of the reference solution have not been preserved, the height anomalies obtained are a good average in most of the domain. The larger search radius also does not show any height anomalies that are of a different order of magnitude than the height anomalies in the reference solution.

Looking at the kinetic energy per unit mass, the kinetic energy increases rapidly after  $500 - 1000h$ , just like in the case of ROCKS. The long time scale development between simulations of different search radius is very similar

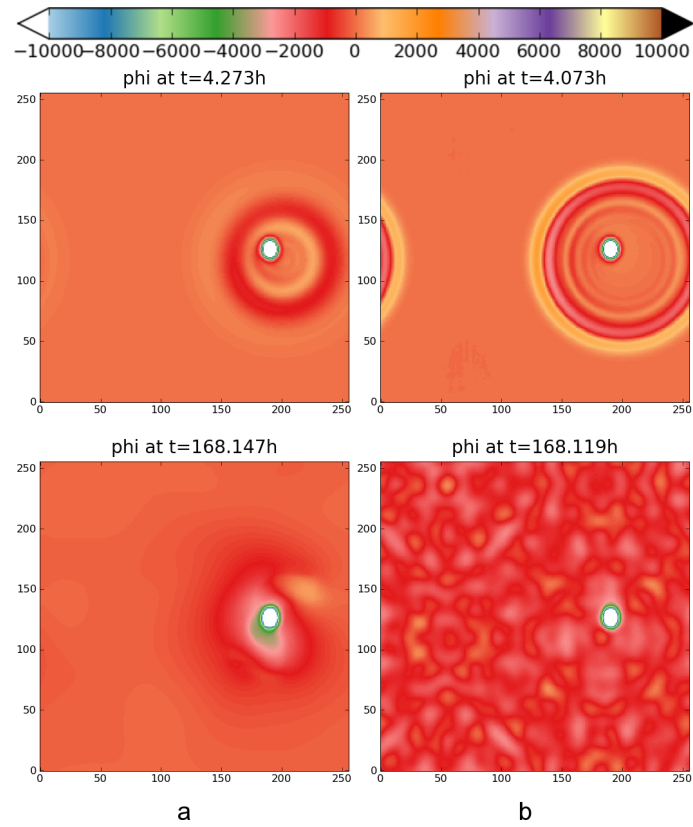


Figure 5.12: Height anomaly  $\varphi$  (in  $m^2/s^2$ ) for a)  $C = 2.5$  and variable off-centring with base  $\alpha_1 = \alpha_2 = 1/2$  and  $\alpha_3 = 0.8$  and search radius  $r_s = 0$  b) reference simulation.

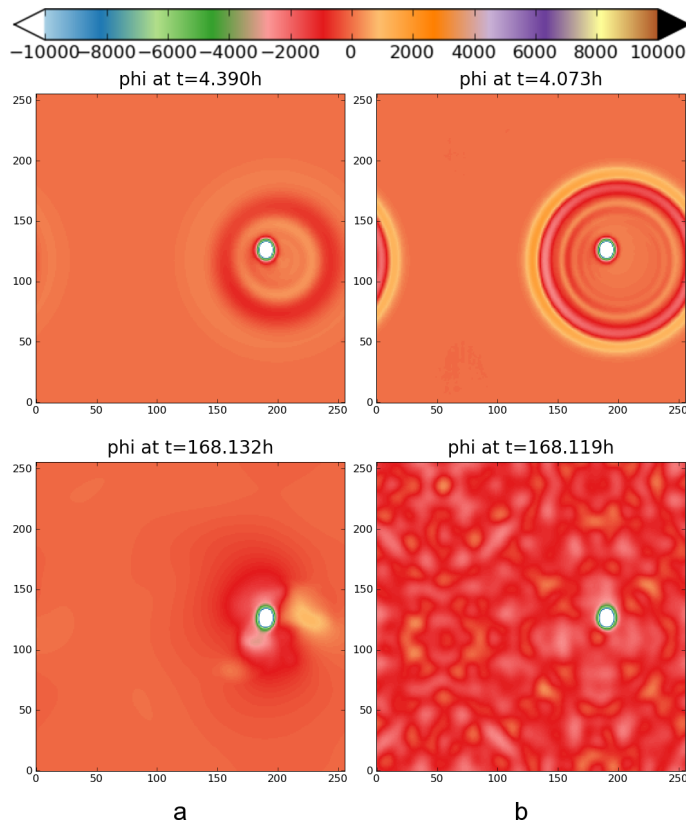


Figure 5.13: Height anomaly  $\varphi$  (in  $m^2/s^2$ ) for a)  $C = 2.5$  and variable off-centring with base  $\alpha_1 = \alpha_2 = 1/2$  and  $\alpha_3 = 0.8$  and search radius  $r_s = 16$  b) reference simulation.

and does not suggest any specific choice of search radius. The kinetic energy evolution for any search radius also differs very little from the one seen in the case of ROCKS with the short time scale development as shown in Fig. 5.15 being virtually indistinguishable from the one seen earlier for ROCKS (Fig. 4.28).

As the solutions obtained with vROCKS compare very well with the reference solution, it is worthwhile comparing the scheme with vFOX (cf. Section 5.2).

Fig. 5.16 shows simulations with vFOX and vROCKS with a Courant num-

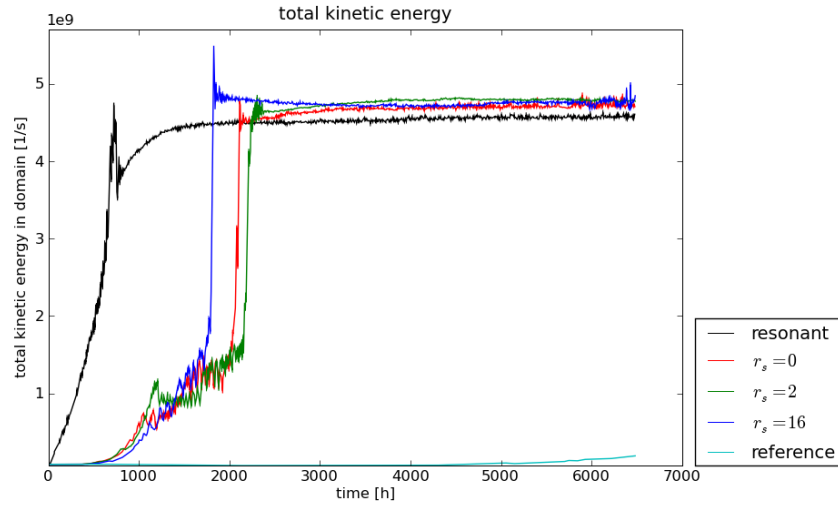


Figure 5.14: Short time scale development of kinetic energy per unit mass in the domain for Courant number  $C = 3$  and height off-centred simulations using  $\alpha_3 = 0.8$  and different search radii  $r$ . Comparison with reference and simulation of constant off-centring.

ber of  $C = 2.5$ , an off-centring parameter  $\alpha = 0.8$  and a search radius  $r_s = 0$  side by side. The snapshot at  $4h$  graphically illustrates the gain when using vROCKS which is very similar to the comparison of the two constant schemes (FOX and ROCKS) in Chapter 4. The wave pattern in vROCKS is much more distinct than in vFOX and again gives the impression that the wave might propagate at a slightly different speed. The differences between vFOX and vROCKS simulations compared in Fig. 5.16 become even more striking after 7 days. The large scale dynamics, as they can be observed in vFOX, have no counterpart in the vROCKS solutions. Furthermore, while the significant height error affects  $\sim 20 - 25\%$  of the computational domain in vFOX, it is confined to a very small region close to the orography in vROCKS.

It remains unclear why the kinetic energy evolution is significantly different

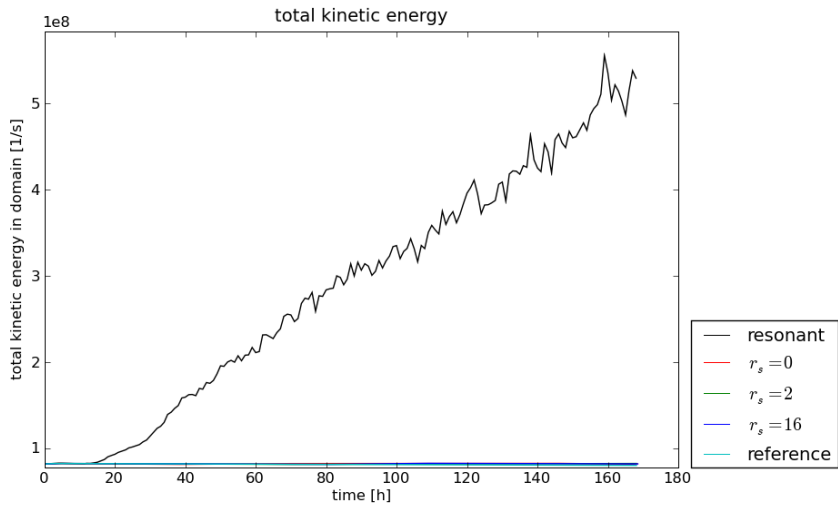


Figure 5.15: Short time scale development of kinetic energy per unit mass in the domain for Courant number  $C = 3$  and vROCKS simulations using  $\alpha_3 = 0.8$  and different search radii  $r$ . Comparison with reference and simulation of constant off-centring.

between the two schemes. Therefore, more weight is given to the behaviour of the height and momentum fields and short time scales.

Comparing vROCKS simulations of different search radii in Fig. 5.17 also reveals a picture very different from the case where all equations are off-centred. While there might be a slight improvement up to a search radius  $r_s = 3$ , the simulations of different search radii are virtually indistinguishable.

This lack of sensitivity to the search radius is not only true for one specific Courant number, as can be verified in Fig. 5.18 where the same comparison is shown for a Courant number  $C = 4$ . For this Courant number, the amplitude seems even less overestimated at any search radius and the height anomalies are generally very smooth.

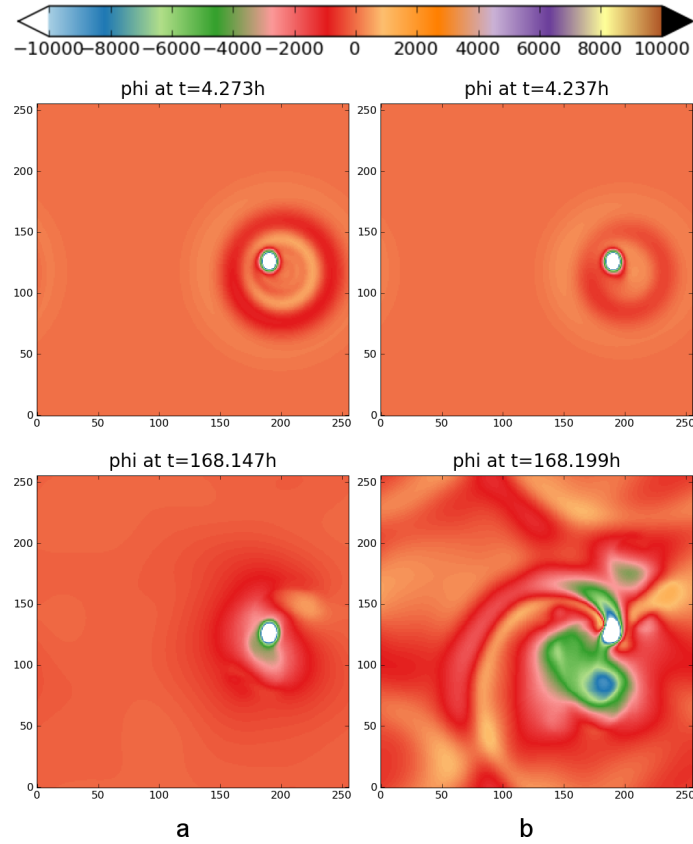


Figure 5.16: Height anomaly  $\varphi$  (in  $m^2/s^2$ ) for  $C = 2.5$  and variable off-centring with search radius  $r_s = 0$  and a) base  $\alpha_1 = \alpha_2 = 1/2$  and  $\alpha_3 = 0.8$  and b) base  $\alpha_1 = \alpha_2 = \alpha_3 = 0.8$ .

If all the results presented so far for vROCKS show little sensitivity to the search radii the value range  $\varphi_{\max} - \varphi_{\min}$  as a function of the search radius  $r_s$  does not confirm that finding. Fig. 5.19 reveals significant volatility for all values  $r_s < 20$  if  $C > 1$ . Only at  $r_s \approx 24$  does the value range saturate. However, at this search radius about 1/3 to 1/2 of the computational domain are off-centred at the maximum off-centring parameter. While for Courant numbers  $C = 3$  and  $C = 4$  the value range falls off exponentially towards the saturation value for  $0 \leq r_s \leq 6$ , it actually grows linearly for the same range of search radii at Courant number  $C = 4$ .

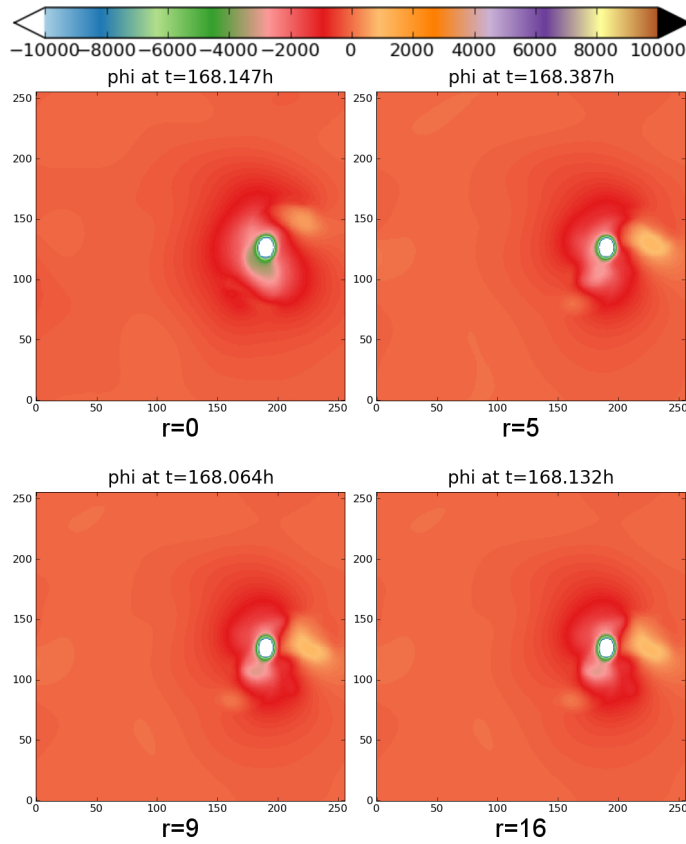


Figure 5.17: Height anomaly  $\varphi$  (in  $m^2/s^2$ ) for  $C = 2.5$  and variable off-centring with base  $\alpha_1 = \alpha_2 = 1/2$  and  $\alpha_3 = 0.8$  and search radii  $r_s \in \{0, 5, 9, 16\}$ .

As the problem of the high volatility in value range does not translate into the snapshots or the kinetic energy development, it most likely is caused by short term over- and undershoots. The plotted value range is defined as the maximum and minimum height anomalies across the whole simulation. The maximum and minimum used to determine this range do not necessarily coincide.

Another very interesting feature of Fig. 5.19 is the level of the saturated value range. While it was above the reference simulation's for vFOX, it is now below the reference simulation's level. This is somewhat unexpected

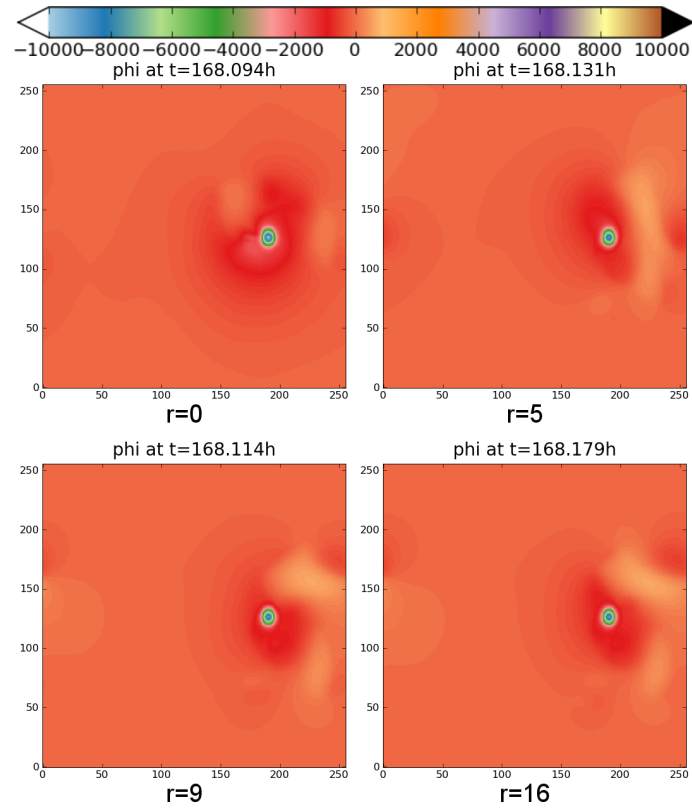


Figure 5.18: Height anomaly  $\varphi$  (in  $m^2/s^2$ ) for  $C = 4$  and variable off-centring with base  $\alpha_1 = \alpha_2 = 1/2$  and  $\alpha_3 = 0.8$  and search radii  $r_s \in \{0, 5, 9, 16\}$ .

because the scheme introduces less numerical damping than vFOX and as a result the solution should show more variability.

Taking all the information shown in the figures referred to above into account, it can be concluded that a choice of  $C < r_s < 2C$  is reasonable for the radius in the vROCKS scheme. While this might not always be the optimal value it is sufficient as a rule of thumb to be applied to all Courant numbers investigated. This value unifies the following aspects observed above. It takes advantage of the early strong decline in value range for some Courant numbers as evident in Fig. 5.19 and achieves less height overestimation at least for Courant number  $C = 2.5$  than would be the case with  $r_s = 0$ .

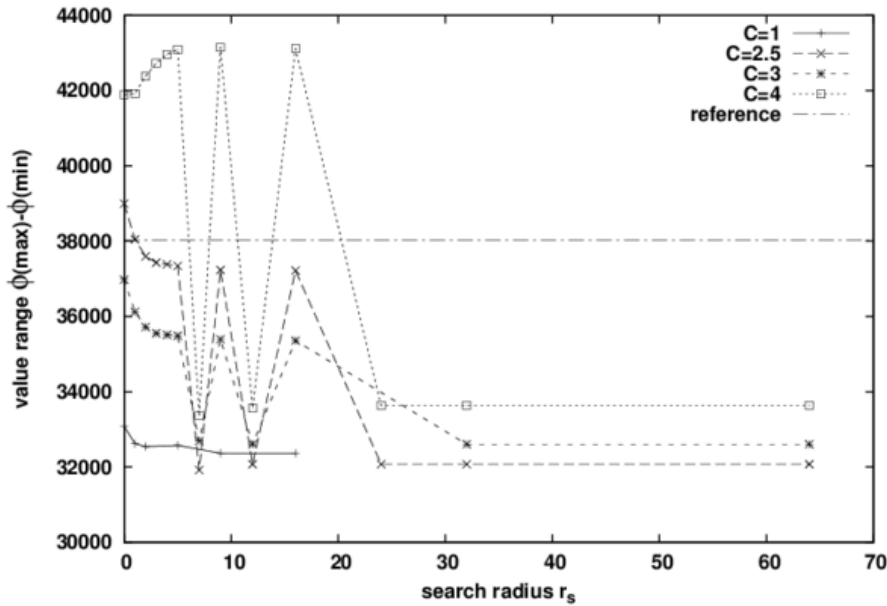


Figure 5.19: Difference between minimum and maximum of  $\varphi$  as a function of the search radius at a base  $\alpha_n = 0.8$  ( $n \in \{1, 2, 3\}$ ) after an integration time of  $168h$ .

## 5.4 Conclusions

Several variable off-centring schemes were designed and evaluated in the context of SWiM. Somewhat unexpectedly, once variable off-centring is chosen the solutions are rather sensitive to the number of equations using  $\alpha_n > 1/2$ . While very smooth and accurate solutions could be obtained with a scheme which only off-centres the height equation with a variable off-centring parameter (vROCKS), there was very strong evidence pointing towards a variable off-centring scheme on all equations (vFOX) being unstable. This was primarily derived from the development of the kinetic energy on a short time scale and the dynamical features of the solutions. As a result, vFOX was ruled out as unfit for the purpose of selectively stabilising the solutions where necessary due to the spurious numerical resonance.

An alternative to the vFOX scheme is to only off-centre the height equation with a variable off-centring scheme (vROCKS). While vROCKS possibly shows some more volatility for small search radii  $r_s$ , this effect is pretty well contained. Furthermore, the scheme seems to converge to its best solution very fast with increasing search radius  $r_s$ . There are remaining questions about stability on long time scales for this approach which could possibly be addressed in a model which involves more than just dynamical processes.

A vROCKS scheme based on moderate off-centring of  $\alpha_3 = 0.8$  with a search radius of  $C < r_s < 2C$  with a possible preference for lower radii in that interval seems feasible. While some dynamical features are lost, the dynamics on average get very close to those of the reference simulation. The resonance is sufficiently well removed and minimal damping introduced.

The stability issues that emerged for ROCKS earlier also affect vROCKS, the variable off-centring scheme derived from it. However, as pointed out in earlier remarks concerning ROCKS, no firm conclusion can be drawn about the viability of such a scheme in the context of a full-fledged GCM. At the same time, such an atmospheric model might actually see more gain from the reduced numerical dissipation because it most likely has significantly larger regions in the computational domain that are sufficiently far away from orographic forcing. In a global climate model, for example, this applies over large parts of the ocean. Therefore, weighing the potential risks and gains, against each other, it makes sense to try schemes as described in the context of SWiM in a full-fledged GCM as well.



## Chapter 6

# Off-Centring in a full GCM

### 6.1 An Introduction to C-CAM

The previous chapters have extensively explored the spurious orographic resonance and how it affects the solutions of a semi-Lagrangian, semi-implicit shallow water model. The shallow water model was a good test bed and made it possible to learn important lessons about how the spurious resonance affects a semi-implicit, semi-Lagrangian model. As explained earlier, there is much benefit in investigating a phenomenon like a spurious resonance in as simple a model as possible. The simple model allows a nearly unobstructed view on the effects of the resonance in the model and in the newly devised variable off-centring scheme in particular. As the interpretation of the results in Chapters 4 and 5 was still difficult at times, it can be expected that firm conclusions will be even harder to draw in the context of a full GCM.

Yet, as interesting as the results in a shallow water model are, the real test of an off-centring scheme is, how it performs in a full-fledged model. As

there are numerous factors that contribute to the solution in a numerical model and as the model has been set up to work well with the current choices of numerical schemes, care must be taken when interpreting the results of making a single change for instance to the off-centring settings. It is nevertheless essential to test the various options for off-centring in the model, which is the purpose of this chapter. This section introduces C-CAM, a semi-implicit, semi-Lagrangian global climate model. In Section 6.2 the effects of the resonance in a C-CAM simulation are determined and compared against the off-centring schemes currently available in C-CAM. Section 6.3 then presents the results obtained when applying the new variable off-centring scheme developed for SWiM in Chapter 5 to this model. Section 6.4 suggests and tests modifications to the variable off-centring scheme to further improve the results. Finally, the results from all the different new variable off-centring schemes are discussed and compared in Section 6.5.

### 6.1.1 C-CAM's Main Features

C-CAM is a global climate model developed by Australia's Commonwealth Scientific and Industrial Research Organisation (CSIRO). It solves the primitive equations on a conformal cubic grid of variable local resolution using the two time level semi-Lagrangian method (McGregor, 2005).

A conformal cubic grid is devised by projecting a grid created on the panels of a cube onto a sphere. An example of such a grid is shown in Fig. 6.1.

A conformal cubic grid (cf. Rančić et al., 1996) has two main advantages over a spherical longitude-latitude grid. Firstly, it does not have strong singular points as the spherical grid has at its poles. Secondly, and more importantly,

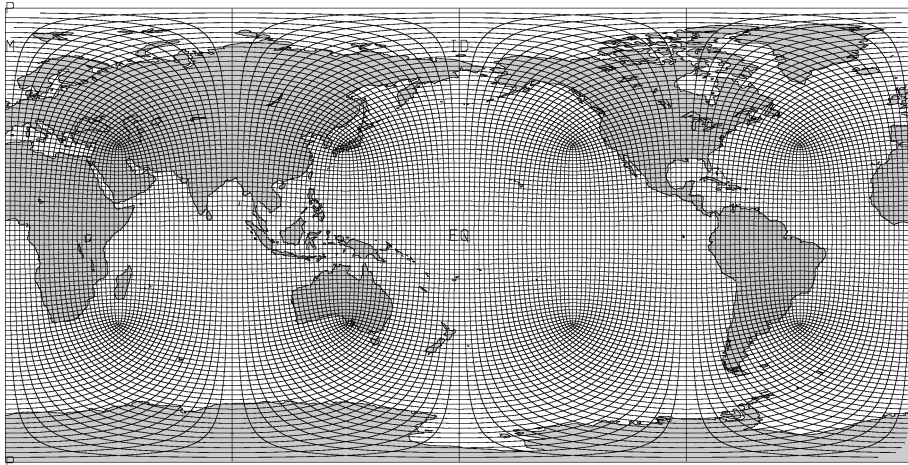


Figure 6.1: Conformal cubic C48 grid with a resolution of  $\sim 200km$ . Courtesy of J. McGregor.

it has a closer to uniform resolution across the globe. As the meridians on a spherical grid approach each other when approaching the poles, the grid resolution has to become finer close to the poles. In combination with the singularity at the pole points, this is usually not desirable because it leads to increased computational cost without much benefit. The conformal cubic grid suffers much less from this weakness and is therefore computationally more efficient than a latitude-longitude grid.

The conformal cubic grid is perfectly orthogonal like the Cartesian grid except for the grid points at the vertices. The angles on which the grid points are arranged in relation to each other are of utmost importance because they affect distances and derivatives. While the derivatives are defined in a very simple fashion on a Cartesian grid, a non-orthogonal grid results in extra terms for derivatives.

The substantial derivative on the cubed sphere is defined as

$$\frac{d_H}{dt} = \frac{\partial}{\partial t} + mu \frac{\partial}{\partial x} + mv \frac{\partial}{\partial y}, \quad (6.1)$$

where  $u$  and  $v$  are the horizontal velocity components and  $m$  is the map factor of the cubic-conformal projection.

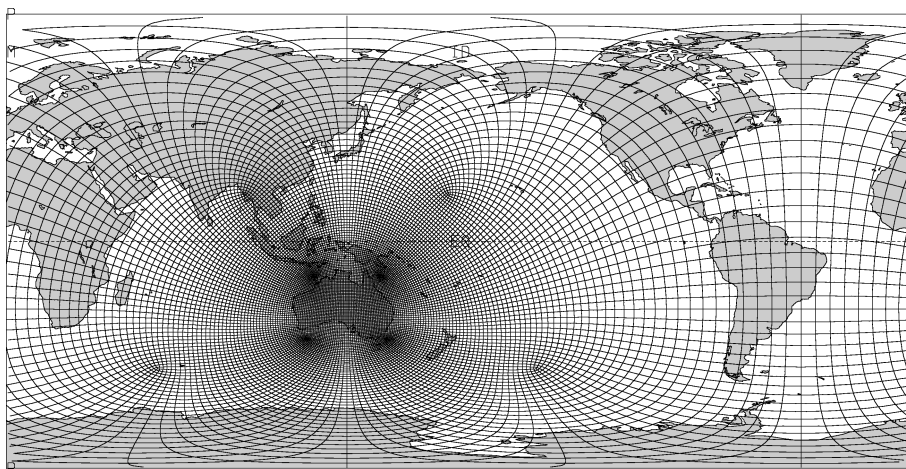


Figure 6.2: Stretched conformal cubic C48 grid with increased resolution over Australia. The Schmidt factor is 3.33. Courtesy of J. McGregor.

The grid resolution in C-CAM can be adapted using the Schmidt transformation (Schmidt, 1977) which allows contracting the grid over a certain region while reducing the resolution further away from that region. An example of a grid with increased resolution over Australia with a Schmidt factor of 3.33 is shown in Fig. 6.2.

### 6.1.2 The Equations in C-CAM

Section 2.1.1 already introduced the primitive equations. As highlighted above, C-CAM solves these equations on the conformal cubic grid. As the

derivative on the conformal cubic grid introduces the map factor  $m$  into the equations, that factor will also feature in the finite difference equations. As the full model equations can become quite complex, the following shows them in just as much detail as is necessary to illustrate how the variable off-centring scheme has been implemented in C-CAM. For more detail the reader is referred to [McGregor \(1996, 2005\)](#) and references therein.

C-CAM uses terrain-following  $\sigma$  coordinates, where  $\sigma = p/p_s$ , the ratio of pressure  $p$  over surface pressure  $p_s$ . The set of equations as solved in C-CAM is described below.

### Horizontal Momentum Equations

$$\frac{d_H u}{dt} + m \frac{\partial \varphi_v}{\partial x} + m R_d T_v \frac{\partial \ln p_s}{\partial x} + \dot{\sigma} \frac{\partial u}{\partial \sigma} = f v + \tilde{N}_u, \quad (6.2)$$

$$\frac{d_H v}{dt} + m \frac{\partial \varphi_v}{\partial y} + m R_d T_v \frac{\partial \ln p_s}{\partial y} + \dot{\sigma} \frac{\partial v}{\partial \sigma} = -f u + \tilde{N}_v, \quad (6.3)$$

where  $\varphi_v$  is the geopotential (including virtual temperature contributions),  $f$  is the Coriolis parameter,  $R_d$  the gas constant for dry air and  $u$  and  $v$  are as above. The  $\tilde{N}_x$  terms represent possible physical parametrisations. The virtual temperature  $T_v$  is defined as

$$T_v = T \left[ 1 + \left( \frac{R_v}{R_d} - 1 \right) q \right], \quad (6.4)$$

where  $T$  is the temperature,  $R_v$  the gas constant for water vapour and  $q$  the mixing ratio of water vapour.

### Temperature Equation

$$\frac{d_H T}{dt} + \dot{\sigma} \frac{\partial T}{\partial \sigma} - \frac{R_d}{c_p} \frac{\partial T}{\partial \sigma} \frac{\omega}{p_s} = \tilde{N}_q, \quad (6.5)$$

where  $c_p$  is the specific heat of water vapour at constant pressure,  $\sigma$  and  $\dot{\sigma}$  the vertical coordinate and its substantial derivative as above and  $\omega$  the vertical pressure velocity.

### Moisture Equation

$$\frac{d_H q}{dt} + \dot{\sigma} \frac{\partial q}{\partial \sigma} = \tilde{N}_q \quad (6.6)$$

### Continuity Equation

$$\frac{d_H \ln p_s}{dt} + D \frac{\partial \dot{\sigma}}{\partial \sigma} = 0, \quad (6.7)$$

where the divergence  $D$  is

$$D = m^2 \left( \frac{\partial u/m}{\partial x} + \frac{\partial v/m}{\partial y} \right). \quad (6.8)$$

### Hydrostatic Equation

$$\frac{\partial \varphi_v}{\partial \sigma} = -\frac{R_d T_v}{\sigma} \quad (6.9)$$

#### 6.1.3 Discretisation and Off-Centring

As mentioned above, C-CAM uses a two time level semi-Lagrangian, semi-implicit scheme to solve the primitive equations. Thus, like all semi-Lagrangian models, C-CAM has to tackle the spurious orographic resonance

described in Section 2.6. In its off-centring schemes, C-CAM uses two independent off-centring parameters  $\varepsilon_a$  for the mass and thermodynamic equations and  $\varepsilon_b$  for the momentum equations.

It would be beyond the scope of this thesis to list the full equations as they are solved in C-CAM. Instead, the following gives the form of all the discretised equations as much as is needed to understand the off-centring concept in C-CAM. For more details, the reader is again referred to [McGregor \(1996, 2005\)](#); [McGregor and Dix \(2008\)](#).

The primitive equations, listed in their continuous form in Section 6.1.2, can be discretised to take the following form. The superscript  $+$  denotes the arrival point (i.e. a grid point) while the superscript  $0$  denotes the departure point, just as in Chapter 1.

#### Surface Pressure Equation

$$\begin{aligned} & \left\{ \ln p_s + (1 + \varepsilon_a) \frac{\Delta t}{2} \left( D + \frac{\partial \dot{\sigma}}{\partial \sigma} \right) \right\}^+ \\ &= \left\{ \ln p_s - (1 - \varepsilon_a) \frac{\Delta t}{2} \left( D + \frac{\partial \dot{\sigma}}{\partial \sigma} \right) \right\}^0, \end{aligned} \quad (6.10)$$

where  $\varepsilon_a$  is the off-centring parameter for thermodynamical and mass equations,  $\Delta t$  the time step and all other symbols are as before.

#### Semi-Lagrangian Derivation of $\dot{\sigma}$ and $\omega/p_s$

$$\dot{\sigma}^+ = (\sigma \bar{D}^1 - \bar{D}^\sigma)^+ + \frac{\sigma \overline{M_{p_s}^1} - \overline{M_{p_s}^\sigma}}{1 + \varepsilon_a}, \quad (6.11)$$

$$\left( \frac{\omega}{p_s} \right)^+ = -(\bar{D}^\sigma)^+ + \frac{\overline{M_{p_s}^\sigma} - \sigma \overline{M_{p_s}}}{1 + \varepsilon_a}, \quad (6.12)$$

where  $M_{p_s}$  represents the advective tendency term of  $p_s$  and  $\overline{M_{p_s}}$  is a mid-point value along the trajectory.

**Temperature Equation**

$$\left\{ T + (1 + \varepsilon_a) \frac{\Delta t}{2} \frac{R_d T}{c_p \sigma} \bar{D}^\sigma \right\} - \left\{ T + (1 + \varepsilon_a) \frac{\Delta t}{2} \frac{R_d T}{c_p \sigma} (\bar{M}_{p_s}^\sigma - \sigma M_{p_s}) \right\} = \text{RHS}, \quad (6.13)$$

using the notation

$$\bar{()^\sigma} = \int_0^\sigma () d\sigma. \quad (6.14)$$

**Momentum Equations**

$$\left\{ u + (1 + \varepsilon_b) \frac{\Delta t}{2} \left( m \frac{\partial P}{\partial y} - f v \right) \right\}^+ - \left\{ u - (1 - \varepsilon_b) \frac{\Delta t}{2} \left( m \frac{\partial P}{\partial y} - f v \right) \right\}^0 = \text{RHS}, \quad (6.15)$$

$$\left\{ v + (1 + \varepsilon_b) \frac{\Delta t}{2} \left( m \frac{\partial P}{\partial y} + f u \right) \right\}^+ - \left\{ v - (1 - \varepsilon_b) \frac{\Delta t}{2} \left( m \frac{\partial P}{\partial y} + f u \right) \right\}^0 = \text{RHS}, \quad (6.16)$$

where  $\varepsilon_b$  is the off-centring parameter for the momentum equations and the linearised augmented height is defined as

$$P = \varphi_v + R_d \bar{T} \ln p_s. \quad (6.17)$$

As in the shallow water case, these equations are then combined into a Helmholtz equation to be solved implicitly. The Helmholtz equation takes the form

$$P_K^+ + (1 + \varepsilon_a) \frac{\Delta t}{2} \sum_{j=1}^K C_{kj} D_j^+ = X_P \quad (6.18)$$

where  $P_K^+$  now is a modified version of the linearised augmented height (6.17) using  $T$  instead of  $T_v$ .

These equations illustrate that the off-centring parameter in the momentum equations (6.15) and (6.16) is decoupled from the off-centring parameter in the thermodynamic and mass equations. This allows independent off-centring of the equations analogous to how it was applied before to the shallow water case in Section 4.3.2.

### C-CAM's Off-Centring Approaches

C-CAM already implements a number of different off-centring schemes. The off-centring parameter  $\varepsilon_a$  in the thermodynamic and mass equations can be set independently from  $\varepsilon_b$ , the one used in the momentum equations. This allows a setup similar to off-centring only the height equation in SWiM when  $\varepsilon_b = 0$  and  $\varepsilon_a \neq 0$ .

Furthermore,  $\varepsilon_a$  can be set to vary across the computational domain. In this variable scheme,  $\varepsilon_a$  is locally determined as a function of the maximum orographic height difference between a grid point and its four nearest neighbours<sup>1</sup>. The off-centring parameter  $\varepsilon_a$  grows linearly with the orographic height difference reaching its maximum value at an orographic height difference of 600m.

---

<sup>1</sup>This is equivalent to  $r_s = 0$  in the scheme introduced in Chapter 5

The default setting for a C-CAM simulation would be  $\varepsilon_b = 0$  and a base (or maximum) off-centring parameter  $\varepsilon_a = 0.15$ , i.e. the mass and thermodynamic equations at grid points with orographic height differences of  $600m$  and more are off-centred at  $\varepsilon_a = 0.15$  and all grid points with smaller orographic height differences are off-centred at the corresponding fraction of this value.

The following sections investigate the spurious resonance as it can be observed in C-CAM and compare the different off-centring settings described above and their effectiveness. Following the comparison of the schemes currently available in C-CAM, a new variable off-centring scheme is introduced and tested. Section 6.3 then compares the results obtained with the new variable off-centring scheme with those obtained from different constant off-centring schemes in C-CAM.

## 6.2 The Spurious Orographic Resonance in C-CAM

To be able to assess how effectively the resonance is removed from the problem by the current off-centring scheme and the newly developed variable one, it is important to know how the resonance actually affects C-CAM's results. To that end, the following shows different simulations whose setup only differs in the off-centring settings but is identical otherwise. As it is the most suitable variable to spot spurious waves, the vertical velocity  $\omega$  is used to gauge the impact of the spurious resonance.

All test simulations in this section were performed as 2 month simulations starting on 1 November 1988. The results shown are monthly averages of

December 1988, based on vertical velocities at 00 GMT and 12 GMT. The first month of the simulation has been discarded to ensure the model is past its spin-up phase. The monthly averaging ensures that the results shown are not just snapshots of transient features. The grid used is an unstretched C48 grid yielding an approximate resolution of  $2^\circ$ .

### 6.2.1 The Resonance in the Centred Equations

To trigger the resonance and determine its effect on the model results, C-CAM was first run without any off-centring applied, analogous to Sections 4.1 and 4.2. As for the shallow water model, the resonance can best be identified by studying the differences between the model results as obtained without off-centring at a Courant number  $C < 1$  and at Courant numbers  $C > 1$ . As a C-CAM simulation is significantly more expensive than the shallow water simulations, this comparison was only performed based on two different time steps resulting in Courant numbers  $C < 1$  for the small time step and  $C > 1$  for the large one.

To illustrate the change in results in the presence of the resonance, Fig. 6.3 shows the vertical velocity  $\omega$  for regions over the Himalayas (left) and Andes (right) for two simulations without any off-centring applied to the equations. The top panels show a simulation with a short time step of  $\Delta t = 600s$  where the Courant numbers are  $C < 1$ , the bottom panels show a simulation at large time step ( $\Delta t = 2h$ ) resulting in large Courant numbers.

Over the Andes some noise occurs for the large time step (Fig. 6.3d) while the flow is very smooth at small time step (Fig. 6.3b). The feature does have a wave like structure reaching from the northeast corner towards the

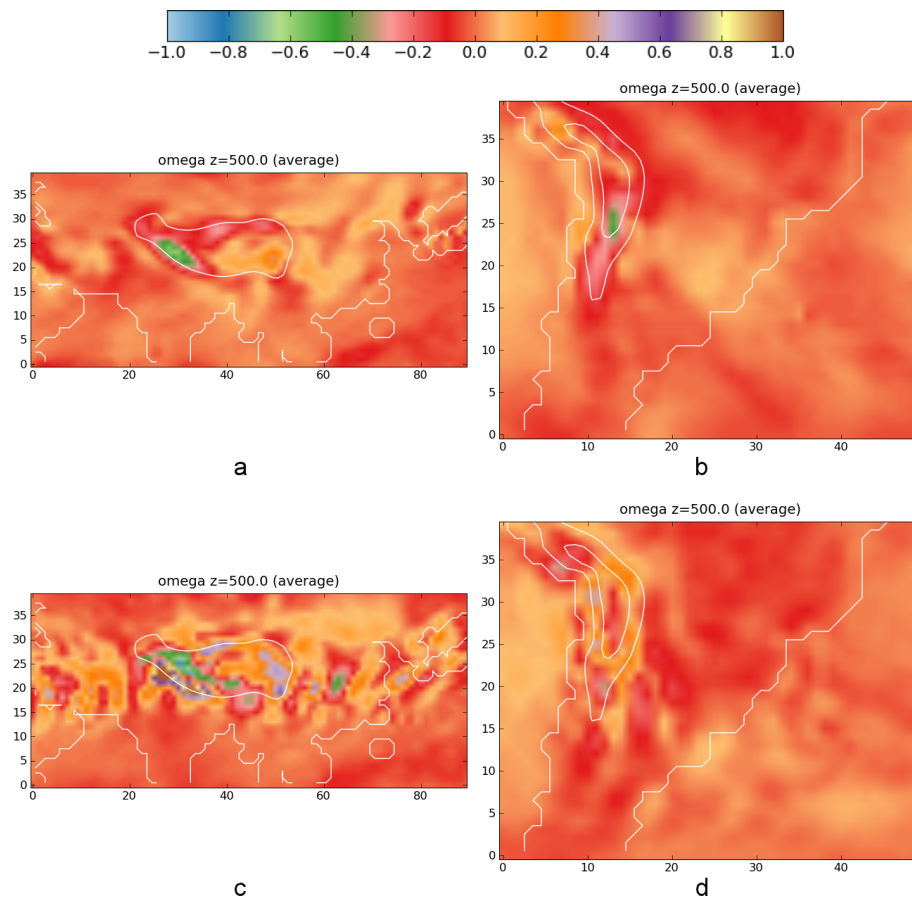


Figure 6.3: Vertical velocity  $\omega$  (in  $Pa/s$ ) at  $500hPa$  in (top) small time step ( $\Delta t = 600s$ ) and (bottom) large time step ( $\Delta t = 2h$ ) simulations with centred equations (monthly average for December 1988) over the Himalayas (a,c) and the Andes (b,d)

centre of the region, but it is impossible to determine with certainty that a standing wave has formed. Over the Himalayas, however, a very clear standing wave pattern (bear in mind that a monthly average is shown) can be seen in the large time step simulation (Fig. 6.3c) extending from close to the western end of the region to its eastern end. This is in stark contrast to the rather smooth flow which can be seen in the small time step model simulation (Fig. 6.3a).

As there is no other difference in the setup of the two models than the time step (and thus the Courant numbers), the noise or wave pattern must be a result of these larger Courant numbers. Knowing that Courant numbers of  $C > 1$  trigger the resonance and the chosen time step of 2h results in Courant numbers of that order of magnitude, the observed difference is almost certainly due to the spurious resonance. As a result of the resonance, a spurious mountain wave has formed.

### 6.2.2 Performance with Full Off-Centring

Having tested the model without off-centring and identified the likely effects of the spurious resonance on the model solution, the next step is to test the effectiveness of the off-centring schemes available in C-CAM in removing it. Fig. 6.4 shows a simulation at the same time step as the resonant simulation in Fig. 6.3 (bottom) but with off-centring at  $\varepsilon_a = \varepsilon_b = 0.1$ . While the wave is significantly damped in comparison with the centred equations, the off-centring is clearly not sufficient to completely remove the spurious resonance. This is in agreement with Rivest et al. (1994) who find a much higher threshold for  $\varepsilon$  is needed to sufficiently remove the spurious resonance. It

also supports the conclusion drawn earlier that the wave pattern is in fact a result of the resonance.

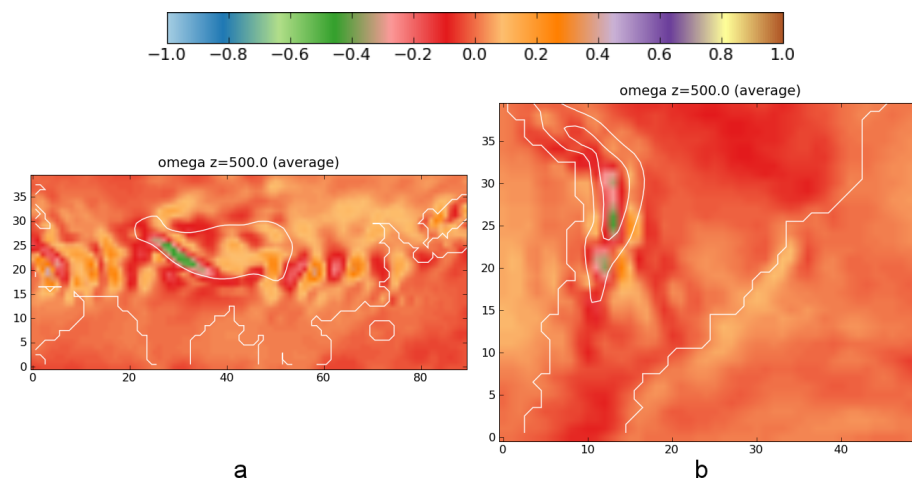


Figure 6.4: Vertical velocity  $\omega$  (in  $Pa/s$ ) at  $500hPa$  with off-centring  $\varepsilon_a = \varepsilon_b = 0.1$

Increasing the off-centring parameter to  $\varepsilon_a = \varepsilon_b = 0.4$  should, according to Rivest et al. (1994), be sufficient to remove the spurious resonance. To test this hypothesis, another simulation was performed with that off-centring parameter, again keeping all other parameters constant. As Fig. 6.5 shows, the vertical velocity is still slightly overestimated in regions where it is relatively high in the reference simulation. However, the wave pattern is rather indistinct in comparison with the clearly resonant simulations earlier. Overall, the off-centred simulation's solution strongly resembles the reference simulation's in Fig. 6.3 (top row) with the added damping restoring the solution to almost the reference solution but not negatively impacting the monthly average otherwise.

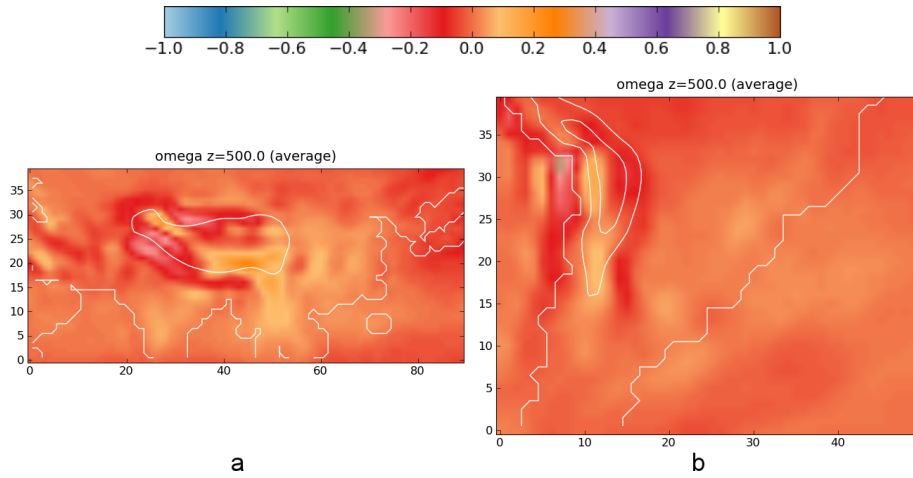


Figure 6.5: Vertical velocity  $\omega$  (in  $Pa/s$ ) at  $500hPa$  with off-centring  $\varepsilon_a = \varepsilon_b = 0.4$

### 6.2.3 Performance with Reduced Off-Centring

In the shallow water case, applying off-centring only to the height equation worked rather well in the short term and yielded rather promising results (cf. Section 4.3.2). The equivalent to that in the primitive equations is to off-centre only the thermodynamic and mass equations. As mentioned earlier, C-CAM is capable of applying off-centring selectively in exactly that manner. Analogous to the tests for the full off-centring scheme, this reduced scheme was tested and compared to the reference solution.

The simulations with the reduced off-centring settings use the same settings as the models discussed in Section 6.2.2. The only difference is that now  $\varepsilon_b = 0$  which reduces the off-centring to only the thermodynamic and mass equations.

In Fig. 6.6 the results for  $\varepsilon_a = 0.1$  are shown. This off-centring parameter was not sufficiently large in the case of full off-centring and should thus not

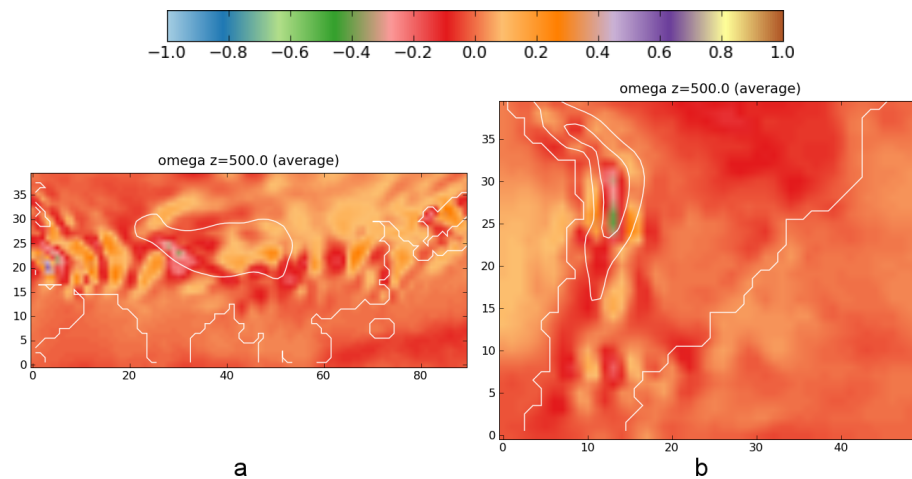


Figure 6.6: Vertical velocity  $\omega$  at  $500hPa$  with off-centring  $\varepsilon_a = 0.1$  and  $\varepsilon_b = 0$

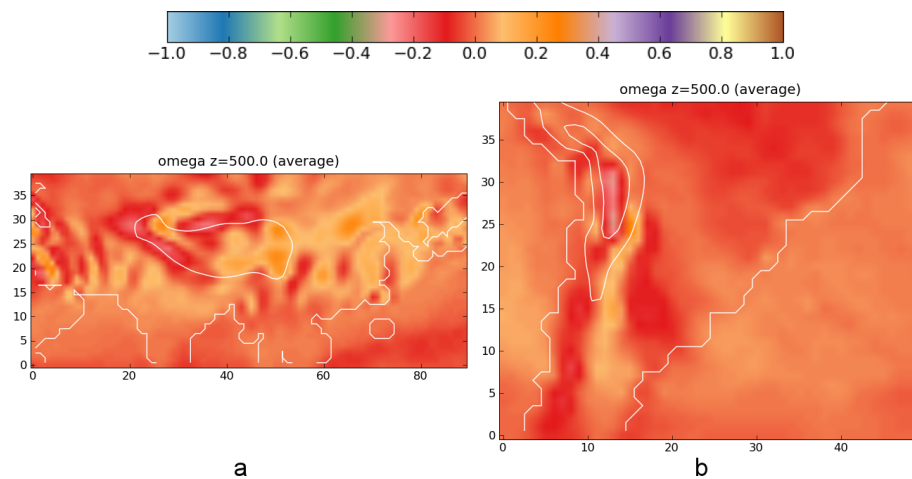


Figure 6.7: Vertical velocity  $\omega$  at  $500hPa$  with off-centring  $\varepsilon_a = 0.4$  and  $\varepsilon_b = 0$

yield perfectly satisfactory results for the reduced scheme, either. While the results clearly show, that the resonance has not been removed entirely, the pattern generally shows smaller amplitudes than in the case of full off-centring (cf. Fig. 6.4). Only on the windward (west) side of the Himalayas does the pattern appear stronger in the case of reduced off-centring. While this does not fully corroborate the findings in the shallow water case (if the time scale is considered short enough), it still is evidence pointing in a similar direction. According to the theoretical findings of Payne (2008), one would expect worse results from a reduced scheme, but this might not actually be the case in practice. The differences between the full and the reduced off-centring schemes are discussed in some more detail in Section 6.2.4.

As for the full off-centring scheme, the value for the off-centring parameter was then increased to  $\varepsilon_b = 0.4$  which yielded satisfactory results in the full off-centring scheme. If the reduced scheme is capable of removing the resonance, it should perform well at this off-centring parameter. The results for a simulation with  $\varepsilon_b = 0.4$  and  $\varepsilon_a = 0$  are shown in Fig. 6.7. They show a reasonably smooth pattern for the vertical velocity  $\omega$  at  $500hPa$  but one that is not as smooth as in the case of full off-centring with the same off-centring parameter. A wave pattern can still be seen in the vertical velocities more easily than in both the fully off-centred case and the reference simulation.

#### 6.2.4 Comparison between Full and Reduced Off-Centring

In SWiM, reasonable results could be achieved with off-centring only the height equation (cf. section 4.3.2). As this is in violation of the findings in Payne (2008), it appears prudent to conduct a closer comparison of the reduced scheme in C-CAM with the fully off-centred scheme.

Over the Himalayas, the results of the reduced scheme (cf. Fig. 6.6) are smoother than those from the fully off-centred scheme (cf. Fig. 6.4). However, on the windward (i.e. west) side of the Himalayas, a wave pattern forms in the reduced off-centring case but not the fully off-centred one. Over the Andes the reduced scheme clearly results in more noise. Thus, the results are ambiguous and do not allow for a firm conclusion.

As an off-centring of  $\varepsilon = 0.1$  is most likely insufficient (as shown above), it seems prudent to repeat the comparison using a larger off-centring parameter. For the larger off-centring parameter of  $\varepsilon = 0.4$  (Figs. 6.5 and 6.6), the reduced off-centring scheme shows more noise than the fully off-centred scheme. Nevertheless, there is still a slight wave pattern visible in the fully off-centred run which is much less distinct in the reduced off-centring scheme. The amplitudes, however, are comparable between the two schemes with a larger area being affected by some noise in the reduced case.

One difference that stands out is the fact that the upward motion on the west side of the Himalayas is more pronounced with higher off-centring. This is rather surprising because it does feature very strongly in the reference simulation (cf. Fig. 6.3 (top)) as well. This is an intriguing feature, and an extension to this study would be to investigate if it is specific to C-CAM or if it also exists in other models.

It is also worth noting that the difference between the two types of off-centring schemes do not reflect those found in simulations with SWiM. As one would expect, the fully off-centred scheme results in the smoother solutions in C-CAM while in SWiM the equivalent of the reduced scheme produced the smoother solutions for the height and momentum fields. This

discrepancy illustrates how findings from a purely dynamical model are only applicable to full-fledged GCMs to a limited extent.

### 6.2.5 Performance of the Existing Variable Off-Centring in C-CAM

As mentioned above, C-CAM already offers a variable off-centring scheme. This section briefly discusses the performance of this scheme to provide a comparison to the more flexible new variable off-centring scheme introduced in the next section.

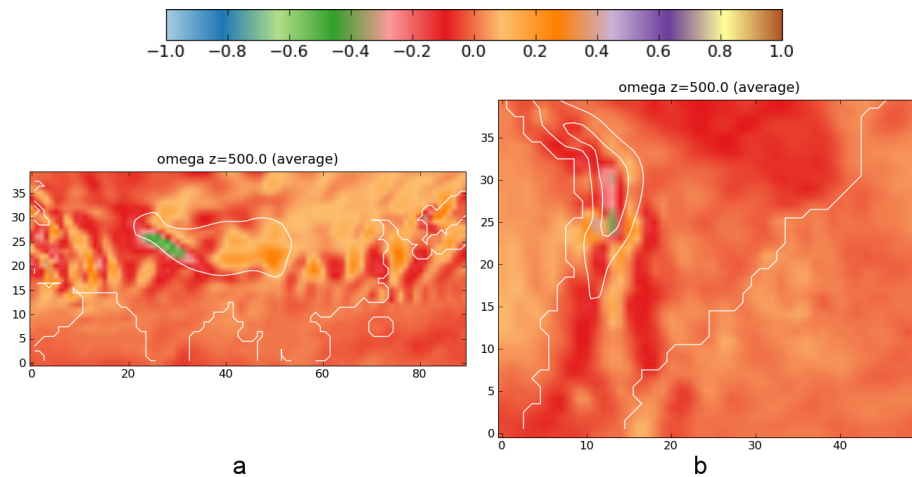


Figure 6.8: Vertical velocity  $\omega$  (in  $Pa/s$ ) at  $500hPa$  with variable off-centring at base (maximum)  $\varepsilon_a = 0.15$  and  $\varepsilon_b = 0$

Fig. 6.8 shows results obtained with the default variable off-centring scheme applied only to the mass and thermodynamic equations with the off-centring parameter set to  $\max(\varepsilon_a(x, y)) = 0.15$ , a default setting used in many C-CAM simulations. As one would expect from the findings above, the resonance is not fully removed from the equations and still affects the results. The results in fact appear slightly worse than those obtained with a constant

reduced off-centring at  $\varepsilon_a = 0.1$ . However, an improvement can be seen compared to the simulation without any off-centring in Fig. 6.3 (bottom). It is well possible, that a higher base value for the off-centring parameter might yield satisfactory results. This will not be explored further because the new variable scheme presented in the next section is much more flexible and can roughly emulate the current off-centring scheme as well.

### 6.3 A New Variable Off-Centring Scheme in C-CAM

As the previous section showed, C-CAM already manages to remove the spurious resonance effectively. However, the constant off-centring schemes in C-CAM add unnecessary numerical damping and the variable off-centring scheme currently available is rather rigid. There is also reason to doubt that the existing variable off-centring scheme effectively removes the spurious resonance. Hence, a new variable off-centring scheme is introduced and thoroughly tested in the following sections.

#### 6.3.1 The implementation of the scheme in C-CAM

In Chapter 5 variable off-centring schemes were devised and tested in the context of the shallow water model SWiM. The new scheme proposed for C-CAM follows the same algorithm as was implemented in SWiM (cf. Chapter 5). It assesses the maximum orographic height difference between any pair of neighbouring grid points in the computational domain at the start of a simulation and then scales all local off-centring parameters against this

maximum orographic height difference. This means that the preset maximum off-centring parameter is applied only in the vicinity of the largest orographic height difference in the domain. All other grid points will have a scaled, smaller off-centring parameter. Over some parts of the ocean, where the orographic height differences vanish, there is no off-centring at all and hence the centred equations are solved.

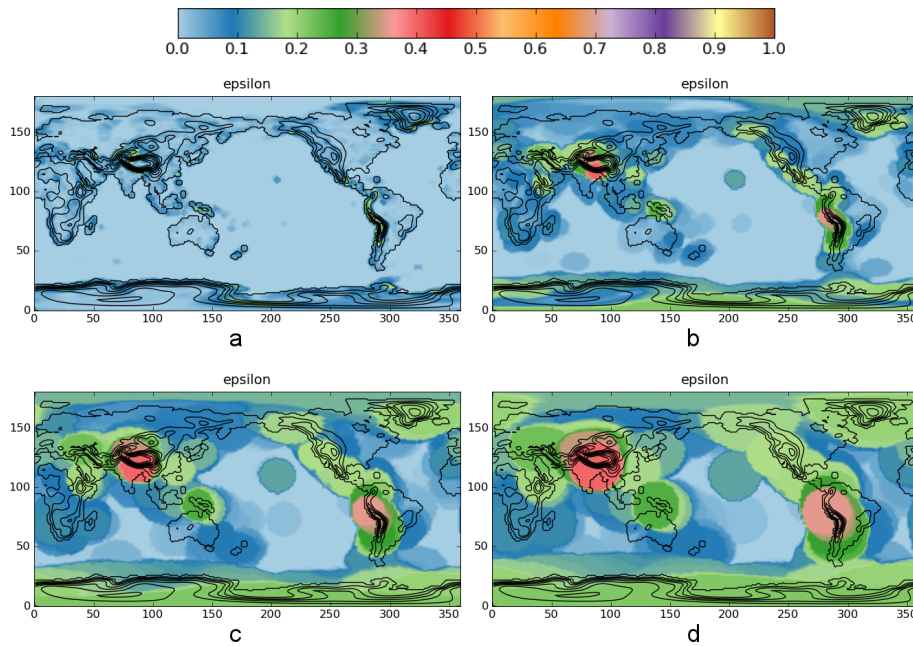


Figure 6.9: Global distribution of off-centring parameter  $\epsilon$  for base  $\epsilon = 0.4$  and no capping. Search radii are a)  $r_s = 0$  b)  $r_s = 1$  c)  $r_s = 2$  d)  $r_s = 3$ .

The new variable scheme as implemented in C-CAM is somewhat more powerful than the one used in SWiM. To be able to emulate the existing variable scheme, it is possible to cap the off-centring parameter at a value of choice. This is similar to the existing variable scheme in C-CAM where the off-centring parameter is only scaled up to a height difference of  $600m$  but constant for any height differences larger than this value. The cap in the new scheme is not defined as a maximum height difference as in the

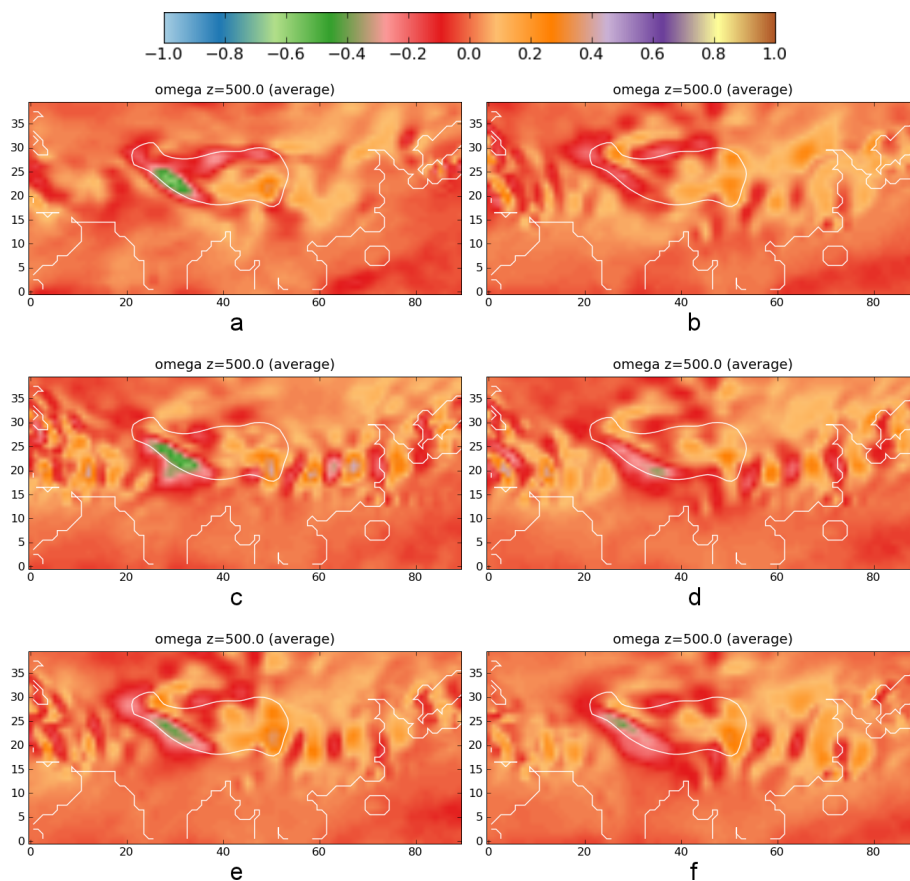


Figure 6.10: Vertical velocity  $\omega$  (in  $Pa/s$ ) at  $500hPa$  with different off-centring settings. a) reference simulation b)  $\varepsilon_a = 0.4$  and  $\varepsilon_b = 0$ . Variable off-centring with  $r_s \in \{0, 1, 2, 3\}$  (c-f) and base  $\varepsilon_a = 0.4$  and  $\varepsilon_b = 0$

existing scheme, but instead, is prescribed as a fraction of the maximum orographic height difference. With this capping mechanism, the scheme can also emulate the currently existing variable off-centring scheme in C-CAM with a suitable value of the cap. The capping property of the scheme is explained and tested in more detail in Section 6.4.1.

From the shallow water experiments in Chapter 5 it was concluded that it is useful to consider height differences within a search radius greater than one grid spacing instead of just between the grid point and its nearest neighbours. Thus, just like in SWiM, such a search radius can be defined and form the basis of the local off-centring parameter. This then means that all orographic height differences within this radius are considered and the local off-centring parameter is based on the maximum orographic height difference within the search radius. The local off-centring parameter  $\varepsilon_a|_{\text{local}}$  can then be expressed as

$$\varepsilon_a|_{\text{local}} = \frac{\Delta z_s|_{\text{local}}}{\Delta z_s|_{\text{max}}} \varepsilon_a, \quad (6.19)$$

where  $\varepsilon_a$  is the off-centring parameter in the thermodynamic and mass equations (cf. Section 6.1.3 and  $\Delta z_s|_{\text{local}}$  is the maximum orographic height difference between any two adjacent grid points within the search radius  $r_s$  and  $\Delta z_s|_{\text{max}}$  the maximum orographic height difference between any two adjacent grid points in the computational domain. Here, the search radius is defined as

$$r_s = 2r_{\text{earth}} \sin \left( s_o \frac{v_{\text{max}} \Delta t}{2r_{\text{earth}}} \right). \quad (6.20)$$

$s_0$  is a constant, which sets the search geometry whose influence will be illustrated below, and  $r_s$  corresponds to the Cartesian distance between 2 points which are separated by a distance  $s = s_0(v_{\max}\Delta t)/(r_{\text{earth}})$  on the sphere's surface.  $v_{\max}$  is chosen as  $100\text{m/s}$ , an estimated maximum value, and  $s_0$  can be set as an input parameter to the model.

With a scheme as described above, the off-centring parameters can vanish over the oceans and be generally rather low away from significant orography. The maximum off-centring parameter is only applied to grid points which are no further away from the largest orographic height difference in the domain than the distance  $r_s$ . All its properties are chosen in a way considered safe (e.g. high velocity estimates) while trying to maximise the impact of a variable scheme by achieving small off-centring parameters in the absence of significant orography. It thus applies the lessons learned from the earlier shallow water experiments to the context of C-CAM.

As the scheme only defines off-centring parameters in an offline calculation, it does not depend on actual Courant numbers. This is why the maximum wind speed has to be estimated in order to calculate a likely maximum Courant number. The grid resolution only affects the field of off-centring parameters in as much as it might change the maximum orographic height differences locally or globally.

As the input parameter  $s_0$  in Eqn. (6.20) can be set to any convenient value, there is a large range of resulting fields of off-centring parameters. Choosing to set  $s_0 = 0$  results in an off-centring scheme where every grid point may have a different off-centring parameter. This is due to the fact that only the orographic height differences with every grid point's nearest neighbours contribute to the local off-centring parameter. If one was to raise

$s_0$  to a value about half the length or width of the computational domain or larger, the scheme would transition into a constant off-centring scheme. All intermediate values of  $s_0$  lead to unique intermediate states. The formula thus reflects the same approach as was chosen for  $r_s$  in SWiM, just that instead of a maximum Courant number an estimate of the maximum velocity is used. So, while  $s_0 = 0$  results in a scheme equivalent to that for  $r_s = 0$  in SWiM, all other values of  $s_0$  do not lead to a trivial equivalent for  $r_s$  in SWiM.

How the choice of  $s_0$  impacts on the local off-centring parameters is illustrated in Fig. 6.9 which shows four examples of the global variation of the off-centring parameter for different search radii and a base (i.e. maximum) off-centring parameter  $\varepsilon_a = 0.4$ . The scheme is uncapped and thus scales linearly between zero and the maximum orographic height difference in the domain.

### 6.3.2 Evaluation Methods and Selection of Key Regions

It was discussed extensively above that off-centring schemes affect the model solutions by adding additional numerical damping throughout the domain with the aim of eliminating spurious resonance features near orography. The purpose of introducing an off-centring scheme which is variable in space is to apply this damping only where it is needed, namely in the vicinity of significant orography. Hence, to test a variable off-centring scheme means evaluating at least two issues, namely its ability to eliminate the spurious resonance near orography and to evaluate the effects of the now reduced numerical damping away from orography.

To determine the sensitivity to off-centring settings and evaluate the new variable scheme, a test setup was devised specifically for the new off-centring scheme. Instead of evaluating monthly averages, all the tests in the following are based on averages obtained from the seasons June-August (JJA) and December-February (DJF) of the years 1996-2005 with the first season considered starting in December 1996 and the last one considered ending in August 2005. The time step was set to 2 hours except for the reference simulation which, as before, was a centred simulation at a time step of  $\Delta t = 600s$ . The model was forced with monthly observational data for sea surface temperature and sea ice fractions.

As vertical velocity has an impact on rainfall, rainfall data obtained from the model was chosen as a secondary means of evaluating the variable off-centring scheme's performance. This is particularly important for the evaluation away from orography, such as the tropical oceans, where the reduced numerical damping in the variable scheme is expected to have some effect. Rainfall data were retrieved as daily averages while vertical velocities shown are always averages of instantaneous values sampled every 12 hours.

Because of the averaging over several seasons, the tests for the new scheme are not directly comparable with the simple proof-of-concept tests performed for the existing off-centring schemes earlier. However, in the interest of continuity and as a quick performance test for the new scheme, the tests shown in Section 6.2 were repeated with a set of different settings for the new variable off-centring scheme.

Fig. 6.10 provides a quick overview of the basic test results. All simulations shown in in the figure used a base  $\varepsilon_a = 0.4$  and  $\varepsilon_b = 0$ . The search radius was varied between  $r_s = 0$  and  $r_s = 3$ . Only solutions for the vertical velocity at

500hPa for the Himalayas region are shown because the tests in Section 6.2 led to the conclusion that the effect was the strongest there.

With increasing search radius, the results clearly improve in terms of the amplitudes decreasing and the wave pattern appearing less and less distinct. While for a search radius  $r_s = 0$  (Fig. 6.10c) the results are very similar to those obtained solving the centred equations at large time step (cf. Fig. 6.3c), search radii  $r_s \in \{1, 2\}$  (Fig. 6.10d,e) already achieve results comparable to those for constant off-centring. The results for  $r_s = 3$  (Fig. 6.10f) appear to have more features in common with the reference simulation than the constantly off-centred case (Fig. 6.10b). Particularly the lee side of the Himalayas shows a rather diffuse pattern for  $r_s = 3$  while it still features a rather clear wave pattern in the constantly off-centred case. The variable scheme thus shows a performance similar to the one of the constant off-centring scheme for all search radii of  $r \gtrsim 1$ .

A variable off-centring scheme likely affects different regions in different ways and to different degrees. In mountainous regions, it is possible that the weakened effective off-centring means that the resonance is not entirely removed and affects the solution negatively. In regions without significant orography, on the other hand, the solution should ideally be similar to the solution of the reference simulation.

To assess how well the new scheme performs with different settings, it is therefore best to find regions where changes in the off-centring scheme (full/reduced, constant/variable, different values of off-centring parameter, etc.) affect the solution most strongly. In other words, those regions which show the most sensitivity to the choice of off-centring scheme and its various parameters need to be identified.

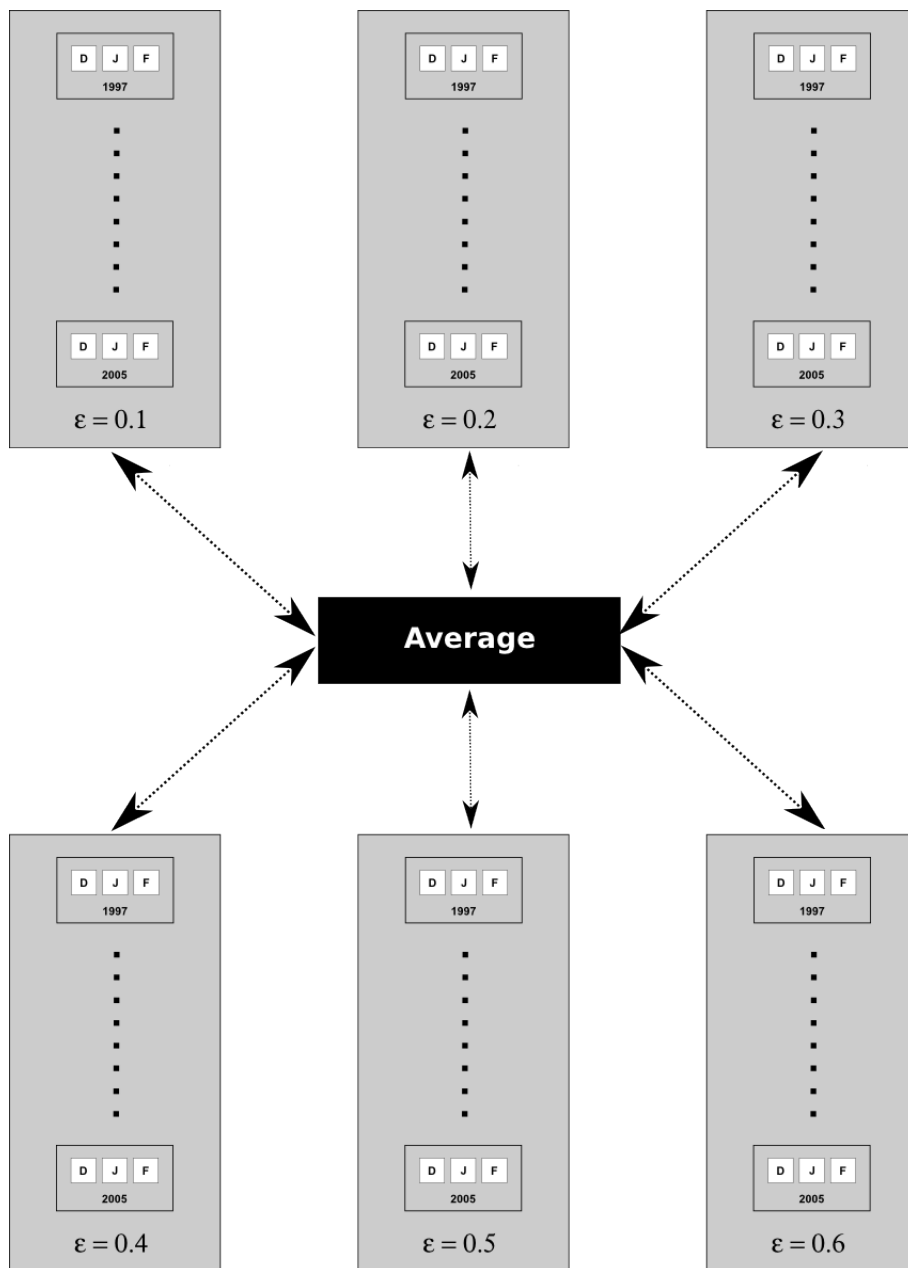


Figure 6.11: Averaging process to determine standard deviation for an ensemble of off-centring schemes (DJF simulations used as example here).

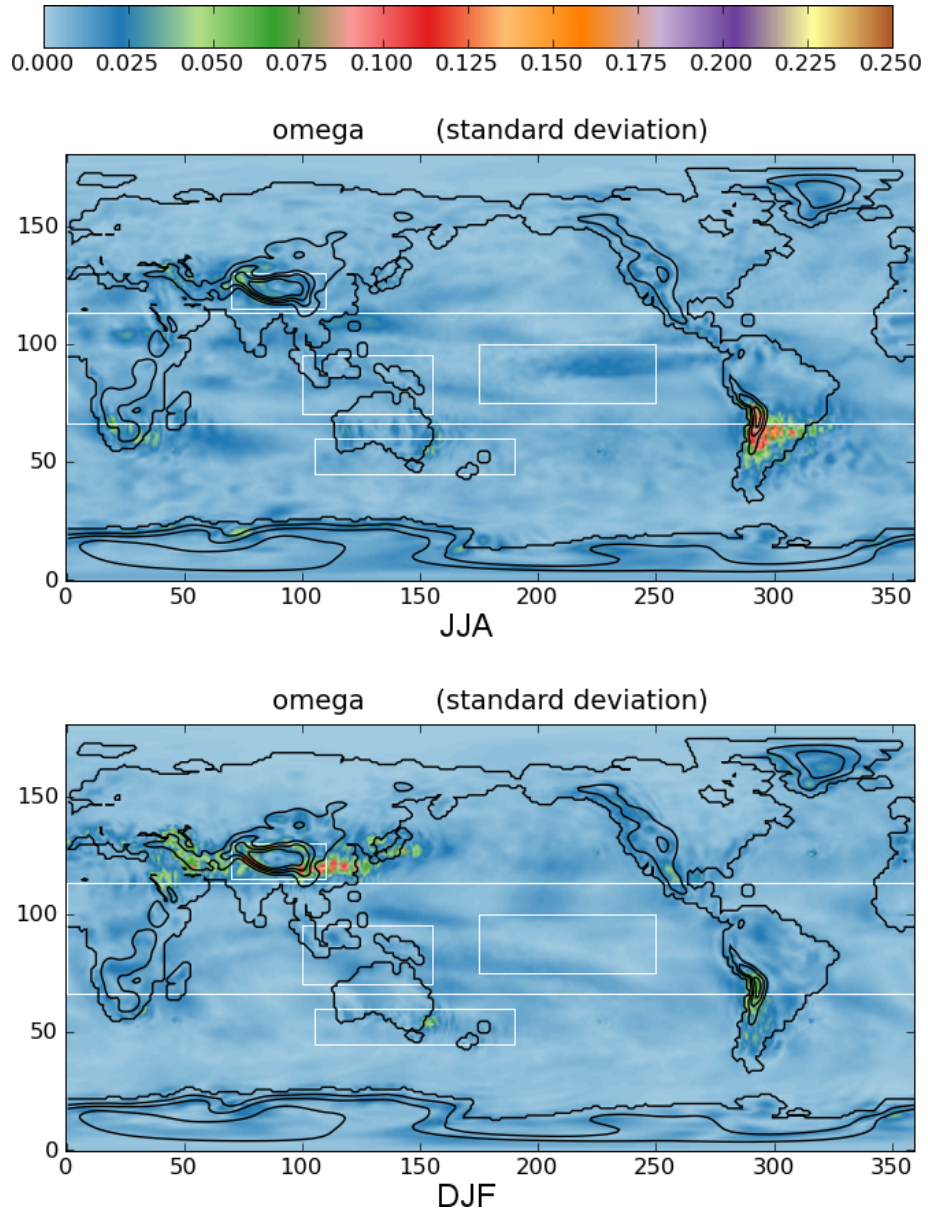


Figure 6.12: Standard deviation of vertical velocity (in  $Pa/s$ ) at  $500hPa$  for different off-centring settings from the global average over all simulations

The simplest way of assessing such sensitivity is the visual comparison as carried out above. The weakness of a simple visual comparison is that it is very subjective. A more objective approach to finding sensitive regions is to calculate the standard deviation across the simulations with different off-centring settings. Fig. 6.11 illustrates the procedure used. First, the ensemble of simulations for each season is averaged to yield an average season for every single off-centring setting (represented by the grey boxes in Fig. 6.11), then an overall ensemble mean is calculated from these average seasons (black box) and the standard deviation around the ensemble mean is calculated for both vertical velocity at  $500hPa$  (Fig. 6.12) and rainfall (Fig. 6.13).

Inspection of the figures allows for the identification of several regions of significant sensitivity. While the high sensitivity in vertical velocity is very much confined to the vicinity of more or less significant orography, the rainfall is affected on a much larger scale. Most likely as a result of the changing circulation, the effect is strongly dependent on the season. Interestingly, the regions of high sensitivity in vertical velocity and rainfall do not necessarily overlap. The vertical velocity shows high sensitivity over the Himalayas in DJF and over the Andes in JJA. Rainfall, on the other hand, is most affected over South America in DJF and over India in JJA.

In Figs. 6.12 and 6.13, a number of regions of high sensitivity can be identified. The two obvious candidates in the vertical velocity maps, are the Himalayas region and the Andes region. Being the most mountainous regions on the globe, these two regions obviously show high sensitivity to off-centring as they are subject to strong orographic forcing. As a consequence, a lack of off-centring should lead to the resonance being triggered in these regions.

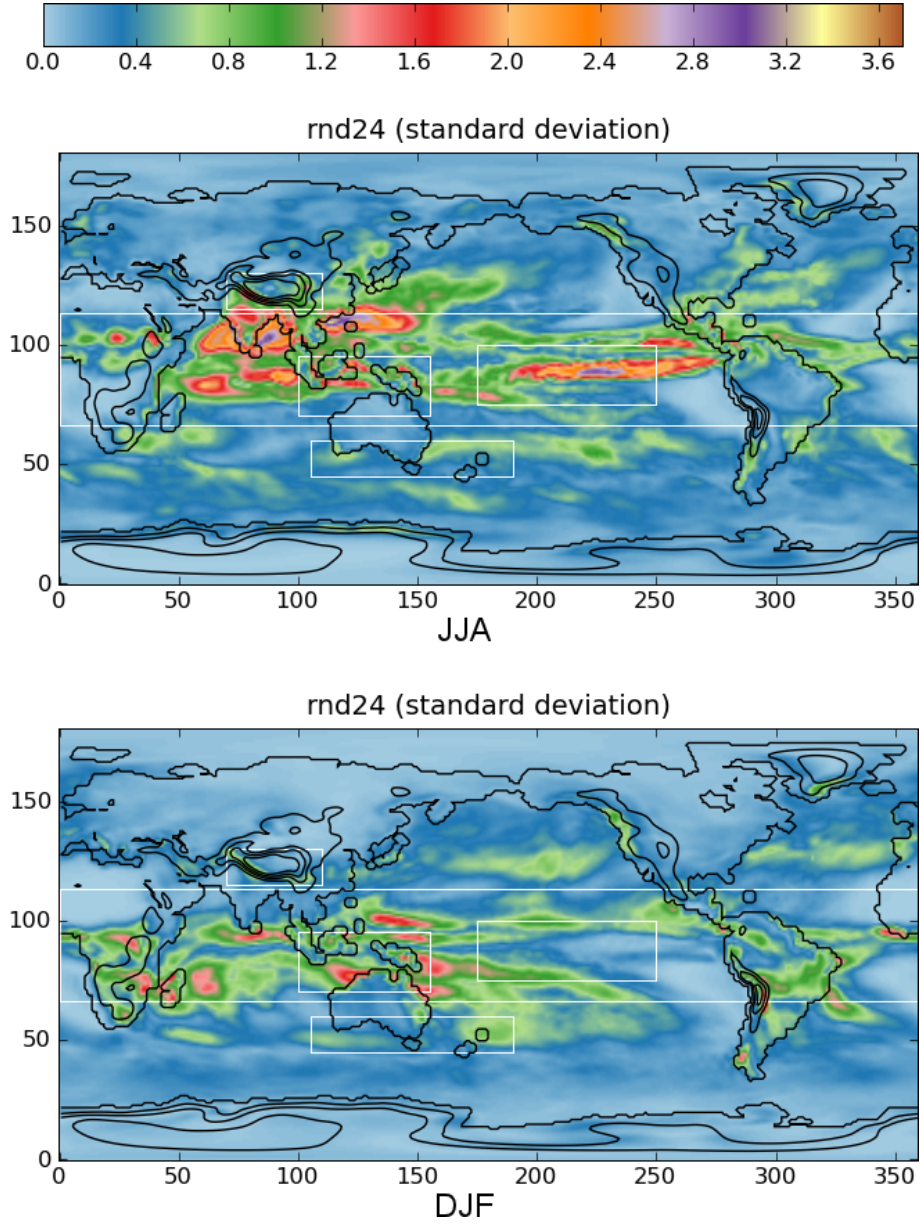


Figure 6.13: Standard deviation of daily rainfall (in *mm*) for different off-centring settings from the global average over all simulations

Based on the rainfall data, a number of other regions can be identified. As already mentioned earlier, the Indian subcontinent, including the sea to either side and Bangladesh and Burma (Myanmar), is strongly affected in JJA, the time of its monsoon season when the rainfall is significantly higher. Over central South America, the sensitivity is most obvious in rainfall for DJF.

Most of the tropical regions, regardless of land or sea areas, show some degree of sensitivity. This is particularly true over Africa, the Indian Ocean, Indonesia and some parts of the Pacific Ocean. In Africa this effect extends beyond the tropical zone into Southern Africa and Madagascar.

Particularly in DJF, there is also some effect over Southern Australia and New Zealand and both in DJF and JJA, some sensitivity can be observed over a wide area in the southern Pacific Ocean including the Australian south coast and New Zealand.

The Pacific and Atlantic Oceans show interesting sensitivity in regions that contain hardly any land mass and hence very little to no orographic forcing. As one can conclude from Fig. 6.9 these regions have very little off-centring applied to them if the search radius in the variable scheme is small.

Based on Figs. 6.12 and 6.13 and the desire to have a mixture of land and ocean, several regions were selected for an in-depth evaluation of the results. The selected regions are highlighted in Fig. 6.13. They are the Himalayas as an example of a region of significant orography, the Pacific Ocean as an example of an orography-free region and Indonesia and southern Australia and New Zealand as regions of intermediate character.

Averages for any physical quantity are only a very simple and crude tool to assess sensitivity and test the impact of a change in the off-centring scheme.

It is therefore necessary to find a means which allows a more comprehensive assessment of the changes resulting from modifications to the off-centring scheme. One such way of differentiating between model results beyond assessing the difference of their averages, is to assess changes to probability density functions (PDFs) of selected variables in the regions of interest identified above. A probability density function describes the relative probability at which a selected variable occurs at a certain value. The average is only one parameter of a PDF and showing the complete distribution of values allows for a more comprehensive evaluation of the off-centring effects discussed above.

Several estimates for probability density functions were obtained by constructing histograms of instantaneous vertical velocity and daily-averaged rainfall. Each histogram was generated using 16 bins of equal size. These bins were defined such that they covered a value range where the end points are values of probability  $\gtrsim 0.01$ . Events occurring at all grid points within the defined region were counted. Events that did not fall into any of the defined bins were ignored. For the normalisation the out-of-range values were still considered to ensure intercomparability of all PDFs. The probabilities are shown on a logarithmic axis.

While there are no reliable observations of vertical velocity, observational estimates of daily rainfall do exist. One frequently used product is that of the Global Precipitation Climatology Project (GPCP, [Adler et al., 2003](#)). Histograms are calculated from the observations in the same way as from the model and are shown for reference. It is worth noting that one should not expect changes in off-centring to necessarily bring the model closer to the observations, as model rainfall strongly depends on a variety of model features, none the least the parametrization of sub-grid scale processes, such

as convection. However, it is still useful to have the observations shown in the graphs to provide some estimate of model sensitivity compared to the size of model error.

To facilitate the discussion, the different schemes shown in comparisons have been named. The reference simulation at small time steps which solves the equations in centred form is referred to as CREF, the centred scheme simulation using a large time step is referred to as CCENT. The names of the off-centring schemes are derived from those used for the ones in SWiM. The constant scheme which off-centres all equations has been labeled CFOX, while the constant scheme which only off-centres the thermodynamic and mass equations is called CROCKS. As the new variable scheme is derived from CROCKS, the whole family of variable schemes is labeled vCROCKS. When referring to a vCROCKS scheme of a certain search radius  $r_s$ , that search radius is appended to the name, i.e. vCROCKS with a search radius  $r_s = 0$  would be referred to as vCROCKS0.

The notation used in the figures that illustrate the PDFs is that  $eps$  refers to  $\varepsilon_a$  and  $r$  to the search radius  $r_s$ . The scheme labeled as  $eps=0$  (*ref*) is CREF while  $eps=0$  refers to CCENT. Variable schemes are marked with a (*b*) after the off-centring parameter, so that a label like  $eps=0.4$  (*b*)  $r=2$ . means a vCROCKS scheme with a base off-centring parameter  $\varepsilon_a = 0.4$  and the search radius  $r_s = 2$ . As CFOX is not shown in the following figures, a value of  $\varepsilon_b = 0$  is implied in all schemes.

### 6.3.3 Evaluation in Regions with Significant Orography

As orographic forcing leads to the spurious resonance which off-centring counteracts, the main benchmark for any new scheme is whether it is able

to remove the spurious resonance in regions of significant orography. Only if the scheme succeeds in maintaining sufficient numerical dissipation in these regions to remove the spurious resonance, can it be considered an alternative to the existing schemes.

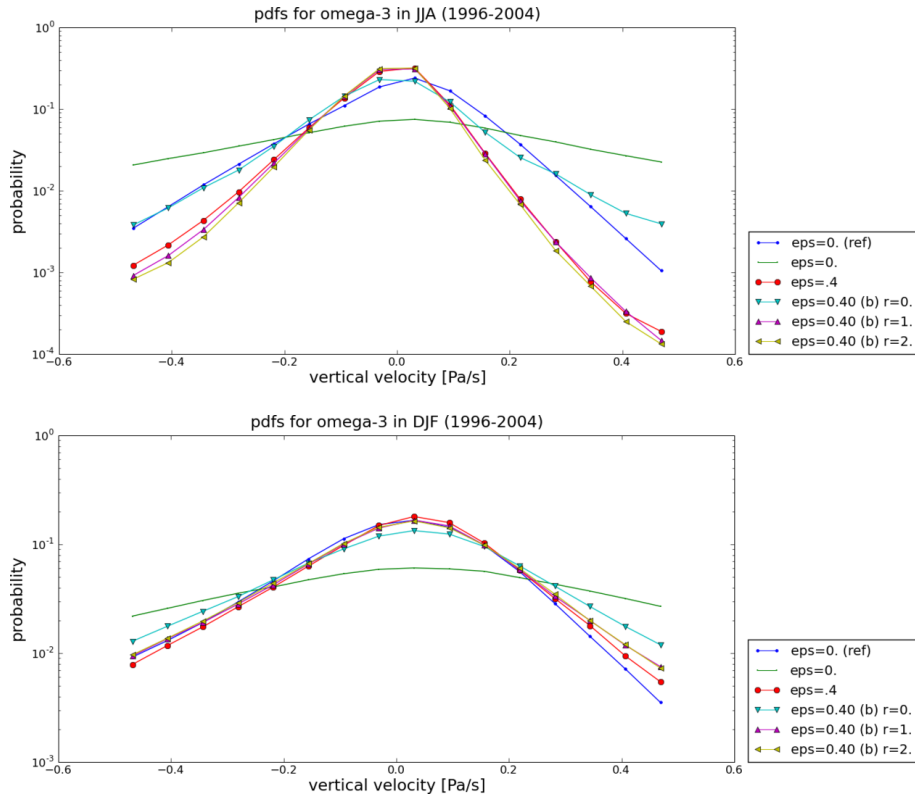


Figure 6.14: Probability density function of vertical velocity  $\omega$  (in  $Pa/s$ ) at  $500hPa$  for different off-centring settings over the Himalayas in JJA (top) and DJF (bottom)

As mentioned above, the two regions of strongest orographic forcing are the Himalayas and the Andes. Fig. 6.14 shows the PDFs for vertical velocity at  $500hPa$  over the Himalayas for the seasons December-February (DJF) and June-August (JJA). The most striking feature in the figure is the large deviation of the CCENT simulation from all other simulations. The spurious resonance leads to a standing wave pattern in this region as was shown above

(cf. Fig. 6.3c) which is reflected in a flattened PDF. High vertical velocities are much more likely to occur than in a simulation unaffected by the spurious resonance.

The performance of the various off-centring options is somewhat seasonally dependent, likely a result of the flow reversal associated with the Asian summer monsoon. All vCROCKS schemes as well as the CROCKS scheme remove velocity peaks in the expected fashion with vCROCKS0 having the least influence. In DJF the vCROCKS0 scheme performs worst in comparison with CREF, while in JJA it performs best because all other off-centring schemes appear to overdamp the solution.

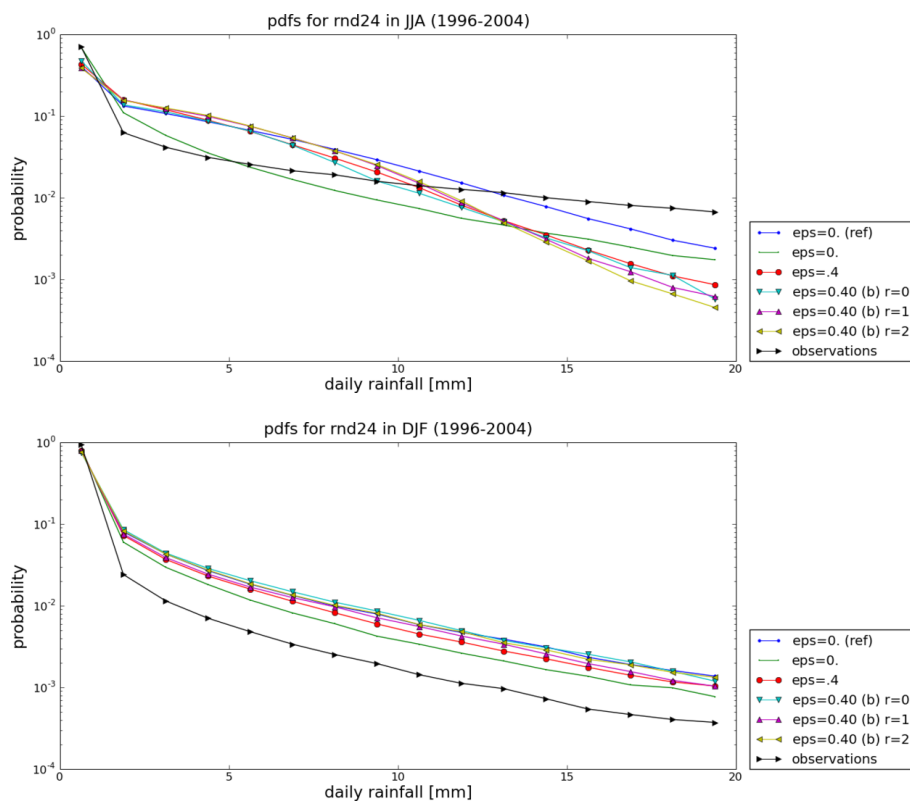


Figure 6.15: Probability density function of daily rainfall over the Himalayas in JJA (top) and DJF (bottom)

The rainfall PDFs for the Himalayas region are shown in Fig. 6.15. The first observation in the figure is that the model results differ strongly from the observations. In the dry season (DJF) the frequency of all rainfall events except the ones in the lowest bin are overestimated in all model simulations. In the Asian summer monsoon season (JJA), on the other hand, the events of the lowest class are still underestimated, medium size events are overestimated and the frequencies of large rainfall events are underestimated again.

Comparing CCENT and the various other off-centred schemes, only CCENT and CROCKS slightly deviate from CREF in DJF, while all vCROCKS schemes match up with CREF. The picture is somewhat more complex in the monsoon season (JJA) where none of the simulations at large time step yields results that are comparable to CREF. CCENT overestimates on the lowest class of events but underestimates on all higher class events relative to CREF. The off-centred simulations match CREF well for low rainfall events but underestimate more the higher the rainfall. This is less pronounced in CROCKS than it is in vCROCKS. The various vCROCKS simulations do not show a clear trend for different search radii.

#### 6.3.4 Evaluation in Regions without Orography

As the variable off-centring scheme's main improvement lies in the reduced numerical dissipation in regions without orography, these regions are another important area to test the effectiveness of the scheme. While it is hard to find a large region without any orography, the oceanic regions are almost free of orography in the test region. No ocean region showed very high

sensitivity in the standard deviation of vertical velocity in Fig. 6.12, but the Pacific Ocean proved very sensitive in rainfall.

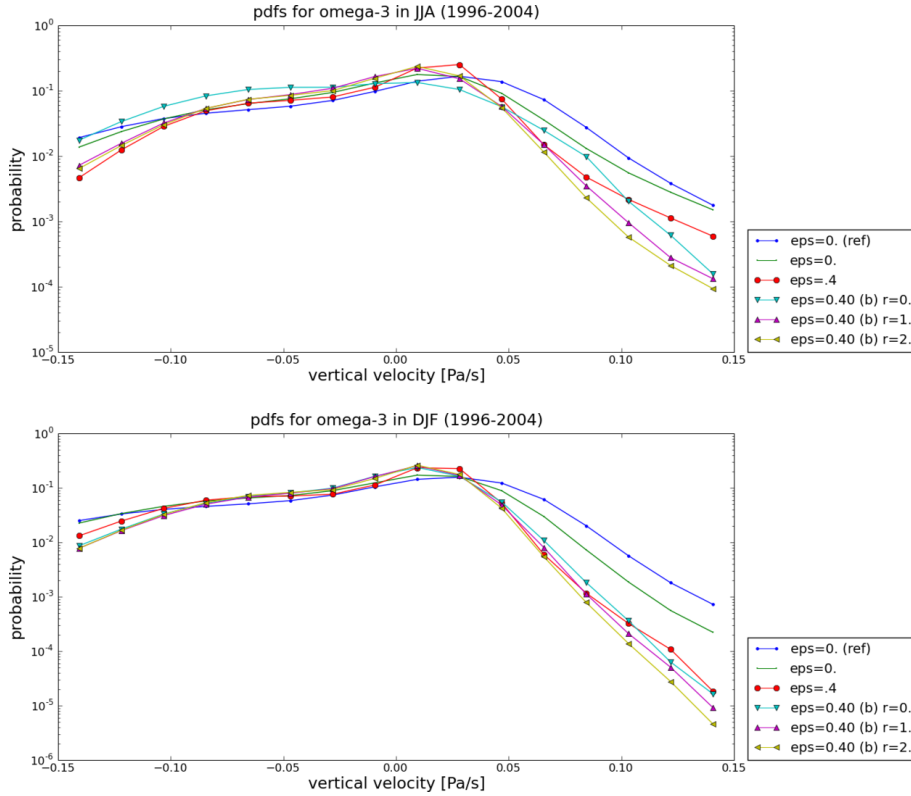


Figure 6.16: Probability density function of vertical velocity  $\omega$  (in  $Pa/s$ ) at  $500hPa$  for different off-centring settings over the Pacific Ocean in JJA (top) and DJF (bottom)

The PDFs for vertical velocity at  $500hPa$  over the Pacific Ocean are shown in Fig. 6.16. In the figure it can be seen consistently for both seasons that the CCENT simulations match the CREF simulation best, in particular for subsiding motion (positive omega). As a result of the lack of orography, the region is not affected by the spurious resonance and the CCENT scheme performs well despite its large time step. In DJF, all off-centred simulations show underestimated downward and fast upward motion. The probability of a small or vanishing vertical velocity is overestimated. The difference

between the various off-centred simulations is generally small.

The more interesting results for the off-centred simulations are those found for JJA. The probabilities for negative and vanishing vertical velocity follow the same pattern as in DJF, with the exception of vCROCKS0. CROCKS still underestimates the fast downward motion but not to the same degree as in DJF. It generally performs slightly better than vCROCKS1 and vCROCKS2, particularly for fast downward motion. vCROCKS0's features are dissimilar to both the CROCKS and the other vCROCKS schemes. While it overestimates all but the fastest upward motion's probabilities, it compares better with CREF than any other off-centred scheme for the slower downward motion. In the faster downward motion, it underestimates probabilities more than the CROCKS scheme but still less than the other vCROCKS schemes.

While no conclusion can be drawn from DJF, the PDFs in JJA indicate that CROCKS and vCROCKS0 perform best in this region.

In Fig. 6.17 the PDFs for rainfall over the Pacific Ocean are shown. The comparison of observations and numerical results shows underestimated probability for the rainfall events in the lowest class but overestimated probability for almost all other events. While CREF overestimates the frequency of occurrence of all higher rainfall events, all other schemes underestimate on the high end of the shown spectrum.

Comparing all other model simulations to the CREF one, the simulations all overestimate probabilities on the low end of the spectrum while underestimating the ones nearer the very high rainfall events. The only general exception is again the lowest class where all but the vCROCKS0 scheme

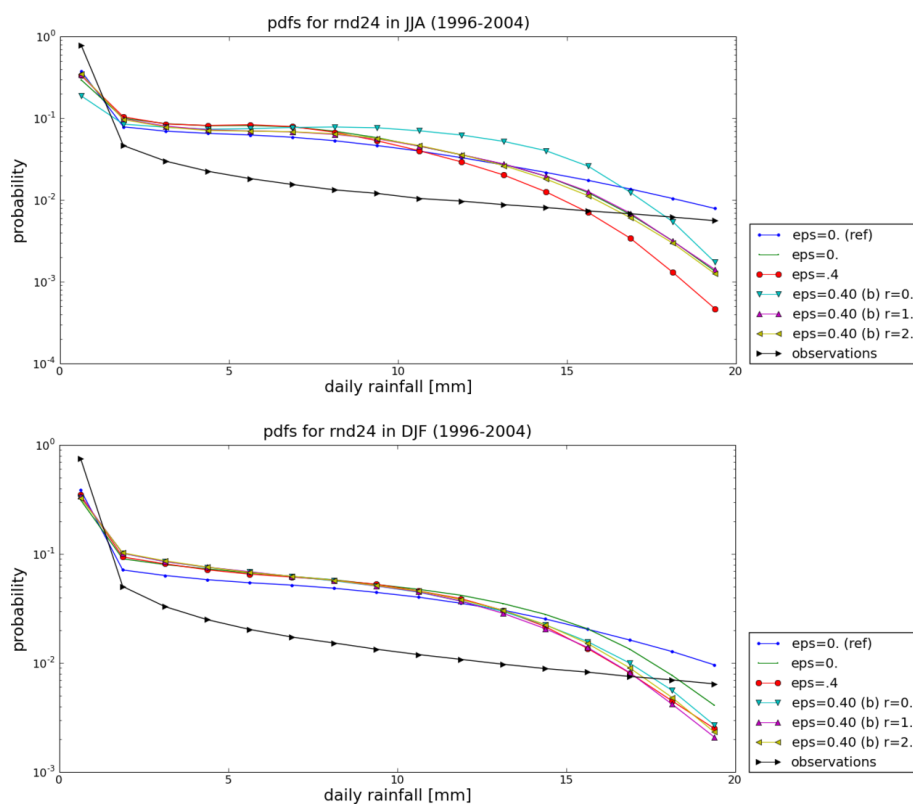


Figure 6.17: Probability density function of daily rainfall over the Pacific Ocean in JJA (top) and DJF (bottom)

match very well with CREF while vCROCKS0 underestimates the frequency of events in this class.

In DJF, only CCENT stands out as performing better than the off-centring schemes when compared to CREF. Very little difference can be seen between the different off-centring schemes with vCROCKS0 possibly performing marginally better than the other schemes.

In JJA, vCROCKS0 is a clear outlier, overestimating probabilities in all but the lowest and the three highest bins. The vCROCKS1 and vCROCKS2 schemes yield near identical results and also match up almost perfectly with CCENT (almost hiding the curve due to the overlap). This also means that these schemes perform best in comparison with CREF. CROCKS underestimates the top half of the shown spectrum and generally performs worst.

### 6.3.5 Evaluation in Regions of Intermediate Character

The previous sections tried to determine if the variable off-centring scheme was able to introduce sufficient numerical dissipation in the presence of strong orographic forcing to remove the spurious resonance and quantify the gain from removing unnecessary numerical dissipation. It used two extreme types of terrain, while Earth's landmass is generally characterised by a constant change of orography, be it large continents with a mix of plains and mountain ranges or islands with sometimes rather high mountains surrounded by the flat ocean.

It is then obvious that another important benchmark for a new scheme has to be, how it performs in these common regions of intermediate character. Two regions that show significant sensitivity in the standard deviation of daily

rainfall in Fig. 6.13 are Indonesia and northern Australia, and southern Australia and New Zealand. Particularly Indonesia exhibits strong sensitivity in either season. Hence, these two regions are investigated more closely in this section.

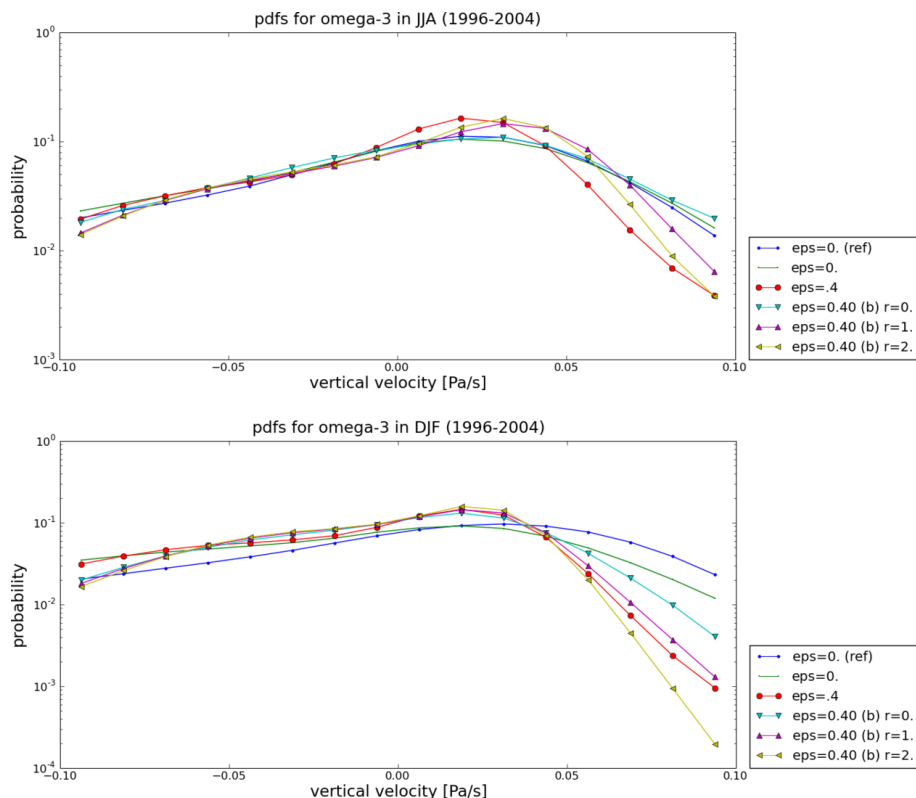


Figure 6.18: Probability density function of vertical velocity  $\omega$  (in  $Pa/s$ ) at  $500hPa$  for different off-centering settings over Indonesia in JJA (top) and DJF (bottom)

Fig. 6.18 shows the vertical velocities at  $500hPa$  over Indonesia and northern Australia. While in DJF all other simulations show higher probabilities than the CREF one for almost all upward and slow downward motion, they match up with it relatively well in the upward motion in JJA. In JJA, the CROCKS scheme shows a clear bias toward slow downward motion and as a consequence it overestimates the probabilities on the slow downward mo-

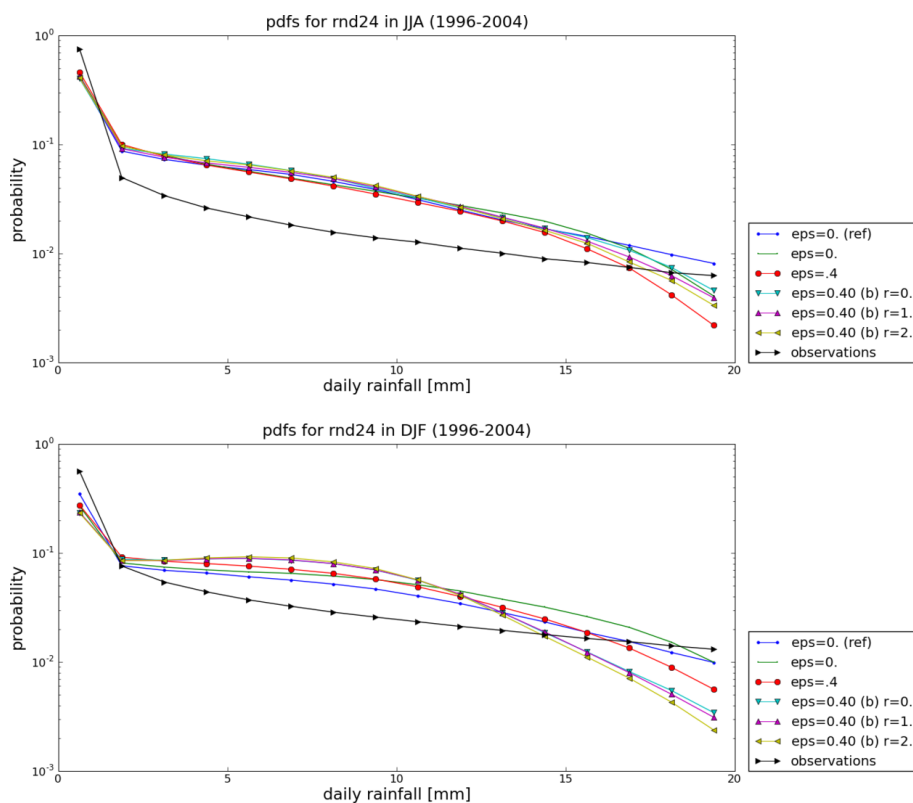


Figure 6.19: Probability density function of daily rainfall over Indonesia in JJA (top) and DJF (bottom)

tion and underestimates it for faster downward motion. vCROCKS1 and vCROCKS2 show very similar PDFs but the peak in probability is shifted towards faster downward motion with the smaller search radius (vCROCKS1) leading to more deviation from the CROCKS scheme's PDF. The CCENT and vCROCKS0 scheme clearly perform best almost matching the CREF scheme.

In JJA, the PDFs from the different simulations diverge significantly in the intermediate and fast downward motion. CCENT performs best, followed by vCROCKS0 and then vCROCKS1. CROCKS performs worse than vCROCKS1 but better than vCROCKS2.

Fig. 6.19 shows the PDFs for rainfall over Indonesia. Compared to the observations, the model simulations show almost the same behaviour as over the Pacific Ocean. As the only exception, even the CREF simulation now underestimates the probability for the two highest bins.

In JJA, all schemes underestimate the probability of high rainfall events. This is more pronounced for stronger off-centring. However, the differences between variable off-centring schemes and the CCENT scheme are small.

In DJF, the differences between the schemes are more pronounced. The CCENT scheme now shows a tendency to overestimate against the CREF scheme while the CROCKS scheme almost matches the CCENT scheme for the lower rainfall events but then diverges to underestimate the three highest bins. The variable schemes show the same trend as CROCKS but more pronounced. The low end of the spectrum is more strongly overestimated, while the high end is more strongly underestimated. Compared with CREF, CROCKS and CCENT show similar quality with CROCKS possibly outperforming CCENT by a small margin.

Fig. 6.20 shows the vertical velocities at  $500hPa$  over southern Australia and New Zealand. Similar to the Himalayas region, the CCENT simulation shows a flattened PDF here, even though the effect is less pronounced. Most likely this region is affected by the spurious resonance. In DJF, all the off-centred simulations show very similar results, underdamping in the upward motion and overdamping in the downward one.

In JJA, the picture is more complex. While vCROCKS0 resembles CCENT, so most likely does not remove the spurious resonance entirely, vCROCKS1 and vCROCKS2 are very similar to CROCKS. Due to the small difference between vCROCKS1 and vCROCKS2 and CROCKS, all three perform

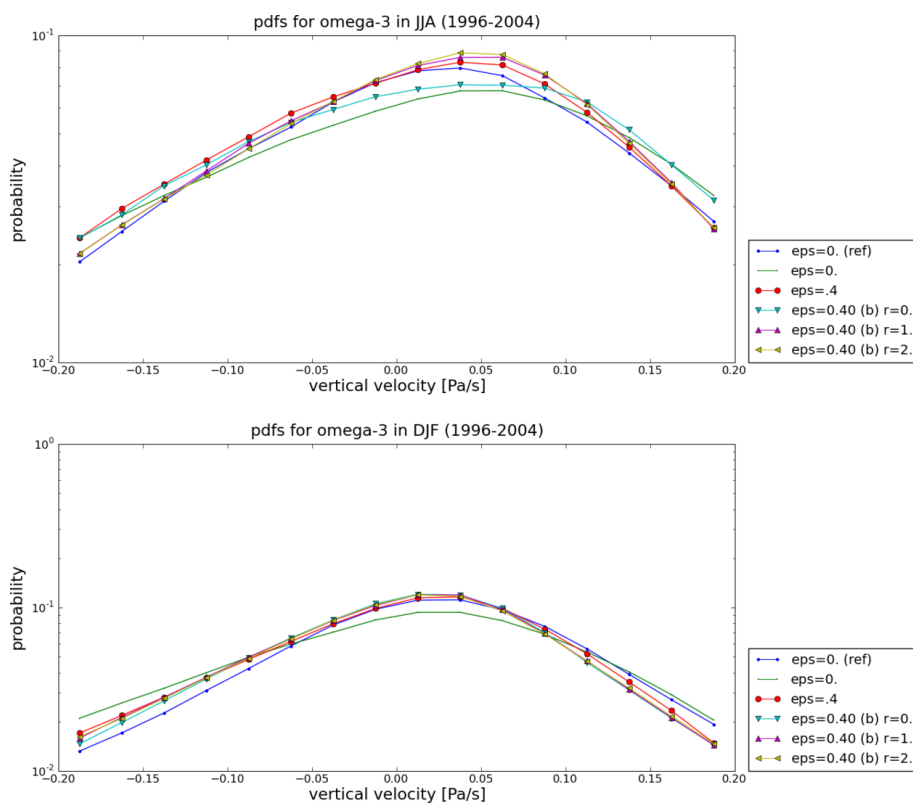


Figure 6.20: Probability density function of vertical velocity  $\omega$  (in  $Pa/s$ ) at  $500hPa$  for different off-centring settings over southern Australia and New Zealand in JJA (top) and DJF (bottom)

equally well in comparison with CREF, clearly outperforming CCENT and vCROCKSO.

In Fig. 6.21 the PDFs for rainfall over southern Australia and New Zealand are shown. The comparison with the observations shows the same bias as was found for Indonesia.

When comparing the different simulations, the most striking feature in the figure for either season is the CCENT simulation. Compared to the CREF simulation it significantly overestimates rainfall probabilities everywhere except in the lowest bin. All other schemes perform very similar to the CREF

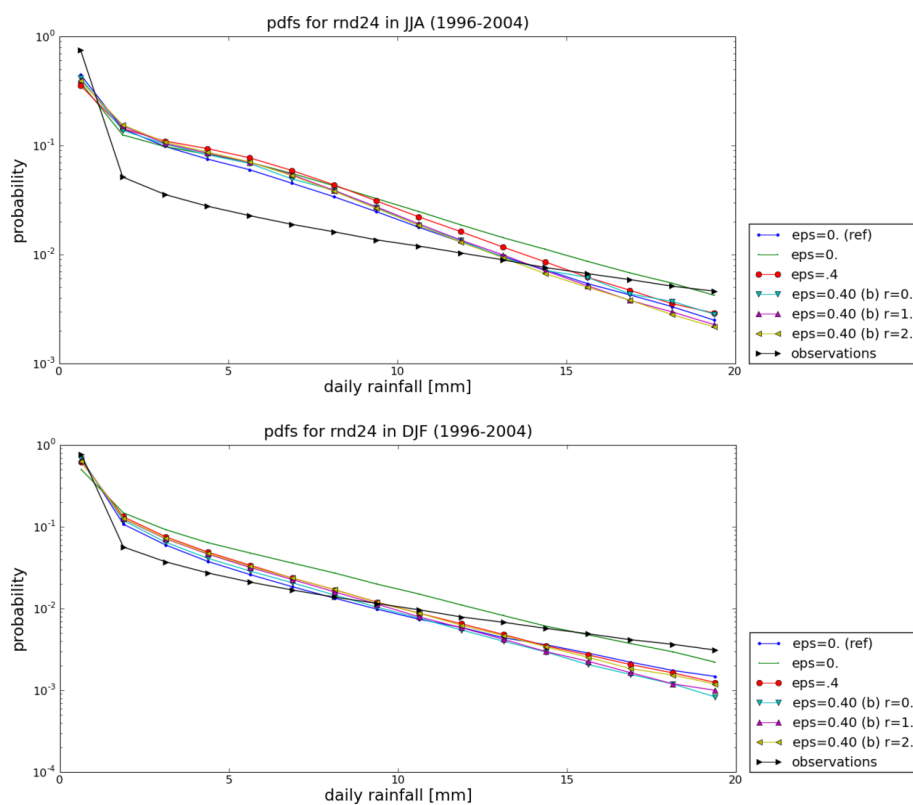


Figure 6.21: Probability density function of daily rainfall over southern Australia and New Zealand in JJA (top) and DJF (bottom)

scheme. In JJA, the vCROCKS schemes perform marginally better than the CROCKS scheme while the opposite is true in DJF.

### 6.3.6 Overall Performance of the Scheme in the Tropics

The preceding section tested the scheme in various types of orography with varying results. As a last test, the whole of the tropics is considered here. On the one hand, large parts of the tropics showed high sensitivity in the standard deviations of rainfall in Fig. 6.13. On the other hand, the tropics are a mixture of all types of terrain, spanning largely orography-free oceans as well as covering half of the Andes. The tropics should therefore give a very good measure of overall performance beyond the benchmarks above obtained from regions of relatively well defined terrain.

Fig. 6.22 shows the PDFs for vertical velocity at  $500hPa$  over the tropics. For either season the CCENT simulation matches the CREF simulation best. The off-centred simulations all show very similar behaviour with the vCROCKS0 simulation's PDF slightly tending towards the CCENT and CREF simulations' PDFs. Except for the CCENT simulation, all simulations differ greatly from the CREF simulation, particularly underestimating fast motion while overestimating vanishing motion.

In Fig. 6.23 the rainfall over the tropics is shown. The comparison of the observations with the model results can be described as almost the same as over southern Australia and New Zealand. However, the CREF simulation now still overestimates the probability even in the highest bin. The CCENT simulation comes very close to the CREF simulation and all off-centred simulations yield very similar results. vCROCKS0 performs marginally better than vCROCKS1 and vCROCKS2 in either season.

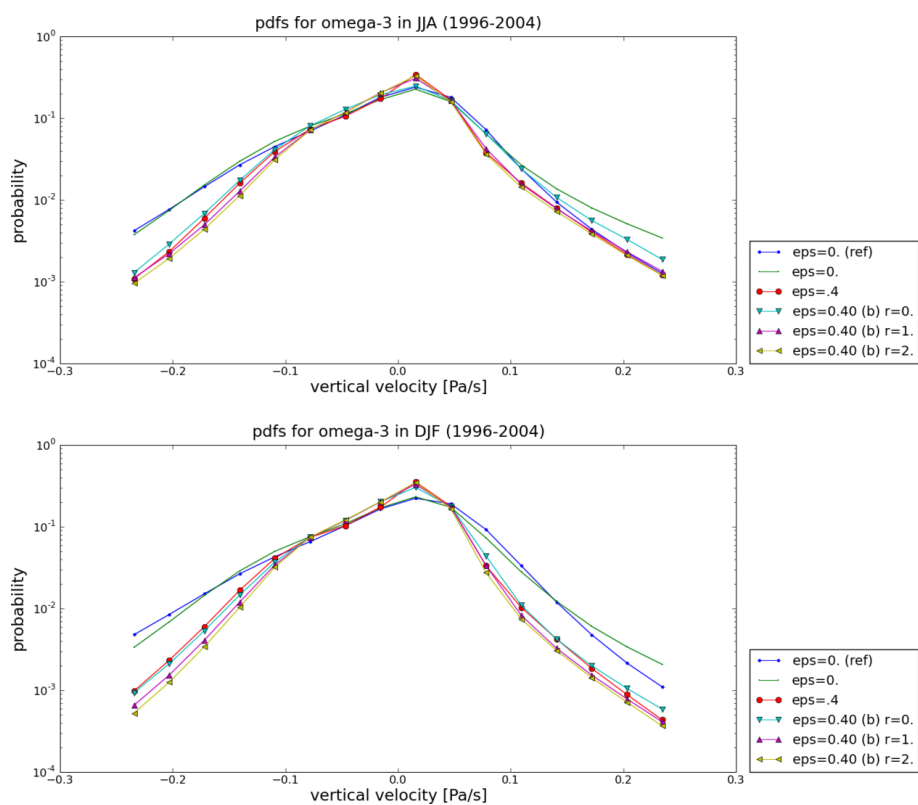


Figure 6.22: Probability density function of vertical velocity  $\omega$  (in  $Pa/s$ ) at  $500hPa$  for different off-centring settings over the tropics in JJA (top) and DJF (bottom)

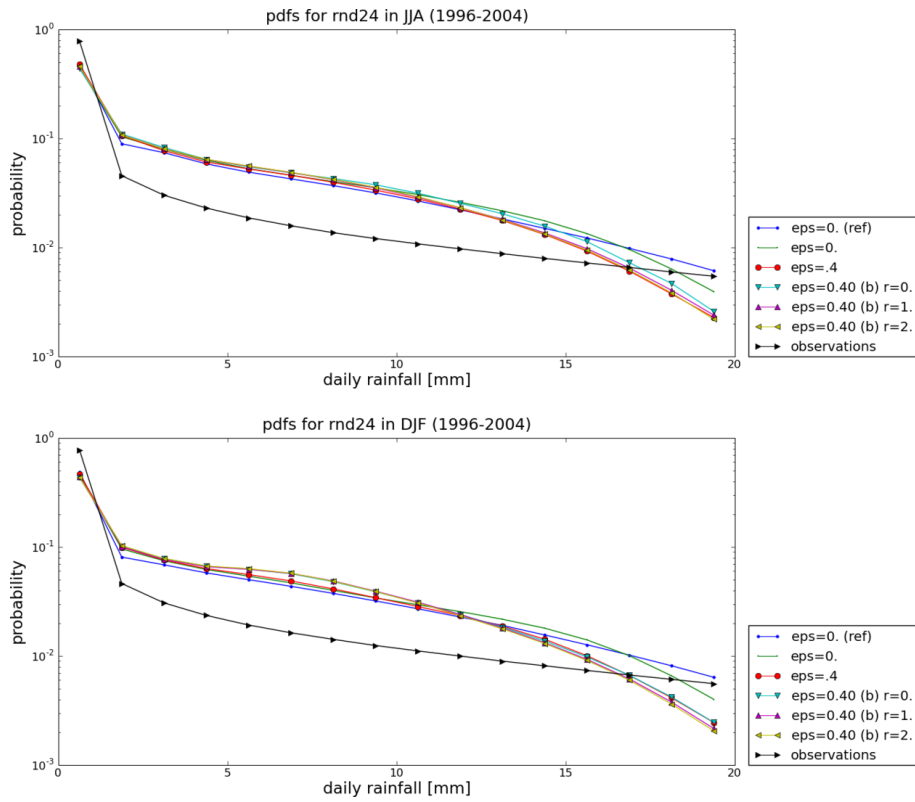


Figure 6.23: Probability density function of daily rainfall over the tropics in JJA (top) and DJF (bottom)

## 6.4 Further Sensitivity Studies with the New Scheme

The combined findings from all regions discussed in the previous section indicate that the variable scheme is likely to match the results achieved with constant off-centring. While not all regions allow a clear conclusion in that concern, both vertical velocity and rainfall PDF comparisons indicate that an improvement could be achieved with a variable scheme. In fact, different from the findings in SWiM there is evidence that a search radius  $r_s = 0$  (vCROCKSO) might be enough to ensure sufficient numerical dissipation to remove the spurious resonance. However, a vCROCKSO scheme clearly has difficulties to remove the spurious resonance over significant orography as could be seen in Fig. 6.14. In an attempt to reconcile sufficient numerical dissipation over significant orography with minimal dissipation over regions free of orography, the following explores modifications to the variable scheme and studies how sensitive the PDFs shown earlier are to such modifications.

### 6.4.1 Sensitivity to Capping the Off-Centring Parameter

One conclusion that could be drawn from the tests of the new scheme in Section 6.3.2 was that a variable scheme at search radius  $r_s = 0$  performed rather well away from orography but could not maintain enough numerical dissipation near significant orography. Furthermore, since the scheme was uncapped, it had the weakness that only at the largest orographic height differences the equations were off-centred at the set base (or maximum) off-centring parameter. This could easily lead to the resonance being triggered near orography of smaller but still significant height differences.

To address these problems, a capping mechanism similar to the one in the existing C-CAM variable off-centring scheme (cf. Section 6.1.3) was introduced into the new variable scheme. Just as the existing variable off-centring scheme, a capped scheme scales the off-centring parameter for a range  $0 < \Delta z_s \leq \Delta z_s|_{\max}$  where  $\Delta z_s$  is the maximum orographic height difference between a grid point and any of its nearest neighbours and  $\Delta z_s|_{\max}$  is the orographic height difference where the off-centring parameter reaches its maximum. All orographic height differences of  $\Delta z_s|_{\max}$  or greater will then result in the maximum off-centring parameter being applied.

In the following, different caps for the orographic height difference are tested. The cap  $c$  is defined such that Eqn. (6.19) becomes

$$\varepsilon_a|_{\text{local}} = \begin{cases} \frac{\Delta z_s|_{\text{local}}}{c \Delta z_s|_{\max}} \varepsilon_a & \text{for } \Delta z_s|_{\text{local}} \leq c \Delta z_s|_{\max} \\ \varepsilon_a & \text{for } \Delta z_s|_{\text{local}} > c \Delta z_s|_{\max} \end{cases}, \quad (6.21)$$

where  $\Delta z_s|_{\text{local}}$  is the maximum orographic height difference between two adjacent grid points within the search radius  $r_s$  and  $\Delta z_s|_{\max}$  the maximum orographic height difference between any two adjacent grid points in the computational domain.

As a scheme at search radius  $r_s = 0$  performed relatively well away from the mountains in the uncapped scheme, the capping is tested with this search radius. The goal of the modification is then to see more numerical damping over significant orography while the orography-free regions should be largely unaffected. Furthermore, some positive effect should be seen in the regions of intermediate character.

In the following, the capping was tested with caps of  $c = 0.8$  and  $c = 0.6$ , i.e. the off-centring parameter scales linearly up to 80% ( $c = 0.8$ ) or 60%

( $c = 0.6$ ) of the maximum orographic height difference in the domain. Only those PDFs which show significant differences are shown. The caps are displayed in the figure legends as *cap*.

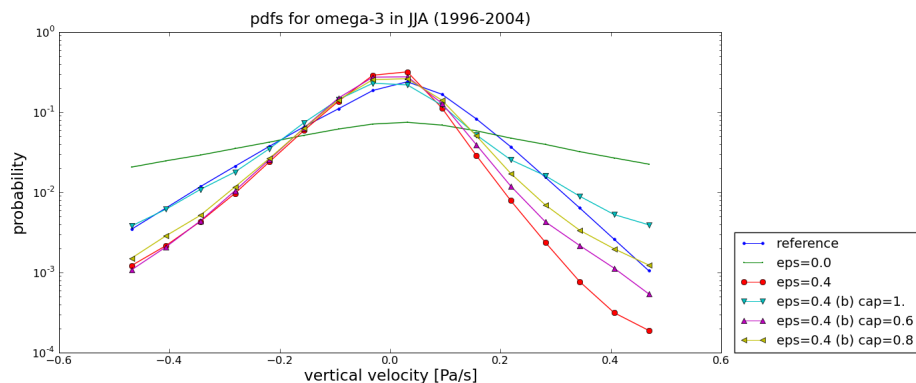


Figure 6.24: Probability density function of vertical velocity  $\omega$  (in  $Pa/s$ ) at  $500hPa$  for different off-centring settings over the Himalayas in JJA. Comparison of capped, uncapped and constant schemes at search radius  $r_s = 0$ .

Fig. 6.24 shows the vertical velocity PDFs for JJA at  $500hPa$  over the Himalayas. The first observation in the figure is that the capping has significant impact on the PDFs. Both capped schemes are visibly damped in comparison with the uncapped scheme. The scheme with cap  $c = 0.8$  only overestimates the probability in the highest positive velocity (fast downward motion) bin but underestimates them everywhere else. This effect is even more pronounced for a cap  $c = 0.6$ . While the capped schemes do not overestimate probabilities of fast downward motion any more, they do underestimate upward motion which the uncapped scheme estimates fairly well. In the upward motion, hardly any difference exists between the capped schemes and the CROCKS scheme. In DJF, the differences are generally smaller than in JJA and therefore not shown.

The rainfall PDFs for JJA in the Himalayas region are shown in Fig. 6.25.

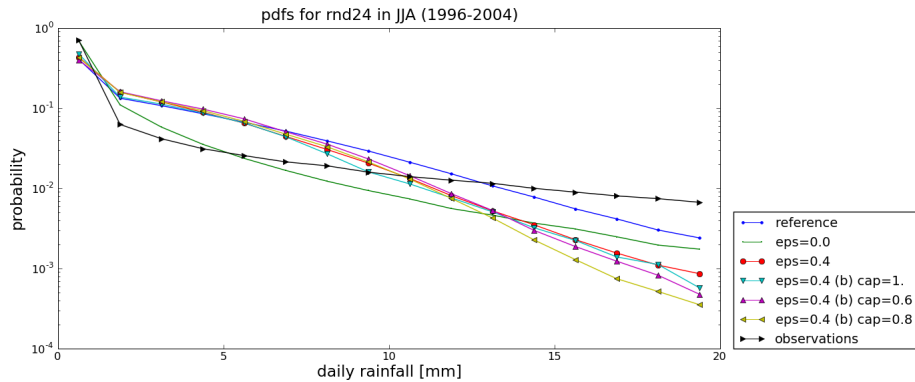


Figure 6.25: Probability density function of daily rainfall for different off-centring settings over the Himalayas in JJA. Comparison of capped, uncapped and constant schemes at search radius  $r_s = 0$ .

A slight shift of the PDF can be noticed in the probability of intermediate range rainfall events and a larger shift for the higher rainfall events. While in the intermediate range the capped schemes both perform marginally better and underestimate probabilities less, they underestimate the probabilities in the high rainfall events more than the uncapped scheme by a bigger margin. The effect is even stronger for the larger cap value  $c = 0.8$  and CROCKS clearly outperforms the capped schemes in the high rainfall events. As DJF shows no obvious differences, the PDFs for that season are omitted here.

The vertical velocity PDFs at  $500hPa$  over the Pacific Ocean for JJA are shown in Fig. 6.26. Except for the two bins of fastest upward motion, the capped schemes still overestimate probabilities on upward motion but less than the uncapped scheme. On the two fastest upward motion bins, they underestimate slightly more than the CCENT scheme but less so than the CROCKS scheme. This is also true for the downward motion, with the CROCKS scheme only underestimating less in the two highest bins. The capped scheme with cap  $c = 0.8$  performs best of all the variable schemes.

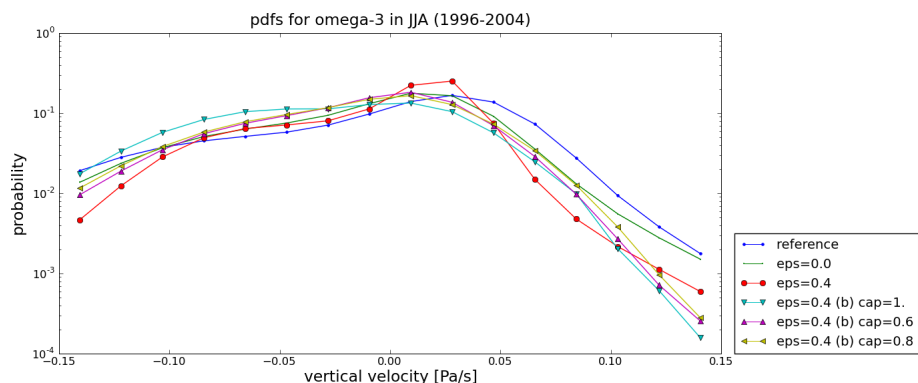


Figure 6.26: Probability density function of vertical velocity  $\omega$  (in  $Pa/s$ ) at  $500hPa$  for different off-centring settings over the Pacific Ocean in JJA. Comparison of capped, uncapped and constant schemes at search radius  $r_s = 0$ .

No significant differences can be observed in the PDFs for DJF and the PDFs for that season are not shown.

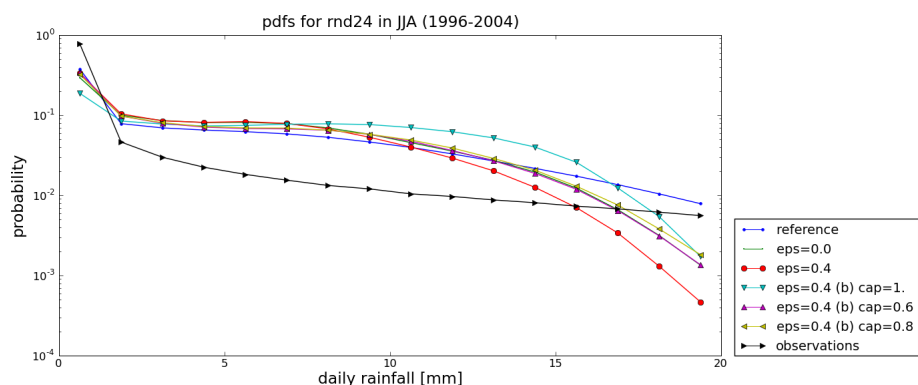


Figure 6.27: Probability density function of daily rainfall for different off-centring settings over the Pacific Ocean in JJA. Comparison of capped, uncapped and constant schemes at search radius  $r_s = 0$ .

Fig. 6.27 shows the rainfall PDFs for JJA over the Pacific Ocean. The capped schemes both yield similar results. They overestimate the probabilities for the intermediate range less and underestimate on the extreme events. However, the cap  $c = 0.8$  leads to a PDF which is almost identical with that

of the CCENT scheme and both capped schemes outperform the CROCKS scheme. The capped scheme with cap  $c = 0.8$  performs marginally better than that with cap  $c = 0.6$ . No significant change can be observed in DJF and the season is thus not shown.

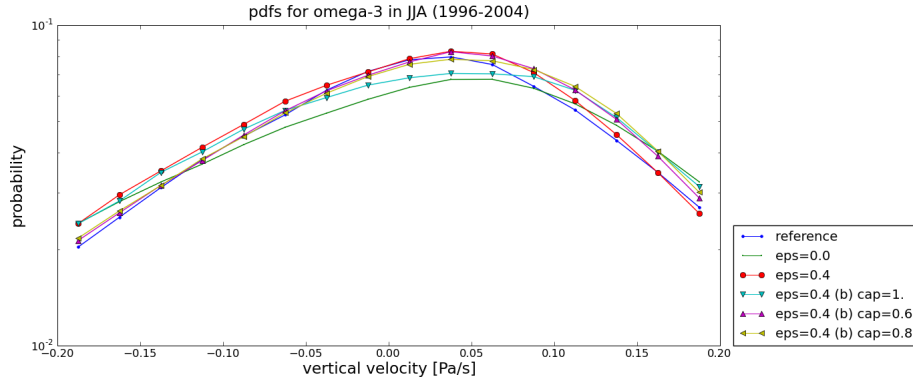


Figure 6.28: Probability density function of vertical velocity  $\omega$  (in  $Pa/s$ ) at  $500hPa$  for different off-centering settings over southern Australia and New Zealand in JJA. Comparison of capped, uncapped and constant schemes at search radius  $r_s = 0$ .

Fig. 6.28 shows the vertical velocity PDFs at  $500hPa$  for JJA over southern Australia and New Zealand. The capping has visible impact on the PDFs so that, in the upward motion, the probabilities from both capped schemes match the CREF scheme very well. In the slow downward motion they overestimate the probabilities by a smaller margin than the uncapped scheme underestimates them. For fast downward motion, the capped schemes yield the same probabilities as the uncapped scheme. The capped schemes thus perform best with the cap  $c = 0.8$  where that cap yields slightly better results for slow downward motion.

The rainfall PDFs over southern Australia and New Zealand for DJF are shown in Fig. 6.29. The performance of the uncapped scheme and the capped scheme with cap  $c = 0.8$  are very similar. The capped scheme with cap

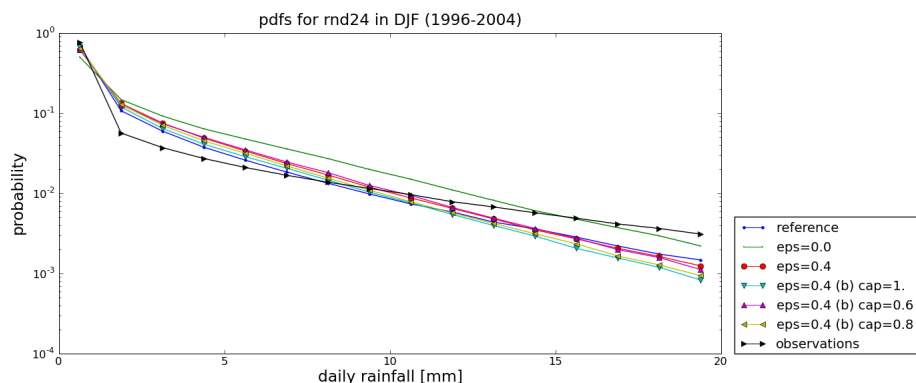


Figure 6.29: Probability density function of daily rainfall for different off-centring settings over southern Australia and New Zealand in DJF. Comparison of capped, uncapped and constant schemes at search radius  $r_s = 0$ .

$c = 0.6$  yields almost the same PDF as the CROCKS scheme. This means that it underestimates less for the lowest class of rainfall events, overestimates more for lower rainfall events and underestimates less for high rainfall events than the other variable schemes. Due to the complex nature of the differences described, it is impossible to judge which of the three variable schemes performs best. No significant differences can be seen in the PDFs in JJA and the season is omitted in the figure. The same applies to the PDFs over Indonesia.

#### 6.4.2 Sensitivity to the Scaling of the Off-Centring Parameter

The capping as tested in the previous section already resulted in some improvement but generally did not have the impact on the PDFs one would hope for. Hence, this section explores modifications to the scaling function used to scale the off-centring parameter according to orographic height differences. In the default scheme as used in the previous section, the off-centring

parameter scales linearly with distance. The term  $\Delta z_s|_{\text{local}} / (\Delta z_s|_{\text{max}})$  in Eqn. (6.19) can be replaced with a term of higher order. The following investigates the impact of a quadratic term and an exponential decay instead of the default linear one. In order to vary only one parameter of the scheme at a time, the capping was removed from the simulations again. Instead, search radii of  $r_s \in \{1, 2\}$  were chosen for the tests to ensure that the numerical dissipation was not too low over significant orography.

### Quadratic Scaling

The simplest way of modifying the linear variable scheme is to change it to a quadratic one. The off-centring parameter then becomes

$$\begin{aligned} \varepsilon_a|_{\text{local}} &= \left( 1 - \left( \frac{\Delta z_s|_{\text{local}}}{\Delta z_s|_{\text{max}}} + 1 \right)^2 \right) \varepsilon_a \\ &= - \left( \left( \frac{\Delta z_s|_{\text{local}}}{\Delta z_s|_{\text{max}}} \right)^2 + \frac{2 \Delta z_s|_{\text{local}}}{\Delta z_s|_{\text{max}}} \right) \varepsilon_a. \end{aligned} \quad (6.22)$$

While the quadratic decay means faster scaling for small orographic height differences, there should be more net off-centring in the domain. For all points, except maximum and no off-centring, the local off-centring parameter will be larger in this scheme than it was in the linear scheme. Thus, at same search radius more damping is introduced locally in comparison.

Fig. 6.30 shows the vertical velocity PDFs at  $500hPa$  over the Himalayas. The quadratic scaling function only affects vCROCKS2 in DJF. All the PDFs for the other variable schemes are almost identical. Where the other schemes match the CREF simulation's PDF well in the upward motion, the

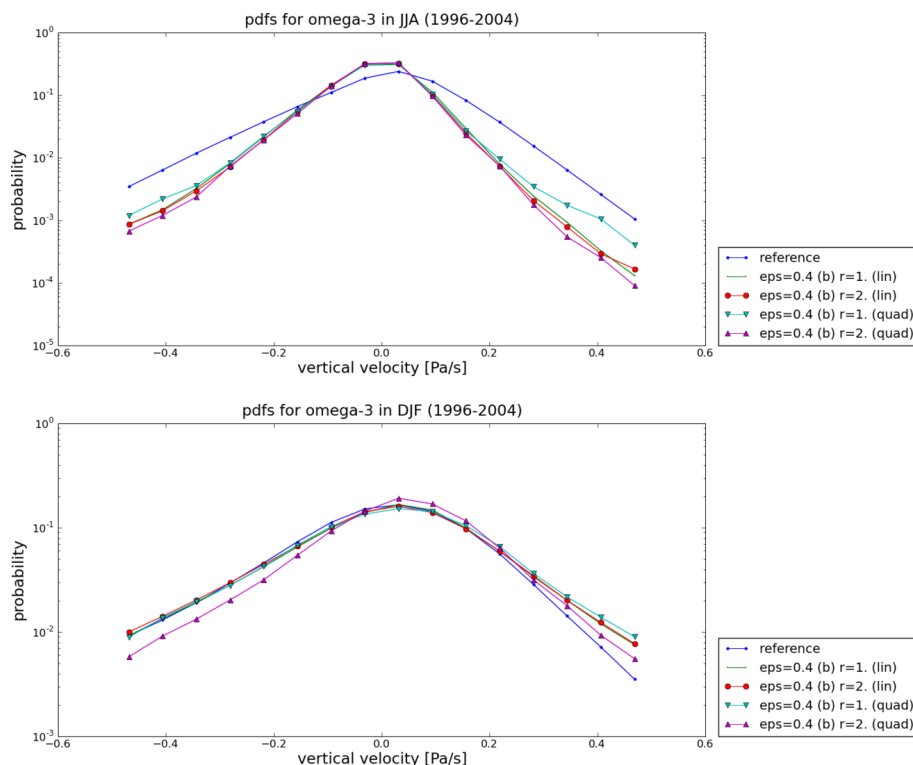


Figure 6.30: Probability density function of vertical velocity  $\omega$  (in  $Pa/s$ ) at  $500hPa$  over the Himalayas in JJA (top) and DJF (bottom). Comparison of linearly and quadratically scaling variable  $\varepsilon_a = 0.4$  (base) at search radii  $r_s \in \{1, 2\}$

vCROCK2 scheme underestimates their occurrence when scaled quadratically. The probabilities for slow downward motion are overestimated in vCROCK2 with quadratic scaling but similar to CREF in all other variable schemes. The occurrence of fast downward motion is overestimated less when using vCROCK2 with quadratic scaling.

In JJA, it is the vCROCK1 scheme with quadratic scaling that stands out. It performs well for fast motion in either direction and matches the quality of the other schemes everywhere else. Particularly for fast downward motion the difference is significant. The vCROCK2 scheme with quadratic

scaling underestimates marginally more than the other schemes in the fast motion of either direction and also matches the other schemes everywhere else. However, the difference is greater between vCROCKS1 with quadratic scaling and all the other schemes than it is for vCROCKS2 with quadratic scaling. Overall, the vCROCKS1 scheme with quadratic scaling probably performs best in this region. This is mainly due to the reasonably large impact in JJA.

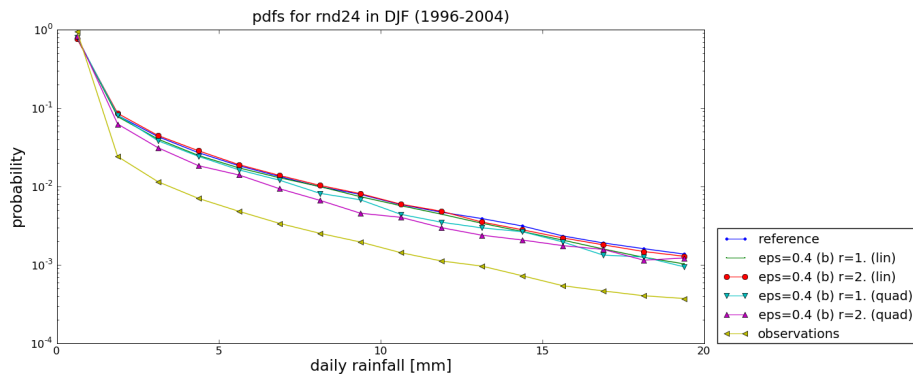


Figure 6.31: Probability density function of daily rainfall over the Himalayas in DJF. Comparison of linearly and quadratically scaling variable  $\varepsilon_a = 0.4$  (base) at search radii  $r_s \in \{1, 2\}$

The rainfall PDFs for DJF in the Himalayas region are shown in Fig. 6.31. Both quadratically scaled schemes underestimate the rainfall everywhere. As the linearly scaled schemes perform well and match up with the CREF scheme in this season, that means that the quadratic schemes both perform worse compared to the reference simulation. There is little effect on the rainfall in JJA (not shown).

Fig. 6.32 shows the PDFs for vertical velocities at  $500hPa$  over the Pacific Ocean. While the quadratic schemes separate from the linear schemes in the upward motion in JJA, the picture is more complex in the downward motion. In the upward motion, the probabilities are higher than in the quadratic

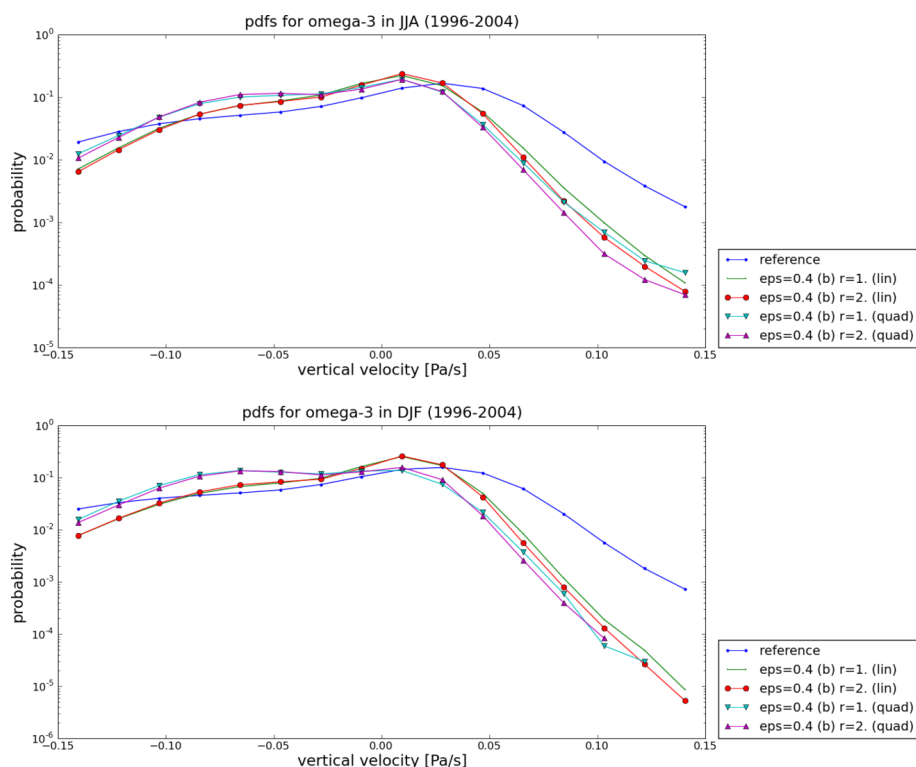


Figure 6.32: Probability density function of vertical velocity  $\omega$  (in  $Pa/s$ ) at  $500hPa$  over the Pacific Ocean in JJA (top) and DJF (bottom). Comparison of linearly and quadratically scaling variable  $\varepsilon$  (base) at search radii  $r_s \in \{1, 2\}$

schemes except for very slow upward motion. This means that for the most part, the quadratic schemes overestimate more but underestimate less in the fast upward motion and the very slow upward motion. No difference can be found between the two quadratic schemes in this range. In the downward motion, vCROCK2 with quadratic scaling underestimates more than the linear schemes everywhere, while this only applies to the slow downward motion for vCROCK1 and quadratic scaling. However, it only performs better than its linear counterpart in the fastest downward motion bin.

In the upward motion, the trend is the same in DJF as in JJA. The behaviour

is also the same in the downward motion except for the fact that the PDFs for the quadratic schemes appear to cut off on the highest (vCROCKS1 quadratic) and second highest (vCROCKS2 quadratic) bins exhibiting vanishing probability there. They therefore underestimate everywhere except for the second highest bin in vCROCKS1 with quadratic scaling. It is hard to judge which scheme performs best in this region but the linear schemes probably compare marginally better, overall.

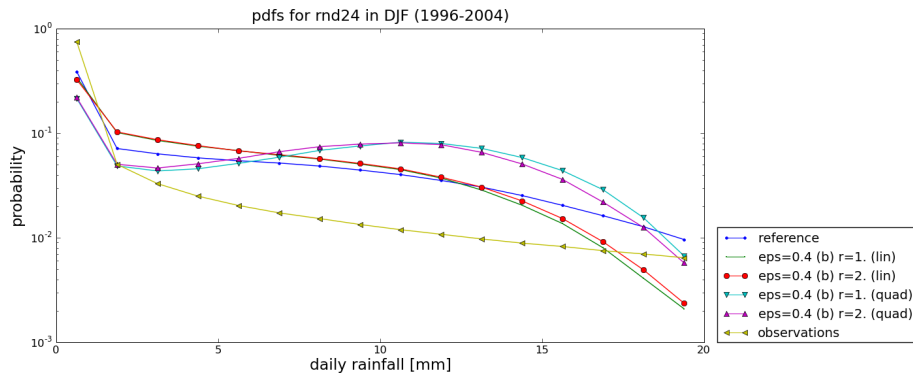


Figure 6.33: Probability density function of daily rainfall over the Pacific Ocean in DJF. Comparison of linearly and quadratically scaling variable  $\varepsilon$  (base) at search radii  $r_s \in \{1, 2\}$

The rainfall PDFs for DJF in the Pacific Ocean region are shown in Fig. 6.33. The impact of the quadratic scaling is qualitatively the same in either season, hence JJA is omitted. While the differences between the two schemes of the same class (linear/quadratic) are small, there is significant impact from the change in scaling function. The low rainfall events all show underestimated probability even where the linear schemes overestimate the frequencies. For intermediate and high rainfall categories the quadratic schemes overestimate but underestimate again on the highest rainfall events shown. In either season, the linear schemes yield better results in comparison with the CREF scheme with the vCROCKS2 scheme performing slightly better

than vCROCKS2.

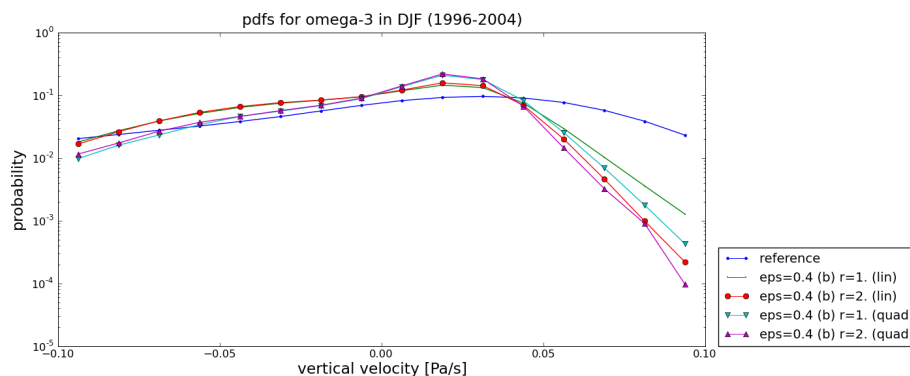


Figure 6.34: Probability density function of vertical velocity  $\omega$  (in  $Pa/s$ ) at  $500hPa$  over Indonesia in DJF. Comparison of linearly and quadratically scaling variable  $\varepsilon = 0.4$  (base) at search radii  $r_s \in \{1, 2\}$

Fig. 6.34 shows the vertical velocity PDFs at  $500hPa$  for DJF over Indonesia. The quadratic schemes underestimate on the fast upward motion and overestimate less on both the slow upward and the slow downward motion. On the fast downward motion, they then underestimate more than their linear counterparts.

Taking the results from both seasons into consideration, the linearly scaled vCROCKS1 scheme still performs best. Between the two quadratic schemes, vCROCKS1 clearly outperforms vCROCKS2.

The rainfall PDFs for Indonesia for DJF are shown in Fig 6.35. The quadratic schemes match on the lowest bin while the linear schemes underestimate the frequency of occurrence in that bin. In the second bin, the quadratic schemes overestimate more than the linear schemes. For the whole intermediate type events, the quadratic schemes overestimate less than the linear schemes but then also underestimate more for high rainfall events. Overall, it is hard to draw a conclusion of which scheme performs best

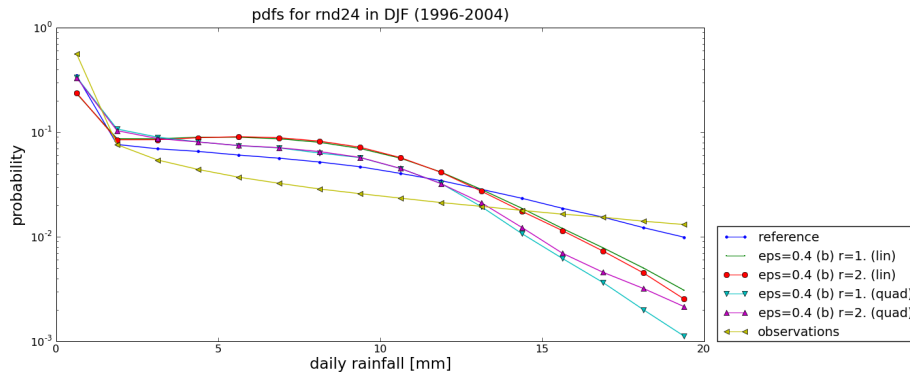


Figure 6.35: Probability density function of daily rainfall over Indonesia in DJF. Comparison of linearly and quadratically scaling variable  $\varepsilon = 0.4$  (base) at search radii  $r_s \in \{1, 2\}$

but the linear vCROCKS1 scheme is likely to slightly outperform all other schemes. Because of slight differences in high rainfall in DJF, vCROCKS2 has to be judged as performing better than vCROCKS1. As the quadratic scaling has little impact in JJA, the results are not shown.

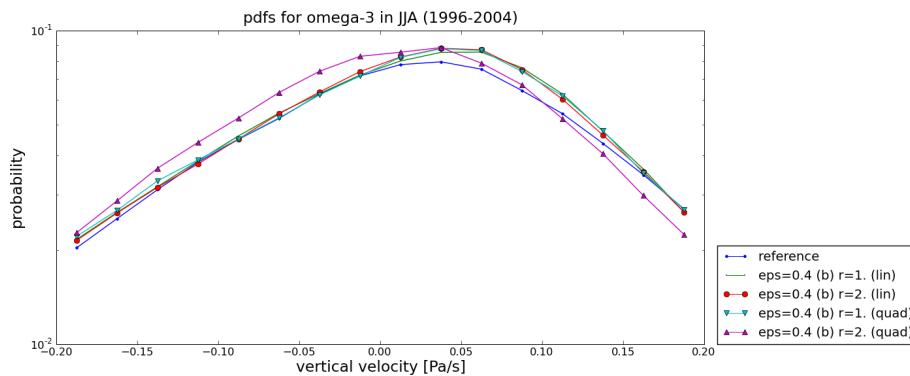


Figure 6.36: Probability density function of vertical velocity  $\omega$  (in  $Pa/s$ ) at  $500hPa$  over southern Australia and New Zealand in JJA. Comparison of linearly and quadratically scaling variable  $\varepsilon = 0.4$  (base) at search radii  $r_s \in \{1, 2\}$

In Fig. 6.36 the PDFs for vertical velocities at  $500hPa$  over southern Australia and New Zealand in JJA are shown. The quadratic vCROCKS1

scheme and the linear schemes are grouped together with very little difference. However, the quadratic vCROCKS2 scheme shifts the peak in probability from downward motion towards vanishing motion. As the whole PDF is shifted, it then overestimates more on the upward motion but less on the downward one, even underestimating on fast downward motion. The result of this shift is that the quadratic vCROCKS1 and the linear schemes perform equally well, while the quadratic vCROCKS2 scheme performs worse overall.

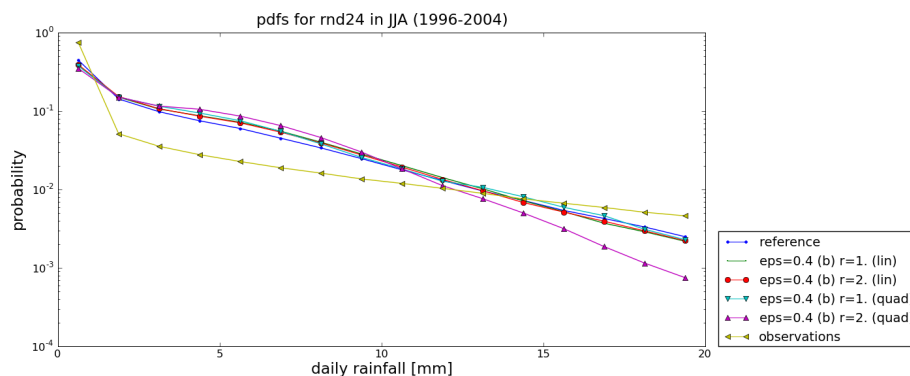


Figure 6.37: Probability density function of daily rainfall over southern Australia And New Zealand in JJA. Comparison of linearly and quadratically scaling variable  $\varepsilon = 0.4$  (base) at search radii  $r_s \in \{1, 2\}$

Fig. 6.37 shows the rainfall PDFs for JJA over southern Australia and New Zealand. Only the quadratic vCROCKS2 scheme stands out overestimating on the intermediate range events and significantly underestimating on the high rainfall events. It thus performs significantly worse than the other schemes. The DJF season is not shown because all schemes show similar results.

### Exponential Scaling

The change of scaling function proved to have some impact on the PDFs. However, particularly over the orography-free and intermediate type regions the effect was not as desired and tended to deteriorate the performance of the schemes. Hence, testing another scaling function holds the potential of improving this weakness of the quadratic scaling. As the quadratic function generally introduced more numerical damping, the scaling function introduced here is an exponential function of the form

$$\varepsilon_a|_{\text{local}} = 1 - \exp\left(-5 \times \left(\frac{\Delta z_s|_{\text{local}}}{\Delta z_s|_{\text{max}}}\right)^2\right) \varepsilon_a. \quad (6.23)$$

For this exponential scaling function, the off-centring parameter first falls off slower than in the linear case but faster than in the quadratic case. From about 80% of the maximum orographic height difference, the off-centring parameters will then always be smaller than in both the linear and the quadratic case.

As this scaling function leads to virtually the same PDFs as the linear one, only one example of these PDFs is shown. Wherever there is a slight difference, the differences are such that the shape of the PDF remains virtually unaltered thus still resulting in almost the same relative probability distribution. The lack of effect from the exponentially scaling scheme becomes particularly striking in Fig. 6.38 where the search radius affected parts of the PDF strongly. Even in this context, the PDFs of same search radius but different scaling function are almost identical.

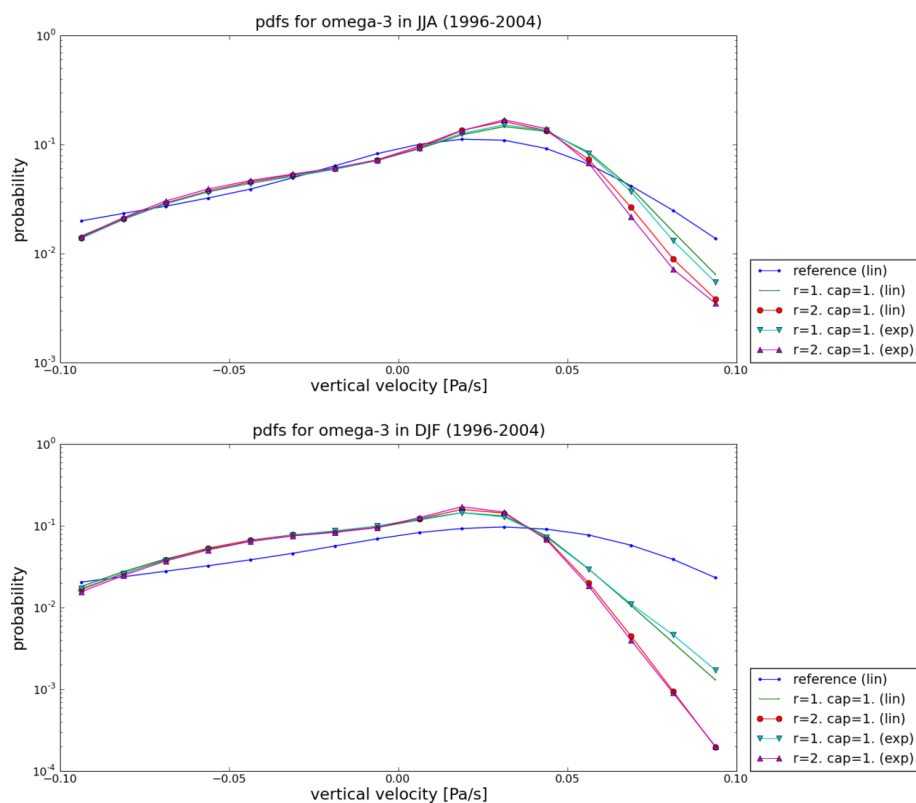


Figure 6.38: Probability density function of vertical velocity  $\omega$  (in  $Pa/s$ ) at  $500hPa$  over Indonesia in JJA (top) and DJF (bottom). Comparison of linearly and exponentially scaling variable  $\varepsilon = 0.4$  (base) at search radii  $r_s \in \{1, 2\}$

## 6.5 Discussion

This chapter introduced C-CAM, a semi-Lagrangian, semi-implicit GCM. It identified the impact of the spurious resonance on C-CAM simulations and tested how effectively the off-centring schemes presently available in C-CAM remove the spurious resonance.

Following on from the insights gained from testing C-CAM without off-centring and with different off-centring schemes and parameters, it then suggested a new variable off-centring scheme for C-CAM. This off-centring

scheme was based on the scheme successfully used in the shallow water model SWiM earlier.

Testing in the context of C-CAM indicated that a variable scheme may make it possible to gain accuracy over regions of little or no orography while maintaining sufficient numerical damping over significant orography to remove the spurious resonance. The schemes with search radii  $r_s > 0$  generally showed good agreement with the CROCKS scheme, which for  $r_s = 0$  was only true away from significant orography.

A common observation in the vertical velocities was that the off-centring schemes often reduced the relative probability of downward motion occurring. In the rainfall, the general trend was a shift of heavy rainfall towards the intermediate class of events. This effect is generally more pronounced in the rainy season and increases with higher search radius  $r_s$ .

Overall, the results indicated that a scheme of small search radius may be preferable because it yields the best results away from significant orography and in intermediate orography type regions. However, it also became clear that a scheme of small search radius had difficulties to maintain sufficient numerical damping over significant orography.

To address the issue of insufficient numerical damping over mountains without having to raise the search radius, the scheme was capped at a fraction of the maximum orographic height difference between two neighbouring grid points. This meant that more orographic features of significant height difference were off-centred with the maximum off-centring parameter. At the same time, regions of little or no orography were still largely unaffected by this modification.

The capped scheme was able to stabilise the vertical velocities over significant orography but there was also some evidence that it might negatively affect rainfall in these areas. While the benefit was sometimes small, the capping showed a beneficial effect in the orography-free and intermediate type regions. This was particularly true over the Pacific Ocean where it improved the rainfall in JJA dramatically measured against the reference simulation of small Courant numbers. These results also indicated that capping with a cap of  $c = 0.6$  generally results in relatively small gain over one with a cap of  $c = 0.8$ . The beneficial effect in the absence of significant orography clearly outweighed the small negative effect on rainfall over significant orography.

To further improve the results, the scaling function was next replaced to scale the off-centring parameter with a quadratic or exponential function. While the exponential function did not seem to have any effect on the PDFs, the quadratic function proved to have major impact particularly on rainfall over the Pacific Ocean. Unfortunately, the quadratic function tended to shift probabilities such that the resulting PDFs generally compared worse with the reference simulation than did the PDFs of the linear scheme. Again, this was particularly true over the Pacific Ocean.

Summing up the conclusions drawn from the experiments conducted with CCAM, it can be considered sensible to use a variable scheme in combination with capping at a high cap value, i.e.  $c > 0.6$ . From the tests of scaling functions presented here, it appears reasonable to use linear scaling. Linear scaling yielded the best results while being the least expensive.

## Chapter 7

# Conclusions

The main goal of this thesis was to investigate the effects of various approaches designed to remove spurious orographic resonance as is commonly observed near orography in models that use semi-Lagrangian, semi-implicit advection schemes. As the techniques usually employ non-equal weights in the treatment of the arrival and departure points in the semi-Lagrangian scheme, such approaches are referred to as "off-centring". Off-centring techniques result in additional numerical damping that is beneficial in removing the spurious resonance near orography, but as traditional approaches apply it equally throughout the domain, numerical damping is introduced in regions where it should not be necessary, such as over the oceans. A particular goal of this thesis was therefore to design and investigate "minimal" off-centring schemes through the application of off-centring to only a subset of the equations and through the application of spatially varying off-centring settings.

As a first step, an analytical assessment of the effects of off-centring previously conducted by [Rivest et al. \(1994\)](#) was extended to investigate the

effects of off-centring only the height equation in the shallow water set of equations. The reduced scheme was examined for stability using the same analysis that Rivest et al. (1994) subjected their full off-centring scheme to. A careful analytical analysis showed that, unlike for the scheme devised by Rivest et al., the resulting resonance condition did not entirely rule out resonance. This is consistent with the work of Payne (2008) who found that off-centring was needed in all equations in order for the solution to stay bounded.

For the purpose of investigating the various off-centring options, SWiM, a custom-built shallow water model, was then designed and various commonly used off-centring approaches were applied and tested in the model. As a first step, the simulations performed by Rivest et al. (1994) were repeated with SWiM and a similar threshold for the required minimum off-centring parameter was found. As a next step, the reduced off-centring scheme (ROCKS) using only the height equation was investigated. As predicted by Payne (2008), mild instability could be observed and the long term solutions may develop into a resonant state. However, there was also some evidence which suggested that in the short term the solutions obtained with this approach might actually be of better quality than those obtained with fully off-centred equations (FOX). There was some indication that the short term solutions for the height and momentum fields may be smoother and more similar to a reference simulation with centred equations and small time steps under the reduced scheme than they are under the full off-centring scheme. The long-term development of the kinetic energy fields seemed less noisy in the FOX scheme. As this discrepancy remains unexplained, the behaviour of height and momentum fields was weighted as more significant.

The findings from the numerical experiments with the traditional, constant off-centring schemes were then used to design an approach that allows for spatially varying off-centring parameters, the so-called variable off-centring scheme. This scheme was meant to reduce numerical damping even further by only adding damping where it was necessary due to the spurious resonance. As the spurious resonance is triggered by orographic forcing, the variable scheme introduced an off-centring parameter which depended on local orographic height differences. The goal of this approach was that the scheme would introduce sufficient numerical damping near orography while altering the original equations gradually, less with growing distance from orography.

The numerical experiments conducted with a range of different variable schemes in SWiM indicated that a variable scheme based on full off-centring (vFOX) suffers from significant instability in the momentum and height fields and is therefore not a viable option. There appears to be no benefit from the off-centring scheme at all with the variable off-centring parameter possibly even boosting the impact of the instability resulting from the spurious numerical resonance.

The variable single-equation off-centring scheme (vROCKS) showed no such signs of instability beyond those already known from its constant equivalent. The stability of the system could be ensured for about the same amount of integration time as in the constant scheme. Judging by the smoothness of the solutions and their resemblance with those obtained in the reference simulation, it became evident that smooth solutions required the consideration of more than just immediate orographic height difference taking into account orographic height differences between more distant grid points to calculate the local off-centring parameter. This led to the introduction of

the notion of a search radius to set optimal off-centring parameters. In conclusion, the shallow water equation experiments showed that the most likely successful approach to "minimum" off-centring is one that off-centres only a certain subset of the equations (e.g., the height equation in the shallow water case) and uses spatially varying off-centring parameters based on orographic height differences within a search radius greater than the grid spacing.

Having demonstrated the utility of variable off-centring in the shallow water equations within certain limits, the approach was transferred to a full GCM, CSIRO's semi-Lagrangian, semi-implicit model C-CAM. Based on the earlier results, the focus was on the evaluation of the variable off-centring scheme applied to a subset of the equations. Analogously to the height equation, only the temperature and mass equations in C-CAM were subject to variable off-centring, while the momentum equations were solved with a centred scheme.

The new variable off-centring scheme (vCROCKS) was subjected to a series of tests and sensitivity studies in C-CAM. The tests were prepared by first identifying the regions most sensitive to changes in the off-centring scheme. A closer examination of vertical velocity and rainfall was then conducted for these regions. As for any off-centring scheme the first test of a variable approach is that it must remove the spurious resonance near orography. At the same time, variable off-centring schemes should show a visible effect in regions away from orography because they reduce the level of numerical damping in those regions. As a consequence, three types of regions were investigated, namely regions of significant orography, regions free of orography and regions having a mixture of both. It should be noted again that due to the complexity of contemporary GCMs, the interpretation of the results of a

single change, like that to the off-centring settings, can be difficult and unambiguous results are often hard to achieve. Nevertheless, some significant conclusions could be drawn from the tests.

The early tests already indicated that variable schemes were able to yield competitive results. Simple visual comparisons for regions of significant orography showed that even a simple linear scheme with intermediate search radius was able to almost reproduce the results obtained with a traditional, constant off-centring scheme. The more detailed study of probability density functions revealed more details which added a level of complexity to these findings. It emerged that in the absence of significant orography it was desirable to only consider the nearest neighbours as the basis for the local off-centring parameter. However, such a scheme was still affected by the spurious resonance in the presence of significant orography.

To devise a scheme that combined the strengths of only considering nearest neighbours with that of introducing sufficient numerical damping over significant orography, the variable off-centring scheme was modified further. Sensitivity studies revealed that the scheme performed more satisfactorily if the height difference used to determine the field of off-centring parameters was capped at a value lower than its absolute maximum. As a result, all grid points above the threshold cap for the orographic height difference with their neighbours were off-centred at the maximum off-centring parameter. This modification allowed the scheme to introduce sufficient numerical damping over significant orography while hardly altering the results in regions without significant orography.

In an alternative bid to improve the variable scheme, the linear scaling of the off-centring scheme was replaced with different scaling functions. While

exponential scaling did not affect the results at all, there was some effect from switching to a quadratic scheme. However, particularly where the differences between the results obtained with the quadratic scheme and the linear one were large, there was evidence that the results had actually deteriorated in comparison with a reference simulation.

Taking into account the evidence of the analytical results, the shallow water experiments and full GCM simulations, it can be concluded that spatially variable off-centring applied to a subset of the equations has the potential to become a viable alternative to the currently used constant off-centring techniques in semi-Lagrangian, semi-implicit models. While the benefits of reduced numerical damping in regions which are unaffected by the spurious numerical resonance are obvious, extensive further research far beyond the scope of this thesis will be necessary to establish if a GCM will stay stable for long enough to use this scheme without further adjustments.

While this thesis already showed some encouraging results which point to sufficient stability and a potential for model improvement from this approach, the scheme could certainly still be developed further in a number of ways. A scaling function could be devised which optimises the distribution of off-centring parameters. Furthermore, the capping approach could be combined with such different scaling functions or a minimum orographic height difference threshold could be introduced below which the centred advection scheme is always in use. With sufficient fine-tuning of both the off-centring scheme and the model as a whole, a variable off-centring scheme certainly has the potential of significantly improving the results from numerical models particularly in regions of little orography provided all potential stability problems are addressed appropriately.

# Bibliography

Adler, R. F., G. J. Huffman, A. Chang, R. Ferraro, P. Xie, J. Janowiak, B. Rudolf, U. Schneider, S. Curtis, D. Bolvin, A. Gruber, J. Susskind, and P. Arkin, 2003: The Version 2 Global Precipitation Climatology Project (GPCP) Monthly Precipitation Analysis (1979-Present). *J. Hydrometeor.*, **4**, 1147–1167.

Arakawa, A. and V. R. Lamb, 1977: Computational design of the basic dynamic process of the UCLA-GCM. *Methods in Computational Physics*, **17**, 173–265.

Bjerknes, V., 1914: Meteorology as an Exact Science. *Monthly Weather Review*, **42**, 11–14, doi:10.1175/1520-0493(1914)42<11:MAAES>2.0.CO;2.

Coiffier, J., P. Chapelet, and N. Marie, 1987: Study of various quasi-Lagrangian techniques for numerical models. *ECMWF Workshop on Techniques for Horizontal Discretization in Numerical Weather Prediction Models*, European Centre for Medium-Range Weather Forecasts, European Centre for Medium-Range Weather Forecasts, Shinfield Park, Reading, 19–46.

- Courant, R., K. Friedrichs, and H. Lewy, 1928: Über die partiellen Differentialgleichungen der mathematischen Physik. *Mathematische Annalen*, **100**, 32–74.
- Fjørtoft, R., 1952: On a Numerical Method of Integrating the Barotropic Vorticity Equation. *Tellus*, **4**, 179–194, doi:<http://dx.doi.org/10.1111/j.2153-3490.1952.tb01003.x>.
- 1955: On the Use of Space-Smoothing in Physical Weather Forecasting. *Tellus*, **7**, 462–480, doi:<http://dx.doi.org/10.1111/j.2153-3490.1955.tb01185.x>.
- Giraldo, F. X., J. B. Perot, and P. F. Fischer, 2003: A spectral element semi-Lagrangian (SESL) method for the spherical shallow water equations. *J. Comput. Phys.*, **190**, 623–650, doi:[http://dx.doi.org/10.1016/S0021-9991\(03\)00300-0](http://dx.doi.org/10.1016/S0021-9991(03)00300-0).
- Haltiner, G. J. and R. T. Williams, 1980: *Numerical Prediction and Dynamic Meteorology*. John Wiley & Sons, 2nd edition.
- Hortal, M., 1998: Aspects of the numerics of the ECMWF model. *Recent developments in numerical methods for atmospheric modelling*, European Centre for Medium-Range Weather Forecasts, European Centre for Medium-Range Weather Forecasts, Shinfield Park, Reading, 453.
- Kaas, E., 1987: *The construction of and tests with a multi-level, semi-Lagrangian and semi-implicit limited area model*. Ph.D. thesis, Geophysics Institute, Copenhagen University, Geophysics Institute, University of Copenhagen, Juliane Maries vej 30, DK-2100 Copenhagen O, Denmark, 117 pp.

- Krishnamurti, T. N., 1962: Numerical Integration of Primitive Equations by a Quasi-Lagrangian Advective Scheme. *Journal of Applied Meteorology*, **1**, 508–521, doi:10.1175/1520-0450(1962)001<0508:NIOPEB>2.0.CO;2.
- Kuettner, J., 1939: Zur Entstehung der Föhnwelle. *Beitr. Phys. Frei Atmos.*, **25**, 251–299.
- Kuettner, J. P., 1938: Moazagotl und Föhnwelle. *Beitr. Phys. Frei Atmos.*, **25**, 79–114.
- Leith, C. E., 1965: Lagrangian advection in an atmospheric model. Technical Report 66, WMO.
- Li, Y. and J. R. Bates, 1996: A study of the behavior of semi-Lagrangian models in the presence of orography. *Quarterly Journal Royal Meteorological Society*, **122**, 1675–1700.
- Lindberg, K. and V. A. Alexeev, 2000: A Study of the Spurious Orographic Resonance in Semi-Implicit Semi-Lagrangian Models. *Monthly Weather Review*, **128**, 1982–1989.
- Lorenz, E. N., 1963: Deterministic Nonperiodic Flow. *Journal of the Atmospheric Sciences*, **20**, 130–141.
- Mathur, M. B., 1970: A note on an improved quasi-Lagrangian advective scheme for primitive equations. *Monthly Weather Review*, **98**, 214–219, doi:10.1175/1520-0493(1970)098<0214:ANOAIQ>2.3.CO;2.
- McGregor, J. L., 1996: Semi-Lagrangian Advection on Conformal-Cubic Grids. *Monthly Weather Review*, **124**, 1311–1322, doi:10.1175/1520-0493(1996)124<1311:SLAOCC>2.0.CO;2.

- McGregor, J. L., 2005: C-CAM: Geometric Aspects and Dynamical Formulation. Technical Report 70, CSIRO Atmospheric Research, Aspendale VIC, Australia.
- McGregor, J. L. and M. R. Dix, 2008: An updated description of the conformal-cubic atmospheric model. *High Resolution Simulation of the Atmosphere and Ocean*, K. Hamilton and W. Ohfuchi, eds., Springer, 51–76.
- Nebeker, F., 1995: *Calculating the Weather: Meteorology in the 20th Century*. Academic Press, New York.
- Payne, T. J., 2008: A linear stability analysis of the semi-implicit semi-Lagrangian discretization of the fully compressible equations. *Quarterly Journal of the Royal Meteorological Society*, **134**, 779–786.
- Pedlosky, J., 1992: *Geophysical Fluid Dynamics*. Springer, 2nd edition.
- Phillips, N. A., 1954: Energy transformations and meridional circulations associated with simple baroclinic waves in a two-level, quasigeostrophic model. *Tellus*, **6**, 273286.
- 1956: The general circulation of the atmosphere: A numerical experiment. *Quarterly Journal of the Royal Meteorological Society*, **82**, 123–164, doi:10.1002/qj.49708235202.  
URL <http://dx.doi.org/10.1002/qj.49708235202>
- Press, W. H., S. A. Teukolsky, W. T. Vetterling, and B. P. Flannery, 2007: *Numerical Recipes 3rd Edition: The Art of Scientific Computing*. Cambridge University Press, New York, NY, USA, 3 edition.

- Purnell, D. K., 1976: Solution of the Advective Equation by Upstream Interpolation with a Cubic Spline. *Monthly Weather Review*, **104**, 42–48, doi:10.1175/1520-0493(1976)104<0042:SOTAEB>2.0.CO;2.
- Rančić, M., R. J. Purser, and F. Mesinger, 1996: A global shallow-water model using an expanded spherical cube: Gnomonic versus conformal coordinates. *Quarterly Journal of the Royal Meteorological Society*, **122**, 959–982, doi:http://dx.doi.org/10.1002/qj.49712253209.
- Richardson, L. F., 1922: *Weather Prediction by Numerical Process*. Cambridge University Press, Cambridge.
- Ritchie, H. and M. Tanguay, 1996: A Comparison of Spatially Averaged Eulerian and Semi-Lagrangian Treatments of Mountains. *Monthly Weather Review*, **124**, 167–181.
- Rivest, C., A. Staniforth, and A. Robert, 1994: Spurious Resonant Response of Semi-Lagrangian Discretizations to Orographic Forcing: Diagnosis and Solution. *Monthly Weather Review*, **122**, 366–376.
- Robert, A., 1969: The integration of a spectral model of the atmosphere by the implicit method. *WMO/IUGG Symposium on NWP*, Japan Meteorological Agency, Japan Meteorological Agency, Tokyo, VII.19–24.
- 1981: A stable numerical integration scheme for the primitive meteorological equations. *Atmosphere Ocean*, **19**, 35–46.
- Robert, A., J. Henderson, and C. Turnbull, 1972: An Implicit Time Integration Scheme for Baroclinic Models of the Atmosphere. *Monthly Weather Review*, **100**, 329–335.

- Saltzman, B., 1967: *The Encyclopedia of Atmospheric Sciences and Astrogeology*, Reinhold Publishing Corporation, chapter Meteorology: A Brief History. 583–591.
- Sawyer, J. S., 1963: A semi-Lagrangian method of solving the vorticity advection equation. *Tellus*, **15**, 336–342, doi:<http://dx.doi.org/10.1111/j.2153-3490.1963.tb01396.x>.
- Schmidt, F., 1977: Variable fine mesh in spectral global model. *Beitr. Phys. Atmos.*, **50**, 211–217.
- Staniforth, A. and J. Côté, 1991: Semi-Lagrangian Integration Schemes for Atmospheric Models - A Review. *Monthly Weather Review*, **119**, 2206–2223.
- Tanguay, M., E. Yakimiw, and H. Ritchie, 1992: A study of the behavior of semi-Lagrangian models in the presence of orography. *Monthly Weather Review*, **120**, 113–123.
- Whelan, R. F., 2000: *Exploring the Monster, Mountain Lee Waves: the Aerial Elevator*. Wind Canyon Books, Brawley, CA, USA, 2nd edition.
- Wiin-Nielsen, A., 1959: On the Application of Trajectory Methods in Numerical Forecasting. *Tellus*, **11**, 180–196, doi:<http://dx.doi.org/10.1111/j.2153-3490.1959.tb00019.x>.
- Williamson, D. L., J. B. Drake, J. J. Hack, R. Jakob, and P. N. Swarztrauber, 1992: A standard test set for numerical approximations to the shallow water equations in spherical geometry. *Journal of Computational Physics*, **102**, 211–224, doi:[10.1016/S0021-9991\(05\)80016-6](https://doi.org/10.1016/S0021-9991(05)80016-6).

- Wurtele, M. G., 1960: Lagrangian Dynamics and the Parcel Method in Atmospheric Models. *Journal of Atmospheric Sciences*, **17**, 661–669, doi:10.1175/1520-0469(1960)017<0661:LDATPM>2.0.CO;2.



# Appendix A

## SWiM Manual

### A.1 Prerequisites and Build Process

SWiM is written in Fortran 90. It was developed on GNU Fortran (`gfortran`) but has been tested in Intel Fortran and should compile on any Fortran 90 compiler. It links against the NetCDF library<sup>1</sup> and requires the NetCDF Fortran module (compiled with the same compiler). It also statically links against the library `sigwatch`<sup>2</sup> to catch system signals.

To build SWiM you might have to adjust `Makefile` to your system because SWiM currently does not use `autotools`. You can then just build the binary with a simple `make`. To build the debug mode binary (output ghost cells, bounds-checking), you can run `make debug` or `make all` to build both binaries at once.

---

<sup>1</sup><http://www.unidata.ucar.edu/software/netcdf/>

<sup>2</sup><http://nrg.me.uk/dist/sigwatch/>

## A.2 Code structure

SWiM consists of several modules which are explained in detail in Tab. A.1.

The main routine can be found in the file `swim.f90`.

Module Name	File Name	Description
<code>grid</code>	<code>grid.f90</code>	Sets up the grid structure and contains routines that are related to the grid like filling ghost cells, setting the off-centring profile, calculating the time step and finding the maximum orography gradient.
<code>helpers</code>	<code>helpers.f90</code>	Helper routines like interpolation, finding departure points, transform coordinates to grid coordinates and calculate derivatives.
<code>init</code>	<code>init.f90</code>	Usually only contains the initialisation routines. For more details refer to section A.7.
<code>tests</code>	<code>tests.f90</code>	Routines to calculate exact solutions. For more details refer to section A.8.
<code>input</code>	<code>input.f90</code>	Handles input from configuration, initialisation and resume files.
<code>integration</code>	<code>integration.f90</code>	All the equations are solved here.
<code>localconfig</code>	<code>localconFig.f90</code>	Allows the main routine and the signal handler (module <code>sighandler</code> ) to exchange some information.
<code>output</code>	<code>output.f90</code>	Handles all output to the NetCDF files (output and resume).
<code>output_debug</code>	<code>output_debug.f90</code>	A copy of the module <code>output</code> but writes the ghost cells to the NetCDF output file as well. The target <code>debug</code> in the makefile uses this module and builds a binary called <code>swim-debug</code> .
<code>sighandler</code>	<code>sighandler.f90</code>	Handles system signals to guarantee clean shutdown on terminate signal.

Table A.1: Modules in SWiM

If you want to add global variables to the code, in most cases these should

be placed in the module `grid`. This module is included by almost all other modules.

### A.3 Configuration options for SWiM

<code>adaptive_timestep</code>	Set to 1 if time step should be adapted to the prescribed Courant number in every time step. Does not work with option <code>dt</code> .
<code>alpha1</code>	Off-centring parameter for height terms in momentum equations. Only has an effect if <code>offcentring</code> is set.
<code>alpha2</code>	Off-centring parameter for Coriolis terms in momentum equations. Only has an effect if <code>offcentring</code> is set.
<code>alpha3</code>	Off-centring parameter for momentum terms in height equation. Only has an effect if <code>offcentring</code> is set.
<code>alpha_search_radius</code>	Sets the radius in which the largest gradient should be found as a basis for the local off-centring parameters. Only has an effect if <code>variable_alpha</code> is set. <sup>1</sup>
<code>cell_size_x</code>	Grid cell size in x in meters.
<code>cell_size_y</code>	Grid cell size in y in meters.

---

<sup>1</sup>For technical reasons, SWiM enforces that the search radius is no larger than the number of ghost cells decremented by one. This ensures that the search algorithm will not try to look for orography values beyond the grid in memory. However, there is no lower limit for the search radius with a value of zero meaning that only the local gradients (i.e. the gradients with the four nearest neighbours) are used. This maximum value is also the default.

<code>coriolis_parameter</code>	Coriolis parameter for used f-plane. Can also be set as a latitude. Options <code>coriolis_parameter</code> and <code>latitude</code> are mutually exclusive.
<code>courant_number</code>	Prescribed maximum Courant number. If <code>adaptive_timestep</code> is set, time step will always be adapted to keep maximum Courant number at this value. Without <code>adaptive_timestep</code> initial time step will be determined from this Courant number and initial conditions. Model will then be run with constant time step.
<code>departure_points</code>	Algorithm to use to find departure points. If unset, algorithm according to ( <a href="#">McGregor, 2005</a> , p. 15) is used. If set, algorithm according to ( <a href="#">Staniforth and Côté, 1991</a> ) will be used. Please refer to section <a href="#">3.3.4</a> for more details. Options <code>courant_number</code> and <code>dt</code> are mutually exclusive.
<code>dt</code>	Set fixed time step in seconds. Options <code>courant_number</code> and <code>dt</code> are mutually exclusive.

<code>ghostcells</code>	Number of ghost cells <sup>2</sup> to use. If <code>variable.alpha</code> is set, this is also the radius (in grid cells) to consider for orography gradient to determine local off-centring parameters.
<code>grid.height</code>	Number of grid cells in y.
<code>grid.width</code>	Number of grid cells in x.
<code>init.from.file</code>	If set, file in <code>resume</code> will be used for initialisation instead of <code>resume</code> .
<code>iterations</code>	Number of iterations to run the model for. If used together with <code>max.time</code> , model run will stop whenever either condition is met.
<code>latitude</code>	Options <code>coriolis.parameter</code> and <code>latitude</code> are mutually exclusive.
<code>max.time</code>	Maximum model time to run in seconds. If used together with <code>iterations</code> , model run will stop whenever either condition is met.
<code>mean.height</code>	Mean height $\bar{\varphi}$ for linearised height equation.
<code>offcentring</code>	Switches off-centring on. Without setting this switch, settings for <code>alphaX</code> have no effect.

---

<sup>2</sup>The term ghost cells refers to copies of grid points near the boundary which artificially enlarge the domain to allow for a simple handling of the periodic boundaries.

<code>orography_type</code>	Determines the way the orographic forcing is done in the equations. Default is as in <a href="#">Rivest et al. (1994)</a> . If set, orographic forcing as in <a href="#">Pedlosky (1992)</a> is used. Please refer to section <a href="#">3.2</a> for details.
<code>output_interval</code>	Output frequency in time steps. Variables $u(x, y, t)$ , $v(x, y, t)$ , $\varphi(x, y, t)$ and $\alpha_n(x, y, t)$ will be written to output file.
<code>output_time_interval</code>	Output frequency in seconds. Variables $u(x, y, t)$ , $v(x, y, t)$ , $\varphi(x, y, t)$ and $\alpha_n(x, y, t)$ will be written to output file. Overrides <code>output_interval</code> .
<code>outputfile</code>	Name of output file.
<code>resume</code>	File to resume from. If the file contains only data for one time step, the model will be initialised with that data instead.
<code>resume_point_interval</code>	Number of time steps between writing resume files. Also see <code>resume</code> for naming scheme of resume files.
<code>resume_file_base</code>	Name base for resume files. Resume file number and <code>.nc</code> will be appended. Defaults to <i>resume with resume files being called <code>resumeXXXXXX.nc</code></i> .
<code>variable_alpha</code>	If set, $\alpha_n$ will be variable over the computational domain as described in section <a href="#">3.5</a> .

## A.4 Command line options

All command line options except for the option that sets the configuration file have equivalents in the configuration file. As Fortran 90 comes without an implementation of `getopt`, the implementation for command line options is rather frail and does only accept command line options that are specified as

```
-x <value>  
--option-x <value>
```

but not ones that are specified without a space between the option and the value or using an equals sign between the option and value.

The accepted options are

<code>-c, --config-file</code>	Name and path of configuration file.
<code>-o, --output-file</code>	Name and path of output file. Cf. variable <code>output_file</code> in configuration file.
<code>-n, --iterations</code>	Number of iterations. Cf. variable <code>iterations</code> in configuration file.

<code>-t, --max-time</code>	Amount of model time to run the model for. Cf. variable <code>max_time</code> in configuration file.
<code>-l, --output-interval</code>	Interval (in time steps) in which output is written. Cf. variable <code>output_interval</code> in configuration file.
<code>-r, --resume-points</code>	How often to write resume files. Cf. variable <code>resume_point_interval</code> in configuration file.
<code>-i, --from-file</code>	Name and path of file to resume or initialise from. Cf. variable <code>resume</code> in configuration file.

and the switch

<code>-nr, --new-run</code>	Sets the <code>init_from_file</code> flag.
-----------------------------	--

SWiM is usually invoked as

```
./swim [<options and switches>]
```

Either a maximum model time or a maximum number of iterations and an output interval have to be set either in the configuration file or on the command line. All other settings are optional as long as they are not required by another option already set. SWiM should always throw an error and exit if the configuration is inconsistent.

## A.5 Off-centring

The off-centring parameters can have to be set independently. If off-centring is switched on (switch `offcentring`, all three off-centring parameters are expected in the config file. If they aren't found, they default to 0.5 (centred).

For the variable off-centring scheme, a search radius can be defined in `alpha_search_radius`. If `alpha_search_radius` is not set, the search radius is set equal to the number of configured ghost cells decremented by one. This value is also the maximum search radius that can be set for technical reasons. Any search radius larger than this number will be lowered to the maximum.

## A.6 Initialisation and Restart

### A.6.1 Initialisation

SWiM model runs are initialised either by the function `initialise_grid` in the module `init` or from a file. If the model run is initialised from a file, the file has to be in NetCDF format and contain at least the variables `u`, `v`, `phi` and `phioro`. All other model parameters need to be defined in the configuration file or on the command line. The NetCDF file needs to have at least the dimensions `x` and `y`. An extra dimension `t` is ignored with the initialisation data read from the first time step in the file.

If the resolution of the initialisation data do not match the resolution set in the model configuration, the input data are assimilated using bi-cubic

interpolation. Assimilation is possible from both higher and lower resolution in the input data.

If initialisation is to be executed by the model code (as opposed to initialisation from file), only the subroutine `initialise_grid` in module `init` needs to be modified.

## A.7 Initialisation routine

If you want to replace the initialisation routine, you need to replace the routine `initialise_grid` in the module `init` (file `init.f90`). The following shows the signature and first lines of the routine. All physical variables set in the configuration file are available in the module. The parameter `test` is explicitly passed to the routine `initialise_grid`.

```
module init
```

```
    use grid
```

```
    implicit none
```

```
contains
```

```
    !> Initialises the grid.
```

```
    !> @param testcase Testcase to run (if configured)
```

```
    subroutine initialise_grid(testcase)
```

```
integer :: i
integer :: j
integer :: testcase

! allocate arrays
allocate(x(xdim+2*gc))
allocate(y(ydim+2*gc))
allocate(uold(xdim+2*gc,ydim+2*gc))
allocate(vold(xdim+2*gc,ydim+2*gc))
allocate(phiold(xdim+2*gc,ydim+2*gc))
allocate(u(xdim+2*gc,ydim+2*gc))
allocate(v(xdim+2*gc,ydim+2*gc))
allocate(phi(xdim+2*gc,ydim+2*gc))
allocate(exact(xdim+2*gc,ydim+2*gc))
allocate(unew(xdim+2*gc,ydim+2*gc))
allocate(vnew(xdim+2*gc,ydim+2*gc))
allocate(phinew(xdim+2*gc,ydim+2*gc))
allocate(phioro(xdim+2*gc,ydim+2*gc))
allocate(alpha(xdim+2*gc,ydim+2*gc,2,3))
allocate(epsilon(xdim+2*gc,ydim+2*gc,3))
...
```

### Restart

Models can be configured to regularly write restart files which can then be used to initialise a new model run with. While initialisation will only read data for one time step and start from these initial conditions, a restart reads

two time levels and a time step  $\Delta t$ . In principle, restarts are performed the same way as initialisations, just that they read in two time levels. The NetCDF file therefore has to have a dimension `t` and at least data for two time levels. If more than two time steps are found in the file, the first two will be used. The starting time is set to the time found in the restart file.

## A.8 Tests

The main routine calls a routine `exact_solution(test)` which is expected to be found in module `tests`. The parameter passed is the parameter `test` from the configuration file. This parameter can be used to distinguish between different test cases in the initialisation routines and the routine to calculate an exact solution.

## A.9 Output format

SWiM writes to NetCDF files. The output and resume files are identical in structure and have a structure as follows.

```
netcdf swim {  
dimensions:  
    x = ... ;  
    y = ... ;  
    t = UNLIMITED ; // (... currently)  
variables:  
    double t(t) ;
```

```
    double x(x) ;
    double y(y) ;
    double phibar ;
    double latitude ;
    double phioro(x, y) ;
    double u(t, x, y) ;
    double v(t, x, y) ;
    double phi(t, x, y) ;
    double exact(t, x, y) ;
    double epsilon1(t, x, y) ;
    double epsilon2(t, x, y) ;
    double epsilon3(t, x, y) ;
}
```

Initialisation and resume files are expected to have this structure, too. However, *x*, *y*, *phibar* and *latitude* will not be read from the NetCDF file but are expected to be found in the configuration file.

## A.10 Plotting Scripts

SWiM comes with several plotting scripts which are all written in Python. They use the python modules matplotlib, pyplot, numpy, getopt and sys. NetCDF is handled using the NIO library but the scripts also contain commented out lines of code which use the Scientific.IO.NetCDF library instead. All scripts have very similar APIs.

### A.10.1 `epsilon-plot.py`

The script `epsilon-plot.py` plots the 2D profile for the off-centring parameters. Only useful in the case of variable off-centring.

Usage: `epsilon-plot.py` [`<options>`] `<NetCDF file>`

```
--minval      Minimum value for colour scale
--maxval      Maximum value for colour scale
-d,--dynamic  Off-centring is dynamic => plot maps
               for every time step
-t, --transpose transpose value matrix before plotting
-p, --prefix  prefix for output files
```

### A.10.2 `oroplot.py`

The script `oroplot.py` plots the 2D profile of the orography.

Usage: `oroplot.py` [`<options>`] `<NetCDF file>`

```
--minval      Minimum value for colour scale
--maxval      Maximum value for colour scale
-t, --transpose transpose value matrix before plotting
-p, --prefix  prefix for output files
```

### A.10.3 `oroplot-slice.py`

The script `oroplot-slice.py` plots a 1D slice through the orography.

```
Usage: oroplot-slice.py [<options>] <NetCDF file> \  
    <dimension (x/y)>  
--minval      Minimum value for colour scale  
--maxval      Maximum value for colour scale  
-p, --prefix  prefix for output files  
-c, --position= position to slice through 2D field
```

### A.10.4 swimplot.py

The script `swimplot.py` plots any time dependent value from SWiM's NetCDF file.

Usage: `swimplot.py` [`<options>`] `<NetCDF file>`

```

                                <time dependent variable>
--colour-min=<minimum value>   Minimum of colour
                                scale (white if under),
                                implies --minval
--colour-max=<maximum value>   Maximum of colour
                                scale (black if over),
                                implies --maxval
-d=<time dependent variable>,
--diff=<time dependent variable> Plot difference
                                <main variable>-<this variable>
-i, --interactive               Plot interactively
                                (requires X)
--minval=<minimum value>       Minimum value for
                                colour scale
--maxval=<maximum value>       Maximum value for
                                colour scale
--minx=<minimum value>        Minimum coordinate in x
                                (default: 0)
--maxx=<maximum value>        Maximum coordinate in x
                                (default: full)
--miny=<minimum value>        Minimum coordinate in y
                                (default: 0)

```

```

--maxy=<maximum value> Maximum coordinate in y
                        (default: full)

-n, --dry-run    Do not plot anything.

-t, --transpose Transpose value matrix before plotting

-p, --prefix=<prefix> Prefix for output files

--quiver=<scale factor> Overlay with quiver plot of
                        velocity (scale with factor)

-x <xmin-xmax> Range in x to plot
                (equivalent to --minx and --maxx)

-y <ymin-ymax> Range in y to plot
                (equivalent to --miny and --maxy)

```

### A.10.5 swimplot-slice.py

The script `swimplot-slice.py` plots a 1D slice through any time dependent value from SWiM's NetCDF file.

Usage: `swimplot-slice.py` [<options>] <NetCDF file>

<time dependent variable>

<dimension (x/y)>

```

--minval          Minimum value for colour scale
--maxval          Maximum value for colour scale
-p, --prefix     prefix for output files
-c, --position=  position to slice through 2D field
-n, --dry-run\t  do not actually run plot but only
                  determine scale

```

### A.10.6 swimplot-vorticity.py

The script `swimplot-vorticity.py` calculates the total absolute vorticity in the domain as

$$\omega_{\text{tot}} = \sum_{\text{domain}} |\partial_x v - \partial_y u| \quad (\text{A.1})$$

and plots the total absolute vorticity function for every NetCDF file passed to the script. The passed labels are output to the generated figure's legend.

Usage: `swimplot-vorticity.py` [`<options>`] `<NetCDF file>` `<label>`  
`[<NetCDF file> <label> ...]`

<code>-c</code>	Use colour (default is monochrome)
<code>--minval</code>	Minimum value for colour scale
<code>--maxval</code>	Maximum value for colour scale
<code>-p, --prefix</code>	prefix for output files
<code>-n, --dry-run</code>	do not actually run plot but only determine scale

### A.10.7 swimplot-energy.py

The script `swimplot-energy.py` calculates the kinetic energy per unit mass in the domain as

$$E_{\text{kin}} = \sum_{\text{domain}} \frac{1}{2} (u^2 + v^2) \quad (\text{A.2})$$

and plots the kinetic energy per unit mass for every NetCDF file passed to the script. The passed labels are output to the generated figure's legend.

